

UNIVERSIDADE DE SÃO PAULO
INSTITUTO DE FÍSICA DE SÃO CARLOS

PATRÍCIA CHRISTINA MARQUES CASTILHO

New experimental system to study coupled
vortices in a two-species Bose-Einstein
condensate ^{23}Na - ^{41}K with tunable
interactions

São Carlos

2017

PATRÍCIA CHRISTINA MARQUES CASTILHO

**New experimental system to study coupled vortices
in a two-species Bose-Einstein condensate ^{23}Na - ^{41}K
with tunable interactions**

Thesis presented to the Graduate Program in
Physics at the Instituto de Física de São Carlos,
Universidade de São Paulo to obtain the degree
of Doctor of Science.

Concentration area: Basic Physics

Advisor:

Prof. Dr. Vanderlei S. Bagnato

Corrected Version

(Original version available on the Program Unit)

São Carlos

2017

AUTORIZO A REPRODUÇÃO E DIVULGAÇÃO TOTAL OU PARCIAL DESTE TRABALHO, POR QUALQUER MEIO CONVENCIONAL OU ELETRÔNICO PARA FINS DE ESTUDO E PESQUISA, DESDE QUE CITADA A FONTE.

Ficha catalográfica revisada pelo Serviço de Biblioteca e Informação do IFSC,
com os dados fornecidos pelo(a) autor(a)

Castilho, Patrícia Christina Marques
New experimental system to study coupled vortices
in a two-species Bose-Einstein condensate ^{23}Na - ^{41}K
with tunable interactions / Patrícia Christina
Marques Castilho; orientador Vanderlei Salvador
Bagnato - versão corrigida -- São Carlos, 2017.
213 p.

Tese (Doutorado - Programa de Pós-Graduação em
Física Básica) -- Instituto de Física de São Carlos,
Universidade de São Paulo, 2017.

1. Bose-Bose mixtures. 2. Feshbach resonances. 3.
Rotating BEC. 4. Stirring beam. 5. Vortex lattice.
I. Bagnato, Vanderlei Salvador, orient. II. Título.

*To my parents, my sister
and the lovely white hair I
acquired during this thesis.*

Acknowledgements

I first would like to thank my parents, Eduardo and Liliana. Thanks to my father, who showed me many worlds; worlds from the past with huge dinosaurs; from the present, teaching me how to read the hours; from the future, creating a computer program named “Paty”; and from the “eternal”, showing me the other planets, stars and comets with his celestial chart. Thanks to my mother, from who I took it all, the desire to learn, to study music, arts, to crochet, to be always in a rush, the will to want to do all and always go beyond my limits.

Thanks to my sister Natássia, younger sister, friend, best friend, strong and determined woman with whom I laugh, cried, played many games, argued some times but always knew I could count on her as she can always count on me.

Thank you to Raul who, besides being the person I chose to spend the most of my life with, is a very good friend with whom I can talk about everything any time, who makes me happy by just being there and who supported me in all the crazy things I wanted to (and thought to) do.

Thank you to Rodrigo, my dearest friend who have followed and helped me all the way to the end of this thesis and makes me miss even more the TV series House.

Thanks to my friend Luana with whom I started my studies in Physics eleven years ago, shared the apartment and had so many good times in everything we decided to do together.

Thank you to all my friends, specially Nicole and Zoe (from whom I had always a surprise when coming back home), Mariana (who was also in Florence by the time I spent there and thought me the way to make Italian friendships), Gustavo (aligned a fiber in the lab even without understanding Physics), Victor (for being a very funny and good person and for cars collection) and Gabriel (for all the work we done together during our undergrad course in cinema), with whom I have a lot of fun during these years and who

helped to clear my head in the most stressful moments while I was doing both my PhD and an undergrad course in Cinema.

Thanks to my former laboratory colleagues and forever friends: Jorge, with whom I learned the way how to work in the lab, for the good (being very precise) and for the bad (being very precise!), learned a little of Spanish, a little of Italian (too!) and could travel together during the time I was in Italy. And Freddy, with whom I could really make the BEC-II work, by the end of my master and who always listened to my crises and gave me lots of advises.

I would like to thank very much the NaK team, starting by my thesis advisor Prof. Vanderlei Bagnato, who from the very beginning of my studies had made me get interested in atomic Physics. Thanks to our permanent collaborator, Giacomo Roati, with whom it was really funny (and exciting! and fast!) to work, that even from the other side of the ocean, was always full of ideas and advises teaching me a lot of how to do experimental atomic physics and with whom I had the pleasure to eat many pizzas in Florence. Thanks to Kilvia, the permanent researcher of the NaK experiment who helped a lot to put all things of this experiment together and working. Thanks to my other colleagues in the NaK experiment: Edwin, that was with me from the time we started building up the experimental system; Emmanuel, the new PhD student, who will have the exciting task of keeping the machine working and start to do new Physics; and Kelli, who stayed with us for a short time but was a really nice person to work with. The undergrad students: Victor, that helped a lot on setting up the Feshbach system; Pedro, who was really calm and always helpful in any occasion; and Pablo, who was very into the experiment and a very funny person who made my working days funnier.

I would also like to thank the 39K team with whom I worked during my intership at LENS, starting by Marco Fattori who made me fell very welcome to the team and taught me a lot of different Physics from what I was used to do in Brazil. Thanks to Giovanni Modugno from whom I learned all I know about Anderson localization. Thanks to Andrea, who I admire for the amazing dedication he has to his work. Thanks to Manuele, who really showed me all the technical details of the 39K experiment such that I could be

able to design a potassium setup for the NaK experiment once I was back. Thanks to the other PhD students, Giulia and Giacomo Spagnoli, who also became a very good friend during the long talks and movies we watched together. Thank you to the other people at LENS that made me my stay much pleasurable: Eleonora, Chiara, Sara, Claudia, Ivana, Lorenzo and Luca.

Thanks to all the other people that work with atomic Physics in our group: Rafael (who was always there to give a help with the dye laser), Pedro (who helped me never forget any PhD deadline), Amilson, Franklin (who helped with the 3D figures), Gustavo, Prof. Emanuel (with whom I could work and learn while assisting him in classes), Prof. Daniel (who helped to improve many technical details of the NaK experiment) and Prof. Phillipe and all the people that worked in his group during these years, specially Paulo and Romain.

I would like to give a special thank you for the theoreticians Monica and André, who were always present to discuss any doubts and possibilities for the experiment.

Thanks to the people from the electronic workshop, specially João, who was always ready to help us with any of the invented electronic circuits we needed for the experiment.

Thanks to the mechanical technicians Evaldo and Leandro, who did all the structural changes and improvements we needed during the years of this PhD.

Thanks to the people of the mechanical workshop, specially Ademir, without who we could not have done none of the results presented in this thesis, since many pieces of the vacuum setup (and much more things) were done in this workshop.

Thanks to all the group secretaries (former and new), Isabel, Cristiane, Bene, Adriane, Wagner, Patricia, who besides helping us with scholarships, buying materials or printing graphs to our weekly meeting with Prof. Vanderlei, were always nice to talk to while taking a coffee.

Thanks to the people on the graduate school secretary, specially Ricardo and Silvio, who helped me in all the bureaucratic things we have to do along the PhD.

Thanks to Neusa, the librarian who revised all this thesis and to Ítalo, the respon-

sible for the printing service at USP, who made an effort in order to print this thesis in time.

Thanks to the supporting agencies CAPES and CNP, the grant #2014/14198 – 0, São Paulo Research Foundation (FAPESP) and to the program “Ciencia sem fronteiras” which gave me the scholarship for my internship in Florence.

“Mrs. Dalloway said she would buy the flowers herself.”

Virginia Woolf (1882 - 1941)

Abstract

CASTILHO, P. C. M. **New experimental system to study coupled vortices in a two-species Bose-Einstein condensate ^{23}Na - ^{41}K with tunable interactions.** 2017. 213 p. Thesis (Doutorado em Ciências) - Instituto de Física de São Carlos, Universidade de São Paulo, São Carlos, 2017.

Two-component fluids can be miscible (if they overlap in space) or immiscible (if they remain phase-separated). In the context of trapped two-species Bose-Einstein condensates (BECs), these miscibility regions can only be fully characterized if one considers the interspecies interaction, the mass ratio and the number of atoms in each species. The dynamics of coupled vortices is different for each miscibility region and exotic vortices configurations (such as, square vortex lattices, “vortex sheets”, *skyrmions*, etc.) are expected to occur. In this thesis, we present the construction of a new experimental system able to produce a two-species Bose-Einstein condensate of ^{23}Na - ^{41}K atoms with tunable interspecies interactions and study the dynamics of coupled vortices in the different miscibility regimes. The BEC of sodium atoms obtained first in a Plug trap and later, in a crossed optical dipole trap, is fully characterized as well as the cold atomic cloud of potassium atoms produced by means of a Gray molasses cooling procedure. In the crossed optical dipole trap, the vortices will be nucleated with the use of a *stirring* beam. Therefore, in the end of this thesis, we present the stirring beam setup and its characterization prior aligning it into the ^{23}Na BEC.

Keywords: Bose-Bose mixtures. Feshbach resonances. Rotating BEC. Stirring Beam. Vortex lattice.

Resumo

CASTILHO, P. C. M. **Novo sistema experimental para a estudo de vórtices acoplados em um condensado de Bose-Einstein de duas espécies atômicas ^{23}Na - ^{41}K com interação variável.** 2017. 213 p. Tese (Doutorado em Ciências) - Instituto de Física de São Carlos, Universidade de São Paulo, São Carlos, 2017.

Um sistema de dois fluídos pode ser miscível (se os fluídos ocupam a mesma região do espaço) ou imiscível (se eles permanecem separados). No caso de condensados de Bose-Einstein (do inglês, “*Bose-Einstein condensate*” - BEC) de duas espécies atômicas aprisionados, as regiões de miscibilidade só podem ser completamente caracterizadas se considerarmos a interação entre as espécies, a razão entre as massas e o número de átomos em cada uma das espécies. A dinâmica de vórtices é diferente para cada região de miscibilidade possibilitando a obtenção de configurações exóticas de vórtices (como, a produção de redes de vórtices quadradas, de folhas de vórtices (do inglês, “*vortex sheets*”), *skyrmions*, etc.). Nesta tese, apresentamos a construção de um novo sistema experimental capaz de produzir um condensado de Bose-Einstein de duas espécies atômicas, ^{23}Na - ^{41}K , com interação variável e estudar a dinâmica de vórtices em diferentes regimes de miscibilidade. O condensado de átomos de sódio, inicialmente obtido na armadilha *Plug* e depois, em uma armadilha ótica cruzada, é completamente caracterizado assim como a nuvem atômica ultra-fria produzida a partir da técnica de molasses cinza (do inglês, “*Gray molasses*”). Na armadilha ótica, os vórtices serão produzidos a partir da utilização de um feixe de laser denominado *stirring*. Assim, ao final da tese, apresentamos o esquema ótico para a produção deste feixe de laser e a sua caracterização antes de alinhá-lo nos átomos.

Palavras-chaves: Misturas bóson-bóson. Resonâncias de Feshbach. Condensados gigantes. Técnica de *stirring*. Rede de vórtices.

List of Figures

Figure 1 – Triangular-shaped vortex lattices observed in liquid ^4He (a) and in atomic BECs (b) and (c).	33
Figure 2 – Pictures showing the surrounds of the NaK vacuum system right after closing it by the end o May 2014 and at the beginning of 2017	37
Figure 3 – Different miscibility regions for a two-component BEC	57
Figure 4 – Possible topologies for a binary mixture of two-species BECs.	60
Figure 5 – Phase-diagram for the miscibility regions of a two-component BEC composed of ^{39}K and ^{87}Rb atoms.	62
Figure 6 – Simulated density profile along the vertical direction for the ground-state of the ^{23}Na - ^{41}K BEC across the different miscibility regions.	67
Figure 7 – Simulated density profile along the vertical direction for the ground-state of the ^{23}Na - ^{41}K BEC for different numbers of sodium atoms and fixed interspecies interaction with $a_{12} = 50a_0$	68
Figure 8 – Simulated density profile along the vertical direction for the ground-state of the ^{23}Na - ^{41}K BEC with the addition of an external magnetic field gradient that partially compensates the gravitational force acting on the atoms.	69
Figure 9 – Comparison between the rotation of a BEC and a rigid-body.	78
Figure 10 – Vortex lattices in rotating weakly-interacting BECs.	80
Figure 11 – Two-component BEC under rotation with coupled vortex lattices.	82
Figure 12 – Density profiles of a rotating two-component BEC in the miscible and immiscible regimes for different rotational frequencies.	84
Figure 13 – Comparison between the phase diagrams for the nucleation of vortices in a two-component BEC with slightly different intraspecies interactions.	85
Figure 14 – Density profiles of a rotating two-component BEC with mass ratio $\eta^* = 2$ and attractive interspecies interaction.	86
Figure 15 – NaK experiment vacuum system	91

Figure 16 – NaK experiment vacuum system composition	92
Figure 17 – Hyperfine energy states of the D ₂ line of sodium atoms.	95
Figure 18 – ²³ Na 2D-MOT setup.	96
Figure 19 – Table containing the sodium 2D-MOT optimized parameters.	96
Figure 20 – Picture of the cigar-shaped 2D-MOT cloud of sodium atoms.	97
Figure 21 – Top view of the complete optical scheme around the science chamber of the NaK experiment.	98
Figure 22 – Characterization of the Dark-SPOT MOT for ²³ Na atoms.	99
Figure 23 – Comparison between the fluorescence signals from the <i>bright</i> and dark- SPOT MOTs of ²³ Na.	100
Figure 24 – Scheme for calculating the normalized absorption image.	101
Figure 25 – Experimental sequence for transferring the atoms from the dark-SPOT MOT to the Plug trap.	103
Figure 26 – Energy of the 3 ² S _{1/2} hyperfine states of sodium atoms (a) and of the 5 ² S _{1/2} hyperfine states of potassium atoms (b) as a function of the applied magnetic field in the low field limit.	106
Figure 27 – Lifetime of ²³ Na (in blue) and ⁴¹ K (in orange) in the Quadrupole trap due only to Majorana losses.	108
Figure 28 – Plug trap potential for sodium and potassium atoms.	111
Figure 29 – Table with the relevant parameters of the Plug trap for sodium and potassium atoms	112
Figure 30 – Lifetime of the ²³ Na atoms in the Plug trap.	113
Figure 31 – Experimental sequence of the sodium atoms trapped in the Plug trap until it reaches the BEC.	114
Figure 32 – Working scheme of the RF-forced evaporative cooling procedure for atoms in the 1, -1⟩ state trapped by a harmonic magnetic trap.	116
Figure 33 – Pictures of the trapped ²³ Na atoms at different steps of the evaporation ramp.	117
Figure 34 – Log-log graph of <i>N vs. T</i>	118

Figure 35 – Images and density profiles for different values of the RF-evaporation frequency below 1 MHz.	119
Figure 36 – Plug trap frequencies measured exciting parametric oscillations of the atomic cloud.	121
Figure 37 – Comparison between the simulated and measured values for the Plug trap parameters.	121
Figure 38 – Level diagrams for the hyperfine states of the D ₁ and D ₂ lines for ³⁹ K and ⁴¹ K.	125
Figure 39 – Stages on mounting the MOPAs used to amplify the power of the light needed for the potassium atoms	127
Figure 40 – Characterization of the 2D-MOPA for amplifying the laser power needed for the potassium MOT.	128
Figure 41 – ³⁹ K 3D-MOT loading as a function of time.	130
Figure 42 – Potassium 2D-MOT optimized parameters.	130
Figure 43 – Scheme of the experimental sequence for trapping the ³⁹ K atoms in the magnetic trap.	132
Figure 44 – Working scheme for the Gray molasses	134
Figure 45 – Absorption and dispersion signals for the D ₁ of potassium atoms.	136
Figure 46 – Optical setup for generating the light resonant with the D ₁ transitions of potassium atoms.	137
Figure 47 – Temperature and atom number of the ³⁹ K atomic cloud as a function of d after 7.5ms of Gray molasses.	138
Figure 48 – Fluorescence signal from the sodium (blue curve) and potassium (orange curve) MOTs.	140
Figure 49 – Simplified experimental sequence for performing the Two-stage MOT loading procedure.	141
Figure 50 – Characterization of the trapped ²³ Na and ³⁹ K atoms after performing the Two-stage MOT loading procedure.	142
Figure 51 – Gravity assisted spin purification scheme for sodium atoms.	144

Figure 52 – Characterization of the gravity-assisted spin purification for sodium atoms.	145
Figure 53 – Comparison between the lifetimes and temperatures of the sodium atoms in the magnetic trap trapped in the $ 1, -1\rangle$ and in the $ 2, 2\rangle$ states, with and without the spin purification.	146
Figure 54 – Lifetime of the ^{23}Na BEC in the Plug trap.	148
Figure 55 – Calculated values for the frequencies and the depths for sodium and potassium atoms in a crossed ODT with $P_1 = P_2 = 5.5\text{W}$ and $w_{01} = w_{02} = 80\mu\text{m}$	151
Figure 56 – Optical setup of the laser beams used to produce the crossed optical dipole trap.	152
Figure 57 – Scheme of the experimental sequence used to produce the BEC of sodium atoms in the crossed ODT.	153
Figure 58 – Characterization of the optical evaporation performed in the crossed ODT.	154
Figure 59 – Bimodal density profile for the atomic cloud in the crossed ODT at different steps of the evaporation.	155
Figure 60 – Measurement of the crossed ODT frequencies.	157
Figure 61 – Lifetime of the condensed cloud in the crossed ODT.	158
Figure 62 – Cross-section view of the vertical MOT beam, the imaging beam and the stirring beam around the science chamber.	160
Figure 63 – Scheme for the optical system of the stirring beam.	161
Figure 64 – <i>In situ</i> images of the sodium atoms in the crossed ODT taken along the horizontal (a) and vertical (b) directions.	162
Figure 65 – In (a) and (b) we show pictures of the crossed AOMs used to produce the stirring beam and in (c) a picture of the diffracted pattern after the previous setup.	163
Figure 66 – Lissajous figures produced by the stirring beam and imaged by a beam profile.	164

Figure 67 – Size of the Lissajous figures produced for $f_{\text{vert}}/f_{\text{horiz}} = 1$ as a function of the modulation amplitude.	165
Figure 68 – Mapping of the stirring beam position in the ^{23}Na BEC while simulating a circle with radius of $\sim 40 \mu\text{m}$	167
Figure 69 – Recently achieved vortex lattice in the BEC of sodium atoms.	168
Figure 70 – Molecular potentials between two atoms.	196
Figure 71 – Scattering length and molecular energy as a function of the external magnetic field.	196
Figure 72 – Measurement of the Feshbach resonances by means of atom loss.	198
Figure 73 – Simulated Feshbach resonances between ^{23}Na and ^{41}K atoms at the $ 1, 1\rangle$ hyperfine state.	199
Figure 74 – Scheme of the Feshbach coils around the science chamber of the NaK experiment.	200
Figure 75 – Stages on building up the Feshbach coils setup.	201
Figure 76 – Characterization of the magnetic field produced by the Feshbach coils for $I = 1 \text{ A}$	202
Figure 77 – (a) Picture of the one Quadrupole coil mounted inside the housing. (b) Scheme of the quadrupole coils setup around the science chamber of the NaK vacuum system, represented in gray.	208
Figure 78 – Measurement of the Plug beam waist around the focus.	209
Figure 79 – Typical absorption (in red) and dispersion (in gray) signals obtained from the saturated absorption spectroscopy and used to frequency lock the Potassium lasers.	212
Figure 80 – Scheme of the laser setup for potassium atoms.	213

List of abbreviations and acronyms

2D	Two-dimensional
3D	Three-dimensional
BCS	Bardeen–Cooper–Schrieffer theory
BEC	Bose-Einstein condensate
C-MOT	Compressed MOT stage
GPE	Gross-Pitaevskii equation
LENS	European Laboratory for Non-Linear Spectroscopy
LFS	Low field seekers
Low-MOT	Low power MOT stage
MOPA	Master oscillator power amplifier
MOT	Magneto-optical trap
MT	Magnetic (quadrupole) trap
ODT	Optical dipole trap
PSD	Phase-space density
QT	Quantum Turbulence
QUIC	Quadrupole-Ioffe configuration
SC	Science chamber
TFA	Thomas-Fermi approximation
VSCPT	Velocity-selective coherent population transfer

List of symbols

h (\hbar)	Planck constant ($h/2\pi$)
k_B	Boltzmann constant
λ_{dB}	de Broglie wavelength
m_i	Atomic mass of the i atomic species
m_{12}	Reduced mass of the two-component system
η^*	Mass ratio between two atomic species
N_0	Number of atoms in the condensate
N_{ex}	Number of atoms in the excited states
T_c	Critical temperature for condensation
μ	Chemical potential
ρ_{PSD}	Phase space density
a	s -wave scattering length
U_0	Effective interaction strength
ξ	Healing length
$V(\mathbf{r})$	Trapping potential
$\bar{\omega}$	Geometric average of the trapping frequencies
a_{ho}	Oscillator length
R_i	Thomas-Fermi radii
a_{ii}	Intraspecies scattering length

a_{ij}	Interspecies scattering length
u_{ii}	Normalized intraspecies interaction strength
u_{ij}	Normalized interspecies interaction strength
Δ	Miscibility parameter
δ	Modified miscibility parameter
α_i	Normalization factor of the two-species wavefunction
\bar{a}	Value for which α_i diverges
a^*	Value for which α_i vanishes
Δn_{norm}	Normalized trap-center density
Γ	Circulation around a closed path
l	Vortex charge
R_{vx}	Vortex radius
ϵ_{vx}	Vortex energy per unit length
Ω	Angular rotation frequency
n_{vx}	Uniform density of vortex
a_Ω	Intervortex spacing
ω_\perp^*	Effective radial trapping frequency for a rotating BEC
t_{TOF}	Time of flight
T_D	Doppler temperature
Γ_{Majorana}	Majorana loss ratio
ρ_{Majorana}	Radius of the Majorana hole

T_{Maj}	Majorana temperature
τ	Lifetime of the trapped atoms
d	Relative detuning in the Gray molasses
D	Absolute detuning in the Gray molasses
U_0^{cross}	Potential depth of the crossed ODT

Contents

1	INTRODUCTION	31
1.1	This thesis	35
1.2	Thesis outline	37
2	TRAPPED TWO-SPECIES BECS WITH TUNABLE INTER- ACTIONS	41
2.1	The non-interacting Bose gas	42
2.2	The weakly-interacting Bose gas	45
2.2.1	The Gross-Pitaevskii equation	46
2.2.2	The Thomas-Fermi Approximation	48
2.2.3	The case of attractive interactions	49
2.3	Two-species BECs	50
2.3.1	The coupled Gross-Pitaevskii equations	51
2.3.2	Overlapping region	54
2.3.3	Non-overlapping region	55
2.3.4	Ground state configurations of a two-species BEC	56
2.3.5	Numerical simulation for the ^{23}Na - ^{41}K two-species BEC	62
3	VORTICES IN A TWO-SPECIES BEC	71
3.1	Dynamics of Bose-Einstein condensates	71
3.1.1	The hydrodynamic equations	72
3.2	Vortices in atomic BECs	74
3.2.1	The properties of a “vortex line”	75
3.2.2	Multi-charged vortices and vortex lattices	76
3.3	Rotating condensates	77
3.4	Vortex lattices in a two-species BEC	80

4	FIRST STEP IN PRODUCING A TWO-SPECIES BEC: SODIUM EXPERIMENTAL SYSTEM	89
4.1	The NaK vaccum system	89
4.2	Sodium 2D and 3D-MOTs	93
4.2.1	A 2D-MOT for sodium atoms	93
4.2.2	Sodium 3D-MOT: the dark-SPOT MOT	95
4.2.3	The absorption imaging technique	100
4.3	From the MOT of ^{23}Na to the Plug trap	102
4.4	The Plug type trap	105
4.4.1	The Quadrupole trap potential and Majorana losses	105
4.4.2	The Plug trap potential	108
4.4.3	A Plug type trap for ^{23}Na - ^{41}K	110
4.4.4	^{23}Na atoms in the Plug trap	112
4.5	The BEC of ^{23}Na atoms in a Plug trap	114
4.5.1	Evaporative cooling of atoms in a magnetic trap	114
4.5.2	The BEC of ^{23}Na atoms	119
5	SECOND STEP IN PRODUCING A TWO-SPECIES BEC: WORKING WITH POTASSIUM ATOMS	123
5.1	The potassium isotopes	124
5.2	The potassium laser system	125
5.2.1	The master oscillator power amplifiers (MOPAs)	126
5.3	From the ^{39}K MOT to the Quadrupole trap	128
5.3.1	The experimental sequence until the magnetic trapping	130
5.4	The Gray Molasses for ^{39}K	131
5.4.1	The Gray molasses working principles	133
5.4.2	Characterizing the Gray molasses for ^{39}K atoms	135
5.5	Initial work with two-species: ^{23}Na and ^{39}K	139
5.5.1	A two-species MOT: ^{23}Na and ^{39}K	139
5.5.2	Two-stage MOT loading	140

5.5.3	Spin Purification for ^{23}Na atoms	143
6	A ^{23}Na BEC TO GENERATE VORTEX LATTICES	147
6.1	The necessity of a new type of trap	148
6.2	The crossed optical dipole trap	149
6.2.1	A crossed optical dipole trap for ^{23}Na and ^{41}K	150
6.3	The new ^{23}Na BEC produced in a <i>crossed</i> ODT	151
6.3.1	Characterizing the evaporative cooling in the crossed ODT	153
6.3.2	Characterization of the ^{23}Na BEC produced in the crossed ODT	155
6.4	The vertical imaging and the stirring beam systems	157
6.4.1	The vertical imaging system	159
6.4.2	Characterizing the stirring beam	161
6.5	Initial evidences of a vortex lattice	167
7	CONCLUSIONS AND PROSPECTS	169
7.1	Conclusions	169
7.2	Prospects	171
	REFERENCES	177
	 APPENDIX	 193
	APPENDIX A – THE MAGNETICALLY INDUCED FES- HBACH RESONANCES	195
A.1	Feshbach resonances in cold atomic systems	195
A.2	The Feshbach resonances between ^{23}Na and ^{41}K	197
A.2.1	Designing the Feshbach coils	198
	APPENDIX B – NUMERICAL SIMULATION: DIMENSION- LESS COUPLED GROSS-PITAEVSKII EQUA- TIONS	203

	APPENDIX C – THE PLUG TRAP SETUP AND CON-	
	FIGURATION	207
C.1	The Quadrupole field configuration	207
C.2	The Plug optical setup	208
	APPENDIX D – THE LASER SYSTEM FOR POTASSIUM	
	ATOMS	211

1 Introduction

The superfluidity phenomenon, as first discovered in 1938 by Kapitza (1) (and independently, by Allen and Misener (2)) in liquid ^4He at a temperature below 2.18 K, was at that time described as a fluid which presents no viscosity and flows without dissipation. In 1941, Landau developed the first model for superfluidity in which he established a critical velocity below which a fluid may exhibit a superfluid behaviour. As a consequence of Landau's phenomenological description, Onsager in 1949 (3) and Feynman in 1955 (4) demonstrated that such quantum fluids are irrotational systems in which rotation can only occur through the nucleation of vortices. These vortices are lines or rings where the fluid's density vanishes and the phase of its macroscopic wave-function has a singularity. In this case, the circulation around a closed path that encloses a vortex will be quantized in units of h/m , with h being the Planck's constant and m the atomic mass of the fluid. Therefore, differently from classical fluids, in quantum fluids angular momentum can only be injected into the system in quantized quantities through the nucleation of quantized (or quantum) vortices.

The existence of quantum vortices in superfluid ^4He was first confirmed in 1961 (5) through the measurement of its quantized circulation¹. Later, in 1979, a more "direct" observation of such vortices was possible by recording the flow of ions immersed in the superfluid. (8) The ions' positions suggested the formation of stationary vortex arrays that tended to organize themselves in triangular shaped structures. In all these experiments, a cylinder filled with superfluid helium was put under rotation in a configuration we will refer to as the "rotating bucket experiment". Different experimental configurations favoured the nucleation of quantized vortices without a preferred orientation and, as also predicted by Feynman (4), a turbulent regime, named "Quantum Turbulence" (QT), was first observed in 1957 (9–12). Even though quantum turbulence initially seems to be more complex than

¹ Previous experimental evidences in favor of the nucleation of quantized vortices in liquid helium were presented in 1956 (6) and in 1958 (7), but no conclusive measurement of the quantized circulation have been given prior to 1961.

classical turbulence, simpler models can be used to describe it and eventually increase our knowledge about its classical analogous. In fact, some recent studies have shown strong similarities between the two types of turbulence. (13, 14)

The study of superfluids suffered a decisive change when, in 1995, three research groups independently observed for the first time the occurrence of Bose-Einstein condensation in dilute weakly-interacting atomic gases of ^{87}Rb (15), ^{23}Na (16) and ^7Li (17). The Bose-Einstein condensation (BEC), characterized by the macroscopic occupation of the ground-state of a quantum system, was initially proposed by Satyendra Nath Bose in 1924 (18) in the context of photons and soon extended to massive particles under the same statistics (*bosonic* particles), by Albert Einstein in 1925. (19) Before the experiments performed in 1995, no clear evidence of BEC had been observed, although some other phenomena have been related to it. In fact, the superfluid behaviour of liquid ^4He was, already in 1938, associated with the occurrence of BEC in such systems. (20) Later works, however, showed that the expected BEC fraction in ^4He at zero temperature is of less than 8% (21) even if the superfluid properties were pretty evident.

Even if BEC does not necessarily implies superfluidity and vice-versa, the link between these two phenomena can be done through the crucial role that irrotationality plays while characterizing the motion of such systems. (22) As it will be discussed in Chapter 3, also Bose-Einstein condensates are irrotational fluids² and, right after the initial studies focused on showing the BEC's quantum nature and on collective excitations of the atomic cloud (23–26), many groups started to pursue the nucleation of quantized vortices as a proof of superfluidity in such systems. Moreover, the size of a vortex, of the order of the *healing length*, $\xi = (8\pi an)^{-1/2}$, where a is the s -wave scattering length and n is the superfluid density, is usually very small in the case of strongly interacting systems composed of liquid helium and the recently achieved dilute weakly-interacting atomic BECs seemed a much better system for performing their real direct observation³.

² The irrotationality of Bose-Einstein condensates is an intrinsic characteristic that follows from the existence of a macroscopic wavefunction that describes it.

³ The vortex sizes in atomic BECs are expected to be three orders of magnitude larger than the ones obtained in superfluid Helium.

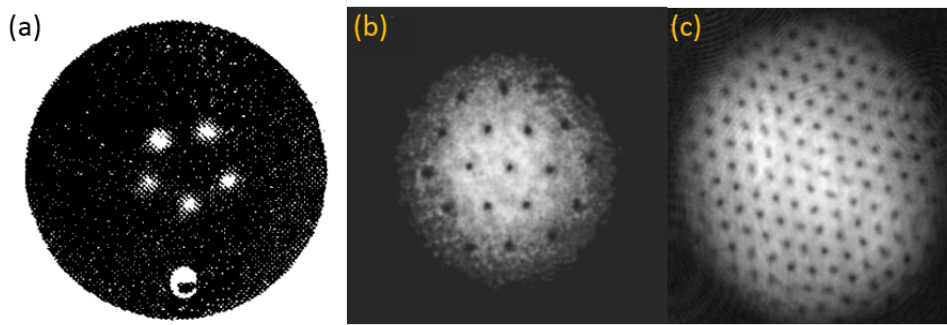


Figure 1 – Vortex lattices observed in liquid ${}^4\text{He}$ (a) and in atomic BECs (b) and (c). The great improvement on the detection of quantum vortices in the latter is clear when comparing these images.

Source: Adapted from Yarmchuk et al. (8), Coddington et al. (34) and Raman et al. (29)

Four years after the experimental realization of atomic BECs, the first quantized vortex line was produced at NIST in a BEC composed of two different hyperfine states of ${}^{87}\text{Rb}$ atoms via the wavefunction engineering technique. (27) The direct analogy with the rotating bucket experiment for liquid helium came one year later by rotating the BEC along one of its trapping axis. (28–30) In the most common configuration, rotation was introduced by rotating a blue-detuned focused laser beam around the condensate usually referred to as *stirring beam*. With this approach, not only one, but some singly-charged vortex lines were nucleated, and its exact number increased linearly with the rotation frequency. The repulsive vortex-vortex interaction makes these vortices to arrange themselves in triangular-shaped lattices (31,32) similar to the ones observed with trapped ions in ${}^4\text{He}$. In Fig. 1, we show a comparison between the vortex lattices observed in liquid helium and in atomic BECs assuring the better conditions achieved with the latter. Atomic BECs with more than 100 vortices were produced while increasing the rotational frequency close to the radial trapping frequency. (33,34)

While the techniques of rotating the BECs always create vortex arrays aligned with the rotation axis, other techniques, which combine rotations and translations of the cloud center of mass (35), can nucleate vortices without a preferred orientation neither a defined circulation. (36) This allowed for the observation of Quantum Turbulence in atomic BECs in 2009. (37) From this initial observation, the properties of a turbulent BEC and its relation with QT in liquid helium are still being explored by different trapping

geometries and methods on how to generate turbulence. (38–44)

Even if the single-component atomic BECs already provided a large variety of phenomena to be investigated⁴, the possibility of simultaneous cool different atomic species by means of sympathetic cooling (48) introduced a richer scenario in dealing with “ultracold atomic mixtures”. Most of the works in two-component atomic gases consider Bose-Fermi mixtures in which interesting features are expected to be observed such as: interspecies Feshbach resonances providing the creation of stable ground-state molecules with large dipole moment (49), boson-induced collapse of the Fermi gas (50,51) and boson-induced superfluidity. (52) This last property was just recently observed, first through the measure of coupled collective modes in a ^6Li - ^7Li mixture (53) and later, with the more appealing evidence of superfluidity by observing coupled vortex lattices in a ^6Li - ^{41}K mixture. (54)

In the context of Bose-Bose mixtures, miscibility plays a fundamental role. Miscibility is an intrinsic property of two-component systems. Two classical fluids are considered miscible if the fluids fully overlap in space forming a homogeneous solution, such as water and ethanol, or immiscible if the fluids remain phase separated, such as water and oil. The miscibility regime a two-component system is expected to be in can be determined by the comparison between the interaction of each fluid with itself and their mutual interaction. For the case of water and oil, the electric charged polar molecules of water tend to remain closer to each other, expelling the non-polar molecules of oil. In considering trapped two-species Bose-Einstein condensates, besides the interspecies interaction, one has to consider the ratio between the mass and number of atoms of each species in order to proper identify the system as miscible or immiscible.

A large variety of bosonic binary systems have been created using different hyperfine levels of the same atomic species (^{87}Rb (48, 55)), different isotopes (e.g., ^{85}Rb - ^{87}Rb (56) and ^{168}Yb - ^{174}Yb (57)) and different elements (e.g., ^{87}Rb - ^{41}K (58–60), ^{87}Rb - ^{133}Cs (61), ^{87}Rb - ^{84}Sr and ^{87}Rb - ^{88}Sr (62), ^{87}Rb - ^{39}K (63) and ^{87}Rb - ^{23}Na (64)), but a complete characterization of the miscible-immiscible phase diagram is still missing. These

⁴ The high level of control of the properties of atomic BECs (density, temperature, atomic interactions, trapping geometry, etc.) soon transformed this systems into a testing ground for different theories related to more complicated systems enclosing different areas of Physics.(27, 45–47)

listed experiments observed miscible and phase-separated regimes without really scanning their parameters and, even though some theoretical papers have predicted the behaviour of Bose-Bose mixtures in the presence of vortices as a function of the interspecies interaction (65–68), just one work could be found in the literature. (69) In this experiment, they performed a preliminary study on the decay of a coupled vortex lattice in which an intermediate “turbulent” regime was observed in one of the two species. The possibility of generating turbulence from the dynamics of coupled vortices is of fundamental interest since it would provide an alternative way of generating QT in a two-component BEC.

In this thesis, we constructed a new experimental system to study coupled vortices and vortex lattices in a two-component Bose-Einstein condensate of ^{23}Na and ^{41}K atoms. These atomic species were chosen relying on the existence of magnetically induced interspecies Feshbach resonances. (70) Two reasonably large interspecies Feshbach resonances are predicted for magnetic fields below 500 G (71), being experimentally easy to access them in the laboratory. With the possibility of changing the interspecies interactions, our new experimental system is suitable to perform a complete characterization of the miscibility regimes, an important property of Bose-Bose systems which remain not fully explored. Once characterized these regimes, it will be possible to study the vortex configurations in each of them. In particular, due to the mass ratio between the species ($\eta^* = m_{^{41}\text{K}}/m_{^{23}\text{Na}} = 1.78 \approx 2$) a stable doubly-charged vortex lattice is expected to occur when considering attractive interspecies interactions. (68) Later, new techniques on how to generate quantum turbulence in a two-component BEC, named “binary quantum turbulence”, could be explored through the counterflow of the two BECs (72), the decay of coupled vortex lattices (69) or even through different patterns of the *stirring* beam (73), across the different miscibility regimes.

1.1 This thesis

The work done during this thesis includes a series of works related with the design and construction of a new experimental system to produce a two-species Bose-Einstein condensate of ^{23}Na - ^{41}K atoms with tunable interspecies interactions for studying coupled

vortex lattices and Quantum Turbulence.

The group have always worked with sodium atoms studying different aspects of these atoms trapped in a magneto-optical trap (MOT). In 2012, we decided to upgrade the previous experimental system for studying cold atomic mixtures, more specifically, ^{23}Na - ^{41}K mixtures, following the scientific goals that have been already introduced. In order to do so, I spent one year of my PhD at the *European Laboratory for Non-Linear Spectroscopy* (LENs) in Italy where I worked in an experimental system able to produce a tunable BEC of ^{39}K atoms. (74) During this time, I participate on the measurement of the mobility edge for 3D Anderson Localization (75) and on setting up a bichromatic optical lattice able to produce a sequence of two-well traps in which a phase transition with hysteresis behaviour was studied. (76) For the purpose of the construction of the NaK machine, the time at LENs gave me the experience on cooling and trapping potassium atoms.

At the beginning of my third year, I was back to Brazil, the last vacuum pieces of the specially designed vacuum system for producing the two-species BEC were arriving and we really could start building up the NaK experiment detailed in this thesis. By the end of May 2014, the vacuum system was finally closed and the first MOT of ^{23}Na atoms was observed in August followed by the ^{39}K MOT, in September. Two pictures comparing the surrounds of the NaK vacuum system right before closing it with its last configuration (January 2017) are displayed in Fig. 2.

Besides this relative fast achievement of the MOT for both atomic species, some problems related with the vacuum quality limited our operation and a lot of time was lost until March of 2016, when we closed the vacuum system for the last time⁵.

The large majority of the results presented in this thesis were obtained during the last year of my PhD. The year of 2016 was very exciting in the NaK experiment. First, we obtained the ^{23}Na BEC in a Plug-type trap (16), followed by a sequence of

⁵ The problems involving our vacuum system were first related to a leak in the connections of two custom designed large viewports and later, on saturation effects in the ionic pump due to a large deposit of potassium atoms. Although being simple problems, their complete resolution took long time because of the typical delays (several weeks) the experimentalist has to face everytime she/he decides to change something on the vacuum system.



Figure 2 – Pictures showing the surrounds of the NaK vacuum system right after closing it by the end of May 2014 (a) and at the beginning of 2017 (b).

Source: By the author.

measurements that aimed to continue to explore the effect of the cooperative two-photon absorption process in a colder cloud (77) than the previous work realized in a MOT. (78) By the middle of the year, we performed a simple study on the light induced losses in the two-species MOT (79) and achieved a ^{39}K atomic cloud at less than $40\ \mu\text{K}$ by performing a D_1 Gray molasses similar to the one described in. (80) Later, the two atomic species were put together in a magnetic trap in an attempt to evaporative cool both atoms into degeneracy. However, strong atom losses and heating avoided an efficient evaporative cooling procedure, and by the end of the year we focused on setting up all the technical details needed to nucleate a vortex lattice in the ^{23}Na BEC by means of a *stirring* laser beam. (28,29,33) We obtained a new BEC of sodium, produced in a crossed optical dipole trap and, after that, we start to set and characterize the *stirring* beam.

1.2 Thesis outline

The construction of cold atomic experiments, as any other very complex experiment, has some pure technical details that can nevertheless be important for understanding its capabilities. In order to produce a lighter main text, this thesis is organized such that these details are inserted as appendices, since they are not important for grasping the main physical ideas but can interest a more careful reader. This is the case for all appendices besides Appendix A, used to describe the mechanism of the magnetically in-

duced Feshbach resonances used to change the interaction in cold atomic clouds and the special case of the interspecies Feshbach resonances for ^{23}Na and ^{41}K .

We start by presenting the theoretical background needed to understand the Physics of a two-component Bose-Einstein condensate in Chapter 2. First, the case of the non interacting Bose gas is considered (section 2.1), followed by the more complete description of a weakly-interacting Bose gas trapped by a harmonic potential (section 2.2). In the latter, the ground-state of the system is obtained by means of the Thomas-Fermi approximation, in the context of effective repulsive interactions between the atoms, and the expected BEC collapse is introduced in the context of attractive interactions. By the end of the chapter, in section 2.3, the two-component picture is introduced by extending the single BEC results in order to write the coupled Gross-Pitaevskii equations (GPEs). The description of the different topological regimes for the ground-state of a two-component BEC with tunable interspecies interactions is first derived in the Thomas-Fermi limit and later with the more powerful technique of evolving the coupled GPEs with imaginary time. (81)

In Chapter 3, we introduce the properties of vortices and vortex lattices in single and two-component BECs. First, we derive the hydrodynamic equations used to describe the dynamic properties of atomic BECs and obtain the important relation that such fluids are irrotational (see section 3.1). Later, in section 3.2, we show the prediction of the nucleation of quantized vortices in such systems and their relevant properties for the case of rotating BECs, described in section 3.3. The complex case of vortices and vortex lattices in a two-component BEC under different miscibility regimes is described in section 3.4, in which we pointed out the parameters for the special case of the ^{23}Na - ^{41}K BEC.

The recently built NaK experiment, together with the characterization of the BEC of sodium atoms obtained in the Plug-type trap, is presented in Chapter 4. The pure technical details related to this chapter are grouped in the Appendix section. In Chapter 5, we present the second step in producing the two-component BEC by describing the experimental system for potassium atoms (in sections 5.1, 5.2, 5.3 and 5.4) and the initial attempts on working with both species (in section 5.5).

A new ^{23}Na BEC suitable for nucleating vortices through the use of a *stirring* beam is presented in Chapter 6. This new BEC was produced in a crossed optical dipole trap, which is described in section 6.2. We present its characterization (in section 6.3), followed by the characterization of the stirring beam and of the different stirring patterns we will be able to use to excite vortices in the two-species BEC (see section 6.4).

Before ending the thesis, in section 7.1 of Chapter 7, we summarize the presented results and, in section 7.2, we discuss some perspectives of interesting experiments to be performed in the recently built NaK experiment.

2 Trapped two-species BECs with tunable interactions

The occurrence of Bose-Einstein condensation in a uniform, non-interacting Bose gas, characterized by the macroscopic occupation of the lowest-energy single-particle state, has been treated in most textbooks on statistical mechanics. (21, 22, 82, 83) Although this system is easy to describe theoretically, its experimental realization was just recently achieved due to the difficulty on realizing a box-like trapping potential. (84) The majority of the previous experiments on atomic BECs relied on harmonic trapping potentials, which change the properties of the condensate when compared to the uniform case. Besides that, atomic BECs cannot be considered as ideal gases but have to be treated in the context of dilute weakly-interacting Bose gases¹, in which, at low temperatures, consider a contact interaction dominated by the s -wave scattering of particles and can be treated with a mean-field approximation. The possibility of changing such interaction by using the magnetically induced Feshbach resonances (70) is one of the most important characteristics of such systems. The existence of broad resonances for bosonic atoms, such as the ones for ^{39}K (85), creates the possibility of studying a variety of phenomena not only with repulsive or attractive effective interactions, but also mimicking the ideal gas case, which is normally easier to model. And, for the case of fermions, such as ^6Li , it creates the possibility of studying the BEC-BCS crossover (86) in a very controlled way and the properties of the system at unitarity. (87) Moreover, two-component systems can be easily produced in the context of trapped gases producing Bose-Bose (48, 56, 58–64) or Bose-Fermi mixtures (53), for which all the previous physics and techniques can be extended giving rise to novel phenomena such as the miscibility phase-transition. (56, 60, 64)

In this second Chapter, we aim to introduce the general context in which this thesis

¹ Due to the relative high densities of atomic BECs, its characteristics strongly depend on the atomic interaction. However, the range of the interaction potential is still much smaller than the mean inter-particle distance and these systems can be considered as being dilute. The diluteness condition takes the form of $\langle N/V \rangle a^3 \ll 1$, with a being the s -wave scattering length which characterizes the atomic interaction.

is inserted by formally describing a dilute weakly-interacting two-component bosonic system trapped by a harmonic trapping potential. Therefore, we start with a brief description of the non-interacting Bose gas in order to show the occurrence of the macroscopic occupation of the lowest-energy single-particle state below a critical temperature (section 2.1), followed by the more realistic case of the weakly-interacting Bose gas (in section 2.2). The ground-state of such a system in the context of *effective* repulsive interaction is obtained by means of the Thomas-Fermi approximation (in 2.2.2) and its behaviour in the context of *effective* attractive interaction (the collapse of the BEC) is discussed in 2.2.3. Finally, in section 2.3, we extend the physics presented in the last sections to account for trapped Bose-Bose mixtures with tunable interspecies interactions. In this context, the Thomas-Fermi approximation is used to provide some intuition on how the system should behave, while a more realistic ground state is obtained by performing a numerical simulation with imaginary time evolution. The possibility of changing the atomic interactions by means of Feshbach resonances is introduced in App. A in the end of this thesis and, in the context of this chapter, we just assume its validity.

2.1 The non-interacting Bose gas

In a gas of N bosons in thermal equilibrium trapped by an arbitrary external potential, $V(\mathbf{r})$, for which the n -th single-particle energy state, $\phi_n(\mathbf{r})$, has energy ϵ_n , the mean-occupation number is given by the Bose-Einstein distribution function

$$f_{Bose}(\epsilon_n) = \frac{1}{e^{\beta(\epsilon_n - \mu)} - 1}, \quad (2.1)$$

with $\beta = (k_B T)^{-1}$, k_B being the Boltzmann constant, T , the temperature of the gas and μ , its chemical potential. This equation is only defined for $\exp[\beta(\epsilon_n - \mu)] > 1$, since a negative mean-occupation number has no physical meaning. According to this, the chemical potential is restricted to a maximum value equal to the lowest-energy of the system ($\mu < \epsilon_0$). The total atom number can be obtained by summing the mean-occupation values for all n -th single-particle energy states such that

$$N = \sum_n f_{Bose}(\epsilon_n). \quad (2.2)$$

In the thermodynamic limit², the energy difference between two consecutive states, let it be n and $n + 1$, is much smaller than the typical energies of the system, such that $(\epsilon_{n+1} - \epsilon_n) \ll k_B T$. Therefore, the energy distribution can be treated as a continuous and the number of atoms is calculated replacing the sum in equation 2.2 by an integral

$$N = \sum_n f_{Bose}(\epsilon_n) \longrightarrow \int_0^\infty g(\epsilon) f_{Bose}(\epsilon) d\epsilon, \quad (2.3)$$

where $g(\epsilon)$ is the density of states that depends on the external trapping potential. For the relevant trapping potentials treated in this thesis, one can define $g(\epsilon)$ as given by a power law in ϵ such that

$$g(\epsilon) = C_\alpha \epsilon^{\alpha-1}, \quad (2.4)$$

where α is the parameter that defines the external trapping potential and C_α , its corresponding constant. One can show (82, 88) that for the case of a three-dimensional box potential with lengths equal to L , $\alpha = 3/2$ and $C_{3/2} = L^3 m^{3/2} / (\sqrt{2} \pi^2 \hbar^3)$. For the case of a three-dimensional harmonic potential with frequencies $(\omega_x, \omega_y, \omega_z)$, $\alpha = 3$ and $C_3 = 1 / (2 \hbar^3 \omega_x \omega_y \omega_z)$, with m being the atomic mass and \hbar , the reduced Planck's constant. Once we know the dependence of $g(\epsilon)$ on ϵ , we can re-write equation 2.3 into

$$N = C_\alpha \int_0^\infty \frac{\epsilon^{\alpha-1}}{e^{\beta(\epsilon-\mu)} - 1} d\epsilon, \quad (2.5)$$

In the thermodynamic limit, the lowest single-particle energy can be neglected³, which results in $\mu < 0$. This means that at high temperatures, the chemical potential is very negative and, as the gas gets colder, the chemical potential increases, reaching zero at the *critical temperature* for condensation, T_c . Above T_c , all the atoms are on the excited states but, as soon as we cross the critical temperature, the population at the lowest-energy single-particle state is no longer negligible. With these considerations, one can obtain an expression for T_c solving equation 2.5 for the case of $\mu = 0$, such that

$$k_B T_c = \frac{N^{1/\alpha}}{[C_\alpha \Gamma(\alpha) \zeta(\alpha)]^{1/\alpha}}, \quad (2.6)$$

where $\Gamma(\alpha)$ and $\zeta(\alpha)$ are the Gamma and Riemann functions, respectively.

² The thermodynamic limit is usually taken by doing $N \rightarrow \infty$ and $V \rightarrow \infty$, keeping $N/V = \text{const}$.

³ That is the reason why the integral on equation 2.3 was done starting from zero.

The 3D box case is of particular interest since, by rearranging Eq. 2.6 into the form

$$n \left(\frac{2\pi\hbar^2}{mk_B T_c} \right)^{3/2} = \zeta(3/2) \approx 2.612, \quad (2.7)$$

it is possible to introduce the concept of *phase-space density* (PSD), with $\rho_{\text{PSD}} = n\lambda_{\text{dB}}^3$, where $\lambda_{\text{dB}} = (2\pi\hbar^2/(mk_B T_c))^{1/2}$ is the de Broglie wavelength. The left side of Eq. 2.7 is exactly ρ_{PSD} and the condition for BEC in an ideal 3D uniform Bose gas could then be written as $\rho_{\text{PSD}} \geq 2.612$. The BEC phenomena can now be interpreted as the overlap of the single-particle wave packets happening when λ_{dB} is of the same order of the interparticle distances ($\propto 1/n^{1/3}$)⁴.

For the 3D harmonic potential, one obtain the well-know relation (82, 88)

$$k_B T_c = \frac{\hbar\bar{\omega}N^{1/3}}{\zeta(3)^{1/3}} \approx 0.94\hbar\bar{\omega}N^{1/3}, \quad (2.8)$$

where $\bar{\omega} = \sqrt[3]{\omega_x\omega_y\omega_z}$ is the geometric average of the trapping frequencies.

Below T_c , the number of particles in the excited states decreases as the the occupation of the lowest-energy single-particle state increases such that the total atom number is conserved. We can explicitly separate the BEC and the excited states contributions for the atom number, N_0 and N_{ex} , respectively, such that

$$N = N_0 + N_{\text{ex}} = N_0(T) + C_\alpha \int_0^\infty \frac{\epsilon^{\alpha-1}}{e^{\beta\epsilon} - 1} d\epsilon, \quad \text{for } T < T_c. \quad (2.9)$$

This has to be done in order to obtain N_0 , since the Bose distribution function is not defined for $\epsilon_0 = \mu = 0$, with ϵ_0 being the energy of the lowest-energy single-particle state. By solving the integral for $N_{\text{ex}}(T < T_c)$ (last term on equation 2.9) and making use of equation 2.6, one finds

$$N_{\text{ex}}(T < T_c) = C_\alpha \Gamma(\alpha) \zeta(\alpha) (k_B T)^\alpha = N \left(\frac{T}{T_c} \right)^\alpha \quad (2.10)$$

Finally, replacing $N_{\text{ex}}(T < T_c)$ into equation 2.9 the expression for the fraction of atoms in the lowest-energy single-particle state (or fraction of atoms in the condensate)

⁴ This result can also be extended to the non-uniform BEC by replacing the density of the uniform gas n by the peak density n_0 of an inhomogeneous system, such that the transition to the condensate occurs locally.

as a function of temperature can be obtained, and it reads

$$\frac{N_0(T)}{N} = \begin{cases} 1 - \left(\frac{T}{T_c}\right)^\alpha & , \text{if } T \leq T_c \\ 0 & , \text{if } T > T_c. \end{cases} \quad (2.11)$$

2.2 The weakly-interacting Bose gas

The case of the ideal gas considered on the previous section is a good starting point in understanding the behaviour of a Bose gas under very low temperatures and predicting the macroscopic occupation of the lowest-energy single-particle state below a critical temperature, giving rise to the Bose-Einstein condensate state. However, experiments on liquid helium and on cold atomic systems deal with interacting atoms. In the former, the system is highly interacting, since BEC occurs in a liquid and its detailed description is far beyond the scope of this thesis. For the latter, the diluteness of the system allow us to treat it as a weakly-interacting Bose gas, where the interaction is given by a mean-field potential, in which just *s*-wave scattering processes are taken into account. In this context, new interesting phenomena appear. In fact, it is due to the presence of interactions that atomic BECs present a superfluid behaviour⁵. In this section, we introduce the Gross-Pitaevskii equation (GPE) in the context of a fully condensed ($T = 0$) weakly-interacting Bose gas and discuss the behaviour of the system under *effective* repulsive or attractive interaction between the particles. A more detailed description can be found in Refs. (22, 82)

⁵ The phenomenological theory developed by Landau in 1941 establishes a critical velocity below which a fluid may exhibit a superfluid behaviour. In Ref. (22) one finds a detailed derivation of Landau's criterion for superfluidity relating the critical velocity with the energy spectrum of elementary excitations, in order to obtain $v_c = \min\left(\frac{\epsilon(\mathbf{p})}{p}\right)$. In the context of atomic BECs, $\epsilon(\mathbf{p})$ is given by the Bogoliubov dispersion relation written as $\epsilon(\mathbf{p}) = \left[\left(\frac{p^2}{2m}\right)^2 + \frac{nU_0}{m}p^2\right]^{1/2}$. The constant U_0 is the effective interaction potential which vanishes for a non-interacting system. Therefore, it is easy to see that, for the case of the ideal Bose gas, $v_c = 0$ (since $\epsilon(p) = p^2/2m$) and an ideal 3D BEC will not present superfluidity properties. However, for the weakly-interacting Bose gas, the Bogoliubov dispersion relation for small momenta is $\epsilon(p) = c_s p$, with $c_s = \sqrt{nU_0/m}$, and superfluidity is supposed to happen if the flow velocity of a weakly-interacting BEC is smaller than the sound velocity in it.

2.2.1 The Gross-Pitaevskii equation

The time-independent many body wave-function for a fully condensed state of N atoms can be written as the symmetrized product of single-particle wave functions, $\phi(\mathbf{r})$, such that

$$\Psi(\mathbf{r}_1, \mathbf{r}_2, \dots, \mathbf{r}_N) = \prod_{i=1}^N \phi(\mathbf{r}_i). \quad (2.12)$$

The single-particle wave functions do not include effects of the correlations between atoms caused by the interactions. In describing the weakly-interacting system, these effects are taken into account in the system's Hamiltonian by adding the effective interaction term, $U_0\delta(\mathbf{r} - \mathbf{r}')$, with $U_0 = 4\pi\hbar^2 a/m$ and a being the s -wave scattering length, assumed to be positive⁶. This interaction term is a contact interaction between two bosons. The system's Hamiltonian may therefore be written as

$$H = H_0 + H_{int} = \sum_{i=1}^N \left[\frac{\mathbf{p}_i^2}{2m} + V(\mathbf{r}_i) \right] + U_0 \sum_{i<j} \delta(\mathbf{r}_i - \mathbf{r}_j). \quad (2.13)$$

The total energy of the system ($E = E_0 + E_{int}$) is defined by the expected value of the system's hamiltonian ($\langle \Psi | H | \Psi \rangle$) which, by using the state in Eq. 2.12 together with the Hamiltonian in 2.13, assumes the form

$$E = N \int d^3\mathbf{r} \left[\frac{\hbar^2}{2m} |\nabla^2 \phi(\mathbf{r})|^2 + V(\mathbf{r})|\phi(\mathbf{r})|^2 + \frac{N-1}{2} U_0 |\phi(\mathbf{r})|^4 \right], \quad (2.14)$$

where the term $N(N-1)/2$ is the number of different pairs one can make with N bosons. At this point it is useful to introduce the wave-function of the condensate state (the order parameter for the transition), $\psi(\mathbf{r})$, written as

$$\psi(\mathbf{r}) = \sqrt{N} \phi(\mathbf{r}), \quad (2.15)$$

such that the density of particles is given in terms of $\psi(\mathbf{r})$ as $n(\mathbf{r}) = |\psi(\mathbf{r})|^2$. By replacing $\phi(\mathbf{r})$ in equation 2.14 and making use of the fact that $N \gg 1$ ⁷, the total energy of the system can be written in terms of $\psi(\mathbf{r})$ as

$$E = \int d^3\mathbf{r} \left[\frac{\hbar^2}{2m} |\nabla^2 \psi(\mathbf{r})|^2 + V(\mathbf{r})|\psi(\mathbf{r})|^2 + \frac{1}{2} U_0 |\psi(\mathbf{r})|^4 \right]. \quad (2.16)$$

⁶ Assuming U_0 to be positive we mean to consider *effective* repulsive interactions between the atoms.

⁷ In this case, $N(N-1)/2 \approx N^2/2$.

The condensed N -particle system is at the lowest energy level. Therefore, in order to find the optimal form for $\psi(\mathbf{r})$ one must minimize equation 2.16 with respect to $\psi(\mathbf{r})$ and its complex conjugate, $\psi(\mathbf{r})^*$, independently, keeping the condition of fixed number of particles:

$$N = \int d^3\mathbf{r} |\psi(\mathbf{r})|^2. \quad (2.17)$$

The Lagrange multiplier for this case is exactly equal to the chemical potential and $\delta E - \mu\delta N = 0$. This is equivalent to minimize the quantity $F = E - \mu N$, which is the free energy of the system, with respect to $\psi(\mathbf{r})^*$ (or $\psi(\mathbf{r})$) such that one can do

$$\frac{\partial}{\partial\psi^*}(E - \mu N) = 0 \text{ }^8. \quad (2.18)$$

Finally, the time-independent Gross-Pitaevskii equation is obtained after solving equation 2.18 and can be written as

$$-\frac{\hbar^2}{2m}\nabla^2\psi(\mathbf{r}) + V(\mathbf{r})\psi(\mathbf{r}) + U_0|\psi(\mathbf{r})|^2\psi(\mathbf{r}) = \mu\psi(\mathbf{r}). \quad (2.19)$$

It is important to note that the GPE has the form of a non-linear Schrödinger equation, in which the potential acting on the bosonic particles is the sum of the external potential ($V(\mathbf{r})$) and the non-linear term $U_0|\psi(\mathbf{r})|^2$ that accounts for the mean field created on each boson by the rest of the system. However, the eigenvalue for the GPE is no longer the energy per particle, ϵ , but the chemical potential. As expected, by doing $U_0 = 0$, one finds $\mu = \epsilon$, which is the case for a non-interacting system⁹.

The analogy between the GPE in equation 2.19 and the non-linear Schrödinger equation can be extended to the time-dependent Schrödinger equation, in such a way one can write the time-dependent Gross-Pitaevskii equation as follows¹⁰

$$i\hbar\frac{\partial\psi(\mathbf{r}, t)}{\partial t} = -\frac{\hbar^2}{2m}\nabla^2\psi(\mathbf{r}, t) + V(\mathbf{r}, t) + U_0|\psi(\mathbf{r}, t)|^2\psi(\mathbf{r}, t), \quad (2.20)$$

with $\psi(\mathbf{r}, t) = \psi(\mathbf{r})e^{-i\mu t/\hbar}$. This last equation allows to extract the dynamic properties of the trapped BECs, which will be developed in Chapter 3. For now, let us focus on the

⁸ This derivative is not too straightforward and some help can be obtained by making use of the fact that $X + \delta X = X(\psi(\mathbf{r}) + \delta\psi(\mathbf{r}), \psi(\mathbf{r})^* + \delta\psi(\mathbf{r})^*)$ and of some others relations found in Ref. (89)

⁹ The chemical potential can be interpreted as the energy cost to add a new particle to the system. In the case of a non-interacting system, this cost is directly given by the energy per particle, ϵ .

¹⁰ The time-dependent GPE can be rigorously derived by means of the action principle (82) or in the context of second quantization. (90)

time-independent GPE in order to obtain an analytical expression for the density profile of the weakly-interacting BEC.

2.2.2 The Thomas-Fermi Approximation

The most important approximation for obtaining an analytical expression for the wave-function of a trapped atomic BEC is the so-called Thomas-Fermi approximation (TFA). In the limit of large atom number (valid for $Na/a_{\text{ho}} \gg 1$, where $a_{\text{ho}} = \sqrt{\hbar/m\bar{\omega}}$ is the oscillator length) and still considering the case of repulsive interactions, the kinetic energy term in equation 2.19 is small compared with the other energies of the system. Therefore, one can neglect the contribution of the kinetic energy and re-write the time-independent GPE in the form of

$$\left[V(\mathbf{r}) + U_0 |\psi(\mathbf{r})|^2 \right] \psi(\mathbf{r}) = \mu \psi(\mathbf{r}), \quad (2.21)$$

such that the density of the condensate can be easily obtained as

$$n(\mathbf{r}) = \begin{cases} \frac{\mu - V(\mathbf{r})}{U_0} & , \text{if } n(\mathbf{r}) > 0 \\ 0 & , \text{otherwise} \end{cases} \quad (2.22)$$

The shape of the density distribution of a condensed cloud will reflect the shape of the trapping potential and its boundaries will be given by equating $V(\mathbf{r})$ with the chemical potential. For the case of a 3D harmonic trapping potential with frequencies $(\omega_x, \omega_y, \omega_z)$, the atomic density profile will have the form of an inverted parabola whose extensions are given by

$$R_i^2 = \frac{2\mu}{m\omega_i^2}, \quad i = x, y, z \quad (2.23)$$

which are called the Thomas-Fermi radii. The normalization condition of Eq. 2.17 provides a relation between the chemical potential and the number of trapped atoms N , with

$$\mu = \frac{15^{2/5}}{2} \left(\frac{Na}{a_{\text{ho}}} \right)^{2/5} \hbar\bar{\omega}, \quad (2.24)$$

By replacing Eq. 2.24 into Eq. 2.23, one can find a more useful expression for the Thomas-Fermi radii

$$R_i = (15Na)^{1/5} a_{\text{ho}}^{4/5} \frac{\bar{\omega}}{\omega_i}. \quad (2.25)$$

Due to the validity of the Thomas-Fermi approximation in most cold atomic systems and the fact that the non-condensed cloud (which will be henceforth referred to as *thermal cloud*) has a Gaussian density distribution, the onset of condensation in such systems is easily identified by the appearance of a bimodal density profile. This signature of the BEC will be later shown for the BEC of ^{23}Na atoms produced in our laboratory and described in Chapter 4.

2.2.3 The case of attractive interactions

The case of *effective* attractive interactions occurs for $a < 0$, which makes the interaction term (last term in Eq. 2.13) to be negative (since, $U_0 \propto a < 0$). Therefore, in order to minimize the interaction energy, the gas tends to accumulate in the region of higher density, diminishing its size. The competition between the interaction and the zero-point kinetic energy gives rise to a local minimum in the energy functional (Eq. 2.16), which can stabilize the system and allow for a metastable BEC to be formed for clouds with atom number below a critical value, N_c . Above N_c , the central density grows too much such that the kinetic term is always smaller than the interaction energy and the energy functional presents no local minimum, the Gross-Pitaevskii equation cannot be solved and the BEC collapses. For a spherical trap, a relation for the critical number N_c can be obtained through a direct integration of the GPE (91) and takes the form of

$$\frac{N_c |a|}{a_{\text{ho}}} \approx 0.575 \quad ^{11}. \quad (2.26)$$

Some alkaline atoms such as ^7Li and ^{39}K have a negative background s -wave scattering length and BEC can only occur if $N < N_c$ or if one can change the nature of the effective interaction with the use of Feshbach resonances. (70) The collapse dynamics for such atomic species, as well as for ^{85}Rb isotope, has been investigated (in (92–94), respectively) and showed a good agreement with the predicted value for N_c .

¹¹ An analytical expression for N_c can be obtained by using a variational approach in deriving the GPE. In this case, a slightly different result is obtained with $N_c |a|/a_{\text{ho}} \approx 0.67$. (82)

2.3 Two-species BECs

The study of two-component quantum gases has gained great attention since the experimental production of a single-component atomic BEC, in 1995. During these last twenty years, a variety of binary quantum mixtures have been created, as it was listed in this thesis introduction. In the context of Bose-Bose mixtures, an important property is their miscibility, which can be characterized by the miscibility parameter

$$\Delta = u_{11}u_{22} - u_{12}^2, \quad (2.27)$$

where $u_{11} = 4\pi\hbar^2 a_{11}/m_1$ and $u_{22} = 4\pi\hbar^2 a_{22}/m_2$ are the strength of the intraspecies interaction, with a_{11} (a_{22}) and m_1 (m_2) being the s -wave scattering length and the mass of species 1 (2). The term $u_{12} = 2\pi\hbar^2 a_{12}/m_{12} = u_{21}$ represents the interspecies interaction, with a_{12} being the interspecies s -wave scattering length and $m_{12} = m_1 m_2 / (m_1 + m_2)$, the reduced mass of the system. In the case of a homogeneous system and for a specific choice of species 1 and 2, the miscibility parameter fully describes its dynamics and the system is said to be miscible (the two components overlap in space) if $\Delta > 0$, or immiscible (they are phase separate) if $\Delta < 0$. However, in the case of trapped systems, the miscibility of the system can also be changed by changing the ratio between the atom number of the different species (N_1/N_2) or due to the difference on the *gravitational sag* of each species. In order to qualitatively find the ground-state of a trapped two-component BEC, one has to consider all listed characteristics. The miscibility region in which the system is found to be (miscible or immiscible) affects some of its properties such as the frequencies of the two-component collective modes (95) and, more relevant to this thesis, the nucleation of coupled vortex lattices (65–68), as it will be discussed in Chapter 3.

In this section, we initially describe the behaviour of a Bose-Bose mixture trapped by a harmonic external potential, extending the results previously obtained for a single weakly-interacting Bose gas in section 2.2 and following the steps presented in references. (82, 95–97) Later, we obtain the ground-state configuration for the specific two-component BEC treated in this thesis (^{23}Na - ^{41}K) by performing a numerical simulation with imaginary time evolution of the coupled Gross-Pitaevskii equations.

2.3.1 The coupled Gross-Pitaevskii equations

A trapped Bose-Bose mixture in the weakly-interacting regime can be modelled by applying the same considerations discussed in the previous section for a single BEC. Let us consider a mixture of two different bosonic atoms, labelled species 1 and species 2, with N_1 and N_2 particles, respectively. The time-independent many body wave-function for the two-component BEC in the mean field approximation can be generalized from equation 2.12 in the form of

$$\Psi(\mathbf{r}_1, \mathbf{r}_2, \dots, \mathbf{r}_{N_1}; \mathbf{r}'_1, \mathbf{r}'_2, \dots, \mathbf{r}'_{N_2}) = \prod_{i=1}^{N_1} \phi_1(\mathbf{r}_i) \prod_{j=1}^{N_2} \phi_2(\mathbf{r}'_j) \quad (2.28)$$

where the positions of particles of species 1 are denoted by \mathbf{r}_i and those of species 2 by \mathbf{r}'_j , and ϕ_1 and ϕ_2 are the corresponding single-particle wave functions. In the context of the weakly-interacting regime, all the interactions (intraspecies or interspecies) can be treated as a contact interaction for which just s -wave scattering processes need to be taken into account. In such a picture, the energy functional of equation 2.14 can be rewritten for a two-component system in the form:

$$E = \int d\mathbf{r} \left[\frac{\hbar^2}{2m_1} |\nabla\psi_1|^2 + \vartheta_1(\mathbf{r})|\psi_1|^2 + \frac{\hbar^2}{2m_2} |\nabla\psi_2|^2 + \vartheta_2(\mathbf{r})|\psi_2|^2 + \frac{1}{2}u_{11}|\psi_1|^4 + \frac{1}{2}u_{22}|\psi_2|^4 + u_{12}|\psi_1|^2|\psi_2|^2 \right], \quad (2.29)$$

in which it was neglected effects of the order of $1/N_1$ and $1/N_2$, small when N_1 and N_2 are large. Here m_i is the mass of an atom of species i , ϑ_i is the external potential and u_{11} , u_{22} and u_{12} are the interaction terms introduced before. The wave-functions ψ_1 and ψ_2 are the condensate wave-functions for each one of the two components, defined as

$$\psi_1(\mathbf{r}) = N_1^{1/2} \phi_1(\mathbf{r}) \quad \text{and} \quad \psi_2(\mathbf{r}) = N_2^{1/2} \phi_2(\mathbf{r}). \quad (2.30)$$

The chemical potentials, μ_1 and μ_2 , are introduced in order to minimize the energy functional subjected to the constraint that the number of atoms of each species is conserved. The resulting time-independent coupled Gross-Pitaevskii equations are

$$\left[-\frac{\hbar^2}{2m_1} \nabla^2 + \vartheta_1(\mathbf{r}) + u_{11}|\psi_1|^2 + u_{12}|\psi_2|^2 \right] \psi_1 = \mu_1 \psi_1 \quad (2.31)$$

$$\left[-\frac{\hbar^2}{2m_2} \nabla^2 + \vartheta_2(\mathbf{r}) + u_{22}|\psi_2|^2 + u_{12}|\psi_1|^2 \right] \psi_2 = \mu_2 \psi_2. \quad (2.32)$$

One can easily see that for the case of vanishing interspecies interactions ($u_{12} = 0$), equations 2.31 and 2.32 are no longer coupled and have the form of the time-independent GPE for each species given by equation 2.19.

We are now interested in finding the ground state of each species while trapped by a harmonic external potential as it is performed in real experiments. Therefore, the total external potential that appears on the GPEs is equal to the sum of the trapping potential with the gravitational one, such that

$$\vartheta_i(\mathbf{r}) = \left[\frac{1}{2} m_i \sum_{j=x,y,z} \omega_j^i x_j^2 + \vartheta_0^i \right] + m_i g z, \quad i = 1, 2, \quad (2.33)$$

where ω_j^i is the angular trapping frequency for species i and axis j , ϑ_0^i is a potential bias and g is the gravitational acceleration constant. Differently from the situation of a single-component BEC discussed in section 2.2, the gravitational potential is already introduced in the GPEs since it will differently affect each species. For instance, if $m_1 \neq m_2$, the vertical equilibrium position is different for atom 1 and atom 2. This gives rise to the so-called *gravitational sag* between two species that can sometimes prevent the observation of exotic phase separated configurations as the ball-and-shell structure. (96) By defining $\bar{\omega}_i = \sqrt[3]{\omega_x^i \omega_y^i \omega_z^i}$ and $\lambda_j = \omega_j^i / \bar{\omega}_i$, which is independent of the atomic species, and applying a change on the coordinates such as $x_j \rightarrow x'_j = \lambda_j x_j$, one can rewrite the total external potential as

$$\vartheta'_i(\mathbf{r}') = \frac{1}{2} m_i \bar{\omega}_i^2 \left[r'^2 + (z' - z'_{0i})^2 \right] + \vartheta_0^{i'}, \quad (2.34)$$

where we have defined $r'^2 = x'^2 + y'^2$,

$$z'_{0i} = -\frac{g}{\lambda_z \bar{\omega}_i^2}, \quad (2.35)$$

is the equilibrium position¹² and

$$\vartheta_0^{i'} = \vartheta_0^i - \frac{1}{2} m_i \frac{g^2}{\lambda_z^2 \bar{\omega}_i^2}. \quad (2.36)$$

¹² The equilibrium position can be easily obtained by setting to zero the force on the vertical direction.

Next, one can translate once again equation 2.34 to the equilibrium position of species 1, defining $dz = z'_{02} - z'_{01}$ and expressing all quantities in dimensionless units, rescaling lengths by $a_{\text{ho}1} = \sqrt{\hbar/(m_1\bar{\omega}_1)}$ and energies by $\hbar\bar{\omega}_1$. Finally, the resulting external potentials can be written as:

$$V_1(\mathbf{r}'') = \frac{1}{2} (r''^2 + z''^2) \quad (2.37)$$

$$V_2(\mathbf{r}'') = \frac{1}{2}\eta (r''^2 + (z'' - dz'')^2), \quad (2.38)$$

where

$$\eta = \frac{m_2}{m_1} \left(\frac{\bar{\omega}_2}{\bar{\omega}_1} \right)^2, \quad (2.39)$$

$$dz'' = \frac{g}{\lambda_z a_{h0} (\bar{\omega}_1)^2} \left(\frac{m_2}{\eta m_1} - 1 \right), \quad (2.40)$$

$x_j'' = \lambda_j/a_{\text{ho}1}x_j$ and $V_i(\mathbf{r}'') = \vartheta_i(\mathbf{r}'')$.

The Gross-Pitaevskii equations for the Bose-Bose mixture (equations 2.31 and 2.32) can be written in terms of the new external potentials, $V_1(\mathbf{r}'')$ and $V_2(\mathbf{r}'')$, and the new variables, \mathbf{r}'' , by writing ∇^2 , ψ_1 and ψ_2 in terms of \mathbf{r}'' and dividing the whole equation by $\hbar\bar{\omega}_1$. If the number of atoms is large, we can rely on the Thomas-Fermi approximation which simplifies the GPEs by neglecting its kinetic terms in order to finally obtain the following pair of coupled equations:

$$V_1(\mathbf{r}) + u_{11}|\psi_1|^2 + u_{12}|\psi_2|^2 = \mu_1 \quad (2.41)$$

$$V_2(\mathbf{r}) + u_{22}|\psi_2|^2 + u_{12}|\psi_1|^2 = \mu_2. \quad (2.42)$$

Here the double prime was omitted to simplify the notation and the rescaled interaction terms are given by $u_{11} = 4\pi a_{11}/a_{h0}$, $u_{22} = 4\pi(a_{22}/a_{h0})(m_1/m_2)$ and $u_{12} = 2\pi a_{12}/a_{h0}(1 + m_1/m_2)$.

The resulting coupled equations in the Thomas-Fermi approximation can be used to find a qualitative solution for the ground state of the two-component BEC. It is worthwhile to note that, for a given set of parameters (u_{11} , u_{22} , u_{12} , N_1/N_2 and m_1/m_2), the

ground-state of the system will present spatial regions in which both species coexist, and regions in which (at least) one of the densities vanishes. We call them the *overlapping* and *non-overlapping* regions, respectively. This is an important classification, since the solutions of Eqs. 2.41 and 2.42 will have different forms depending on the region we are solving it for. Once we know how to write both forms and the shape of the boundary surfaces that separates both regions, the general solution can be found preserving the normalization condition for the total wave-functions. We focus on describing this self-consistent method on what follows.

2.3.2 Overlapping region

By defining $\gamma_1 = u_{12}/u_{11}$ and $\gamma_2 = u_{12}/u_{22}$ together with the miscibility parameter given in equation 2.27, the solutions of equations 2.41 and 2.42 in the overlapping region take the form

$$|\psi_1|^2 = \alpha_1 [R_1^2 - r^2 - (z - z_{c1})^2], \quad (2.43)$$

$$|\psi_2|^2 = \alpha_2 [R_2^2 - r^2 - (z - z_{c2})^2], \quad (2.44)$$

where the radii R_i are defined as

$$R_1^2(\mu_1, \mu_2) = \frac{2(\mu_1 - \gamma_2\mu_2)}{1 - \eta\gamma_2} + \frac{\eta\gamma_2}{(1 - \eta\gamma_2)^2} dz^2 \quad (2.45)$$

$$R_2^2(\mu_1, \mu_2) = \frac{2(\mu_2 - \gamma_1\mu_1)}{\eta - \gamma_1} + \frac{\eta\gamma_1}{(\eta - \gamma_1)^2} dz^2, \quad (2.46)$$

the position of each center of mass along z as

$$z_{c1} = -\frac{\eta\gamma_2}{1 - \eta\gamma_2} dz \quad (2.47)$$

$$z_{c2} = \frac{\eta}{\eta - \gamma_1} dz \quad (2.48)$$

and the normalization factors α_1 as

$$\alpha_1 = u_{22} \frac{1 - \eta\gamma_2}{2\Delta} \quad (2.49)$$

$$\alpha_2 = u_{11} \frac{\eta - \gamma_1}{2\Delta}. \quad (2.50)$$

The behaviour of the system in the overlapping region can be qualitatively understood by noticing that the right-hand side of equations 2.43 and 2.44 have to be positive since $|\psi_1|^2, |\psi_2|^2 \geq 0$. The overlapping region is defined as the intersection of the spherical surfaces Σ_i defined by the equation $R_i^2 = r^2 + (z - z_{ci})^2$ and identified by the sign of α_i : if $\alpha_i > 0$, the region to be considered is the one inside the surface Σ_i ; if $\alpha_i < 0$, one should consider the region outside the surface.

2.3.3 Non-overlapping region

In the non-overlapping region, that is, regions for which one of the two densities vanishes¹³, the wave functions for the remaining atomic species (ψ_{01} or ψ_{02}) have the usual form of the Thomas-Fermi profile for a single BEC, since there is no interaction between atoms of different species. They can be written as:

$$|\psi_{01}|^2 = \frac{1}{2u_{11}}(2\mu_1 - r^2 - z^2) \quad (2.51)$$

$$|\psi_{02}|^2 = \frac{\eta}{2u_{22}} \left(\frac{\mu_2}{\eta} - r^2 - (z - dz)^2 \right). \quad (2.52)$$

In this case, these solutions are defined inside a region of space whose boundary is delimited by surfaces Σ_{0i} of equation $R_{0i}^2 = r^2 + (z - z_{ci}^0)^2$, with $R_{01}^2 = 2\mu_1$, $R_{02}^2 = 2\mu_2/\eta$, $z_{c1}^0 = 0$ and $z_{c2}^0 = dz$, without depending on the sign of external parameters. From equations 2.51 and 2.52 one can conclude that the interaction between different species in the overlapping region influences the non-interacting portion of the cloud only through a re-normalization in the atomic density, since

$$\int d\mathbf{r} |\psi_i^{\text{Total}}|^2 = N_i, \quad \psi_i^{\text{Total}} = \psi_i + \psi_{0i}, \quad (2.53)$$

without changing the shape of the non-interacting wave function. The continuity condition of the wave function at the interface between each region requires $\psi_1 = \psi_{01}$ on a surface defined by Σ_2 for which $|\psi_2|^2$ vanishes, and vice-versa.

¹³ Which means that $|\psi_1|^2 = 0$ or $|\psi_2|^2 = 0$

2.3.4 Ground state configurations of a two-species BEC

The general solution for the density distribution of both species at any point of the space must be found in a self-consistent way through the equations obtained for the overlapping and non-overlapping regions after imposing the normalization condition of equation 2.53. These calculations are long and it is not always possible to find an analytical solution¹⁴. Fortunately, it is still possible to formulate some general considerations by looking at Δ and the interspecies interaction strength, u_{12} . Let us fix the intraspecies interaction strengths, u_{11} and u_{22} , and consider the possibility of changing u_{12} . In this situation, it is important to notice that the sign of the factors α_i depends on the interplay between the sign of Δ (which changes its sign for $u_{12} = \bar{u} = \sqrt{u_{11}u_{22}}$, independently of i , making $u_{12} = \bar{u}$ a pole¹⁵ for α_i) and the sign of the numerators appearing on equations 2.49 and 2.50. Looking the numerator of those expressions, the critical value of u_{12} that makes α_1 (or α_2) equal to zero is found to be $u_1^* = u_{22}/\eta$ ($u_2^* = \eta u_{11}$). These latter values also define poles for the vertical position of the interacting profiles centers of mass z_{ci} . If we assume $u_{11} > u_{22}$, the critical value for u_{12} that is inside the region in which $\Delta > 0$ is $u^* = u_1^* = u_{22}/\eta$.

As it was defined in the end of the section 2.3.1, u_{11} , u_{22} and u_{12} are proportional to the s -wave scattering lengths a_{11} , a_{22} and a_{12} , respectively, such that it is possible to find the values for a_{12} that corresponds to \bar{u} and u_i^* with

$$\bar{a} = 2 \left(\frac{\sqrt{m_1 m_2}}{m_1 + m_2} \right) \sqrt{a_{11} a_{22}} \quad (2.54)$$

$$a^* = 2 \left(\frac{m_2}{m_1 + m_2} \right) a_{11}. \quad (2.55)$$

Differently than the values for u_{12} (\bar{u} and u^*), \bar{a} and a^* do not depend on the trapping frequencies and are, therefore, more general. We summarize all these considerations in the graphs for the rescaled positions z_{ci}/dz and for the factors α_i as a function of a_{12} depicted in Fig 3.

¹⁴ In Ref. (96), one can find a more complete discussion of the steps needed to obtain the ground state densities for each component at an specific set of parameters (giving rise to different overlapping/non-

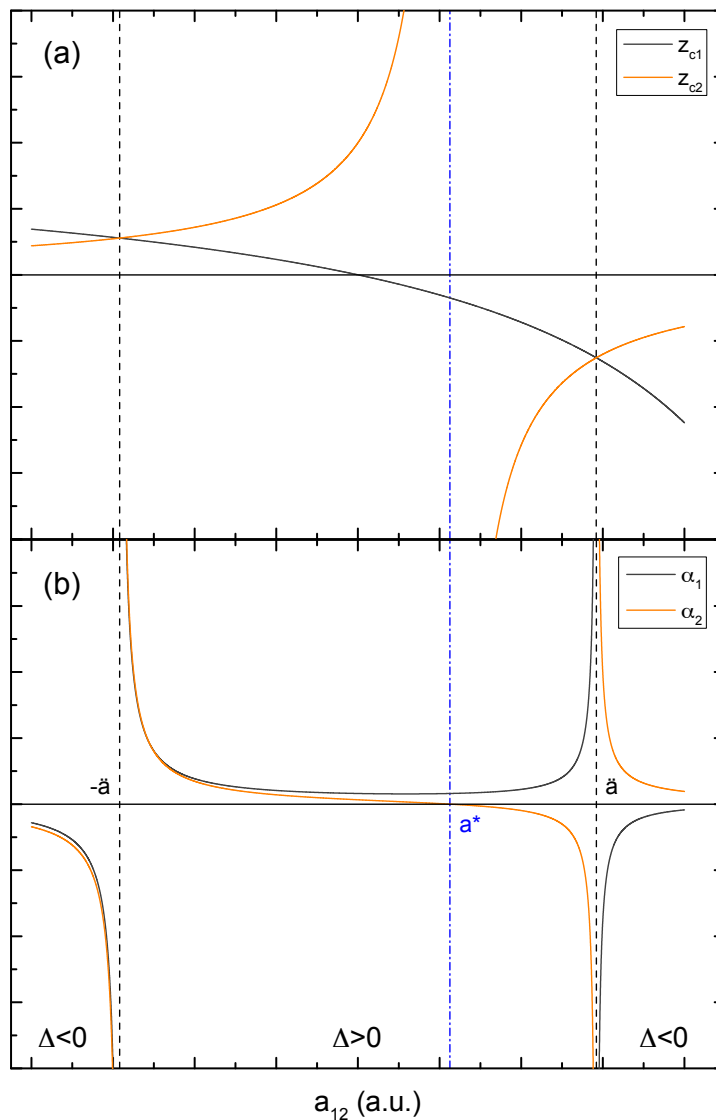


Figure 3 – (a) Rescaled positions, z_{c1}/dz and z_{c2}/dz , and (b) factors α_1 and α_2 as a function of a_{12} . On both graphs the relevant values for a_{12} (\bar{a} and $a^* = a_2^*$) are indicated as well as the regions for which $\Delta > 0$ and $\Delta < 0$.

Source: By the author.

There are three different parameter regions one can identify from the graphs of Fig. 3:

1. $a_{12} < -\bar{a}$, with $\Delta < 0$: the constants α_i are both negative and no overlapping solutions are allowed in this range. This can be explained by noticing that as one approaches $-\bar{a}^{(+)}$ the condensates eventually collapse. (98, 99)¹⁶

overlapping regions) and the useful normalization conditions in its appendix section

¹⁵ A “pole” for α_i , i.e., a value for which α_i diverges.

¹⁶ Even if the intraspecies interactions (a_{11} and a_{22}) are both positive, when $a_{12} \leq -\bar{a}$ the interspecies interaction becomes dominant and the two-component BEC collapses.

2. $-\bar{a} < a_{12} < \bar{a}$, with $\Delta > 0$: the two condensates can coexist and overlap in some region delimited by $|dz| < R_{01} + R_{02}$.
3. $a_{12} > \bar{a}$, with $\Delta < 0$: the strong mutual repulsion leads to a phase separation between the two condensates (100,101). Once the BECs enters in the phase separated region, even if the strength of the interspecies interactions is increased, the interface between the two condensates do not change keeping the same shape as the one obtained when considering $a_{12} = \bar{a}$.

Here it is important to remind the reader that we are treating the problem in the Thomas-Fermi limit (at $T = 0$) and that some finite temperature corrections may lead to changes in the transition points listed above. (99,102) But we are going to focus on the simplest $T = 0$ case in the following discussion about the topology of the two-component BEC in each listed region.

In the parameter regions **1** and **3**, the possible topology configurations are straightforward since, in the first, the two BECs collapsed due to the negative intraspecies scattering length and, in the region **3**, the two BECs are phase separate and both present a standard Thomas-Fermi profile dislocated from the center of the trap. It is in region **2** that interesting topology configurations appear as summarized in Fig. 4 adapted from Ref. (97). We can divide then in two classes:

- **External overlap**: in this case, the separation between the centers of mass of the two condensates, $|dz|$, is larger than the difference of the radii of the non-interacting profiles, $|R_{01} - R_{02}| < |dz| < R_{01} + R_{02}$, which correspond to Fig. 4(a)-(c). The overlapping region is defined by the intersection area of surfaces Σ_1 and Σ_2 (given by the dashed lines in the figure) and its shape is determined by the interspecies scattering length a_{12} . The three possible configurations of “external overlap” are shown in Fig. 4 for $-\bar{a} < a_{12} < 0$ in (a), $0 < a_{12} < a^*$ in (b) and $a^* < a_{12} < \bar{a}$ in (c). The case for $a_{12} \geq \bar{a}$ represented in (d) is a phase separate situation for which the two BECs “sits” side-by-side repelling each other.

- **Internal overlap:** in this case, one species is fully surrounded by the other species, which means $|dz| < |R_{01} - R_{02}|$. Depending on the strength of a_{12} , the species can completely overlap (“full overlap”) or evolve to a phase separate configuration with a shell-type topology. The first, illustrated in Fig. 4 (e) and (f) occurs for $\bar{a} < a_{12} < 0$ and $0 < a_{12} < a^*$, respectively. As a_{12} is increased beyond a^* , $a^* < a_{12} < \bar{a}$, a region containing just the inner species appears in the center of its distribution (see Fig. 4 (g)) and we call this configuration a “partial overlap”. Finally, when $a_{12} \geq \bar{a}$ the system is phase separate with a ball-and-shell type topology (see Fig. 4 (h)).

The resolution of the ground-state for the two-components has to be done in a self-consistent way and it relies on numerical calculations. A step-by-step procedure is well described on Ref. (96) Nevertheless, there are still assumptions that can be done without recurring to numerical methods. Let us write the Thomas-Fermi radii along the z direction for the non-interacting BECs recurring to Eq. 2.25 as

$$R_z^i = (15N_i a_{ii})^{1/5} (a_{h0}^1)^{4/5} \left(\frac{\bar{\omega}_i}{\omega_z^i} \right), \quad (2.56)$$

and the *gravitational sag* as

$$\Delta z = z_{01} - z_{02} = -\frac{g}{(\omega_z^1)^2} \left(1 - \frac{m_2}{m_1} \right). \quad (2.57)$$

The condition for the “external overlap” can be identified as $|dz| > |R_{01} - R_{02}| = |R_z^1 - R_z^2|$ which gives

$$|\Delta z| > (15a_{11})^{1/5} (a_{h0}^1)^{4/5} \left(\frac{\bar{\omega}_1}{\omega_z^1} \right) \left| N_1^{1/5} - \left(\frac{a_{22}m_1}{a_{11}m_2} \right)^{1/5} N_2^{1/5} \right|. \quad (2.58)$$

With this last relation for Δz , one can see that the ratio between the number of atoms of species 1 and 2, N_1/N_2 , defines which kind of overlap, “external” (left column of Fig. 4) or “internal” (right column of Fig. 4) the system is most probably to be.

A recent paper (95) theoretically discuss the phase diagram of a trapped Bose-Bose mixture (in their case, they considered ^{87}Rb and ^{39}K in order to match with the experiment described in (63)) first, at $T = 0$ and later, at finite temperature. They treat the ratios between the interaction strengths (a_{11}/a_{12} , a_{12}/a_{22}) and the number of atoms

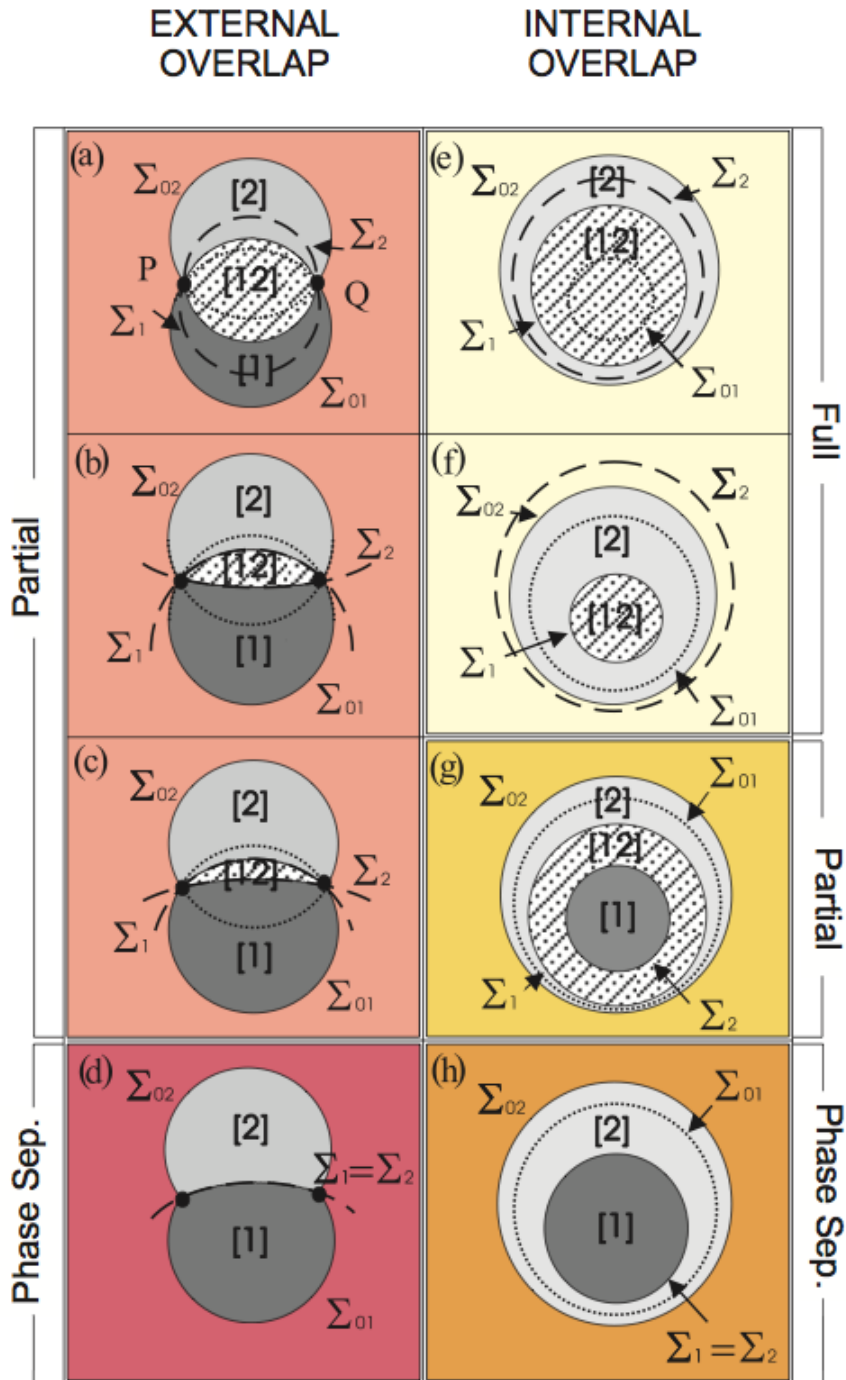


Figure 4 – Possible topologies for a binary mixture of two-species BECs. The cases for “external” and “internal” overlaps are represented in the left and right column, respectively. The lines represent different values for the interspecies scattering length, a_{12} , such that: for (a) and (e), $-\bar{a} < a_{12} < 0$; for (b) and (f), $0 < a_{12} < a^*$; for (c) and (g), $a^* < a_{12} < \bar{a}$; and for (d) and (h) it is represented the phase separate regimes with $a_{12} > \bar{a}$. The relevant surfaces Σ_{01} , Σ_{02} , Σ_1 and Σ_2 are indicated in each scheme as well as the dark (light) gray areas that represents the regions occupied by the non-interacting condensate 1 (2). The white dashed areas represent regions in which both condensates coexist.

Source: Adapted from Catani. (97)

(N_1 and N_2) as independent variables in such a way that they were able to construct the phase diagrams presented in Fig. 5. The white dashed line represents the curve for $\Delta = 0$ and the color scale represents the value of the normalized trap-center density, Δn_{norm} , which is defined as

$$\Delta n_{\text{norm}} = \frac{n_{c1}(\mathbf{0})}{\max n_{c1}(\mathbf{r})} - \frac{n_{c2}(\mathbf{0})}{\max n_{c2}(\mathbf{r})}. \quad (2.59)$$

The value of the Δn_{norm} will depend on how the two species overlap: $\Delta n_{\text{norm}} = 0$ if the species strongly overlap, and $\Delta n_{\text{norm}} = \pm 1$ if they strongly repel each other, with the sign depending on which species sits at the center of the trap. This new quantity was defined in order to qualitatively identify the miscibility of the system, that is, the superposition of both species. If one look to inset (h) of Fig. 5, the system would be classified as miscible, but species seems to be partially overlapped. This duality came from the fact that the system is not homogeneous. We have already presented the idea that in the non-homogeneous case, things would be more complicated. In such case, the number of atoms of each species also plays an important role changing the value of Δn_{norm} even if the $\Delta = 0$ is unchangeable.

Interestingly, the Δn_{norm} is also a parameter closely related to how the dipole mode¹⁷ is affected by varying Δ . For a specific set of N_1 and N_2 , the damping rate and the frequency of the oscillations increase at the same point for which Δn_{norm} also starts to change, resulting in a change of the miscibility region of the system. The possibility of using dipole modes to investigate the state of a two-component system is very powerful since it is an easy measurement to be performed in the laboratory. Recently, it was used to prove the occurrence of superfluidity in both components of a Bose-Fermi mixture composed by ^6Li and ^7Li atoms. (53) And it can also be investigated in the presence of vortices.

¹⁷ The dipole mode is defined as the motion of the center of mass of the trapped atomic cloud, which, for the case of a single-component BEC, will oscillate in each direction with the corresponding trapping frequency.

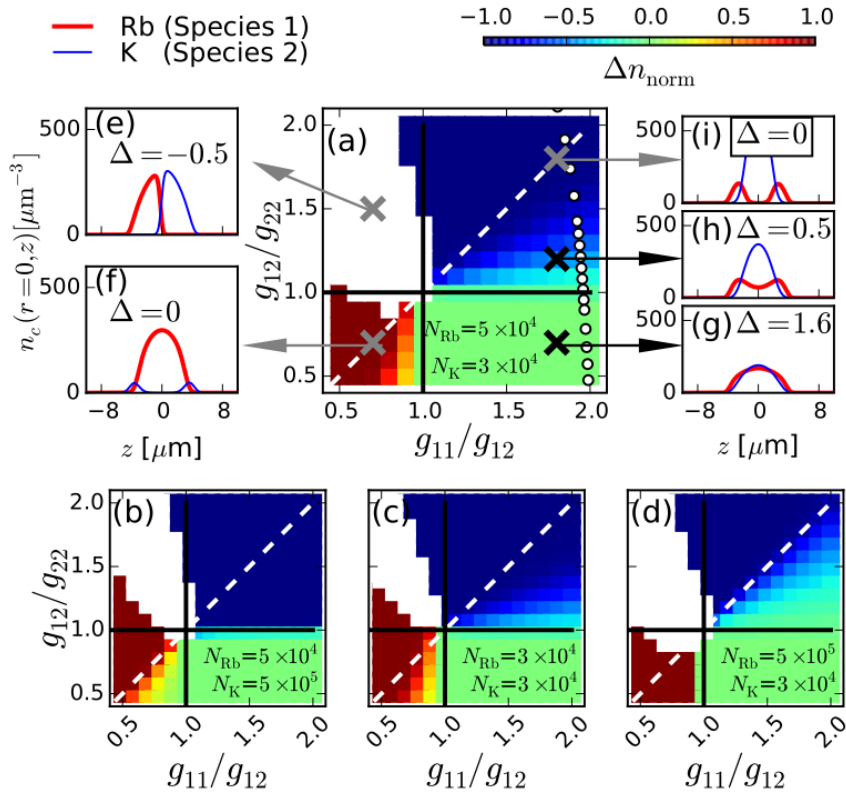


Figure 5 – (a)-(d) Ground-state phase diagram of a trapped $^{87}\text{Rb} - ^{39}\text{K}$ at $T = 0$ for different atom numbers. The color scale represents the values of the normalized trap-center density, Δn_{norm} for each set of a_{11}/a_{12} , a_{12}/a_{22} , $N_1 = N_{\text{Rb}}$ and $N_2 = N_{\text{K}}$ in the symmetrical phase. The asymmetrical phase is shown in white. The density profiles at different regions are shown in (e)-(i). The white circles indicates the regions which can be accessible by using Feshbach resonances in the experiment and the white dashed lines are the curves for $\Delta = 0$. It is interesting to see how the transition on Δn_{norm} deviates from the curve for $\Delta = 0$ as one changes the ratio N_1/N_2 . Source: Adapted from Lee et al. (95)

2.3.5 Numerical simulation for the $^{23}\text{Na} - ^{41}\text{K}$ two-species BEC

In the previous sections, we presented the possible ground-state topologies for a two-component Bose-Einstein condensate with tunable interspecies interactions. This was done relying on the Thomas-Fermi approximation which neglects the kinetic terms of the coupled Gross-Pitaevskii equations that describe the system (see Eqs. 2.41 and 2.42). Even if this approximation gives a simple analytical solution for the case of a single component BEC (see section 2.2), when considering two-components the scenario becomes much more complex due to the existence of overlapping and non-overlapping regions between the components and its complete solution is not always possible. A more powerful

technique for obtaining the ground-state of a two-component BEC accounts for a numerical simulation with imaginary time evolution of the coupled GPEs, Eqs. 2.31 and 2.32. Therefore, before ending this Chapter, we introduce the imaginary time evolution numerical procedure and apply it to the specific case of the two-component BEC composed of ^{23}Na and ^{41}K atoms, whose experimental system has been developed during the time of this thesis. The possible ground-state configurations in the miscible and immiscible regimes are discussed in detail presenting their relevant experimental parameters.

The numerical procedure for obtaining the ground-state of the two-component BEC consists of projecting onto the minimum of the GPEs each initial trial state by propagating them in imaginary time. (81) For simplicity, let us first consider the case of a single component BEC whose dynamical properties are given by the time-dependent GPE introduced in section 2.2 and re-written below:

$$i\hbar \frac{\partial \psi(\mathbf{r}, t)}{\partial t} = -\frac{\hbar^2}{2m} \nabla^2 \psi(\mathbf{r}, t) + V(\mathbf{r}, t) + U_0 |\psi(\mathbf{r}, t)|^2 \psi(\mathbf{r}, t). \quad (2.60)$$

This equation has the form of a time-dependent non-linear Schrödinger equation and the time evolution of one of its eigenstates, $\psi_n(\mathbf{r}, t)$ with $H\psi_n(\mathbf{r}, 0) = E_n\psi_n(\mathbf{r}, 0)$, is easily obtained as:

$$\psi_n(\mathbf{r}, t) = \psi_n(\mathbf{r}, 0) e^{-\frac{iE_n}{\hbar} t}. \quad (2.61)$$

If we consider an initial trial state given by a linear combination of the eigenstates of Eq. 2.60, with $\Psi(\mathbf{r}, 0) = \sum_n c_n \psi_n(\mathbf{r}, 0)$, its time evolution is obtained by evolving each eigenstate individually and we can simply write:

$$\Psi(\mathbf{r}, t) = \sum_n \psi_n(\mathbf{r}, t) = \sum_n \psi_n(\mathbf{r}, 0) e^{-\frac{iE_n}{\hbar} t}. \quad (2.62)$$

Therefore, if we calculate $\Psi(\mathbf{r}, t)$ for $t = -i\tau$, the complex exponentials in Eq. 2.62 are replaced by exponentials decays with decay constants given by E_n/\hbar . Since the ground-state of a system is the state with smaller energy, by evolving $\Psi(\mathbf{r}, t)$ for sufficient long τ only the contribution due to the ground-state remains¹⁸.

The previous equations are only useful to provide some intuition on why the imaginary time evolution of a wavefunction would recover the ground-state of the system.

¹⁸ This is true if the projection of the trial function $\Psi(\mathbf{r}, 0)$ onto the ground-state $\psi_0(\mathbf{r}, 0)$ is not null, which means $c_0 \neq 0$.

However, while performing the numerical simulation and choosing an arbitrary initial trial state it is not common to know its decomposition into the eigenstates of the system and the time evolution for $\Psi(\mathbf{r}, t)$ has to be calculated in a more general way with:

$$\Psi(\mathbf{r}, t) = e^{-i\frac{\widehat{H}}{\hbar}t}\Psi(\mathbf{r}, 0). \quad (2.63)$$

If we assume the imaginary time evolution considering $\tau = \Delta t$ to be infinitesimal, the resulting exponential can be expanded in series and the time evolution for $\Psi(\mathbf{r}, t + \Delta t)$ is simply given by:

$$\Psi(\mathbf{r}, t + \Delta t) \approx \Psi(\mathbf{r}, t) - \widehat{H}\Psi(\mathbf{r}, t)\Delta t. \quad (2.64)$$

This last equation is the one used to perform the numerical simulation. In order to achieve sufficient long times, let it be $t_{\text{final}} = T\Delta t$, Eq. 2.64 is calculated T times. The resulting wavefunction obtained after each time is normalized in order to preserve the atom number.

For the case of a two-component Bose-Einstein condensate whose statical properties are described by the time-independent coupled Gross-Pitaevskii equations (Eqs. 2.31 and 2.32), two wavefunctions (one for each species) have to be evolved in imaginary time simultaneously, since the density profiles will mutual affect each other. In addition, numerical simulations are better performed with values close to unity which makes it necessary to work with the dimensionless coupled GPEs. The detailed derivation of the dimensionless coupled GPEs is presented in App. B, here we just introduce the form of the resulting equations given as:

$$\left[- \left(\frac{1}{\lambda_x^2} \frac{\partial^2}{\partial x_1^2} + \frac{1}{\lambda_y^2} \frac{\partial^2}{\partial y_1^2} + \frac{1}{\lambda_z^2} \frac{\partial^2}{\partial z_1^2} \right) + \left(\frac{x_1^2}{\lambda_x^2} + \frac{y_1^2}{\lambda_y^2} + \frac{z_1^2}{\lambda_z^2} \right) + G_1 z_1 \right. \\ \left. + u_{\text{GP1}} |\psi_1^1(\mathbf{r}_1)|^2 + u_{\text{GP12}} |\psi_2^1(\mathbf{r}_1)|^2 \right] \psi_1^1(\mathbf{r}_1) = 2\mu_1^1 \psi_1^1(\mathbf{r}_1), \quad (2.65)$$

$$\left[- \left(\frac{1}{\lambda_x^2} \frac{\partial^2}{\partial x_1^2} + \frac{1}{\lambda_y^2} \frac{\partial^2}{\partial y_1^2} + \frac{1}{\lambda_z^2} \frac{\partial^2}{\partial z_1^2} \right) + \left(\beta_x^2 x_1^2 + \beta_y^2 y_1^2 + \beta_z^2 z_1^2 \right) + G_2 z_1 \right. \\ \left. + u_{\text{GP2}} |\psi_2^1(\mathbf{r}_1)|^2 + u_{\text{GP21}} |\psi_1^1(\mathbf{r}_1)|^2 \right] \psi_2^1(\mathbf{r}_1) = 2\frac{m_2}{m_1} \mu_2^1 \psi_2^1(\mathbf{r}_1). \quad (2.66)$$

The procedure is done choosing as “scale” the parameters of species 1 such that all energies are rescaled by $\hbar\bar{\omega}_1$ and lengths $i = x, y, z$ by $a_i^1 = (\hbar/m_1\omega_i^1)^{1/2}$. Therefore, the

dimensionless wavefunctions for each species $\psi_{1(2)}^1(\mathbf{r})$ can be easily related with the real wavefunctions by:

$$\psi_{1(2)}(\mathbf{r}) = \sqrt{\frac{N_{1(2)}}{a_{\text{ho}1}^3}} \psi_{1(2)}^1(\mathbf{r}). \quad (2.67)$$

The dimensionless chemical potentials are obtained through $\mu_{1(2)} = \hbar\bar{\omega}_1\mu_{1(2)}^1$ and the constants in Eqs. B.12 and B.18 are given by $\beta_i = a_{\text{ho}1}^2(a_i^1)^2/(a_i^2)^4$, $G_{1(2)} = 2m_{1(2)}^2 a_z^1 a_{\text{ho}1}^2 g/\hbar^2$, $u_{\text{GP}1(2)} = 8\pi a_{11(22)} N_{1(2)}/a_{\text{ho}1}$ and $u_{\text{GP}12(21)} = 4\pi a_{12} N_{2(1)} m_{1(2)}/a_{\text{ho}1} m_{12}$.

Once we have the dimensionless coupled GPEs, it is possible to perform the numerical simulations. We used a program written in C++ and defined a three-dimensional grid and a trial wavefunction with a Gaussian distribution for which it is possible to calculate its time evolution as given in Eq. 2.64 at each grid's point.

In our specific case of the two-component mixture composed of ^{23}Na - ^{41}K atoms, the species 1 is associated with the potassium isotope, with $a_{11} \approx 60a_0$ (103) and the species 2 with the sodium atoms, with $a_{22} \approx 52a_0$ (104) and a_0 being the Bohr radius. We optimize the simulation parameters keeping a grid of $49 \times 49 \times 49$ ¹⁹ with step size of $0.8 \mu\text{m}$ and a time interval $\Delta t = 50 \mu\text{s}$. The number of potassium atoms was kept fixed at 5×10^4 and we could vary the number of sodium atoms between 1×10^4 and 1×10^6 ²⁰ and the interspecies scattering length, a_{12} ²¹. The typical integration times were around $T = 30000$ s before achieving the ground state of the system.

Different miscibility regimes and ground state configurations (with internal or external overlaps) were observed as a function of the number of atoms in the ^{23}Na BEC and of the difference between the gravitational sag of each species. In Fig. 6, we present a first phase diagram of the density profile along the vertical direction for each species of the two-component BEC (^{23}Na in blue and ^{41}K in orange) as a function of the interspecies

¹⁹ We used an odd number of points for the grid in order to make it symmetric (going from $-L$ to L in each direction) with its central point being the origin of our system of coordinates.

²⁰ This choice was done since, in the experiment, the potassium will be sympathetic cooled by the sodium making it easier to vary the number of atoms of the second species.

²¹ The interspecies s -wave scattering length between ^{23}Na and ^{41}K , both in $|1, 1\rangle$, in the absence of an external magnetic field is expected to be given by $a_{12} \approx 252a_0$.(71) Therefore, without changing the interspecies interaction, the system is found to be in a very phase-separated regime. As it is presented in Ref. (71) and discussed in App. A, there are some Feshbach resonances between ^{23}Na - ^{41}K that occur for magnetic fields below 600G, easily achievable in the laboratory, such that we could expect to be able to explore different miscibility regimes by tuning a_{12} .

scattering length a_{12} . Two different number of atoms for the ^{23}Na BEC are presented in the figure ($N_{\text{Na}} = 50 \times 10^4$ atoms, in the upper row and $N_{\text{Na}} = 5 \times 10^4$ atoms, in the lower row) while the number of atoms for the ^{41}K BEC was kept constant. The difference in the gravitational sag is easily observed in the density profiles. Both species have their center of mass dislocated from the center of the trap (identified as $0 \mu\text{m}$ on the vertical position scale) according to the direction of the gravity. Since the trap is less confined for sodium²², this atomic cloud sits below.

In the region of attractive interaction ($a_{12} < 0$), the two-species tend to get closer to each other, increasing their atomic density until they reach the critical point with $a_{12} = -\ddot{a} = -53.6a_0$, below which no possible overlapping solution can be found and the BECs collapse. In the region for $a_{12} > 0$ where the interspecies interaction is repulsive, the overlap between the species decreases as we increase a_{12} until the critical point with $a_{12} = \ddot{a} = 53.6a_0$, after which the system enters in the immiscible region. By increasing the number of sodium atoms, it is possible to see that the overlapping region between the two species also increases in the miscible region however, as soon as we enter in the phase-separated regime, the two-component system exhibits an external overlap configuration.

The external overlap configuration for the ground-state of a two-component BEC is not the best configuration to nucleate and study coupled vortices since the vortex configurations are strongly affected by the interspecies interactions. Therefore, in order to properly observe the exotic vortex configurations that will be described in Chapter 3, one should look for configurations with large overlapping region between the species, which will lead to an internal overlap configuration in the immiscible regime. If we recover the condition for the occurrence of external overlap derived in the Thomas-Fermi approximation (Eq. 2.58) one can see that, by changing the number of atoms in the condensates it is possible to migrate from one configuration to the other. In Fig. 7, we present the vertical density profile for different numbers of sodium atoms, fixed $N_{^{41}\text{K}} = 5 \times 10^4$ and fixed $a_{12} = 50a_0$. An almost internal overlap configuration is obtained only when

²² In order to perform the simulations, we considered the atoms trapped in a crossed optical dipole trap (ODT) with frequencies $f_x^{^{41}\text{K}} = f_y^{^{41}\text{K}} = 148$ Hz and $f_z^{^{41}\text{K}} = 189$ Hz, for the potassium BEC and $f_x^{^{\text{Na}}} = f_y^{^{\text{Na}}} = 107$ Hz and $f_z^{^{\text{Na}}} = 148$ Hz, for the sodium BEC.

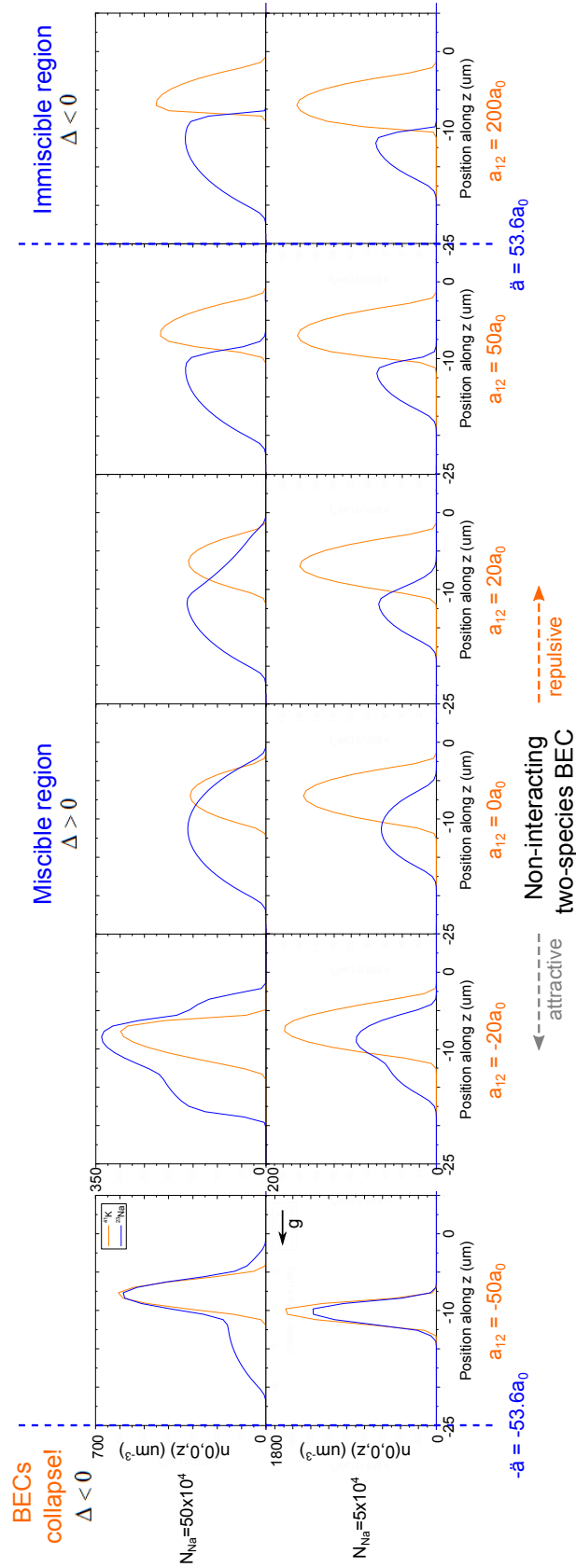


Figure 6 – Simulated density profile along the vertical direction for the ground-state of the ^{23}Na - ^{41}K BEC across the different miscibility regions. The number of potassium atoms was kept constant with $N_{^{41}\text{K}} = 5 \times 10^4$ while we changed the number of sodium atoms with $N_{\text{Na}} = 50 \times 10^4$ atoms, in the upper row and $N_{\text{Na}} = 5 \times 10^4$ atoms, in the lower row.

Source: By the author.

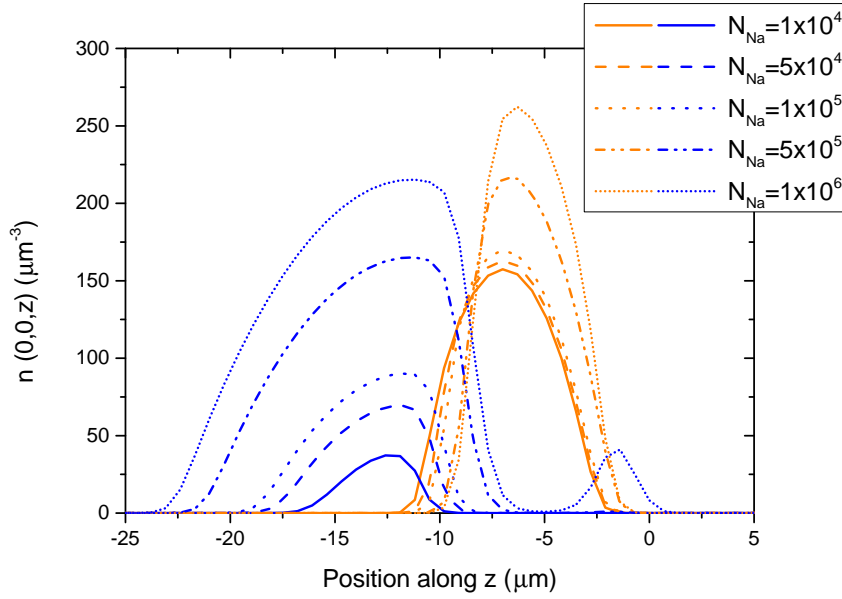


Figure 7 – Simulated density profile along the vertical direction for the ground-state of the ^{23}Na - ^{41}K BEC for different numbers of sodium atoms and fixed interspecies interaction with $a_{12} = 50a_0$. By increasing N_{Na} , the overlap region between the species also increases achieving a partial internal overlap configuration for $N_{\text{Na}} = 1 \times 10^6$ atoms, represented by the short-dashed curves.

Source: By the author.

$N_{\text{Na}} = 1 \times 10^6$ atoms. As it will be discussed in Chapter 6, 1×10^6 was the maximum atom number observed in the BEC of sodium in our experiment. When working with the two-species, we expect this number to decrease such that we would not be able to achieve the internal overlap configuration with the atom numbers we expect to have.

Another approach to bring the ^{23}Na - ^{41}K BECs to the internal overlap configuration can be done by partially compensating the gravitational force acting on the atoms. In fact, considering $N_{\text{Na}} = 50 \times 10^4$ and $N_{^{41}\text{K}} = 5 \times 10^4$, a magnetic gradient of only 2.15 G/cm (of around 0.15% of the magnetic gradient that compensate gravity for the potassium atoms in the $|1, 1\rangle$ state) is enough to match the equilibrium position of the two species. In Fig. 8 (a) we compare the density profile along the vertical direction for non-interacting two-component BEC ($a_{12} = 0$) with and without the addition of the magnetic field. With this magnetic field gradient, as soon as we increase the repulsive interspecies interaction (with $a_{12} > 0$), the sodium BEC surrounds the potassium BEC achieving the internal overlap configuration as the system enters in the phase-separated regime, as it can be seen in Fig. 8 (b), (c) and (d).

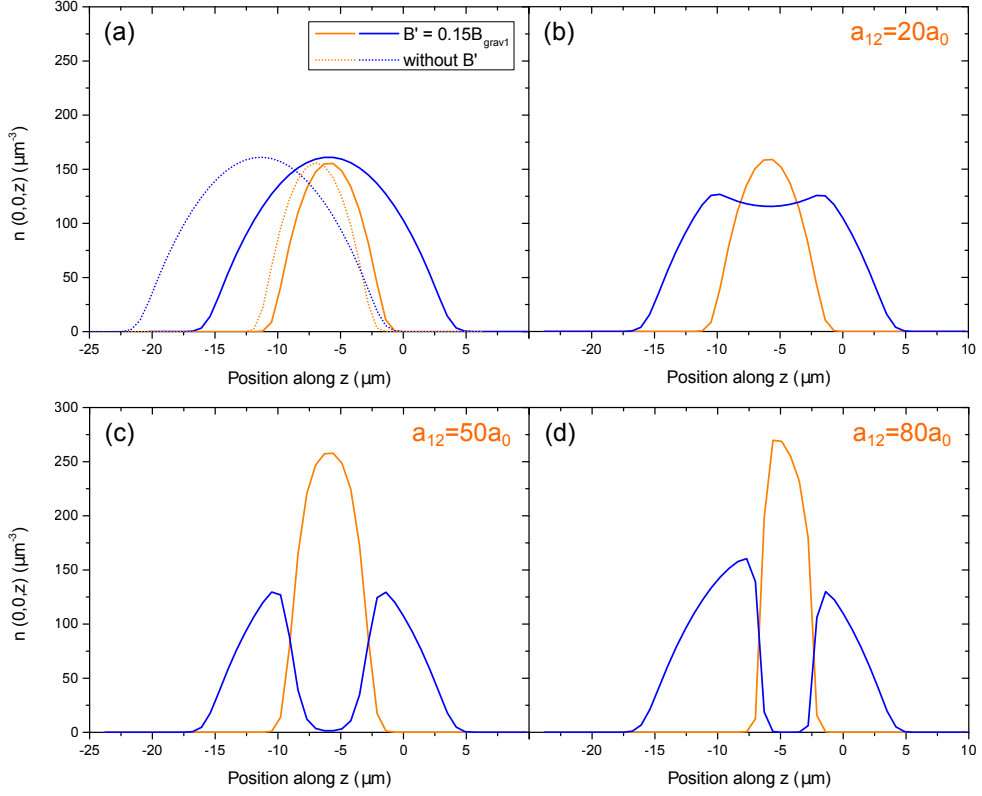


Figure 8 – Simulated density profile along the vertical direction for the ground-state of the ^{23}Na - ^{41}K BEC with the addition of an external magnetic field gradient that partially compensates the gravitational force acting on the atoms. In (a), we compare the density profiles with and without the magnetic field gradient for the non-interacting two-species BEC. For $B' = 0.15B_{\text{grav}1}$, with $B_{\text{grav}1}$ being the field that totally compensates gravity for the potassium atoms, we observe that the center of mass along the vertical direction for each species almost coincide. With this field and increasing the repulsive interspecies interaction ($a_{12} > 0$) it is possible to see that the system enters in an internal overlap configuration, in (b), (c) and (d). Source: By the author.

The possibility to explore different miscibility regions with attractive and repulsive interspecies interactions and different ground-state configurations, with internal or external overlap between the species, makes the two-component BEC of ^{23}Na - ^{41}K atoms a promising candidate to complete characterize the miscible-immiscible phase-diagram for trapped atomic BECs. The properties of the system at each configuration could be studied, specially the nucleation procedure and the dynamics of coupled vortices, which is the topic of the following Chapter.

3 Vortices in a two-species BEC

The intent of this Chapter is to describe and motivate the generation of vortices in a rotating weakly-interacting two-component condensate composed by ^{23}Na and ^{41}K atoms. In Chapter 2, we first modelled the description of a trapped weakly-interacting Bose gas at $T = 0$ by deriving the Gross-Pitaevskii equation. Later, we extended this result to obtain the expected ground state for our particular two-component BEC in the different miscibility regimes according to the parameters Δ , a_{12} and N_1/N_2 . However, the dynamic properties of such systems, obtained when dealing with the time-dependent GPEs, have not been treated in this thesis so far. Therefore, in section 3.1, we start by introducing the hydrodynamic equations for a single-component BEC in order to show that such fluid is irrotational. The only way to induce rotation in these fluids is through the nucleation of quantized vortices, which are described in section 3.2, followed by a simple argument that states that a multi-charged vortex is not stable and would break itself into singly charged vortices, forming a vortex lattice. With these elements, we are able to describe a rotating BEC (in section 3.3) and, in the end of the chapter (section 3.4), we generalize our results to the two-species BEC, for which coupled vortex lattices and “exotic” vortex structures (e.g., square vortex lattices and vortex sheets) are expected to appear.

3.1 Dynamics of Bose-Einstein condensates

In order to treat the dynamic properties of Bose-Einstein condensates at $T = 0$, one has to look at the time-dependent Gross-Pitaevskii equation introduced in the previous chapter in the form of

$$i\hbar \frac{\partial \psi(\mathbf{r}, t)}{\partial t} = -\frac{\hbar^2}{2m} \nabla^2 \psi(\mathbf{r}, t) + V(\mathbf{r}, t) \psi(\mathbf{r}, t) + U_0 |\psi(\mathbf{r}, t)|^2 \psi(\mathbf{r}, t), \quad (3.1)$$

with $\psi(\mathbf{r}, t) = \psi(\mathbf{r}) e^{-i\mu t/\hbar}$ and $\psi(\mathbf{r}) = \sqrt{N} \phi(\mathbf{r})$ being the order parameter for the transition. From this equation, one can deduce a pair of equations which resemble the hydrodynamic equations for a normal ideal fluid. These equations are introduced in the following,

in which they are used to obtain the usual size of localized perturbations in the condensate wave function and to conclude that the velocity field of a BEC is irrotational.

3.1.1 The hydrodynamic equations

The hydrodynamic equations are useful to study the motion of fluids and can be also applied in the context of trapped weakly-interacting Bose gases. We began by deriving the continuity equation for the condensed atoms from the time-dependent Gross-Pitaevskii equation. This can be easily done by multiplying equation 3.1 by $\psi^*(\mathbf{r}, t)$ and subtracting from the resulting equation its complex conjugate, in such a way that one finds

$$\frac{\partial}{\partial t} |\psi(\mathbf{r}, t)|^2 + \nabla \cdot \left[\frac{\hbar}{2mi} (\psi^* \nabla \psi - \psi \nabla \psi^*) \right] = 0, \quad (3.2)$$

which has the same form of the one obtained from a linear Schrödinger equation since the non-linear term on the GPE is real. Equation 3.2 can be rewritten in the form of a continuity equation for the particle density, such that

$$\frac{\partial n}{\partial t} + \nabla \cdot (n\mathbf{v}) = 0, \quad (3.3)$$

where $n = |\psi|^2$ and \mathbf{v} is the fluid velocity field, defined as

$$\mathbf{v} = \frac{\hbar}{2mi} \frac{(\psi^* \nabla \psi - \psi \nabla \psi^*)}{|\psi|^2}. \quad (3.4)$$

In order to obtain simple expressions for the density and the velocity field, one can redefine the order parameter $\psi(\mathbf{r})$ in terms of an amplitude f and a phase ϕ ,

$$\psi = f e^{i\phi}, \quad (3.5)$$

such that $n = f^2$ and the velocity field is written in terms of the phase as

$$\mathbf{v} = \frac{\hbar}{m} \nabla \phi. \quad (3.6)$$

This last equation brings up an important result: in the absence of a singularity in ϕ , the motion of the condensate must be irrotational, since

$$\nabla \times \mathbf{v} = \frac{\hbar}{m} \nabla \times \nabla \phi = 0. \quad (3.7)$$

¹ This relation is also true when considering a two-component BEC, since each condensate can be characterized by an independent order parameter (see Eq. 2.30).

Irrotational velocity fields are a typical characteristic of superfluids, for which rotation can only occur through the nucleation of quantized vortices. (3, 22, 105) We will return to this when deriving the properties of vortices in atomic BECs, in section 3.2.

The expression for the phase ϕ in terms of n and \mathbf{v} can be derived by keeping the real part of Eq. 3.1 while inserting the new definition of the order parameter (equation 3.5)² to obtain

$$\hbar \frac{\partial \phi}{\partial t} + \left(\frac{1}{2} m \mathbf{v}^2 + V + U_0 n - \frac{\hbar^2}{2m\sqrt{n}} \nabla^2 \sqrt{n} \right) = 0. \quad (3.8)$$

The equation of motion for the velocity field is then obtained by taking the gradient of the previous equation together with the definition in 3.6, which leads to

$$m \frac{\partial \mathbf{v}}{\partial t} = -\nabla \left(\mu' + \frac{1}{2} m \mathbf{v}^2 \right) \quad (3.9)$$

where $\mu' = V + nU_0 - \hbar^2/(2m\sqrt{n})\nabla^2\sqrt{n}$. The term nU_0 in the expression for μ' is associated with the chemical potential for a uniform Bose gas. From the Gibbs-Duhem relation at $T = 0$, changes in the chemical potential are related with changes in the pressure of the gas, P , with $dP = nd\mu$, such that equation 3.9 can be rewritten as

$$\frac{\partial \mathbf{v}}{\partial t} = -\frac{1}{mn} \nabla P - \nabla \left(\frac{\mathbf{v}^2}{2} \right) - \frac{1}{m} \nabla V + \frac{1}{m} \nabla \left(\frac{\hbar^2}{2m\sqrt{n}} \nabla^2 \sqrt{n} \right). \quad (3.10)$$

This last equation can be compared with Euler's equation written in the form

$$\frac{\partial \mathbf{v}}{\partial t} - \mathbf{v} \times (\nabla \times \mathbf{v}) = -\frac{1}{mn} \nabla P - \nabla \left(\frac{\mathbf{v}^2}{2} \right) - \frac{1}{m} \nabla V. \quad (3.11)$$

There are two main differences between these last two equations. First, the term $\mathbf{v} \times (\nabla \times \mathbf{v})$ which appears as the second term on the left hand side of equation 3.11 vanishes for the case of the BEC and, therefore, does not contribute to Eq. 3.10. And second, the last term on the right hand side of Eq. 3.10, that does not appear in the definition of Euler's equation, is related with the spatial variations of the magnitude of the wave function of the condensed state. This term is referred to as the *quantum pressure* term³ and it

² The imaginary part of the resulting equation will be equal to the continuity equation (Eq. 3.3) written in the new variables f and ϕ .

³ Here we denote by "quantum (or normal) pressure term" the term in Eq. 3.10 that is proportional to the quantum (or normal) pressure.

is also interesting to note that only this term contains the Planck's constant. If one considers the spatial scale of variations of the condensate wave function to be given by l , then one can show that the normal pressure term would scale as $1/(mn)\nabla P \sim nU_0/(ml)$, and that the *quantum pressure* term would scale as $1/m\nabla(\hbar^2/(2m\sqrt{n})\nabla^2\sqrt{n}) \sim \hbar^2/(m^2l^3)$. By equating both pressure terms, we find a characteristic length, ξ , which defines the regimes for which the *quantum pressure* ($l \ll \xi$) or the normal pressure ($l \gg \xi$) dominates equation 3.10. This characteristic length is usually referred to as *healing length* (or *coherence length*) and is defined as

$$\xi = \frac{\hbar}{\sqrt{2mU_0n}}. \quad (3.12)$$

In doing the Thomas-Fermi approximation discussed in Chapter 2, one assumes that the variations of the condensate wave function are small, neglecting the *quantum pressure* term. Consider, for instance, a BEC in the Thomas-Fermi approximation subjected to a localized perturbation. Close to this perturbation, TFA is no longer valid. But, far from it, at distances larger than ξ , TFA is valid again. Following these arguments we can associate ξ with the characteristic size of localized perturbations in a BEC.

3.2 Vortices in atomic BECs

As discussed in section 3.1.1, the possibility of describing a Bose-Einstein condensate in terms of a macroscopic wave function $\psi = \sqrt{n}e^{i\phi}$ sets the velocity field to be proportional to the gradient of ϕ (see Eq. 3.6), making the fluid to be irrotational at any point where the phase ϕ is not singular (since, $\nabla \times \mathbf{v} = 0$). Therefore, from Stokes' theorem, the circulation Γ around a closed path C must vanish if the velocity field presents no singularity in the region S delimited by C , which means

$$\Gamma = \oint_C \mathbf{v} \cdot d\mathbf{l} = \int_S (\nabla \times \mathbf{v}) d^2S = 0. \quad (3.13)$$

The motion of a condensate is thus much more restricted than that of a classical fluid. However, rotation is still possible around a “line” where ϕ is singular. These “lines” are vortices (“vortex lines” or “vortex rings”⁴) where the condensate density vanishes. In the

⁴ It is possible to show that the vortices cannot terminate on the fluid. (106) Therefore, those are the possible vortex structures.

following, we discuss the properties of “vortex lines” in atomic BECs.

3.2.1 The properties of a “vortex line”

In the presence of a singularity in the phase of the condensate wave function, the circulation around a closed path that encloses its singularity is no longer zero and may be written as

$$\Gamma = \oint_C \mathbf{v} \cdot d\mathbf{l} = \frac{\hbar}{m} \Delta\phi, \quad (3.14)$$

where $\Delta\phi$ is the phase variation along the path C . Since the condensate wave function is single-valued, $\Delta\phi$ must be equal to $2\pi l$, with l an integer, and the circulation becomes:

$$\Gamma = l \frac{h}{m}, \quad (3.15)$$

with l being the vortex charge.

In order to derive the energy of the vortex, one can note that the equations satisfied by the velocity field (Eqs. 3.6 and 3.7) are of the same form of the ones satisfied by a magnetic-static field \vec{B} in free space. The vortex lines are in this context the source of the velocity field, just like as electric current lines are the source of magnetic fields (107) and the velocity field can be obtained from a Biot-Savart type law:

$$\mathbf{v}(\mathbf{r}) = \frac{l\hbar}{2m} \int_{\mathbf{r}'} \frac{(\mathbf{r}' - \mathbf{r})}{|\mathbf{r}' - \mathbf{r}|^3} d\mathbf{r}'. \quad (3.16)$$

For a vortex line aligned along the z axis it has the simple form of:

$$\mathbf{v}(r, \theta, z) = \frac{l\hbar}{mr} \hat{\theta}. \quad (3.17)$$

From Eq. 3.17 one can see that the modulus of $\mathbf{v}(r, \theta, z)$ is inversely proportional to the distance from the vortex core r . This is completely different from what one would obtain for a classic fluid with $\mathbf{v} = \mathbf{r} \times \Omega$, where the velocity increases linearly with the distance to the rotation axis⁵. Even if the velocity field diverges as $r \rightarrow 0$, the density of the BEC vanishes with r^2 and the energy of the vortex is finite. One can estimate the size of a vortex, R_{vx} , by considering the competition between the centrifugal force, which

⁵ The classical limit of a rigid-body rotation is recovered when we treat a fast rotating BEC where a vortex lattice appears, as it will be discussed before the end of this chapter.

prevents the atoms to fill the vortex core, and the mean-field term of the Gross-Pitaevskii equation, which tends to distribute the atomic density:

$$\frac{l^2 \hbar^2}{m R_{vx}^2} = U_0 n \Rightarrow R_{vx} \sim |l| \sqrt{\frac{\hbar^2}{m U_0 n}} \sim |l| \xi. \quad (3.18)$$

This result is not a surprise. Since it was discussed in section 3.1.1, the *healing length* is the typical size for perturbations in the condensate wave function.

Under the assumption that the radial size of the system is much bigger than the vortex core ($R_{\perp} \gg \xi$), the energy of the vortex can be approximated by the kinetic energy of the atoms outside the vortex core region (108) and

$$E_{vx} = \int_{\xi}^{R_{\perp}} d^2 r \int dz \left(n(\mathbf{r}) \frac{m v^2}{2} \right). \quad (3.19)$$

For a uniform cylindric condensate with density n_0 , radius R_{\perp} and length L , the vortex energy per unit length ($\varepsilon_{vx} = E_{vx}/L$) can be written as

$$\varepsilon_{vx} = n_0 \frac{\pi l^2 \hbar^2}{m} \log \left(\frac{R_{\perp}}{\xi} \right), \quad (3.20)$$

and the corresponding angular momentum per particle along z is

$$L_z = m(\mathbf{r} \times \mathbf{v}) \hat{z} = l \hbar, \quad (3.21)$$

which does not depend on the radius. The energy of a vortex can also be derived directly from minimizing the energy functional accounting for the vortex line inside the fluid. For more details on it, see Ref. (82)

3.2.2 Multi-charged vortices and vortex lattices

Once we derived the energy per unit length and the angular momentum per particle of a vortex line with charge l , it becomes clear that angular momentum can only be injected into the condensate in quantized units of \hbar . For the case of $L_z = \hbar$, a singly charged vortex (with $l = 1$) is nucleated inside the cloud. In equilibrium, this vortex sits at the center of the BEC.

Now, if more than one quanta of angular momentum is transferred to the BEC ($L_z > \hbar$), it is possible to create a multi-charged vortex. The energy per unit length of

such a vortex is given by Eq. 3.20 with $|l| > 1$. Since $\varepsilon_{vx} \propto l^2$, it is easy to see that for example, a vortex with charge l will have an energy larger than two vortices with charges l_1 and l_2 with $l_1 + l_2 = l$. Therefore, multi-charged vortices are unstable and tend to break apart in l singly charged vortices which arrange themselves in a lattice. (108) In addition to this simple argument it follows (see next section) that, in order to minimize the energy of a rotating BEC, one should mimic the behaviour of rigid-body rotation which is only possible by considering a uniform distribution of vortices in the condensate.

3.3 Rotating condensates

The direct equivalence with the rotating bulk experiment in superfluid helium (5–8) is to rotate the BEC along one of its trapping axes. This can be done for instance by stirring a blue-detuned laser beam⁶ in the condensate. (28, 29) In this case, in the laboratory frame, the atoms experience a time-dependent potential and it becomes easier to describe the condensate in the rotating frame of the stirring beam. In this rotating frame, the Hamiltonian of the system is given by (82, 108)

$$H' = H - \Omega \cdot \mathbf{L} = \sum_{i=1}^N \left(\frac{\mathbf{p}_i - m(\Omega \times \mathbf{r}_i)^2}{2m} + V(\mathbf{r}_i) - \frac{m}{2}(\Omega \times \mathbf{r}_i)^2 \right) + U_0 \sum_{i < j} \delta(\mathbf{r}_i - \mathbf{r}_j). \quad (3.22)$$

and it can be used to calculate the ground state of the system. In this thesis, we consider the case of “slow” rotation in which $nU_0 \gg \hbar\Omega$ but $L_z \gg \hbar$ such that a vortex lattice can be nucleated. The description of the system under fast rotation ($nU_0 \ll \hbar\Omega$) relies on the occupancy of the lowest Landau levels (LLL) (82, 109), for which it is predicted the occurrence of the Quantum Hall effect. (110–112)

Even considering “slow” rotations, as one increases the angular frequency of the rotating condensate it is expected that the system approaches the classical limit for rigid body rotation. In the classical limit, the velocity field should be given by $\mathbf{v}_i = \Omega \times \mathbf{r}_i$ and the first term of Eq. 3.22, which represents the kinetic energy on the rotating frame, would

⁶ In order to properly perform the rotation on the condensate through the use of a stirring beam, some relevant parameters have to be taken into account. The size of the stirring beam has to be smaller than the condensate (with $w_0 \approx 0.5R_{\text{TF}}$) and its resulting repulsive potential has to produce only a small perturbation on the trapping potential, being of the order of the chemical potential of the BEC ($U_0^{\text{stir}} \sim \mu$). We will come back to these parameters in Chapter 6, when describing our stirring beam optical setup.

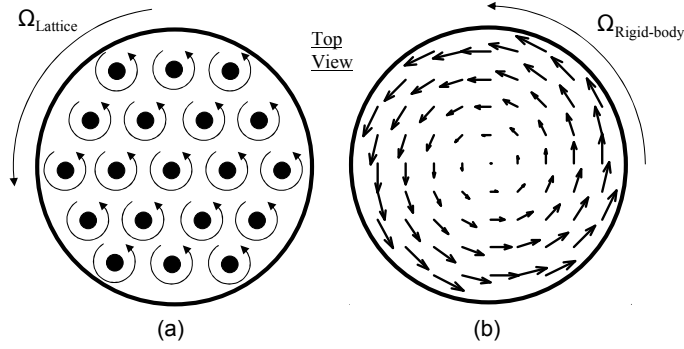


Figure 9 – Comparison between the rotation of a BEC with a vortex lattice (a) and a rigid-body rotation, in (b).

Source: Adapted from Haljan. (114)

vanish. However, this cannot be everywhere true for a condensate, since $\nabla \times \mathbf{v}_i = 2\Omega \neq 0$. As first suggested by Feynman, in 1955 (105), the limit of rigid body rotation for a condensate is only achieved when creating a large uniform array of vortices aligned in the direction of the angular velocity. In this limit, the point-like vorticity of the individual vortices is replaced by a diffuse and uniform vorticity. (113) A simple but very illustrative picture comparing a rigid-body rotation with a condensate with a vortex lattice is shown in Fig. 9, adapted from Ref. (114)

If one defines the number of singly charged vortices per unit area, n_{vx} , given by

$$n_{vx} = \frac{2m\Omega}{h} = \frac{1}{\pi a_\Omega^2}, \quad (3.23)$$

the average circulation per unit area is $\gamma = n_{vx}h/m = 2\Omega$, as for rigid-body rotation and the length $a_\Omega = \sqrt{\hbar/m\Omega}$ defines the intervortex spacing.

The total energy in the rotating frame is given by:

$$E' = \int d\mathbf{r} \left[\frac{1}{2}nm(\mathbf{v} - \Omega \times \mathbf{r})^2 + n \left[V(\mathbf{r}) - \frac{1}{2}m(\Omega \times \mathbf{r})^2 \right] + \frac{1}{2}U_0n^2 \right]. \quad (3.24)$$

This last equation is minimized by assuming the average velocity field as $\mathbf{v} = \Omega \times \mathbf{r}$ such that

$$n(\mathbf{r}) = \frac{1}{U_0} \left(\mu' - V(\mathbf{r}) + \frac{1}{2}m(\Omega \times \mathbf{r})^2 \right), \quad (3.25)$$

where μ' is the chemical potential in the rotating frame. Eq. 3.25 has a usual Thomas-Fermi distribution plus a correction due to the centrifugal term. In a harmonic trapping

potential, the radial trapping frequency is then replaced by an effective radial trapping frequency with $\omega_{\perp}^* = (\omega_{\perp}^2 - \Omega^2)^{1/2}$. This effective frequency changes the Thomas-Fermi radii in such a way that the cloud would expand (shrink) in the radial (axial) direction as a function of Ω with:

$$\frac{R_{\perp}(\Omega)}{R_{\perp 0}} = \left(1 - \frac{\Omega^2}{\omega_{\perp}^2}\right)^{-3/10} \quad \text{and} \quad \frac{R_z(\Omega)}{R_{z0}} = \left(1 - \frac{\Omega^2}{\omega_{\perp}^2}\right)^{1/5}, \quad (3.26)$$

where $R_{\perp 0}$ and R_{z0} are the static Thomas-Fermi radii. Therefore, the aspect ratio of the rotating cloud would also depend on the rotating frequency and it has been used as a tool to infer the actual angular velocity of the rotating BECs. (115–117)

When increasing the angular frequency Ω of the rotating BEC, the density of vortices increases linearly (see Eq. 3.23) and the intervortex spacing, a_{Ω} , becomes smaller. The limiting situation when the vortex cores touch each other happens for $a_{\Omega} \sim \xi$ or $\hbar\Omega \sim nU_0$. Another effect on increasing the rotation is that, in the case of a harmonically trapped condensate, the effective radial trapping frequency gets smaller while the radial size of the cloud increases (see Eqs. 3.26). The density and, consequently, the effect of interactions decrease, reducing the frequency for which the vortices overlap. When $nU_0 \ll \hbar\Omega$, it is possible to demonstrate that the condensate populates only states in the lowest Landau level (LLL). (82, 109) As $\Omega \rightarrow \omega_{\perp}$ the number of states in the LLL becomes larger than the number of atoms and the system evolves from a condensate with a large vortex lattice to a strongly correlated quantum system closely related with the Quantum Hall effect. (110–112)⁷ This behaviour sets an upper limit for the rotation frequency with $\Omega \rightarrow \omega_{\perp}$.

The uniform distribution of vortices in the condensate could in principle arrange itself at different configurations but, as it was shown by Tkachenko in 1966 (118, 119), a triangular-shaped lattice, known as ‘‘Abrikosov lattice’’, has the lowest energy. In experiments, these triangular vortex lattices have been widely observed and some images of atomic weakly-interacting BECs with such lattices are presented in Fig. 10. When dealing with a two-component BEC, other vortex lattice geometries and exotic vortex structures

⁷ It is possible to show that the Hamiltonian of rotating neutral particles resembles the Hamiltonian of charged particles subjected to a magnetic field. However, this demonstration is far beyond the scope of this thesis.

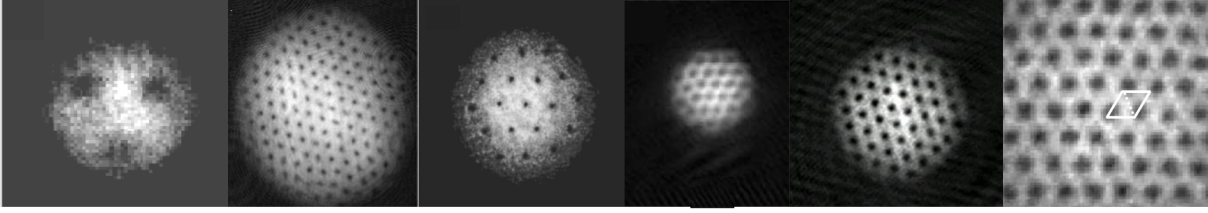


Figure 10 – Vortex lattices produced while rotating different Bose-Einstein condensates. The number of vortices is changed in each image but all lattices present a triangular-shape arrangement of the vortex cores as it can be easily seen in the zoom presented in the figure in the right.

Source: Adapted from Madison et al. (28), Raman et al. (29), Coddington et al. (34), Bretin et al. (120) and P. C. Haljan (114), respectively.

are possible due to the interaction between the different components.(65–68) Such coupled vortices are described in the next section.

3.4 Vortex lattices in a two-species BEC

In a rotating two-species BEC, the vortex lattice properties can be obtained by extending the Hamiltonian of Eq. 3.22 to a two-species Hamiltonian, as it was done in Chapter 2 to obtain the static coupled Gross-Pitaevski equations. In this new context, the energy functional in the rotating frame can be written as:

$$E' = \int d\mathbf{r} \left[\sum_{i=1,2} \left(\frac{1}{2} m_i (\mathbf{v}_i - \Omega \times \mathbf{r}_i)^2 n_i + \left[V_i(\mathbf{r}_i) - \frac{1}{2} m_i (\Omega \times \mathbf{r}_i)^2 \right] n_i + \frac{1}{2} u_{ii} n_i^2 \right) + u_{12} n_1 n_2 \right], \quad (3.27)$$

where we have used the same notation of Chapter 2. As for the single-component, large two-component BECs with many vortices have a superfluid flow that mimics the rigid-body behaviour with an average velocity field given as $\mathbf{v}_i \approx \Omega \times \mathbf{r}_i$. With this condition, the first term of Eq. 3.27 vanishes and the energy functional assumes the form:

$$E' = \int d\mathbf{r} \left[\sum_{i=1,2} \left(\left[V_i(\mathbf{r}_i) - \frac{1}{2} m_i (\Omega \times \mathbf{r}_i)^2 \right] n_i + \frac{1}{2} u_{ii} n_i^2 \right) + u_{12} n_1 n_2 \right]. \quad (3.28)$$

When minimizing E' with respect to n_1 and n_2 under the constraint of fixed number of particles for each component, one finds the coupled rotating GPEs:

$$U'_1(\mathbf{r}) + u_{11} n_1 + u_{12} n_2 = \mu'_1 \quad (3.29)$$

$$U'_2(\mathbf{r}) + u_{22} n_2 + u_{12} n_1 = \mu'_2, \quad (3.30)$$

that strongly resemble Eqs. 2.41 and 2.42 in the Thomas-Fermi limit. As for the case of the single BEC, the only difference is that $U_i' = \frac{1}{2}m_i\omega_i^*r_i^2$ is the effective trapping potential with $\omega_{\perp i}^* = (\omega_{\perp i}^2 - \Omega^2)^{1/2}$ and $\omega_{zi}^* = \omega_{zi}$, and μ_i' are the chemical potential of each component in the rotating frame⁸.

As for the statical properties of two-components BECs discussed in Chapter 2, the inter-species interaction is a fundamental key in nucleating vortices and vortex lattices. The miscibility regime in which the system is found to be affects the vortex lattices structures. Since the BEC with a vortex lattice is the ground state of the system in the rotating frame, also here one can use a numerical simulation procedure with imaginary time evolution, similar to the one described in the end of Chapter 2, in order to obtain the density profiles of the rotating two-component BEC. (65–68, 121) In this section, I focus on discussing the results of three papers (65, 67, 68) which treat systems that most resemble our experimental setup.

For simplicity, let us first present the case in which $a_{11} = a_{22} = a$, $m_1 = m_2 = m$, $\omega_1 = \omega_2 = \omega$ and $N_1 = N_2 = N$ are fixed and the interspecies interaction (a_{12} , with $a_{12} > 0$ for repulsive interspecies interaction) and the rotation frequency (Ω) could vary. Such a system could be used as a first approximation for experiments working with different states of the same isotope (for example, on the $|1, -1\rangle$ and $|2, 1\rangle$ ⁸⁷Rb mixture (122)). On following the discussion presented by Kasamatsu et al. in (65), it is useful to define a modified miscibility parameter:

$$\delta = a_{12}/a, \quad (3.31)$$

such that the system is miscible if $\delta < 1$ and immiscible if $\delta > 1$ ⁹.

In the miscible region, two types of regular vortex lattices are expected to occur. First, for $\delta = 0$, the two-components do not interact and the formation of vortex lattices happens as in the case of the single component BEC described in section 3.3 with triangular shaped lattices. As δ is increased, the vortex cores in one component shift their

⁸ In the case of rotating two-component BEC, we did not include the gravitational potential as it was done in Chapter 2, however a fully description of the system has to take into account the difference in the gravitational sag of each species.

⁹ This condition for miscible and immiscible regimes is equivalent to the one defined in Chapter 2 for the miscibility parameter Δ , such that $\Delta = a^2(1 - \delta^2)$.

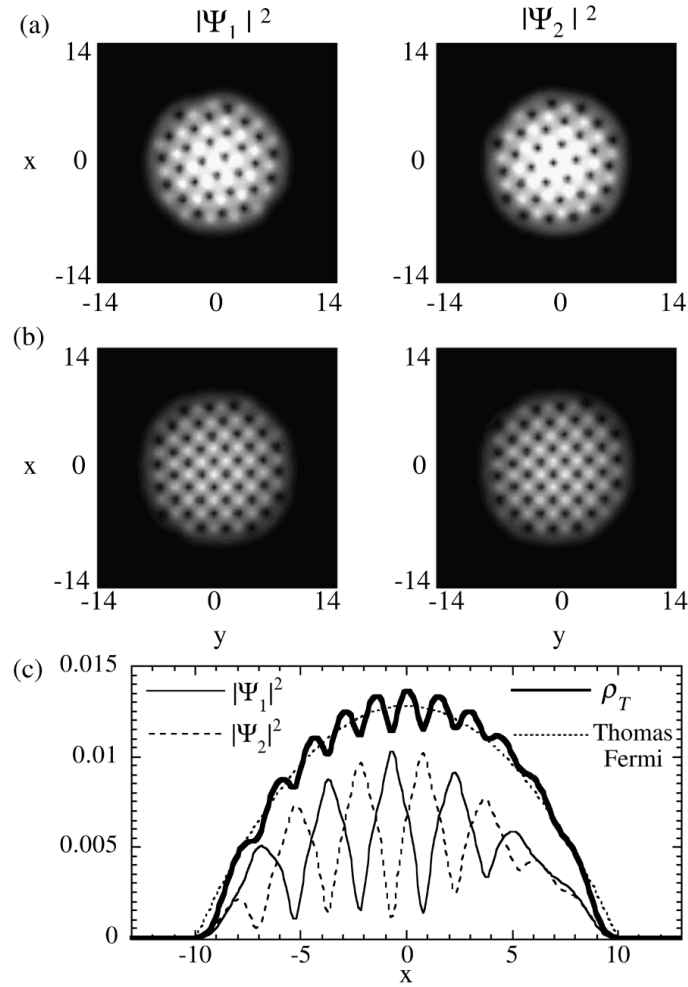


Figure 11 – Two-component BEC under rotation with coupled vortex lattices. The density profiles of each species is presented for two different rotating frequencies $\Omega = 0.6\omega$ in (a) and $\Omega = 0.75\omega$ in (b). The interspecies interaction was kept fixed at $\delta = 0.7$. In (c), the cross-section profile along $y = 0$ is shown such that it is easy to see the *coreless* vortices.

Source: Adapted from Kasamatsu et al. (65).

positions and no longer overlap with the vortex cores in the other species. The triangular shaped lattices get distorted and achieve a stable square shaped configuration for sufficient large δ which depends on the rotation frequency. In Figure 11, we present the images of the density profiles of the two-component BECs for $\delta = 0.7$ and $\Omega = 0.6\omega$ (in (a)) and $\Omega = 0.75\omega$ (in (b)) adapted from Ref. (65). In (c), a cross-section of the density profile in (b) shows that the lattices present interlocked or *coreless* vortices, which means that, on the stable square configuration, density peaks in one component represents density holes in the other species.

A simple argument can be constructed in order to explain the reason why the

square shaped vortex lattices are stabilized in two-components BECs. From Eq. 3.28, we can alternatively write the interaction of the system as:

$$E_{\text{int}} = \int d\mathbf{r} a \left[(1 + \delta) \rho_T^2 + (1 - \delta) S^2 \right] / 4, \quad (3.32)$$

where $\rho_T = |\psi_1|^2 + |\psi_2|^2$ is the total density of the system and $S = |\psi_1|^2 - |\psi_2|^2$, the “spin” variable¹⁰. The first term on Eq. 3.32 can be minimized if δ is increased such that ρ_T is smoothed, causing shifts in the positions of the vortex cores of each component. The second term can be associated with the interaction energy between spins in the Ising model. (83) When $(1 - \delta) > 0$ the system is found to be in an antiferromagnetic state where square lattices are stabilized. As δ increases approaching $\delta = 1$, vortices in the same component begin to overlap and, as it is further increased, “vortex sheets” start to appear. In the limit where $\delta > 1$, the system enters in a ferromagnetic phase: the condensates are phase-separated and form domains of the same spin component. A complete scan through the possible regimes for different vortex lattice structures considering equal masses and slightly different intraspecies interactions ($a_{11} = 53.35\text{\AA}$ and $a_{22} = 56.65\text{\AA}$)¹¹ can be seen in Fig. 12, adapted from Ref. (67) In this case, the δ parameter is obtained by doing $a = \sqrt{a_{11}a_{22}}$. The limits with $(1 - \delta) > 0$ and $\delta > 1$ are depicted in the left and right column for $\delta = 0.7$ and $\delta = 1.15$, respectively. For the first, as soon as we start rotating the two-component BEC, vortices are nucleated in the traditional triangular shaped lattice (see part (a) in the figure). By increasing the rotational frequency, more vortices appear (b) and the vortex lattice assumes a square shaped configuration, as it can be seen in (c). In the other limit (left column in Fig. 12), the condensates are phase separated and for small rotating frequencies, they rotate individually as single “droplets” (see part (d) in the figure). As soon as the frequency is increased, vortices could be generated still preserving the phase separated characteristic of the system. For even larger rotating frequencies, the “vortex sheets” are formed, as it can be seen in (f).

In our experiment with a two-component BEC composed of ^{23}Na - ^{41}K atoms, the mass ratio between the species $\eta^* = m_1/m_2$ is also relevant when producing coupled

¹⁰ With the definition of S , spin up corresponds to the density peaks of ψ_1 at the vortex cores of ψ_2 and vice-versa for spin down.

¹¹ These interactions are used in order to proper match the experimental parameters for the results presented in reference (122).

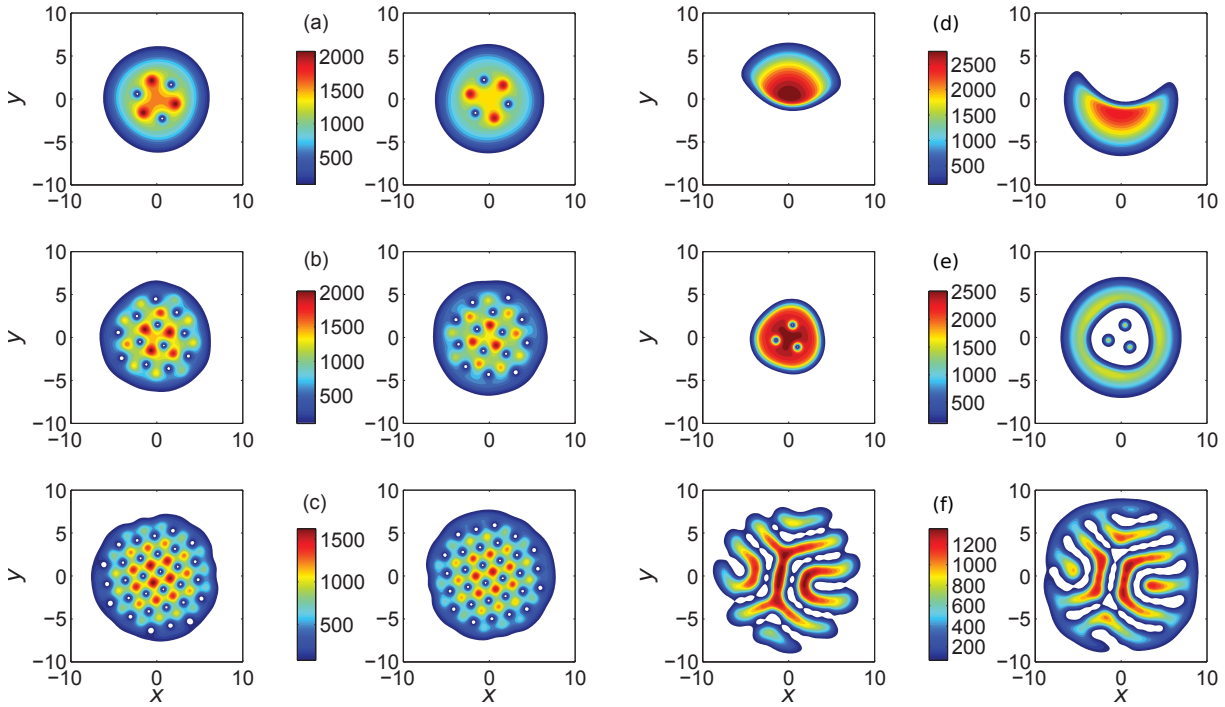


Figure 12 – Density profiles for component 1 (left columns) and for component 2 (right columns) of a rotating two-component BEC with slightly different a_{11} and a_{22} . In (a), (b) and (c), the system is in the miscible regime ($1 - \delta > 0$) and, while increasing the rotation frequency ($\Omega = 0.25, 0.5$ and 0.75 , respectively) for a fixed interspecies interaction ($\delta = 0.7$) the vortex lattices evolve from having a triangular shape to a square coreless vortex lattice. In (d), (e) and (f), the system is in the phase-separated regime ($\delta = 1.15 > 1$) such that while increasing the rotation frequency ($\Omega = 0.1, 0.5$ and 0.9 , respectively) the system evolves from rotating “droplets” to presenting vortex sheets.

Source: Adapted from Mason et al. (67).

vortex lattices. We identify component 1 with the ^{41}K isotope and component 2 with the ^{23}Na isotope such that $\eta^* \sim 1.78$. Since the vorticity of each vortex is equal to h/m_i , with m_i being the mass of the corresponding component, the number of nucleated vortices in the potassium cloud is going to be almost two times larger than the number nucleated in sodium and the vortex cores would naturally not coincide. However, in the most similar case simulated in (67), the square shaped vortex lattice configuration was not observed and the system presented always triangular coreless vortex lattices. The authors justify it with the impossibility of generating large number of vortices in one of the components but no further discussion is made in order to clarify if it is an specific limitation of the simulated system or if there is some intrinsic reason why it happens. In addition to that, slightly different parameters in their numerical simulation (equal or slightly different a_{11} and a_{22} , for example) give reasonably different phase diagrams for the vortices configurations.

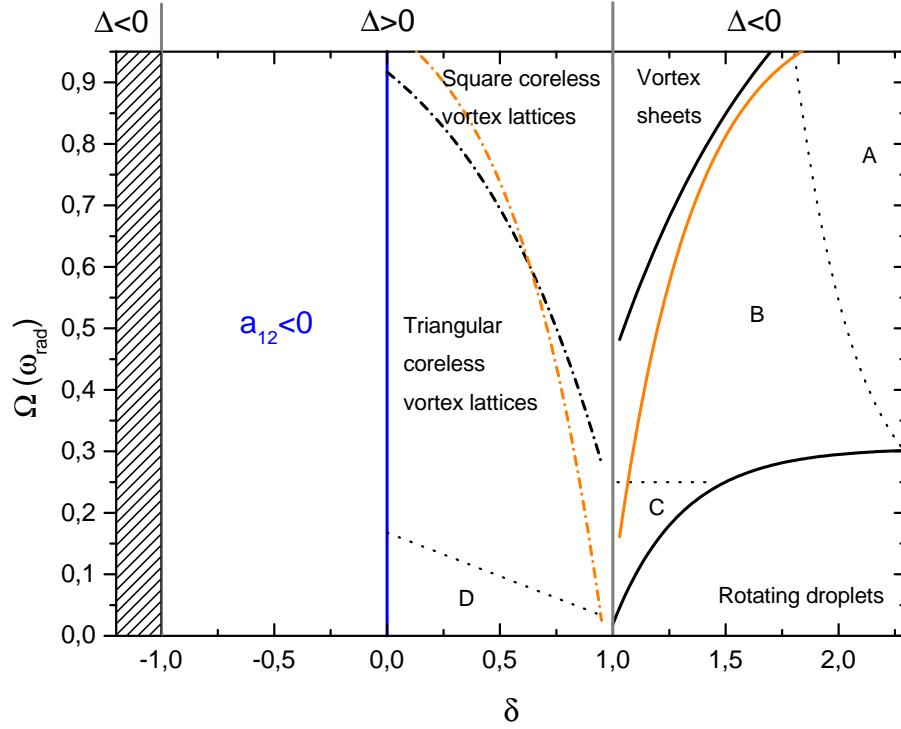


Figure 13 – Phase diagram $\Omega \times \delta$ for the different vortex lattices structures in a two-component BEC with $m_1 = m_2 = m$, $\omega_1 = \omega_2 = \omega$ and $N_1 = N_2 = N$. For the curves in orange, it was considered $a_{11} = a_{22} = 53.35\text{\AA}$ while for the curves in black, it was used a slightly different intraspecies interaction strength with $a_{11} = 53.35\text{\AA}$ and $a_{22} = 56.65\text{\AA}$. Beside the small deviation from the curves which separate the regions with triangular-square coreless vortex lattices and with vortex sheets from the phases below, new regimes appear (named A, B, C and D), discussed in the main text, in the case with slightly different a_{11} and a_{22} .

Source: By the author when adapting the results presented by Mason et al. (67)

The comparison between these phase diagrams is found in Figure 13. For the curves in orange it was considered $a_{11} = a_{22} = 53.35\text{\AA}$ while for the curves in black it was used a slightly different intra-species interaction strength with $a_{11} = 53.35\text{\AA}$ and $a_{22} = 56.65\text{\AA}$. Besides the acceptable small deviation between the curves which separate the regions with triangular-square coreless vortex lattices and with vortex sheets from the phases below, completely new regimes appear (named A, B, C and D) in the case with slightly different a_{11} and a_{22} and therefore, we cannot assume that the square lattices are not going to be observed in our setup. The regions A, B and C are associated with the generation of spin textures known as *skyrmions* (123,124) followed (A and B) or not (C) by vortices, while, in region D, no vortices are nucleated in the condensates.

The region for attractive interspecies interaction presents another interesting phe-

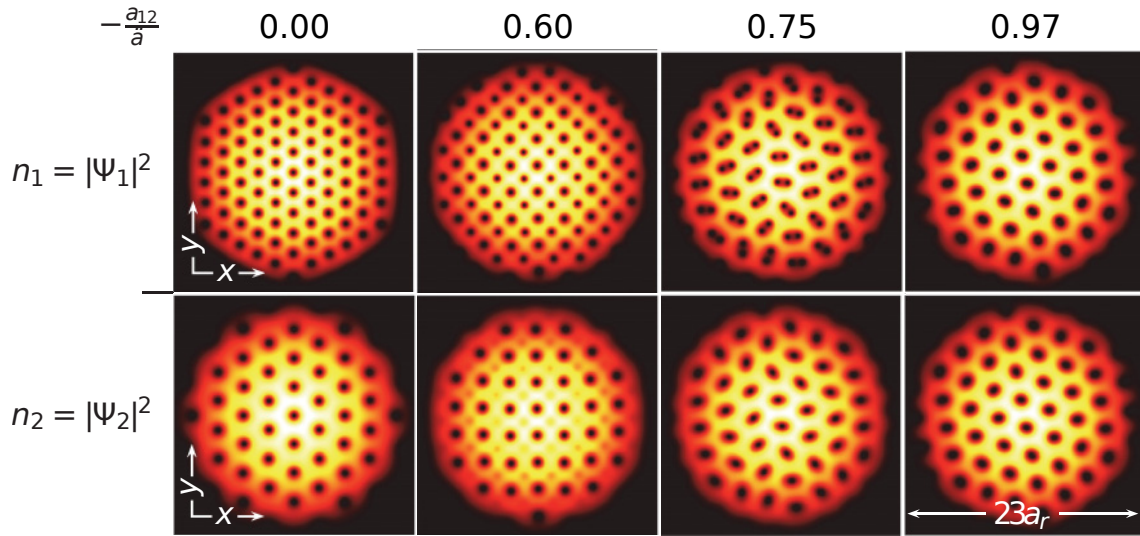


Figure 14 – Density profiles of a rotating two-component BEC with mass ratio $\eta^* = 2$ and attractive interspecies interaction. The rotation frequency was kept fixed with $\Omega = 0.97\omega_{\perp}$ and a_{12} was varied such that configuration of the vortex lattices change from triangular shaped lattices to a doubly charged vortex lattice in component 1, passing through a square and a paired vortex lattice configurations. Source: Adapted from Kuopanportti et al. (68)

nomenon and in order to discuss the expected behaviour for our two-component BEC, we present the results from the numerical simulations presented by Kuopanportti et al. in Ref. (68) Differently from the case with repulsive interspecies interactions considered so far, attractive interspecies interaction, that happens for $a_{12} < 0$ (and $\delta < 0$), will force the vortices of each component to overlap. Depending on both the atomic mass ratio and on the strength of the interspecies interaction, stable overlapping square lattices or even lattices with doubly charged vortices in one component are supposed to occur. In (68), four different mass ratios were studied and the one that most approaches our experimental system has $\eta^* = 2$. The simulated density profiles for each component at a fixed rotation frequency $\Omega = 0.97\omega_{\perp}$ and different negative a_{12} are shown in Figure 14.

In the case of vanishing interspecies interaction, both components present triangular shaped vortex lattices, as it can be seen if Fig. 14 (a). As the strength of the attractive interspecies interaction is increased, the vortices gradually arrange themselves into square shaped lattices (b). A further increase recovers the triangular lattice but with pairs of vortices in species 1 overlapping with single vortices in species 2 (see profiles in (c)). Finally, achieving interaction strengths close to the limiting value of $-\bar{a}$ defined in Chap-

ter 2 (see Eq. 2.54) the pair of vortices in species 1 merge into stable doubly charged vortices, as it can be seen in Fig. 14 (d). Such stable multicharged vortex lattice has not been observed so far and the possibility of controlling its decay through the control of the interspecies interaction transforms our system into an interesting test-bed for vortex dynamics models. From a broader perspective of the Bose-Bose mixtures, their analogue aspects with rotating superfluid ^3He systems and with certain regimes of two-dimensional electron systems, further expand the importance of the study of two-species BECs, as it can shed light on the latter long-standing challenges of many-body physics.

Two main experiments in coupled vortex lattices are reported in the literature. In the first, performed in 2014 by Schweikhard et al. (69), the coupled vortex lattices were observed in a spinor ^{87}Rb BEC where they studied the evolution of such lattices in the miscible regime (with $a_{12} > 0$). While the vortex lattice in one state was long-lived, a fast decay was observed in the other state followed by a pseudo-turbulent regime. In 2016, the second experiment performed by X.-C. Yao et al. in (54) studied coupled vortex lattices in a Bose-Fermi mixture composed of ^{41}K and ^6Li providing a clear evidence of boson-induced superfluidity. (52) In their case, the system is in the miscible regime (with $a_{Li-K} = 60.7a_0$) and, due to the large mass imbalance between the species, diamond shaped lattices were observed in ^6Li . In a vast range of stirring parameters, they confirmed the expected factor of ≈ 6 ($\eta = m_{^{41}\text{K}}/m_{^6\text{Li}} \approx 6.3$) in the number of nucleated vortices between the species. In addition, they describe a decrease in the critical rotating frequency for which vortices start to appear in the Fermi gas when the potassium cloud is present, showing the strong relevance of the interspecies interaction during the process. In the specific case of our NaK experiment, the features observed by Schweikhard et al. in (69) and X.-C. Yao et al. in (54) can be directly reproduced with the advantage that we could extend the investigation region to all the regimes described in this section by tuning the interspecies interaction strength¹² and access different miscibility regimes for the two-component BEC. Besides, the decay of coupled vortex lattices with the possibility of generating a turbulent regime is of fundamental interest to our experiment in the search for new mechanisms to

¹² The interspecies interaction strength can be changed by means of the magnetically induced Feshbach resonances expected to occur between ^{23}Na and ^{41}K atoms, as detailed in App. A.

produce Quantum Turbulence in a two-species BEC.

4 First step in producing a two-species BEC: sodium experimental system

In this Chapter, we present the common experimental tools for the production of the ^{23}Na - ^{41}K BEC. The characterization of such tools are presented as we describe the steps in the experimental sequence until the achievement of the Bose-Einstein condensate of sodium atoms in the Plug trap. First, we describe the NaK vacuum system (in section 4.1), followed by the sodium 2D and 3D-MOTs characterization, in section 4.2. In 4.3, we summarize the processes involved in transferring the Na atoms from the MOT to the Plug trap. Later, the Plug type trap working principles and its characterization for the trapped sodium atoms are described in section 4.4. The evaporative cooling process that cools the atoms in the Plug trap is described in 4.5.1. And finally, in section 4.5.2, we present the characterization of the Bose-Einstein condensate of ^{23}Na obtained in the Plug trap.

4.1 The NaK vacuum system

Cold atom experiments need a clean environment in order to produce dilute atomic samples at a few nanokelvins. This can only be obtained with a good vacuum system. Many different vacuum setups have been successfully used to study Bose-Einstein condensation (or degenerate Fermi gases) (125–127) but most of them rely on two differential pumping stages: a first one, named “high vacuum stage” (with $P \sim 10^{-9}$ Torr), contains the atomic source (ovens, dispensers, etc.), and a second one, named “ultra-high vacuum stage” (with $P \sim 10^{-11} - 10^{-12}$ Torr), which presents the necessary conditions to study degenerate quantum gases. For this configuration, at least two vacuum chambers connected by a differential pumping stage are needed. In the past years, compact sources of atoms have gained great attention due to the high atomic fluxes obtained with two-dimensional magneto-

optical traps (2D-MOTs) for rubidium (127), potassium (128) and lithium atoms. (129) For sodium atoms, high atomic flux from a 2D-MOT was only produced in 2013 by the group of Gabriele Ferrarin in Trento (130) and we choose to follow their approach at the NaK machine.

The vacuum system of the NaK experiment is presented in Fig. 15 and is composed by three vacuum chambers: two *source chambers*, on the sides, in which the 2D-MOTs of each atomic species is independently produced, and a *central chamber*, named *Science chamber* (SC), in which the 3D-MOT and further, the BEC of the two-species are produced. Each 2D-MOT chamber is connected to the Science chamber from opposite sides through thin metallic tubes which provide a differential pumping of 10^{-3} and 10^{-4} with respect to the 2D-MOT chamber of sodium and potassium atoms, respectively. Metallic valves were placed right after the differential pumping tubes in order to be possible to close each part of the system and keep its vacuum even if another part has to be open¹. Three ion pumps (Varian Vaclon Plus 75L/s) are connected to the NaK vacuum system pumping each of its three regions (K 2D-MOT, Na 2D-MOT and Science chamber) in order to keep their pressure around $10^{-9} - 10^{-11}$ Torr after performing the *baking* procedure². After the *baking*, the ultra-high vacuum environment in the SC is obtained with the use of a titanium sublimation pump (Agilent - *Titanium Sublimation Cartridge* 916-0050). The titanium released from this pump sticks to the internal walls of the vacuum system and adheres the particles that collide with it keeping a cleaner environment. The titanium cartridge is installed in the cylinder behind the science chamber (see Fig. 15) which is water cooled during the time the pump is operating. Finally, two vertical and one horizontal optical tables were installed around the vacuum system in order to better align the necessary optics around the vacuum chambers.

¹ In cold atom experiments it is common to open the vacuum system from time to time in order to replace the atomic source. In working with complex vacuum setups with more than one chamber, it is useful to keep the vacuum in the other chambers while replacing the atomic source since the procedure used to achieve high (or ultra-high) vacuum is technically complicated and can last several weeks.

² The necessary vacuum for realizing experiments with cold atoms is only achieved after performing a *baking* procedure during which the vacuum system is connected to a turbo pump (Pfeiffer Vacuum, model HiCube700) and heated at temperatures higher than 100°C in order to remove impurities and, mostly, water.

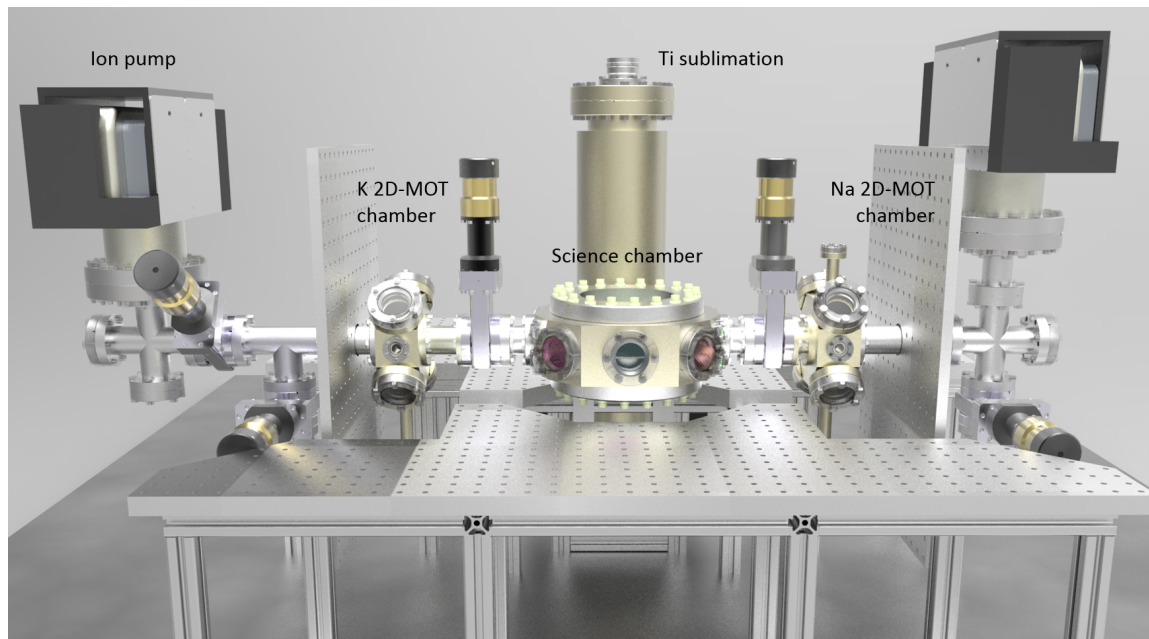


Figure 15 – Front view of the vacuum setup of the NaK experiment. The two *source chambers* (on the sides) are connected to the *Science chamber* (in the center) through thin metallic tubes which provide a differential pumping of 10^{-3} and 10^{-4} with respect to the 2D-MOT chambers of sodium and potassium, respectively. The system is pumped by three ion pumps and one titanium sublimation pump. Five metallic valves were installed in order to isolate the system from the environment and each of the three chambers, independently.
Source: By the author.

The 2D-MOT chambers were done with stainless steel 316L³. On their bottom, it is placed an oven that contains an ampoule of sodium (Aldrich Chemical Company Inc. [7440-23-5] Na F.W. 22.99 26,271-4 5g) or potassium atoms (Aldrich Chemical Company Inc. K [7440-09-7] F.W. 39.10 24,485-6 5g). The ovens have the shape of a “cup” with height $h = 50$ mm and internal diameter $d = 35$ mm. A 100 mm long tube with diameter $d_{\text{tube}} = 17$ mm connects the ovens with the 2D-MOT chambers. Around the ovens we use a ceramic resistor (Heatcon OP24764) which can heat them up to 300°C . The usual operating oven temperatures are 250°C for sodium and 30°C for potassium.

In a high vacuum ambient, potassium atoms becomes vapor at room temperature and one can work with a “vapor cell” in order to perform the 2D-MOT (128). For doing so, the whole K 2D-MOT chamber is kept at 42°C in order to avoid that the potassium atoms stick at its metallic internal walls. We use a silicon resistor placed around the chamber in

³ The stainless steel 316L is a common material used in cold atom experiments since it is non-magnetic and presents a very low degassing.

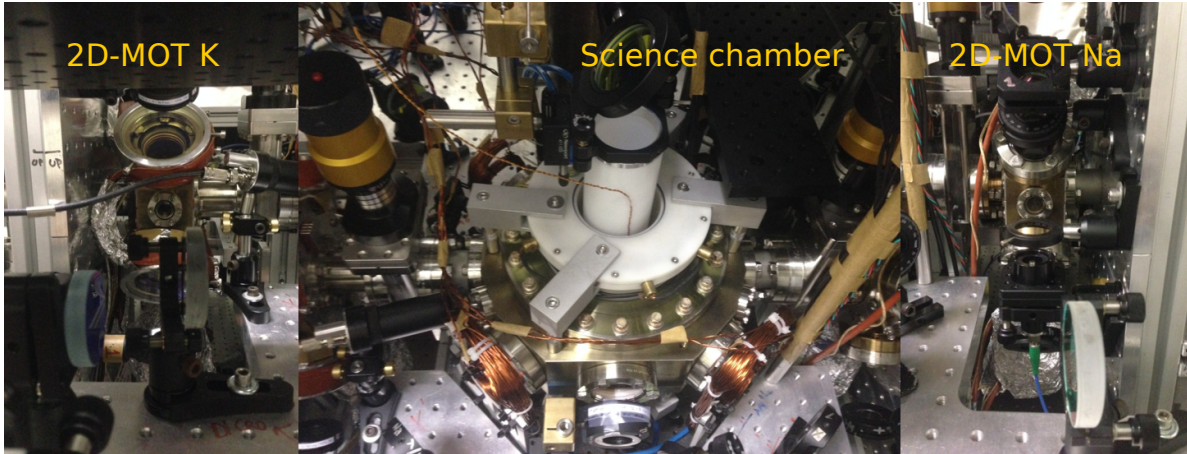


Figure 16 – NaK experiment vacuum system composition with pictures from the 2D-MOT chamber of potassium atoms (left), the science chamber (center) and the 2D-MOT chamber of sodium atoms (right).

Source: By the author.

order to heat it. In addition, external viewports are placed on each viewport used for the 2D-MOT for keeping the glass uniformly heated. In the case of the sodium atoms, it is not possible to work with a vapor cell and the chamber is kept at room temperature while the tube that connects the oven with the 2D-MOT chamber, as well as the top viewport, are heated at 150°C and 85°C , respectively. The top viewport will be used to perform an adapted Zeeman-slower while operating the sodium 2D-MOT, as it is explained in section 4.2 of this chapter.

The Science chamber was drawn to enable the loading of the 3D-MOT of each species independently and maximize the optical access. In this way, the two 2D-MOT chambers are connected on opposite sides and six viewports CF35 were placed at the xy -plane of the chamber. Eight CF16 viewports were also placed on the same plane but with an angle along the vertical direction that orients them to the center of the chamber. Finally, two custom designed re-entering viewports with 89mm of clear aperture were placed along the vertical direction. A composition of the real vacuum system with the optics and the coils surrounding it is illustrated in Fig. 16.

All the light needed to cool, manipulate and image the atoms is produced in a separated table (named, *laser table*) and it is brought to the vacuum system (on the *experiment table*) by the use of single-mode polarization maintaining optical fibers. The

details of the laser setup for sodium and potassium atoms are presented in (77) and in Chapter 5, respectively.

4.2 Sodium 2D and 3D-MOTs

The experimental production of ^{23}Na Bose-Einstein condensates has been widely explored since its first realization in 1995 (16) and, although a few groups have adapted some steps of the experimental sequence until the BEC (130–132), the original experimental sequence is still very efficient being able to produce BECs with around 10^6 atoms every 20s. In the case of the NaK experiment, a small modification was implemented to the original experimental sequence changing the source of pre-cooled atoms from the Zeeman slower used before (16, 125) to a 2D-MOT. (130, 133)

In this section, we describe the setup of the 2D-MOT for sodium atoms and present its optimized parameters obtained by increasing the total number of atoms loaded in the 3D-MOT performed at the science chamber.

4.2.1 A 2D-MOT for sodium atoms

The initial 2D-MOTs developed for rubidium and potassium atoms (127, 128) were simply loaded from a vapor cell, since both atomic species became vapor at almost room temperature while placed in a high-vacuum environment. However, in order to have sufficient vapor pressure for loading the 2D-MOT of sodium atoms, one needs to heat it at temperatures higher than 200°C making it difficult to work with a vapor cell. As it was previously developed for lithium (129), the 2D-MOT can still be efficiently used for sodium atoms by adding an adapted “Zeeman slower” which pre-cool the atoms to be trapped in the 2D-MOT (130). The combination of 2D-MOT + “Zeeman slower” has proven to be as efficient as the traditional Zeeman slowers in producing high atomic fluxes, as it can be seen from the direct comparison realized in our previous sodium experiment. (133)

The 2D-MOT, as the usual 3D-MOT, uses the combination of radiation pressure force with a spatially linearly dependent magnetic field to cool and confine the atoms. (134) In working with alkaline atoms, two frequencies, named *cooling* and *re-*

pumper, are needed in order to create a closed cooling transition. For sodium atoms, the used transitions are shown in Fig. 17 and both are probed with light around 589 nm. Two circularly polarized retro-reflected laser beams with frequencies of both cooling and repumper transitions perpendicularly cross in the center of the 2D-MOT vacuum chamber. A two-dimensional quadrupole magnetic field⁴ is produced by four sets of nine permanent magnets each (K&J Magnetic Inc. BX082 with dimensions of (3.2, 12.7, 25.4) mm and magnetization $\mathbf{M} = (10.5 \times 10^5, 0, 0)$) mounted as it is displayed in Fig. 18 (a). The resulting magnetic field gradient along the beam's propagation direction is of 60 G/cm. Along the vertical direction, in which travels the atomic flux coming from the oven, the residual magnetic field can be used to perform an adapted "Zeeman slower". In this way, another laser beam with light far red detuned from the atomic transitions ($\delta \sim -200\text{MHz}$) is aligned counter-propagating with the atomic flux. Its polarization is set to be along the y -axis which, in combination with the magnetic field, will result in a circularly polarized light for the atoms (see Ref. (130)). Finally, a *push* beam guide the pre-cooled atoms in the 2D-MOT to the science chamber. In Fig. 18 (b), we show the complete setup for performing the ^{23}Na 2D-MOT.

The optimization of the 2D-MOT parameters is done by increasing the total atom number loaded in the 3D-MOT performed in the science chamber. Once the beam and magnets were proper aligned, we could scan the power and frequency of each beam while keeping the oven temperature fixed at 240°C. A complete characterization of our 2D-MOT parameters can be found in. (77, 133) Here, we just present the final optimized values for the 2D-MOT parameters in Fig. 19. The given detunings were calculated with respect to the corresponding atomic transition defined in Fig. 17. With these parameters a flux of 1×10^{10} atoms/s arriving in the SC was measured from the initial loading of the 3D-MOT⁵. When completely optimized, the 2D-MOT of sodium atoms can be seen by eye presenting a cigar shape, as it can be seen in the picture of Figure 20.

⁴ This field presents a linear magnetic field gradient in the plane of the laser beams and has a vanishing magnetic field in the perpendicular direction for $x = 0$ and $y = 0$.

⁵ A more detailed description on how to obtain the atomic flux from the loading of the 3D-MOT is given in Chapter 5 in the context of potassium atoms.

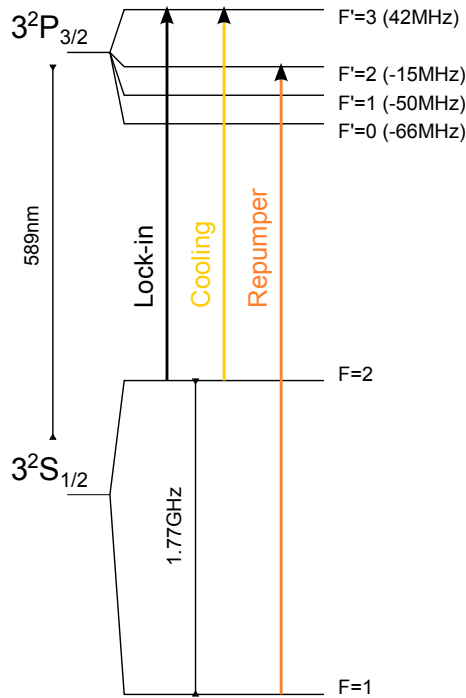


Figure 17 – Hyperfine energy states of the D_2 line of sodium atoms. The *cooling* and *repumper* transitions used in magneto-optical traps are indicated by the vertical lines in yellow and orange, respectively. The black vertical line (*lock-in*) represents the frequency in which the output laser light is stabilized.
Source: By the author.

4.2.2 Sodium 3D-MOT: the dark-SPOT MOT

The sodium 3D-MOT optical setup around the science chamber, together with all the other light beams used in the experiment (imaging, potassium 3D-MOT, Plug and ODT lights) is illustrated in the scheme of Figure 21. Custom designed dichroic mirrors from Laseroptik combine the sodium and potassium lights with themselves and with the Plug or the ODT lights as it is indicated. It is important to point out that we are going to continuously cite Fig. 21 while describing the experimental sequence and that the propagation directions used in the expressions for the Plug (in section 4.4) and ODT laser beams (in Chapter 6) are defined from the axis of this figure.

The 3D-MOT of sodium atoms in the SC is done with a linear gradient of magnetic field (~ 11 G/cm) produced by a pair of coils in anti-Helmholtz configuration⁶, three circularly polarized retro-reflected laser beams with frequency near the cooling transition

⁶ This coils are also the responsible for generating the magnetic field of the Quadrupole trap described in section 4.4 of this chapter.

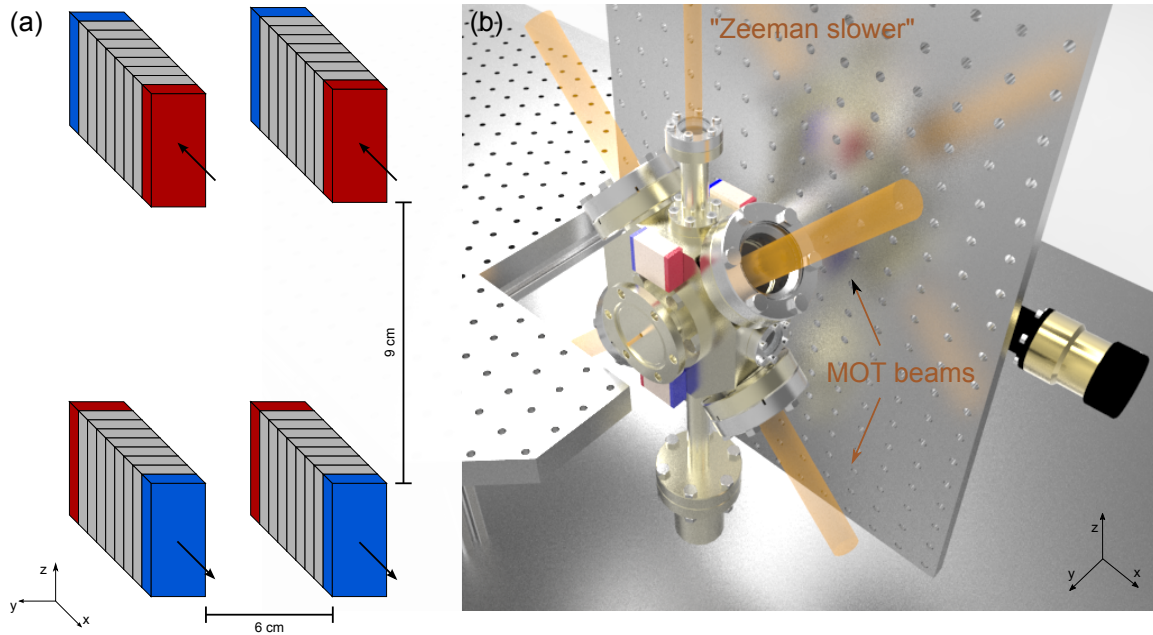


Figure 18 – ^{23}Na 2D-MOT setup. In (a), it is displayed the arrangement of the permanent magnets around the 2D-MOT chamber. The black arrows indicate the magnet's field orientation. The complete setup for performing the ^{23}Na 2D-MOT is shown in (b) in which we present a zoom into the Na 2D-MOT chamber (see Fig. 15). The four sets of magnets, the 2D-MOT beams and the adapted "Zeeman slower" beam are indicated.

Source: By the author.

	Detuning (MHz)	Power (mW)
2D-MOT cooling	-13	150
2D-MOT repumper	-54	50
Zeeman cooling	-275	100
Zeeman repumper	-334	30
Push	+12	0.4

Figure 19 – Table containing the sodium 2D-MOT optimized parameters for $T_{\text{oven}} = 240^\circ\text{C}$ and $B'_{2\text{D}} = 60\text{G/cm}$. The given detunings were calculated with respect to the corresponding atomic transition defined in Fig. 17

Source: By the author.

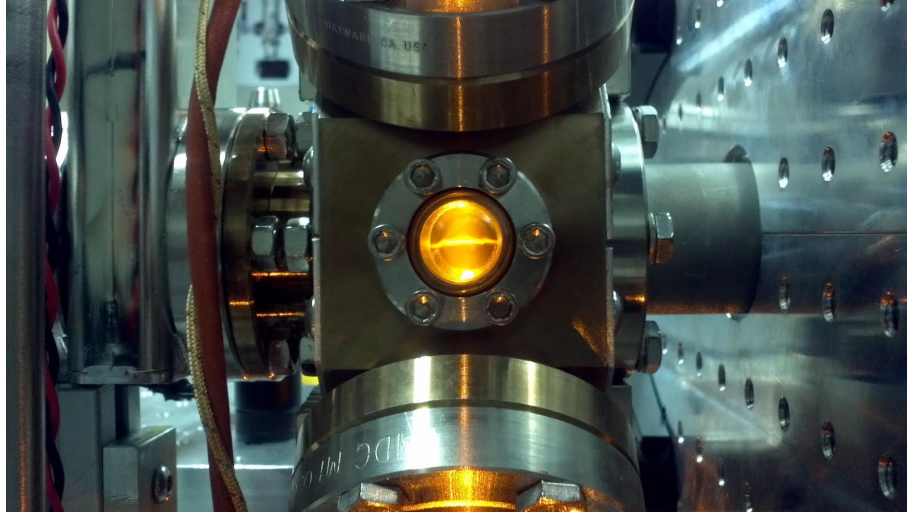


Figure 20 – Picture of the cigar-shaped 2D-MOT cloud of sodium atoms.
Source: By the author.

($\delta_{\text{cool}} = -16.5$ MHz) and one single-pass laser beam near the repumper transition ($\delta_{\text{rep}} = -8$ MHz). The repumper beam has a “hole” (dark-SPOT) at the center of its intensity profile that is imaged in the atoms by a 1:1 telescope, such that just cooling light arrives to the center of the 3D-MOT. In this way, the atoms in this central region are not pumped back to the $F = 2$ ground state (see Fig. 17) and stop interacting with the cooling light, decreasing the re-scattered radiation and increasing the density of the atomic cloud. This 3D-MOT configuration is usually referred to as “Dark-SPOT MOT”. (135)

The dark-SPOT is produced by a “mirror-mask” and its size in the repumper beam can be optimized in order to achieve a maximum phase-space density ($\propto N/T^{3/2}$) of the atoms trapped in the magnetic quadrupole trap⁷. In Figure 22 (a) we present the values for the number of atoms in the Quadrupole trap after adding a RF-*knife* of 30 MHz⁸ as a function of the dark-SPOT size, which presents a maximum around 5.0 and 5.5 mm. Therefore, we decided to work with the dark-SPOT of 5.4 mm. In order to show the better efficiency of the dark-SPOT MOT for sodium atoms, we compared the percentage change in the loading rate of the 3D-MOT (proportional to the 2D-MOT

⁷ The processes involved in the transference of the atoms from the Dark-SPOT MOT to the magnetic quadrupole trap and its trapping principles are going to be described in sections 4.3 and 4.4, respectively. For now, we just assume they do not change in order to be able to optimize the parameters of the Dark-SPOT MOT.

⁸ The radio-frequency is used to cool the atoms once they are in a magnetic trap, as it will be explained in the last section of this chapter.

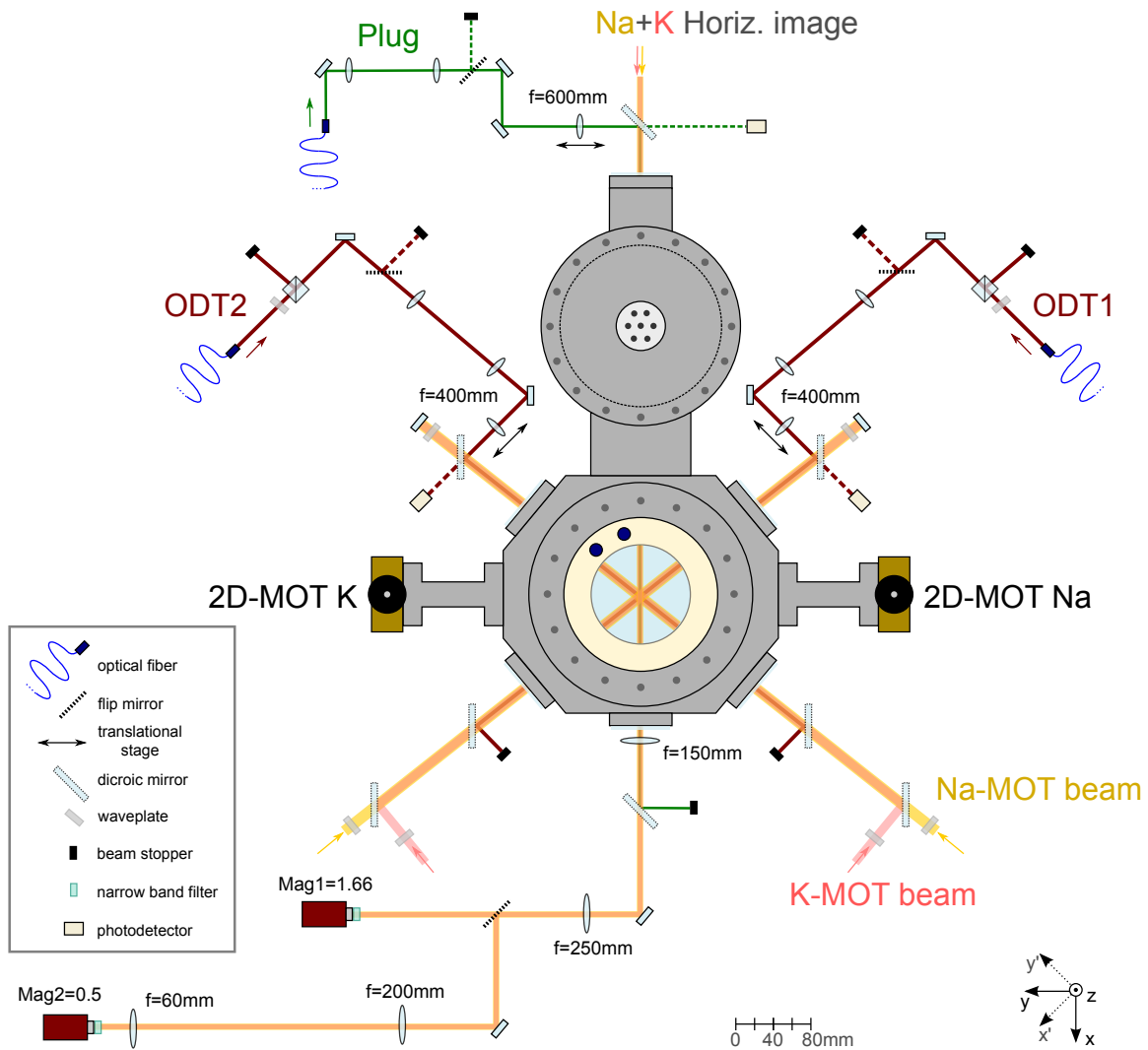


Figure 21 – Top view of the complete optical scheme around the science chamber of the NaK experiment. The sodium and potassium lights (yellow and light red lines, respectively) are combined together and with the Plug (green line) or ODT (dark red lines) lights with the use of dichroic mirrors. The focal length of the lenses that focus the Plug and the ODTs light are indicated as well as the focal length of the two horizontal imaging systems with magnifications $\text{Mag1} = 1.6$ and $\text{Mag2} = 0.5$. Source: By the author.

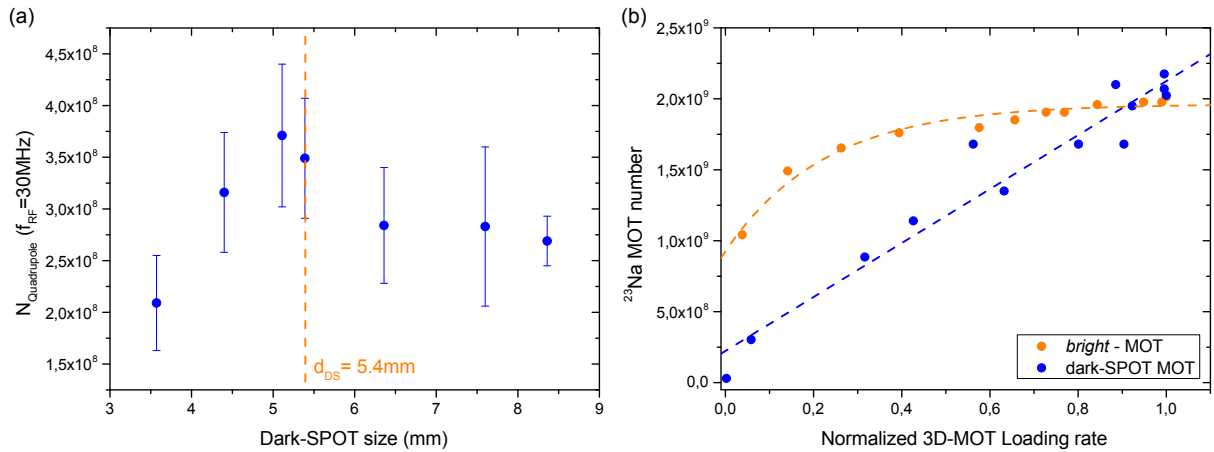


Figure 22 – (a) Number of the atoms trapped in the magnetic quadrupole trap after adding a RF-*knife* of 30MHz for different sizes of the dark-SPOT in the repumper laser beam of the Dark-SPOT MOT. (b) Number of atoms in the quadrupole trap as a function of the normalized loading rate of the 3D-MOT atomic flux. While in the case of the *bright*-MOT the trapped atom number saturates above a certain critical loading rate (or 2D-MOT atomic flux), for the Dark-SPOT MOT it continues to linearly grow.

Source: By the author.

atomic flux) measured from the fluorescence signal while loading the 3D-MOT in the two different configurations (*dark* and the usual 3D-MOT or *bright*) and the total number of atoms in each case for different parameters of the 2D-MOT. These comparisons are shown in the graph of Fig. 22 (b) for number of atoms in the 3D-MOT *vs.* the its normalized loading rate. It is easy to see that, while in the *bright*-MOT configuration (orange circles), the number of trapped atoms saturates above a certain critical atomic flux, in the dark-SPOT MOT configuration (blue circles), it continuous to grow linearly. In fact, after this measurement we could still improve the number of atoms in the dark-SPOT MOT by a factor of 3.

The MOT fluorescence while operating it in the dark-SPOT MOT configuration is dramatically reduced when compared with the usual 3D-MOT, as it can be seen in the fluorescence signals captured by a photodiode for both configurations presented in Fig. 23 (a) or in the pictures in Fig. 23 (b) and (c) taken under the same conditions. Therefore, the number of atoms cannot be obtained from the fluorescence signal of a dark-SPOT MOT and it is common to perform an imaging of the atomic cloud in order to obtain the correct number of atoms as well as its temperature. This is also the case for

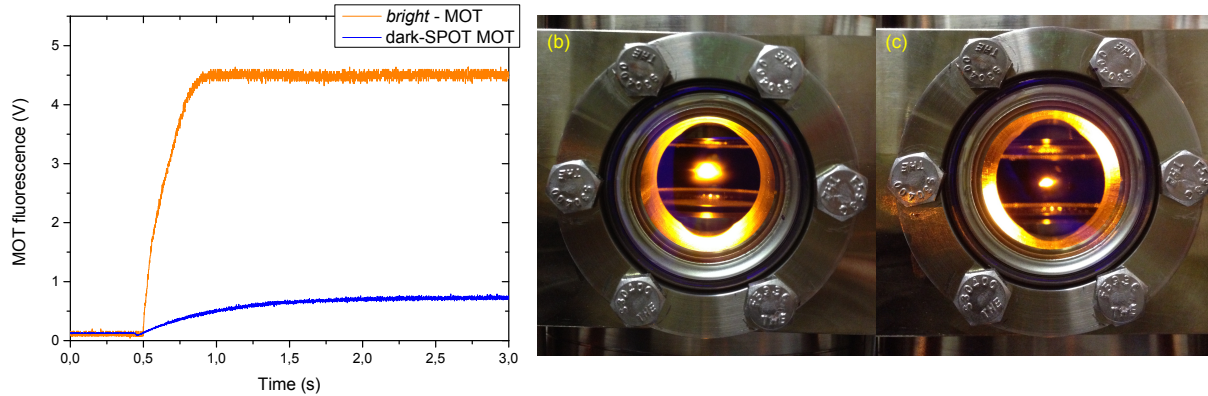


Figure 23 – (a) MOT fluorescence signals captured by a photodiode for the usual 3D-MOT (red curve) and for the Dark-SPOT MOT (orange curve). In (b) and (c), it is shown pictures done under the same conditions of the 3D-MOTs in the *bright* and in the dark-SPOT MOT configurations, respectively. As for the graph in (a), it is also possible to see from the pictures that the fluorescence of the Dark-SPOT MOT is much lower than the one of *bright*-MOT despite the fact their numbers are approximately the same.

Source: By the author.

detecting the atoms in the further stages of the experimental sequence. For these reasons, we describe the absorption imaging technique used in the NaK experiment in the following section before describing the next stages on the experimental sequence. This description is also applicable to the case of potassium atoms.

4.2.3 The absorption imaging technique

The absorption imaging technique (24) has been the most common tool used to detect the atoms in cold atomic experiments. Briefly, this technique consists on shining the atoms with laser light resonant with one of the atomic transitions and observe the “shadow” caused by the atomic cloud due to the absorption and scattering of the incident photons. After the atomic cloud, a set of lenses focus the “shadow” image on a CCD. This shadow will reflect the atomic density profile such that it is possible to obtain, among other properties, the number of atoms.

The laser beam intensity, $I(x, y)$, propagating in an absorbing medium along \hat{z} is described by the Beer-Lambert law:

$$I(x, y) = I_0(x, y) \exp\left(-\sigma \int n(x, y, z) dz\right), \quad (4.1)$$

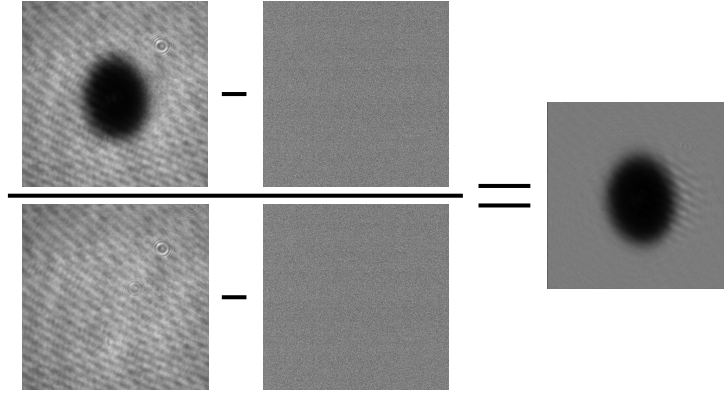


Figure 24 – Example of the calculation of the normalized absorption image used to extract all the properties of the atomic clouds in the NaK experiment. In this case, the image was taken from sodium atoms after cooled in the Plug trap.

Source: By the author.

where $I_0(x, y)$ is the initial laser beam intensity, σ is the absorption cross-section and $n(x, y, z)$ the density of the absorbing medium. The two-dimensional density profile of the medium can be obtained by integrating $n(x, y, z)$ along \hat{z} , such that:

$$\rho(x, y) \equiv \int n(x, y, z) dz = -\frac{1}{\sigma} \ln \frac{I(x, y)}{I_0(x, y)}. \quad (4.2)$$

Therefore, by comparing the laser beam intensity profiles with and without the absorbing medium, one obtains the medium two-dimensional density profile. In cold atomic experiments this comparison is done by capturing three images in a CCD: one of the laser beam in the presence of the atomic cloud ($I(x, y)$), named *probe with atoms*; a second one of just the laser beam ($I_0(x, y)$), named *probe without atoms*; and a last one without any light ($I_D(x, y)$), named *dark* that, subtracted from the previous images can eliminate the light presented in the background. In Fig. 24 we show the previous described calculation done with real experimental images taken from sodium atoms after being further cooled in the Plug trap⁹. The total atom number can be easily obtained from the integration of $\rho(x, y)$:

$$N = \int \rho(x, y) dx dy. \quad (4.3)$$

Absorption images of atomic clouds are normally done after releasing the atoms from the MOT (or from a conservative trap) and letting them freely expand in the presence

⁹ Here we use an image from the atoms in the Plug trap to illustrate the absorption image calculation since the atomic cloud at this stage is smaller than it is in the Dark-SPOT MOT.

of the gravitational force during a fixed time, named *time of flight* (TOF). In this way, one can avoid saturation effects due to the high densities of trapped atomic clouds (or *in situ* clouds). Cold, but still not condensed, atomic clouds are usually called *thermal clouds* and, during t_{TOF} , they assume an isotropic Gaussian density profile with:

$$\rho_{\text{T}}(x, y) = \frac{N_{\text{T}}}{2\pi\sigma_x\sigma_y} \exp\left(-\frac{1}{2}\left[\frac{(x-x_0)^2}{\sigma_x^2} + \frac{(y-y_0)^2}{\sigma_y^2}\right]\right), \quad (4.4)$$

where N_{T} is the number of *thermal* atoms, σ_x and σ_y are the Gaussian widths along \hat{x} and \hat{y} , respectively, and (x_0, y_0) are the coordinates for the center of the atomic cloud.

The temperature of the thermal cloud can be extracted from the Gaussian profile obtained from the absorption image if t_{TOF} is varied. For a long time of flight (in our case, longer than 10 ms), the initial size of the atomic cloud can be neglected and, by applying the energy equipartition theorem, one finds the temperature to be given by:

$$T = \frac{m}{k_B} \left(\frac{\sigma_i}{t_{\text{TOF}}}\right)^2. \quad (4.5)$$

In the NaK experiment, we use an horizontal imaging system with two different magnifications ($M_{\text{MOT}} = 0.5$ and $M_{\text{NaK}} = 1.6$, as indicated in Fig. 21) to image both sodium and potassium atoms. A CCD camera from Allied Vision model Stingray F-145 is used to capture the images that compose the normalized absorption image described in Fig. 24. A program written in LabView controls the CCD, process the images and obtain the number of atoms and the temperature of the atomic clouds by performing a Gaussian adjust to the obtained density profile.

4.3 From the MOT of ^{23}Na to the Plug trap

Magneto-optical traps, as the one described in the previous section, are usually only the first stage on experiments dealing with Bose-Einstein condensates. Even in cases for which the temperatures reached with such traps are of the order of the critical temperature for condensation (as it is the case for Strontium atoms in the *red*-MOT (136)), it is necessary to transfer the atoms to a conservative trap where it is possible to achieve the high phase-space densities required for BEC. In this trap, another cooling procedure, named *evaporative cooling* (137), is normally performed until the production of Bose-

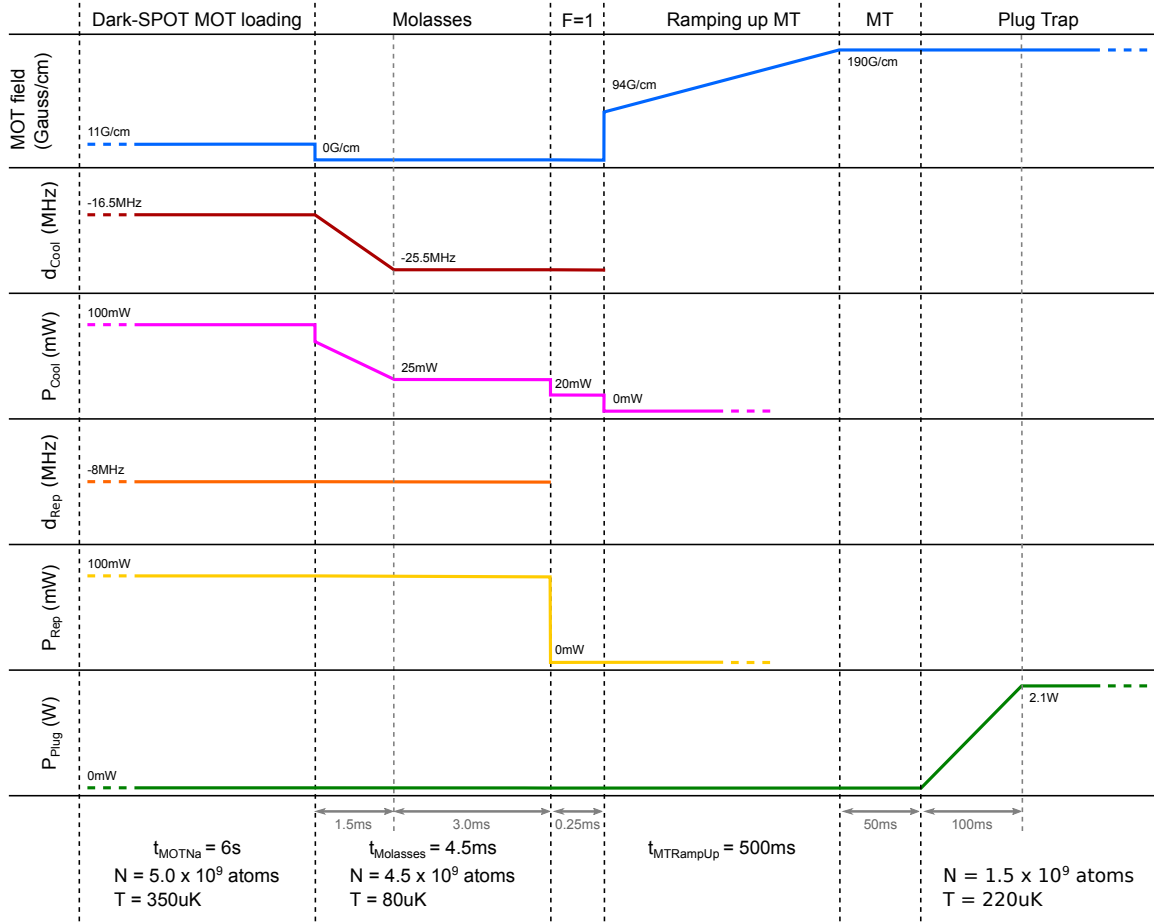


Figure 25 – Experimental sequence for transferring the atoms from the dark-SPOT MOT to the Plug trap.

Source: By the author.

Einstein condensates. The transference of the atoms from the MOT to such conservative traps is the most critical step in BEC experiments and the addition of intermediate stages can improve it.

In the NaK experiment we add a molasses and a pre-pump stages before transferring the sodium atoms to the Plug trap. An scheme of this part of the experimental sequence for the ^{23}Na atoms is presented in Fig. 25 and a brief description of these intermediate stages is presented in the next parts of this section.

The ^{23}Na *dark*-molasses

The molasses technique, done by abruptly switching off the magnetic field of the MOT and letting the atoms expand just in the light field, can cool atomic clouds below

their Doppler limit ($T_D = \hbar\Gamma/2k_B$). This is possible because another cooling mechanism appears when considering Zeeman-degenerate atoms, named *Sisyphus cooling* (134) and the new cooling limit is, in principle, set by the energy when absorbing a photon.

In the case of our sodium atoms, we call this molasses as *dark-molasses* because we keep the dark-SPOT in the repumper beam during this process. The *dark-molasses* is done in two parts: a *ramp* part during which the magnetic field is abruptly turned off and the detuning and power of the cooling light are ramped to their final molasses values, which are kept constant during the *constant* and final part of the ^{23}Na *dark-molasses*. Each part last 1.5 ms and 3.0 ms, respectively. The repumper light (detuning and power) is not changed during this stage. In the end of the *dark-molasses* stage we obtain $4.5 - 5 \times 10^9$ atoms at $80 \mu\text{K}$.

The pre-pump stage

Before trapping the atoms in the Plug trap, one need to transfer them to an specific hyperfine state $|F, m_F\rangle$. In the case of large sodium MOTs, it is sufficient to perform only a pre-pump process which can transfer the atoms to an specific $|F\rangle$ state (16,138), usually the $|F = 1\rangle$ state such that the atoms are uniformly spread between the three m_F states ($m_F = -1, 0, 1$). Only the $m_F = -1$ state is magnetically trappable¹⁰ but, even trapping just 1/3 of the total atom number, the pre-pump for sodium atoms can produce larger BECs than when performing a full optical-pump procedure to the $|2, 2\rangle$ state, due to its low efficiency (around 75% (139)) and the difficulties on evaporatively cool the resulting atomic cloud. (140)

The pre-pump of the ^{23}Na atoms in the NaK experiment is done by turning off the repumper beam used in the Dark-SPOT MOT and letting the atoms expand during $250\mu\text{s}$ in the presence of just the cooling light. As the cooling transition is not closed, after a few cycles the atoms are all in the $|F = 1\rangle$ state without any heating of the atomic cloud.

¹⁰ As it is explained in the next section of this chapter.

4.4 The Plug type trap

The Plug type trap has proven to be a very efficient trap for trapping and cooling sodium atoms (16,139) and for these reasons it is the conservative trap we initially choose for producing the Bose-Einstein condensate of ^{23}Na atoms in the NaK experiment. In this section, we first describe the trapping principles, the losses mechanisms and the configuration of the Plug trap designed to trap both ^{23}Na and ^{41}K atoms, followed by its characterization for the trapped sodium atoms.

4.4.1 The Quadrupole trap potential and Majorana losses

Magnetic traps have been widely used in cold atom experiments due to its large capture volume and high collision rates between the trapped atoms, which is essential for an efficient evaporative cooling procedure (16, 141, 142). One of the most common configurations is the magnetic Quadrupole trap (MT) produced by a pair of coils in anti-Helmholtz configuration. In this configuration, the current passing through the coils have opposite circulation and the generated magnetic field near the center of the trap presents a linear gradient with $\vec{B} = 0$ at the center. The atomic trapping potential is proportional to this field gradient and can be written as:

$$U_{\text{Quad}} = \mu B' \sqrt{\frac{x^2}{4} + \frac{y^2}{4} + z^2}, \quad (4.6)$$

where μ is the atomic magnetic moment and B' , the magnetic field gradient along the coils axis (in this case, chosen to be along \hat{z}).

The magnetic trapping of neutral atoms is given by the interaction between the magnetic field and the atomic magnetic moment, banding the energy structure of the hyperfine atomic states. The graphs presented on Fig. 26 show the energies of the hyperfine states for sodium (a) and potassium (b) atoms as a function of the applied magnetic field calculated with the Breit-Rabi formula. (143) From the Maxwell's equations, one can prove that in free space it is not possible to create a local maximum in the magnetic field. Thus, magnetic traps presents regions of minimum magnetic field and, only the states that minimize their energy while decreasing the amplitude of the magnetic field are trappable.

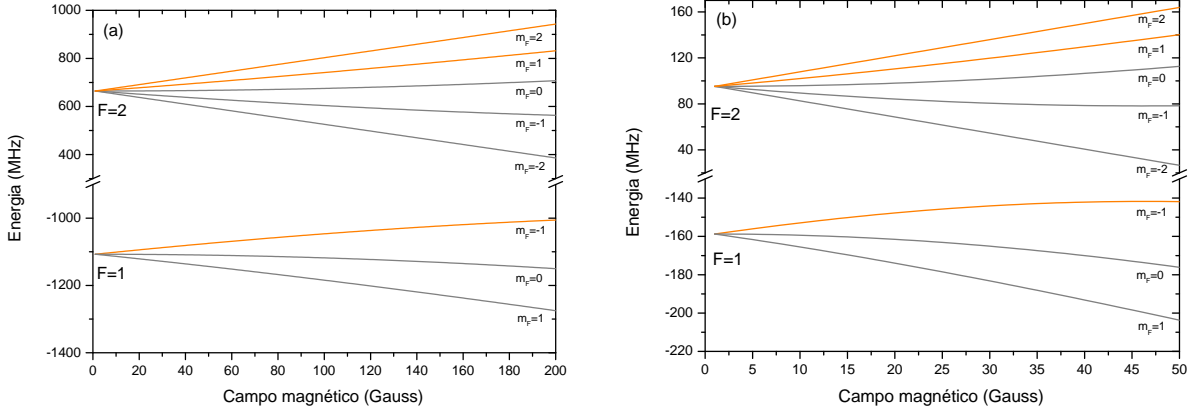


Figure 26 – Energy of the $3^2S_{1/2}$ hyperfine states of sodium atoms (a) and of the $5^2S_{1/2}$ hyperfine states of potassium atoms (b) as a function of the applied magnetic field in the low field limit. The *low field seekers* states are indicated in orange.
Source: By the author.

These states are known as *low field seekers* (LFS). For the case of sodium and potassium atoms, we can identify the states $|F = 1, m_F = -1\rangle$, $|F = 2, m_F = 1\rangle$ e $|F = 2, m_F = 2\rangle$ (in orange in the graphs of Fig. 26) as the LFS states in the limit of low magnetic field.

In experiments interested in study atoms at low temperatures (of the order of a few microkelvin or lower), there is a complication on working with magnetic quadrupole traps: at the center of the trap, near the region in which the magnetic field is zero (see Eq. 4.6), non-adiabatic transitions to hyperfine states no longer trappable are possible, leading to losses. These transitions are called *Majorana spin flips*. (144) Briefly, the atomic magnetic moment orients itself with the applied magnetic field (B_{ext}), adiabatically following the field orientation as it moves in the trap. If the change in the magnetic field is fast enough, the magnetic moment cannot follow it and non-adiabatic transitions between states with different magnetic moment (which means, different m_F) starts to occur. A simple condition to avoid the occurrence of the Majorana spin flips can be written comparing the precession frequency of the atomic magnetic moment (the Larmor frequency, $\omega_L = \mu_B g_F m_F |\vec{B}_{\text{ext}}| / \hbar$) with the variation of the magnetic field (141), such as

$$\omega_L \gg \left| \frac{dB_{\text{ext}}/dt}{B_{\text{ext}}} \right|, \quad (4.7)$$

where μ_B is the Bohr magneton, g_F is the hyperfine Landé g-factor and B_{ext} is the external magnetic field due to the trap.

For the case of low magnetic field, ω_L tends to zero and the condition of Eq. 4.7 is no longer satisfied creating a region around $\vec{B}_{\text{ext}} = 0$, named *Majorana hole*, in which the atoms can scape from the trap. By assuming this region to be given by a sphere around the center of the quadrupole trap, one can estimate its radius as given by:

$$\rho_{\text{hole}} = \sqrt{\frac{2v\hbar}{\mu_B g_F m_F B'}} , \quad (4.8)$$

where v is root-mean-square atomic velocity. In the case of a quadrupole trap with $B' = 200$ G/cm, the radius of the Majorana hole for sodium atoms at the Doppler temperature, $T_D^{\text{Na}} = 235$ μK , is $\rho_{\text{hole}}^{\text{Na}} = 3.06$ μm . While for potassium atoms at the same conditions with $T = T_D^{41\text{K}} = 145$ μK , $\rho_{\text{hole}}^{41\text{K}} = 2.35$ μm . The loss rate due to the Majorana losses, Γ_{Majorana} , can be estimated from the flux of atoms that pass through the Majorana hole and is given by:

$$\Gamma_{\text{Majorana}} = \frac{\hbar}{m} \frac{24^{1/3}}{32} \left[\frac{g_F m_F \mu_B B'}{k_B T} \right]^2 , \quad (4.9)$$

where m is the mass of the atom we are considering. It is easy to realize from Eq. 4.9 that the losses are increased as the atomic cloud gets colder, reducing the lifetime of the atoms in trap ($\tau_{\text{Majorana}} = 1/\Gamma_{\text{Majorana}}$). In Fig. 27 we show the lifetime due to the Majorana losses as a function of the temperature of the atomic cloud for both ^{23}Na and ^{41}K trapped in the $|F = 1, m_F = -1\rangle$ hyperfine state. Usual magnetic traps have lifetimes of the order of dozens of seconds and we can consider $\tau_{\text{trap}} = 50$ s (dashed black line in the figure), enough to perform an efficient evaporation of the atoms and observe the BEC. Such lifetime is achieved for $T_{\text{Na}} = 19$ μK and $T_{\text{K}} = 14$ μK ¹¹ and it decreases while decreasing the temperature. For temperatures around 5 μK (still above the usual critical temperatures for condensation), the lifetime in the quadrupole trap for sodium and potassium atoms is just 3.5 s and 6.3 s, respectively and the Majorana losses makes it impossible to achieve the Bose-Einstein condensation in a pure quadrupole trap.

¹¹ We are going to recover these values in section 4.4.3 while describing the Plug trap configuration of the NaK experiment.

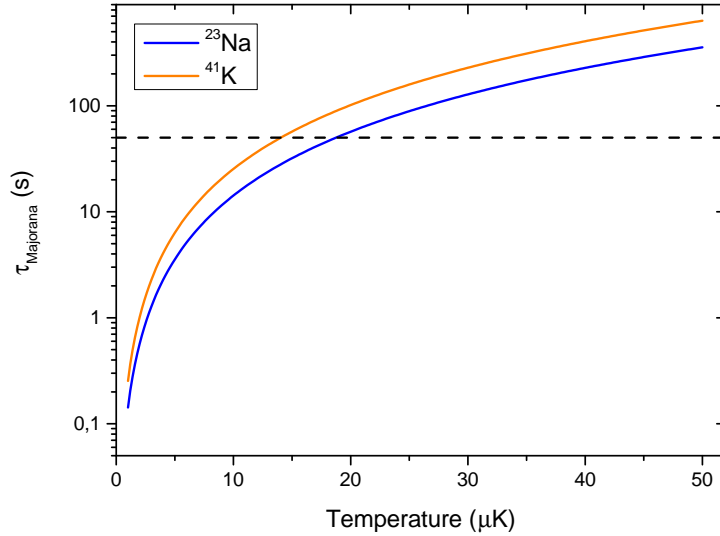


Figure 27 – Lifetime of ^{23}Na (in blue) and ^{41}K (in orange) in the Quadrupole trap due only to Majorana losses. The dashed black line represents the reference lifetime of 50 s enough for performing an efficient evaporation and achieve the BEC. Source: By the author.

4.4.2 The Plug trap potential

In order to avoid the Majorana Spin Flips, some different magnetic trapping configurations have been used in experiments dealing with cold atoms as, for example, the *TOP-type* trap (141), the *Quadrupole-Ioffe configuration* (QUIC) trap (142) or adding an optical dipole trap (*red-detuned*, in a *Hybrid* trap (145) or *blue-detuned* in a *Plug-type* trap (16)) to the quadrupole. This last configuration has proven to be a nice approach when working with ^{23}Na atoms (16, 146, 147). In the experiment of M. Zwierlein group at MIT (139, 146) it has also been used as the first trapping stage to produce stable ground-state molecules of ^{23}Na - ^{40}K (49) and for these reasons it was the choice done for the NaK experiment. In the *Plug* trap, a focused blue-detuned laser beam is aligned passing through the center of the Quadrupole trap, creating a barrier which repel the atoms from the region where $\vec{B} = 0$, dramatically reducing the probability of the Majorana losses to happen.

Optical Dipole traps (ODTs) rely their trapping principles on the dipole force originated from the interaction between the induced electric dipole moment of the atoms with the electric field of a focused laser beam with frequency far from the atomic reso-

nance. (148) Under specific conditions, the potential produced by such a laser beam with waist w_0 can be simplified as:

$$U_{\text{ODT}} = \frac{3\pi c^2 \Gamma_0}{2\omega_0^3 \Delta} I(\vec{r}), \quad (4.10)$$

where c is the vacuum light velocity, ω_0 and Γ_0 are, respectively, the angular frequency and the decay rate of the atomic transition, $\Delta = \omega - \omega_0$ is the difference between the laser and the atomic transition frequencies, named detuning of the laser and $I(\vec{r})$ is the laser intensity.

In the case of a Gaussian focused laser beam propagating along \hat{x} ¹², the intensity profile is given by the following equation:

$$I(\vec{r}) = I(r, x) = \frac{2P}{w_0^2} \frac{1}{1 + (x/x_R)^2} e^{\frac{-2r^2}{w_0^2} \frac{1}{1 + (x/x_R)^2}}, \quad (4.11)$$

where P is the laser power, $x_R = \pi w_0^2/\lambda$ is known as the Rayleigh length and $r = \sqrt{y^2 + z^2}$. Replacing Eq. 4.11 into Eq. 4.10, one obtains the optical trapping potential. It is easy to see that the potential is going to be attractive if $\Delta < 0$, which means, for laser beams which are *red*-detuned with respect to the atomic transition, or repulsive for $\Delta > 0$ and *blue*-detuned laser beams.

The Plug trap potential obtained by the combination of the Quadrupole trap potential (Eq. 4.6) with the ODT potential for a *blue*-detuned laser propagating along \hat{x} and aligned with the center of the quadrupole (Eqs. 4.10 with 4.11) is given by:

$$U_{\text{Plug}} = \mu B' \sqrt{\frac{x^2}{4} + \frac{y^2}{4} + z^2} + U_0 \frac{1}{1 + (x/x_R)^2} e^{\frac{-2r^2}{w_0^2} \frac{1}{1 + (x/x_R)^2}}, \quad (4.12)$$

where $U_0 = 3c^2 \Gamma P / \omega_0^3 \Delta w_0^2$ is the depth of the optical potential. Since the transition frequency of each species (Na and K) is different, the optical depth which will represent the height of the optical barrier in the center of the trap is going to be smaller for potassium than it is for sodium. With this in mind one can design a trapping configuration that will be able to expel both species from the Majorana hole. The details of the final configuration for the Plug trap of the NaK experiment is going to be discussed in the next section.

¹² The choice of propagating the beam along \hat{x} is done since by assuming the axis defined in Fig. 21, this is the direction in which the plug laser beam propagates in the experiment.

4.4.3 A Plug type trap for ^{23}Na - ^{41}K

The Plug trap potential designed for trapping both ^{23}Na and ^{41}K atoms at the $|F = 1, m_F = -1\rangle$ hyperfine states is presented on Figure 28. The optical barrier in the center of the quadrupole trap can be clearly seen on Fig. 28 (b) in which the potential along $(0, y, 0)$ is plotted. As previously discussed, the barrier height for potassium atoms is almost a factor of 2.3 lower than the one for sodium. The curves on the other graph, (a) in Fig. 28, represents the Plug trap potential along $(x, y_{\min}, 0)$ (solid lines) and $(0, y_{\min}, z)$ (dashed lines). While adding the plug beam to the quadrupole trap, the atoms accumulate around the region in which the resulting potential is minimum (in this case, chosen to be y_{\min}) and, for small displacements around y_{\min} the potential is approximately harmonic with frequencies given by:

$$\omega_x = \sqrt{\frac{g_F m_F \mu_B B'}{2m y_{\min}}}, \quad \omega_y = \sqrt{\frac{4y_{\min}^2}{w_0^2} - 1} \omega_x, \quad \omega_z = \sqrt{3} \omega_x. \quad (4.13)$$

Even if the optical barrier is lower for ^{41}K , it has to be able to repel the atoms from the Majorana hole as one achieves the temperature for which the losses start to be relevant. For simplicity we can assume that the Majorana losses start to be relevant when $\tau_{\text{Majorana}} = \tau_{\text{trap}} = 50$ s, represented by the dashed black line in Fig. 27 in section 4.4.1. As previous discussed, such lifetime is achieved for $T_{\text{Na}} = 19 \mu\text{K}$ and $T_{\text{K}} = 14 \mu\text{K}$.

Two important plug beam parameters are essential in designing the height of the optical barrier: first, the beam waist w_0 that should be bigger than the Majorana hole ($w_0 \gg \rho_{\text{Majorana}}$) such that at ρ_{Majorana} the optical barrier has at least 70% of its total value, ensuring that only the hottest atoms penetrate the barrier; and second, the laser power P . Comparing the parameters from previous works with a Plug trap (16, 149) we choose a waist around $40 \mu\text{m}$. In order to safely repel atoms with T_{Na} and T_{K} obtained from Fig. 27, the difference ΔU between the barrier height (U_0) and the minimum trapping potential ($U_{\text{Plug}}(0, y_{\min}, 0)$) has to be ten times larger than these temperatures. Due to limitations on the laser power¹³, we can only work with 4W, leading to $\Delta U_{\text{Na}} = 224 \mu\text{K}$

¹³ We use a Coherent Verdi V10 with a maximum output power of 10W to generate the light of the Plug and we loose some power in the optical setup that is described in Appendix C.

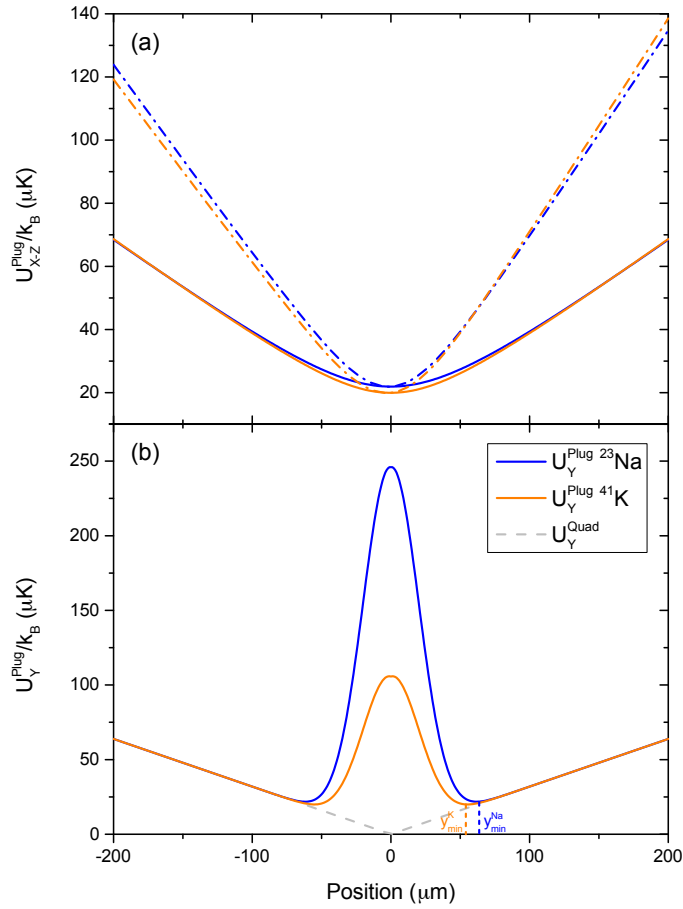


Figure 28 – Plug trap potential for sodium (in blue) and potassium atoms (in orange). The positions where the potential is minimum is different for each species as it can be seen in (b) for the potential along \hat{y} . The quadrupole potential along \hat{y} is represented by the gray dashed line. The potential along the \hat{x} (solid lines) and \hat{z} (dashed lines) are displaced in (a), and were calculated for the proper $y = y_{min}$ of each atomic species.

Source: By the author.

and $\Delta U_K = 86 \mu\text{K}$, in principle not sufficient to suppress the losses of the ${}^{41}\text{K}$. However, the initial work with sodium atoms in our experiment (see the next section of this chapter) has shown that we could obtain a large BEC (with almost 10^6 atoms) using half of the power for the plug beam and we could expect that $P = 4 \text{ W}$ would also work for potassium. The Plug trap relevant parameters for sodium and potassium atoms with $B' = 200 \text{ G/cm}$, $w_0 = 40 \mu\text{m}$ and $P = 4 \text{ W}$ are summarized in Fig. 29.

Once the main parameters of the Plug trap were defined, one can draw and realize each of its parts: the coils for the quadrupole field and the laser beam for the plug. Due to restrictions of the vacuum system, the quadrupole coils are separated by 62 mm making

	^{23}Na	^{41}K
y_{\min}	$64\mu\text{m}$	$55\mu\text{m}$
f_x	213Hz	172Hz
f_y	651Hz	441Hz
f_z	369Hz	300Hz
U_0	$245\mu\text{K}$	$105\mu\text{K}$
$U_{\text{Plug}}(0, y_{\min}, 0)$	$22\mu\text{K}$	$20\mu\text{K}$
$\Delta(U_0)$	$224\mu\text{K}$	$86\mu\text{K}$

Figure 29 – Table with the relevant parameters of the Plug trap for sodium and potassium atoms calculated with $B' = 200\text{ G/cm}$, $w_0 = 40\ \mu\text{m}$ and $P = 4\text{ W}$.

Source: By the author.

necessary the use of high currents ($I > 40\text{ A}$) in order to obtain the needed magnetic field gradient. For this reason, a specially designed cooling system was implemented in the experiment and its characterization as well as the coils and optical setup for the Plug beam are presented in the Appendix C. In the last part of this section, we characterize the Plug trap for sodium atoms before starting with the *evaporative cooling* procedure.

4.4.4 ^{23}Na atoms in the Plug trap

After the pre-pump stage described in section 4.3, the ^{23}Na atoms are transferred to the Plug trap following the last part of the experimental sequence presented in Fig. 25. The magnetic field is abruptly switched on at a magnetic field gradient $B'_{\text{Catching}} = 94\text{ G/cm}$. This value is optimized as the lowest magnetic field that allows all trappable atoms to remain at the magnetic trap. After that, the field is adiabatically ramped up to its Plug trap value $B'_{\text{Plug}} = 190\text{ G/cm}$ during 500 ms. Once the atoms are trapped in the pure Quadrupole trap, the Plug beam can be turned on by ramping the laser intensity from zero to $P_{\text{Plug}} = 2.10\text{ W}$ in 100 ms. The plug beam waist measures $w_0 \approx 43\ \mu\text{m}$ ¹⁴. Finally, we obtain 1.5×10^9 atoms at $200 - 220\ \mu\text{K}$ trapped in the Plug trap.

The first important measurement done in the Plug trap is the *lifetime* of the

¹⁴ The measurement of the plug beam waist can also be found in Appendix C

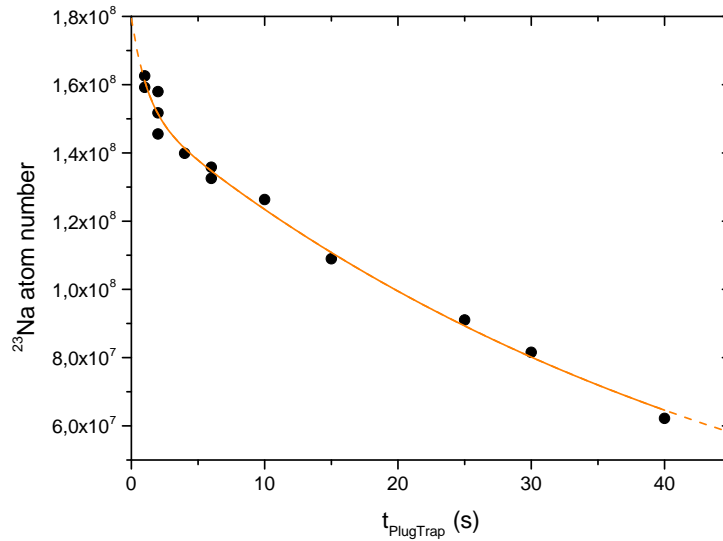


Figure 30 – Number of trapped atoms as a function of the time in the Plug trap. The *lifetime* of the Plug trap is defined as the time for which the atom number falls to $1/e$ of its initial value. In our experiment, $\tau_{\text{Plug}} \cong 46$ s.
Source: By the author.

trapped ^{23}Na atoms, which is related with the collisions of this atoms with the residual background. Besides evaluating the vacuum quality in the SC, long lifetimes are desirable in order to perform an efficient evaporative cooling of the atoms, as it will be discussed in section 4.5.1. In Figure 30, the number of atoms as a function of the time in the Plug trap, t_{Plug} , is shown. The lifetime of the Plug trap is defined as the time for which the atom number falls to $1/e$ of its initial value and, in the case of our experiment, is given by $\tau_{\text{Plug}} \cong 46$ s, enough to perform the evaporative cooling procedure.

The alignment of the Plug beam in the beginning of the Plug trap is not critical since the atomic cloud has temperatures much higher than the temperatures for which the Majorana losses starts to dominate. As we cool the atoms, the Plug beam alignment has shown to be the most critical parameter in our experiment changing the shape and the number of atoms in the condensate. For the results and discussions presented in this thesis, we consider the Plug to be at its best alignment position¹⁵.

¹⁵ The best alignment of the Plug beam is usually done by first, increasing the number of atoms trapped at around $20 \mu\text{K}$ (when the Majorana losses starts to dominate) and latter, by adjusting the shape of the ^{23}Na BEC. Sometimes, a marginal BEC appears and it only disappears with a big loss of the atoms in the principal BEC and we choose to work with it. A detail analysis of the Plug beam alignment and its effects can be find in Ref. (149)

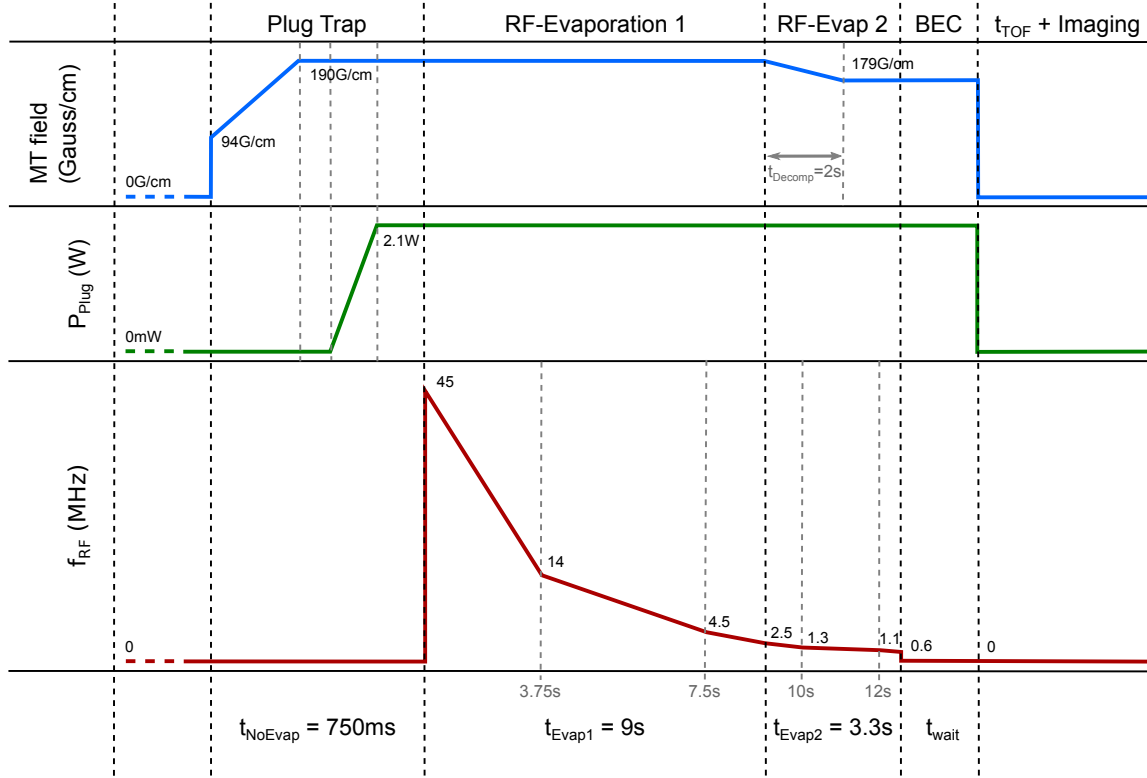


Figure 31 – Experimental sequence of the sodium atoms trapped in the Plug trap until it reaches the BEC.

Source: By the author.

4.5 The BEC of ^{23}Na atoms in a Plug trap

Once large numbers of ^{23}Na atoms are trapped in the Plug trap with a long lifetime (longer than 20s), one can perform the *evaporative cooling* procedure in order to observe the Bose-Einstein condensate. (137) In the NaK experiment, since the atoms are trapped by a magnetic potential, RF-forced evaporation is applied. A briefly introduction to the working principles of such technique and its characterization for our ^{23}Na atomic cloud is presented in section 4.5.1. The experimental sequence for sodium atoms from their transference to the Plug trap until they reach the BEC is illustrated in Figure 31 and the ^{23}Na BEC achieved in the Plug trap is characterized in section 4.5.2.

4.5.1 Evaporative cooling of atoms in a magnetic trap

The evaporative cooling working principle consists in selectively remove the most energetic atoms leading to the thermalization of the atomic cloud at a lower temperature

such that the rate for which T is decreased is larger than the atom loss. (137) With this condition, it is possible to increase the *phase-space density* of the trapped cloud and eventually, achieve the BEC.

The evaporative cooling efficiency will strongly depend on the ratio between the elastic and inelastic collision rates. The first one, responsible for the thermalization of the atomic cloud is basically given by three factors:

$$\Gamma_{\text{el}} = n\sigma_{\text{el}}\langle v \rangle, \quad (4.14)$$

where n is the atomic density, σ_{el} is the elastic cross-section that, for the case of cold sodium atoms can be given by the s -wave scattering length, a_{Na} , and $\langle v \rangle$ is the mean atomic velocity. In the case of atoms trapped by a generic 3D potential $U(r) \propto r^p$, $n \propto T^{-3/p}$ and, since $\langle v \rangle \propto \sqrt{T}$, Eq. 4.14 is proportional to:

$$\Gamma_{\text{el}} \propto \frac{N(T)}{T^{3/p-1/2}}. \quad (4.15)$$

The larger elastic collision rate is obtained by setting $p = 1$ which represents a linear trapping potential. This is the case of the Plug trap potential in the limit of high temperatures (beginning of our evaporation). While decreasing the temperature of the atomic cloud, the trapping potential becomes approximately harmonic with $p = 2$ and $\Gamma_{\text{el}} \propto \frac{N(T)}{T}$. In order for the evaporative cooling procedure to be efficient (*run-away evaporation*), the temperature must decrease in a faster rate than the atom losses such that the elastic collision rate does not decrease. This condition can be written as $N(T) \propto T^s$, with $s \leq 1$. The competing term given by the inelastic collision rate accounts for the possible inherent losses of the trap: background collisions, three-body collisions, etc. In systems with long lifetime of the trapped atoms, this last collision rate can be neglected if one perform a fast evaporation $t_{\text{evap}} \ll \tau_{\text{Trap}}$.

For the case of atoms trapped in magnetic traps, the evaporative cooling can be performed by the use of radio-frequency (RF) radiation¹⁶. (150) Due to the inhomogeneity of the magnetic field, the energy splitting of the different m_F states is going to be position

¹⁶ This is the simple way to perform the evaporation in a magnetic trap. However, when dealing with two-components systems in which one species should be sympathetic cooled by the other, the evaporative cooling by means of RF radiation is no longer an option and micro-wave radiation has to be used.

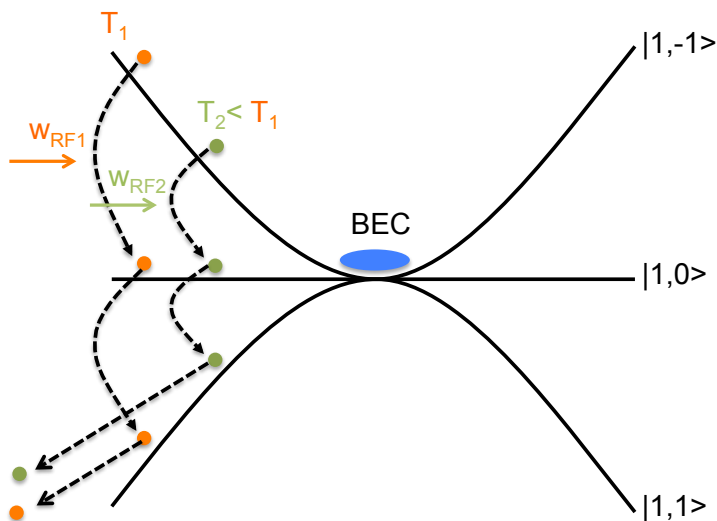


Figure 32 – Working scheme of the RF-forced evaporative cooling procedure for atoms in the $|1, -1\rangle$ state trapped by a harmonic magnetic trap. RF radiation with an initial frequency (ω_{RF1}) is used to transfer the hottest atoms to the $|1, 1\rangle$ state in which they are expelled from the trap. By decreasing the RF frequency, colder atoms are no longer trappable and the remaining atomic cloud can thermalize at a lower temperature increasing its phase-space density until it reaches the BEC.
Source: By the author.

dependent. Since only the hottest atoms reaches regions with high magnetic field, which will result in larger energy splitting, one can selectively remove these atoms by applying radio-frequency radiation at high frequencies. In our experiment, $f_{RF} = 45$ MHz is enough to almost not affect the trapped atomic cloud. By decreasing the RF frequency, colder atoms can be removed. If we slowly remove the atoms from the trap, the atomic cloud can rethermalize at a colder temperature and increase its phase-space density. A scheme of the RF-forced evaporation for atoms in the $|1, -1\rangle$ state trapped in a harmonic magnetic trap is illustrated in Figure 32. A first frequency for the RF radiation (ω_{RF1}) is set and used to excite m_F transitions in order to transfer the hottest atoms to the $|1, 1\rangle$ state in which they are expelled from the trap. Next, the RF frequency is ramped down to a lower value ($\omega_{RF2} < \omega_{RF1}$) such that colder atoms are transferred to $|1, 1\rangle$ and further expelled. This procedure is repeated until the cloud achieves the BEC.

In the NaK experiment, the radio-frequency radiation is generated by a two-loop circular antenna with $d = 38$ mm done with a 0.7 mm cooper wire. A 50Ω resistance is connected in series with the antenna in order to match the impedance of the wave-

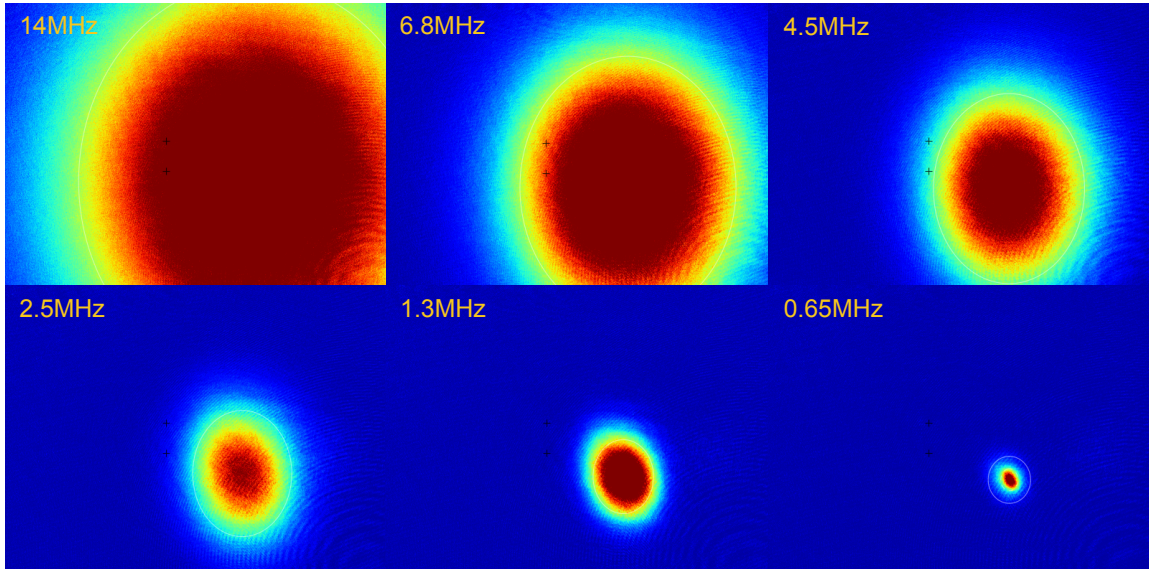


Figure 33 – Pictures of the trapped ^{23}Na atoms at different steps of the evaporation ramp. As the cloud decreases its size, it also increases its density as it is expected for an efficient evaporative cooling procedure. These images were taken after 10ms of time of flight.

Source: By the author.

function generator (a Stanford Research Systems synthesizer able to generate radiation up to 2 GHz). After the synthesizer, the radiation is amplified by a power amplifier such that 26 dBm arrives to the antenna. The antenna is placed below the Quadrupole coils along the \hat{z} direction. This position was chosen since it is the closest we could get from the atomic cloud ($d_{\text{atoms}} \approx 32$ mm, still distant when compared with other experimental setups).

The optimized evaporation ramp for the ^{23}Na atoms in the Plug trap is presented in the experimental sequence of Fig. 31. The total evaporation procedure lasts 12.3 s but it can be splitted in three parts: **(i)** evaporation at *high field* (first 9 s, from 45 MHz to 2.5 MHz), **(ii)** evaporation at *ramping-down field* (from 9 s to 11 s and 2.5 MHz to 1.2 MHz) and **(iii)** evaporation at *low field* (during the last 1.3 s, from 1.2 MHz to variable values between 1.0 – 0.3 MHz, depending on the condensate fraction we want to obtain). In Figure 33, we present images taken after 10 ms of time of flight of the sodium atoms at different steps of the evaporation ramp. It is easy to see that, as the cloud decreases its size (gets colder), it increases its density revealing an efficient evaporation of the atoms in the Plug trap.

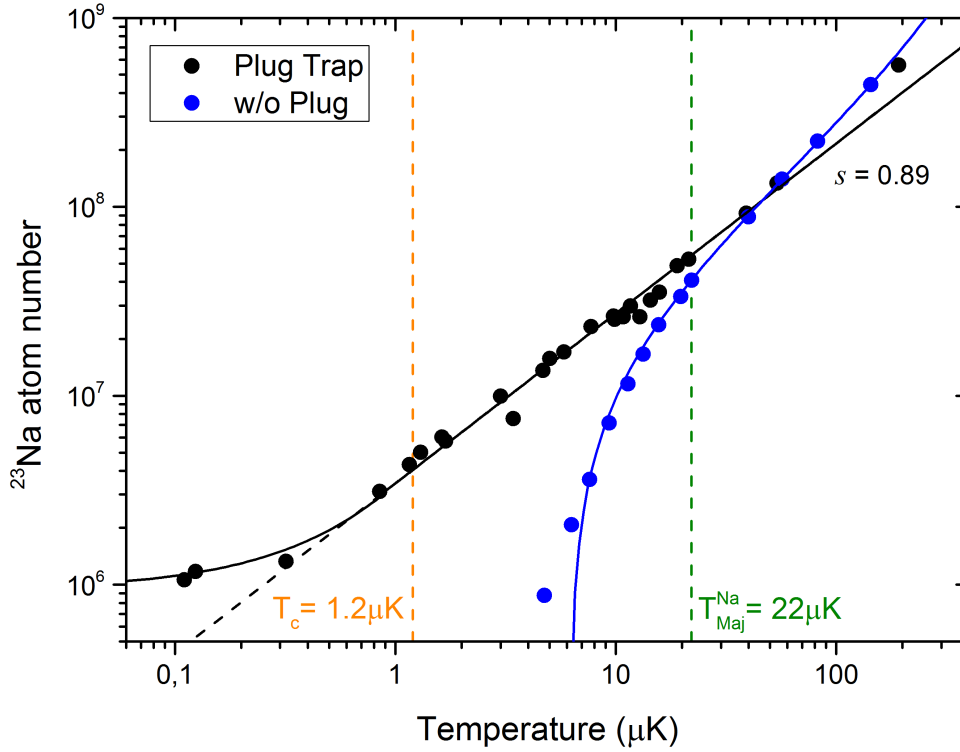


Figure 34 – Log-log graph of N vs. T . The optimized evaporation of the ^{23}Na atoms in the Plug trap (black circles) and just in the Quadrupole trap (blue circles) are displayed as well as the critical temperature for condensation (orange dashed line with $T_c \approx 1.2 \mu\text{K}$) and the Majorana temperature (green dashed line with $T_{\text{Maj}}^{\text{Na}} \approx 22 \mu\text{K}$). The slope of the log-log curve of N vs. T for the optimized case has $s = 0.89 < 1$ as it is expected.

Source: By the author.

A more quantitative characterization of the evaporative cooling procedure can be done with the log-log graph of N vs. T shown in Figure 34. Different curves are presented in the graph: one due to the optimized evaporation ramp described in Fig. 31 (black circles) and one without the addition of the Plug beam to the Quadrupole trap (blue circles). The critical temperature for condensation is indicated by the orange dashed line with $T_c \approx 1.2 \mu\text{K}$. It is clear to see that, without the addition of the plug beam, it is impossible to achieve the BEC region since the number of trapped atoms dramatically decreases after a critical temperature (indicated by the green dashed line with $T_{\text{Maj}}^{\text{Na}} \approx 22 \mu\text{K}$, near the expected value discussed in section 4.4.1) for which the Majorana losses start to take over. The slope of the log-log curve for the optimized evaporation in the Plug trap (black solid line) has $s = 0.89$ and it decreases further when crossing T_c revealing an efficient production of the sodium BEC. The complete sequence (MOT + evaporation in the Plug

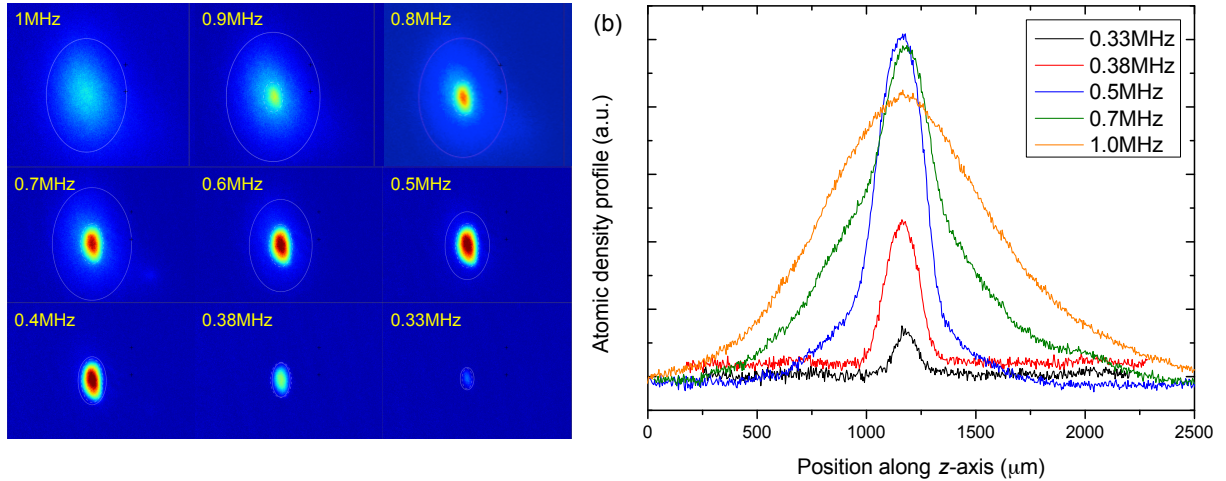


Figure 35 – (a) Images from the ^{23}Na BEC taken after $t_{\text{TOF}} = 22$ ms for different final values of the RF-evaporation. For frequencies below 1 MHz, a condensed cloud appears in the center of the atomic distribution. This can also be seen with the appearance of a bimodal atomic density profiles, as presented in (b). The potential bottom is obtained for $f_{\text{RF}} = 0.33$ MHz.

Source: By the author.

trap) lasts less than 20 s.

4.5.2 The BEC of ^{23}Na atoms

By the end of the evaporative cooling, for RF-frequencies below 1 MHz, the BEC of ^{23}Na atoms is obtained for clouds with around 3.5×10^6 atoms and a critical temperature of $T_c \approx 1.2 \mu\text{K}$. The clear evidence for condensation appears as the bimodal density profile during time of flight, as discussed in Chapter 2. The usual BEC atom numbers are of the order of $8 - 10 \times 10^5$ atoms and the condensate fraction can be varied from 0 to 90% by tuning the final RF-frequency from 1 MHz to 0.33 MHz, as it is shown in Figure 35. Temperatures as low as 100 nK were observed.

Once the BEC is observed, it is interesting to finish to characterize the trapping potential of the Plug trap. The first useful parameter one can compare with the simulations is the trap's bottom potential, $U_{\text{Plug}}(0, y_{\text{min}}, 0)$, which can be easily obtained from the lowest RF-frequency for which there are still a few atoms trapped. In our experiment, it happens for 0.33 MHz which is equivalent to a potential bottom $U_0 = 16.5 \mu\text{K}$.

Further, one can measure the trapping frequencies. The most common methods

to measure the frequencies of a harmonic trapping potential consist in exciting dipolar or parametric (149) oscillations of the atomic cloud. In the case of an optically plugged trap, since the potential is considered harmonic only at its very bottom, dipole oscillations would rapidly bring the atoms to non-harmonic regions, damping and masking the oscillations. A better choice is the use of parametric oscillations that can be performed with the addition of a small oscillatory perturbation to the harmonic potential. In the NaK experiment, this perturbation is done by modulating the current in the Quadrupole coils such that $I(t) = I_0[1 + \epsilon \sin(2\pi f_{\text{mod}}t)]$, where $I_0 = I_{\text{Decomp}}$, $\epsilon = 0.05$ and f_{mod} is the modulation frequency. The modulation is applied during 200 ms and an additional 500 ms is used as a thermalization time.

In Fig. 36, we display the number of atoms in the condensate (a) and the temperature of the atomic cloud (b) obtained from images taken after $t_{\text{TOF}} = 20\text{ms}$ as a function of f_{mod} . The coupling occurs for $f_{\text{mod}} = f_i$, with f_i being the i -axis trapping frequency. At these frequencies, the kinetic energy of the trapped atoms increases exponentially with time diminishing the BEC atom number as it can be seen in the figure. By comparing the obtained central frequencies from the parametric oscillation with the behaviour expected from the simulations, we associate $f_x = 212$ Hz and $f_z = 317$ Hz. The f_y value is expected to be at frequencies higher than 500 Hz and due to the high impedances of the Quadrupole trap, it is not possible to modulate the field at such high frequencies.

We summarize the comparison between our calculations and the measured parameters in Fig. 37. The simulation was done considering $B' = B'_{\text{Decomp}} = 179\text{G/cm}$, $P_{\text{Plug}} = 2.1\text{W}$ and $w_0 = 43\mu\text{m}$ and the Plug beam to be aligned in the center of the Quadrupole trap. Small displacements from the trap center changes the Plug trap parameters and could explain the small discrepancies presented between the simulated and the measured values.

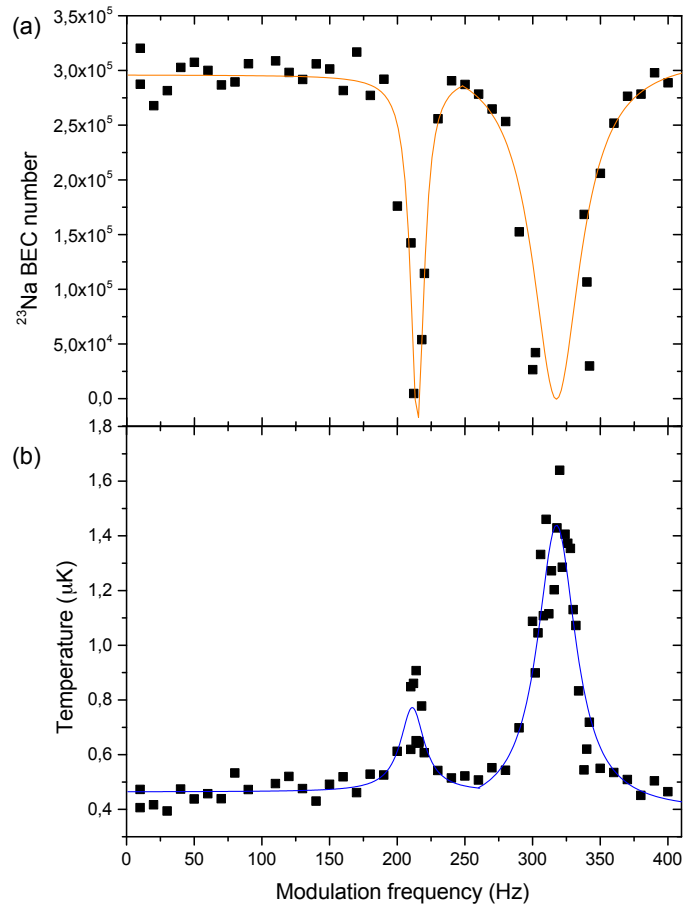


Figure 36 – Plug trap frequencies measured exciting parametric oscillations of the atomic cloud. At modulation frequencies equal to one of the trapping frequencies ($f_{\text{mod}} = f_i$) the strongest coupling occurs resulting in a reduction of the condensate atom number, in (a), and a increase in the temperature of the atomic cloud, in (b). Source: By the author.

	Simulated values	Measured values
y_{min}	$60\mu\text{m}$	$?\mu\text{m}$
f_x	208Hz	211Hz
f_y	544Hz	not measured
f_z	361Hz	317Hz
$U_{\text{Plug}}(0, y_{\text{min}}, 0)$	$19.4\mu\text{K}$	$16.5\mu\text{K}$

Figure 37 – Table with the comparison between the simulated and measured values for the Plug trap parameters considering $B' = B_{\text{Decomp}} = 179\text{G/cm}$, $P_{\text{Plug}} = 2.1\text{W}$ and $w_0 = 43\mu\text{m}$. Source: By the author.

5 Second step in producing a two-species BEC: working with potassium atoms

The second step in producing the two-species BEC was to start working with the potassium atoms alone and in the presence of sodium. This was a fundamental part of this thesis, since the group has not been working with potassium atoms for some time now (the last experiment was performed before 2000 in a magneto-optical trap) and we had to learn all the technical details on cooling and trapping it from scratch. Differently from other alkaline atoms, such as rubidium or sodium, the small energy splitting between the energy levels of the potassium excited states makes it difficult to cool the atomic sample below the Doppler temperature and different cooling procedures, such as the Gray molasses (80, 151, 152), have to be implemented. However, the difficult in cooling it is compensated by many advantages of the potassium isotopes, that have been widely explored in cold atomic experiments. (49, 58, 63, 80, 85, 97, 103, 151, 153)

In this Chapter, we start by presenting the most relevant characteristics of potassium isotopes in the context of cold atoms, in section 5.1. The small energy difference between its bosonic isotopes (^{39}K and ^{41}K) facilitates the design of a laser system able to study both of them, as it is described in section 5.2. Later, in section 5.3, we present the experimental sequence from the MOT of ^{39}K atoms to its magnetic trapping. The Gray molasses cooling procedure and its characterization for the ^{39}K atoms in the NaK experiment are better described in section 5.4. And, by the end of the chapter, in section 5.5, the initial results on working with ^{23}Na and ^{39}K atoms are discussed while performing the two-species MOT or while loading each MOT independently.

5.1 The potassium isotopes

In the past two decades, many experiments have been working with potassium atoms. (49, 58, 63, 80, 85, 97, 103, 151, 153) Some important characteristics (also important for the NaK experiment) can be listed to justify such interest. **(i)** There are three stable potassium isotopes, two of which are bosons (^{39}K and ^{41}K) and one is fermion (^{40}K). **(ii)** The potassium bosonic isotopes can be studied in the same experimental system with minor changes in the laser frequencies due to the proximity of their energy levels, as seen in Fig. 38. In addition to that, the not so broad separation between their ground-state hyperfine levels $F = 1$ and $F = 2$ (of $\approx 450\text{MHz}$ for ^{39}K and $\approx 254\text{MHz}$ for ^{41}K) allows the use of a single laser to generate both *cooling* and *repumper* lights needed in a MOT and indicated in the figure. **(iii)** Even if the ^{39}K has a natural abundance much bigger than the other isotopes (of around 93.26%), the ^{41}K with a natural abundance of 6.73% can still be studied without using an enriched source of atoms. And **(iv)**, the ^{39}K isotope has a very large Feshbach resonance at low magnetic field ($B_0 \approx 32\text{ G}$ with $\Delta \approx -55\text{ G}$, for the $|1, -1\rangle$ and $B_0 \approx 403\text{ G}$ with $\Delta \approx 52\text{ G}$, for the $|1, 1\rangle$ (85)) which enables a sensible tuning of the scattering length and make it possible to study the properties of a non-interacting system with very high precision. (75)

However, not all characteristics of the potassium isotopes favor their use in cold atomic experiments. In fact, the small separation between the excited hyperfine states of the D₂ line (of around 33.8 MHz for ^{39}K and just 22.8 MHz for ^{41}K between $|F' = 0\rangle$ and $|F' = 3\rangle$, see Fig. 38) makes it difficult to obtain a closed cooling transition. Typically, for a potassium MOT, more *repumper* light is needed in order to keep the atoms in the cooling cycle. In addition, the optical molasses stage (154), which could cool the atoms below the Doppler limit, do not work as good as for other alkaline atoms such as rubidium. For the case of the ^{39}K , the group of G. Modugno developed an adapted molasses technique that diminishes this limitation, achieving temperatures around $25\ \mu\text{K}$ ¹. (155) Another approach, which uses the D₁ atomic transitions in order to perform a *Gray molasses* (156), has demonstrated to be a good path in cooling ^{39}K and ^{40}K isotopes, achieving

¹ For the ^{41}K the lowest reported temperature was around $50\ \mu\text{K}$.

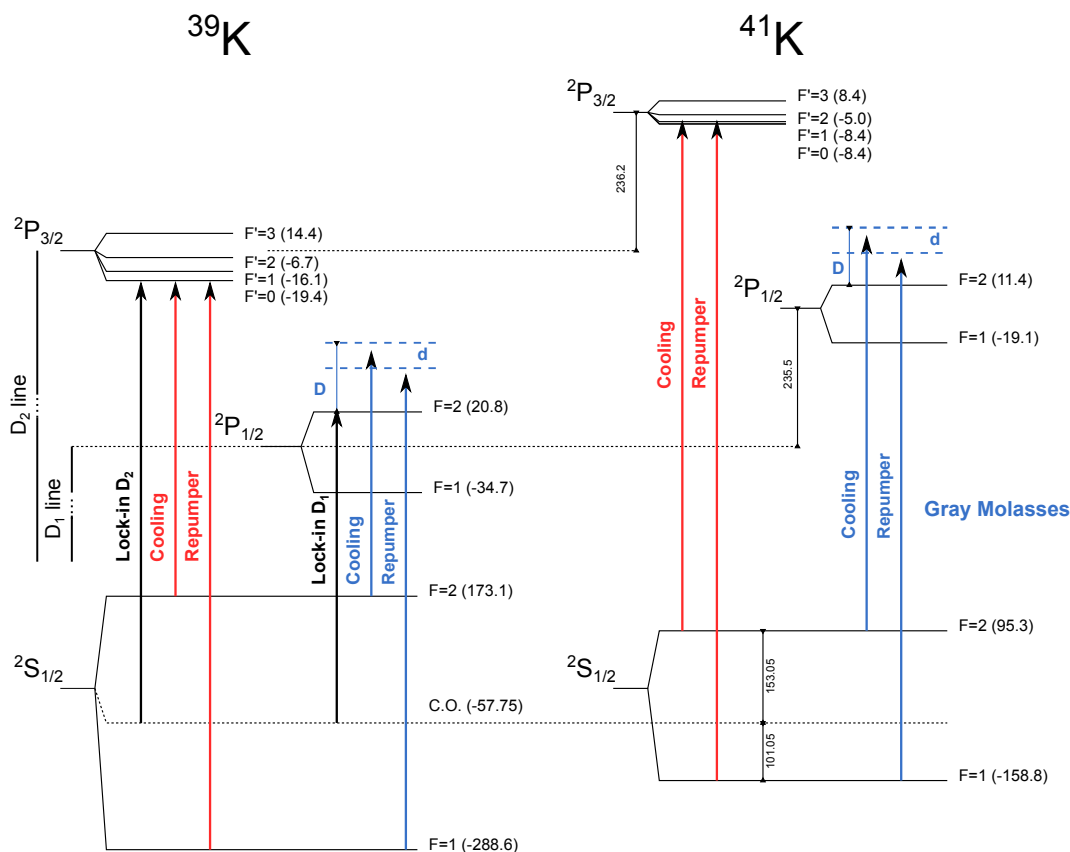


Figure 38 – Level diagram for the hyperfine states of the D₁ and D₂ lines for ³⁹K and ⁴¹K. The respective cooling and repumper transitions are illustrated. The *lock-in* points for the D₁ and D₂ lasers are done in the ground state crossover of the ³⁹K and is indicated by the vertical black line. The letters *D* and *d* are the absolute and relative detunings for the cooling and repumper lights with respect to the D₁ line transitions, respectively, and are going to be better explained in section 5.4. Source: By the author.

temperatures around 6 μ K and 20 μ K, respectively. (80, 151) Recently, it was also used to cool ⁴¹K, achieving temperatures as low as 42 μ K. (152)

In the NaK experiment we decided to follow the Gray molasses approach in order to cool the potassium atoms below the Doppler temperature, as it will be described in section 5.4 of this chapter.

5.2 The potassium laser system

The laser system for cooling and trapping potassium atoms was designed in order to make it possible to change the atomic species to be studied between the bosonic potassium isotopes (³⁹K and ⁴¹K) with minor changes in the optical setup. In fact, we could

design it such that only the frequencies of the AOMs used in the saturated absorption spectroscopy (157) needed to be changed. The whole laser system for potassium atoms is described in detail in Appendix D. Here, we just point out a new feature introduced by this optical setup that was never realized in the group before.

5.2.1 The master oscillator power amplifiers (MOPAs)

One disadvantage to work with potassium atoms is the necessity of high laser powers to efficiently cool the atoms during the MOT. Thus, even with two Toptica TA-Pro lasers which provide an output laser power of 1 W², extra amplification stages are necessary in order to have more than 300 mW for each MOT arriving in the *experiment table*. Homemade “master oscillator power amplifiers” (MOPAs) mounted with a *tapered amplifier* chip from Eagleyard (EYP-TPA-0765-01500-3006-CMT03-0000), able to provide 1.5 W by injecting a laser beam of just 50 mW, were produced and used as the last amplification stages for the 2D and 3D-MOT in the optical setup. The design of these MOPAs was done by the researchers at LENS, in Florence and offered to us as part of our collaboration. Pictures of the chip and of the stages on mounting the MOPA are shown in Fig. 39. The chip is mounted in an isolated copper support with stabilized temperature by the use of a ceramic peltier (from Elfa Distrelec) and a thermocouple (from GE Measurement & Control). Two aspheric lenses with $f_1 = 4.51$ mm (Thorlabs C230TMD) and $f_2 = 4.03$ mm (Thorlabs C340TME) are used to focus the injection beam into the chip and collimate the amplified output beam along the vertical direction, respectively. After the MOPA case, a cylindric lens with $f_3 = 100$ mm is used to collimate its horizontal direction and an optical isolator (Thorlabs IOT-5-780-MP) prevents optical feedback. In addition to the temperature control, the chip needs a current supply which in our case was adapted from the Toptica DLX-Pro laser controller which are able to provide the maximum chip’s operating current of 3 A.

In our system two MOPAs are used, named 2D and 3D-MOPA. In each of them, D₂ cooling and repumper lights are simultaneously coupled with a total injection power

² See Appendix D.

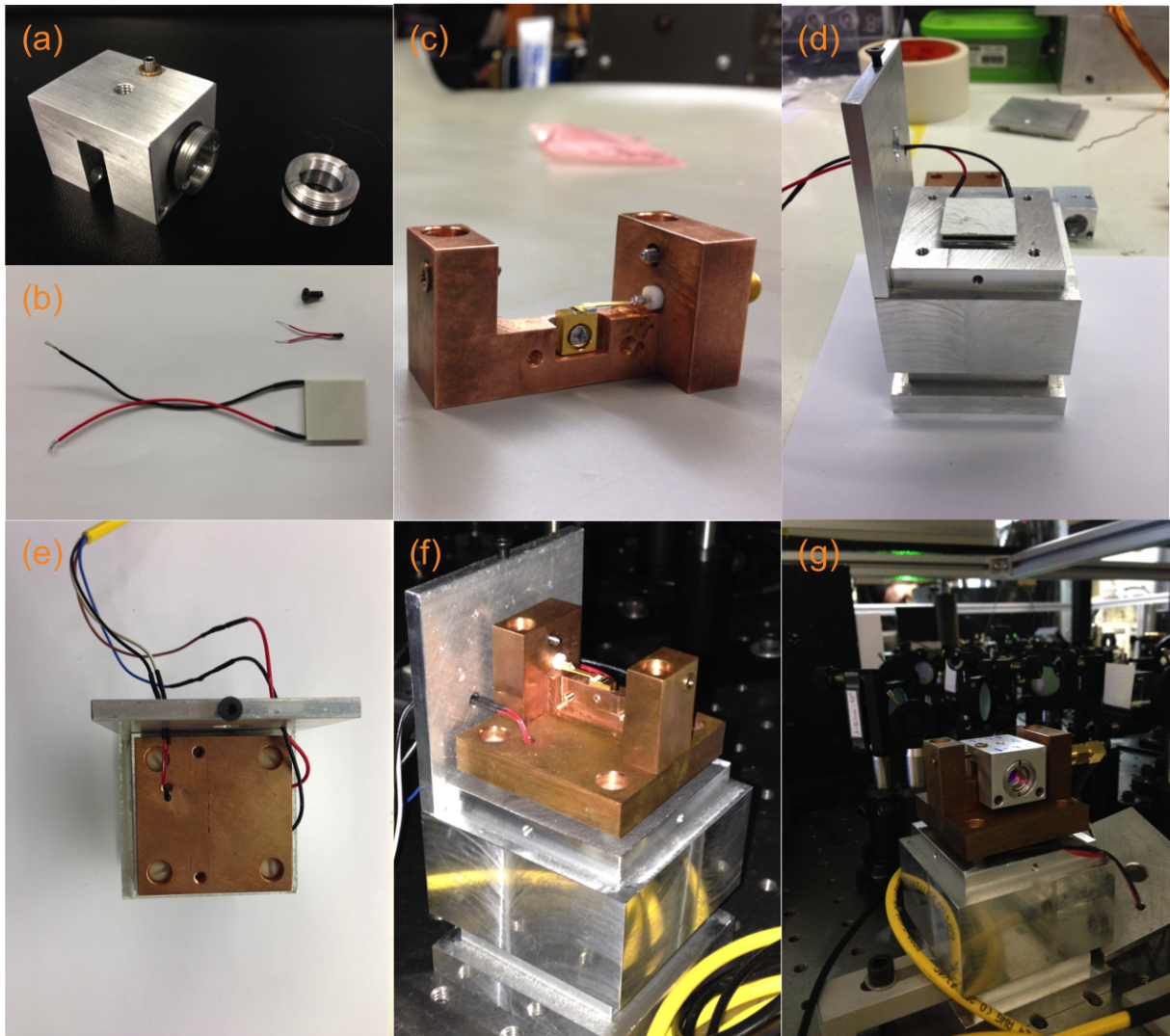


Figure 39 – Stages on mounting the MOPAs used to amplify the power of the light needed for the potassium atoms. In (a) it is shown the support and the lenses used to focus and vertically collimate the MOPA injection and output laser beams, respectively. In (b) it is shown the peltier and the thermocouple used to stabilize the chip temperature. The chip already mounted on its copper support is illustrated in (c). In (d), (e) and (f) we show a sequence of pictures while assembling all the parts together. And finally, the mounted MOPA aligned in the experiment and amplifying the light (red light in the center of the lens) is presented in (g).

Source: By the author.

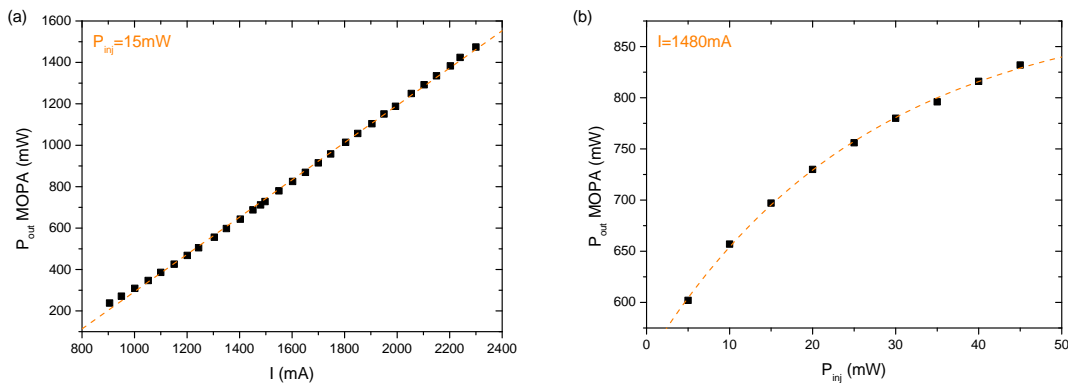


Figure 40 – Characterization of the 2D-MOPA as a function of (a) the current (for $P_{\text{inj}} = 15 \text{ mW}$) and (b) the injection power (for $I = 1480 \text{ mA}$).

Source: By the author.

of 45 mW (with a 50/50 ratio, in the case of the 2D-MOPA and a 80/20 ratio, in the case of the 3D-MOPA). The MOPAs temperatures are set to 20.1°C for the 2D and 21.0°C for the 3D. With a current of 2100 mA, the output power after the optical isolator is of the order of 1.1 W in both cases. The 2D-MOPA's responses as a function of the current (for $P_{\text{inj}} = 15 \text{ mW}$) and the injection power (for $I = 1480 \text{ mA}$) are shown in Fig. 40 (a) and (b). The corresponding curves for the 3D-MOPA present the same behaviour. After passing the beams through an AOM (which will act as a fast switch) and coupling them into the fibers, we obtain a power in the *experiment table* of around 300 mW for the 2D-MOT and 340 mW for the 3D-MOT.

5.3 From the ^{39}K MOT to the Quadrupole trap

In this section, we describe and characterize the experimental sequence for loading the 3D-MOT of ^{39}K and transferring the atoms to the magnetic Quadrupole trap already presented in section 4.4. Since the source of atoms is not enriched with ^{41}K , we decided during the time of this thesis to work with the ^{39}K (the most abundant potassium isotope) in order to prove the capability of the NaK experimental system in producing a cold cloud of potassium atoms by using the Gray molasses technique. In addition, this is the first time in which a 2D-MOT and the Gray molasses (for any atomic species) are used in the group and, by working with ^{39}K atoms, we were able to compare our results with the ones

presented in Ref. (80)³

The 2D-MOT of ^{39}K atoms is loaded from the potassium vapor that fills the K 2D-MOT chamber. (128) Differently from the 2D-MOT for ^{23}Na , once the vacuum system is closed and the desired pressure is achieved, the potassium oven is initially heated (up to 100°C) in order to fill up the K 2D-MOT chamber, then cooled back down to the chamber's temperature of around 42°C . The pressure of the K 2D-MOT chamber increases to 10^{-8} Torr. With this approach, there is no need to use the adapted Zeeman slower described for the ^{23}Na 2D-MOT. The pre-cooled atoms in the 2D-MOT are transferred to the science chamber guided by the *push* laser beam, where they are re-captured in a 3D-MOT. The 2D-MOT parameters are always optimized in order to maximize the atom number in the 3D-MOT and, consequently, the atomic flux arriving at the SC. In Fig. 41, we show the ^{39}K 3D-MOT loading curve obtained from the MOT fluorescence captured by a photodetector. The atomic flux coming from the 2D-MOT can be approximately obtained by performing a linear adjust to the initial part of the loading curve. In our system, the optimized atomic flux of ^{39}K is equal to 1.3×10^7 atoms/s and the optimized 2D-MOT parameters for a magnetic field gradient of ~ 30 G/cm⁴ are listed in the table of Fig. 42. Usually, fluxes up to 1×10^{10} atoms/s have been reported in the literature for ^{39}K (74, 128) and we justify this discrepancy with the fact that we do not make use of a *retarding beam*⁵. However, even with such a low atomic flux, the number of atoms in the 3D-MOT (around 1×10^8 atoms) is enough to obtain the two-species BEC if one *sympathetic cools* (58) the potassium with the sodium atoms.

For detecting the atoms in the following steps of the experimental sequence and to better characterize the atom number in the 3D-MOT as well as its temperature, one usually performs an image of the atomic cloud. Also in the case of potassium atoms, we

³ As previous discussed, by the time we start building up the NaK experiment, the Gray molasses for ^{41}K had not yet been done and therefore, there was no data to compare with. The ^{41}K Gray molasses was just recently reported in Ref. (152)

⁴ The 2D-MOT of potassium atoms works with a much lower magnetic field gradient than the 2D-MOT for sodium reported in Chapter 4 and it is produced by four sets with only four magnets each.

⁵ The *retarding beam* is a beam with a hole in the middle that travels in the opposite direction of the *push* beam creating an imbalanced molasses along the non-trappable axis of the 2D-MOT. The addition of this beam normally improves in more than one order of magnitude the atomic flux coming out from the 2D-MOTs. (74, 128)

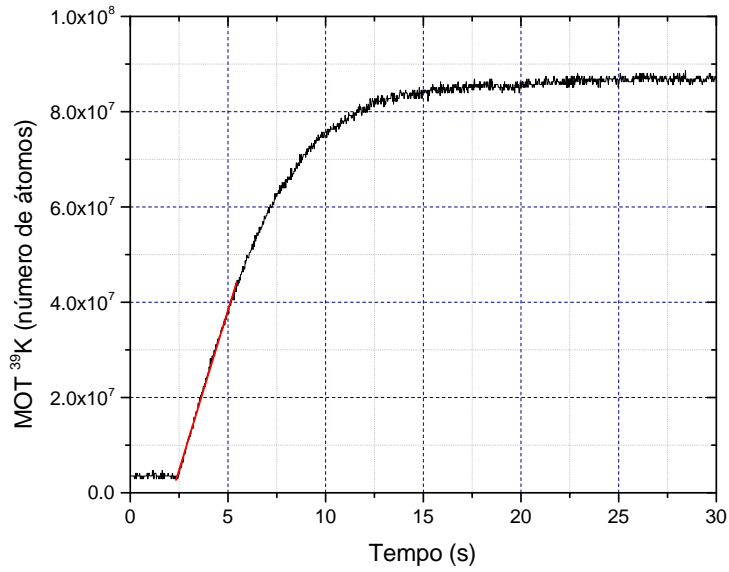


Figure 41 – ^{39}K 3D-MOT loading as a function of time. The 3D-MOT loading rate proportional to the 2D-MOT atomic flux can be obtained by performing a linear adjust at the initial part of the 3D-MOT loading curve (red curve) for which we obtained 1.33×10^7 atoms/s.

Source: By the author.

	Detuning (MHz)	Power (mW)
2D-MOT cooling	-21	150
2D-MOT repumper	-18	150
Push (cooling+repumper)	the same	0.26

Figure 42 – Potassium 2D-MOT optimized parameters for $B'_{2D} = 30\text{G/cm}$.

Source: By the author.

use the absorption imaging technique described in section 4.2.3.

5.3.1 The experimental sequence until the magnetic trapping

As previously discussed, the transference of the atoms from the MOT to a conservative trap is one of the most critical steps in cold atomic experiments. In order to improve this transference, some intermediate processes are usually implemented. In the case of potassium atoms, the standard sub-Doppler cooling procedure, which uses light in the D_2 transition, is not efficient due to the difficulty in creating a closed cooling transition. To circumvent this problem, the use of a Gray molasses stage with light close to the D_1 line transition has proven to be a nice approach for all the potassium isotopes, achieving

temperatures of $6\ \mu\text{K}$, $20\ \mu\text{K}$ and $42\ \mu\text{K}$ for ^{39}K , ^{40}K and ^{41}K , respectively. (80,151,152) Therefore, the sequence described in reference (80) was used as an initial guide for our experiment. In Fig. 43, we show the optimized sequence for trapping the ^{39}K atoms in the magnetic trap. The changes done in the intensity and detuning of the light beams and in the magnetic field as well as the number of atoms and the temperature of the atomic cloud for the different steps of the experimental sequence are indicated.

After loading the ^{39}K 3D-MOT, a “Low Power MOT” stage (Low-MOT) is added in which all the MOT parameters are kept constant except for its laser power, which is reduced in order to minimize photon rescattering processes and compress the atomic cloud. Latter, we use a “Hybrid C-MOT” (80) in which the magnetic field is increased, the cooling light (from the D_2 line) is turned off and the remaining D_2 repumper is combined with D_1 cooling light during 15 ms. After this compression step, the atomic cloud assumes a small and more symmetric shape. This is essential in matching the size of the atomic cloud to the characteristic volume of the Quadrupole trap. In the following, the Gray molasses is implemented by switching off the magnetic field and the D_2 repumper light is exchanged by the D_1 repumper, leaving the atoms to expand in the D_1 light field. Finally, before transferring the atoms to the Quadrupole trap, a “Pre-Pump” stage is used to pump the atoms to the $|F = 2\rangle$ state by switching off the D_1 light and turning on just the D_2 repumper light. The magnetic trap is loaded right after the “Pre-Pump” stage by abruptly switching on the magnetic field at three times the MOT gradient and adiabatically ramping it up to $B' \approx 200\ \text{G/cm}$. In the end, $2/5$ of the atoms in the Gray molasses are trapped in the Quadrupole (since after the “Pre-Pump”, $1/5$ of the atoms are in the $|2, 2\rangle$, $1/5$ of the atoms are in the $|2, 1\rangle$ and the others are distributed among the non-magnetically trappable states). Finally, we obtain 1×10^7 atoms at $240\ \mu\text{K}$ in the magnetic trap.

5.4 The Gray Molasses for ^{39}K

The cooling technique called *Gray molasses* was first proposed in (158–161) and realized with light from the D_2 transitions for rubidium and cesium atoms. Nowadays, the

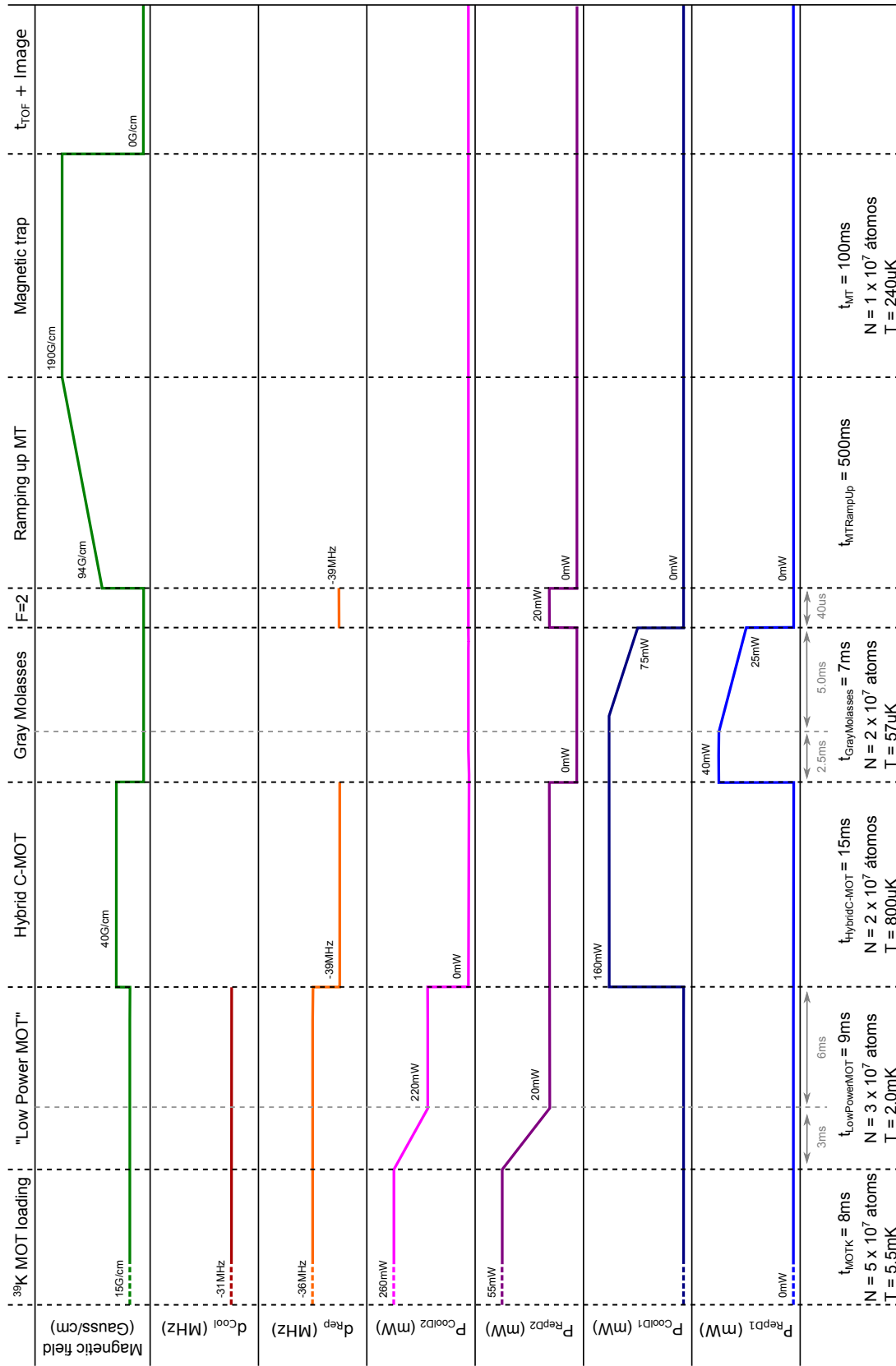


Figure 43 – Scheme of the experimental sequence for trapping the ³⁹K atoms in the magnetic trap. We show the change on the relevant parameters at each process as well as the process duration time and number of atoms and temperature of the atomic cloud. Source: By the author.

same technique done with light slightly detuned from the D_1 transition is vastly used to efficiently cool atoms that present a small hyperfine splitting of the excited states in the D_2 line, as it is the case of lithium (162), potassium (80, 151, 152) and lastly sodium (163) atoms. In this section, we describe its working principles (5.4.1) following the discussion presented in (151) and the characterization of the Gray molasses for the ^{39}K atoms done in the NaK experiment (5.4.2).

5.4.1 The Gray molasses working principles

The Gray molasses working principle relies on the the existence of two fundamental states, a “*dark*” and a “*bright*” state and on their coupling with an excited state, and “Sisyphus cooling”, the mechanism that allows the temperature of the D_2 molasses to go beyond the Doppler cooling limit. (154) The *dark* state does not couple with light and cannot be excited. The *bright* state, however, can couple with light and be excited to the excited state. Its energy shift is positive for a positive detuning of the light and it varies with position according to the change in the light intensity (which has a standing wave pattern due to the superposition of two counterpropagating laser beams, as it can be seen in Fig. 44 (a)). A mechanism can couple the *dark* and *bright* states such that this transference is most probable to occur at the positions in which their energy difference is minimum, i.e. at the bottom of the *bright* state potential. On the other hand, the atoms in the bright state will be preferentially excited to the excited state at the top of the energy hill. Therefore, in average, once an atom is transferred to the *bright* state it losses its kinetic energy by climbing the potential well, being excited and transferred back to the *dark* state, in a similar way as it happens for Sisyphus cooling. Finally, as the atoms get colder, the coupling between the *dark* and *bright* fundamental states is decreased and they accumulate at the *dark* state in a process called “*velocity-selective coherent population transfer*” (VSCPT).(164)

The Gray molasses can be simply modelled by using a Λ system in which two ground states, $|g_1\rangle$ and $|g_2\rangle$, are coupled through light to an excited state $|e\rangle$. For the case of alkaline atoms, $|g_1\rangle$ and $|g_2\rangle$ are identified with the $F = 1$ and $F = 2$ states, respectively,

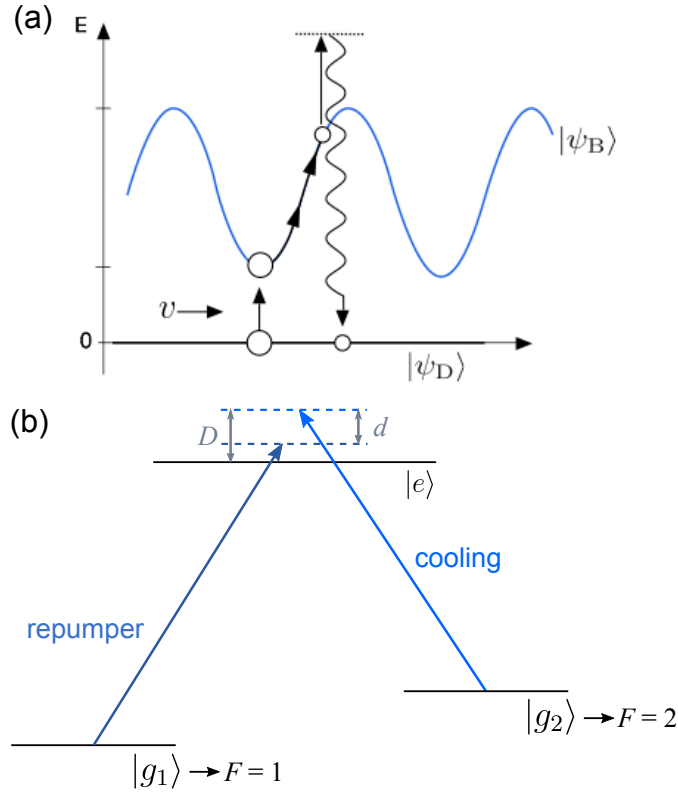


Figure 44 – Working scheme for the Gray molasses. In (a), we show the energies of the *dark* and *bright* states ($|\psi_D\rangle$ and $|\psi_B\rangle$, respectively) and their coupling with the excited state ($|e\rangle$) as a function of the atom position. In (b), we present the Λ system used to model the Gray molasses in the case of potassium atoms. The absolute and relative detunings (D and d , respectively) are also indicated in the scheme. Source: (a), adapted from Fernandes in (151); (b) By the author.

which are coupled with the excited state through the repumper and cooling lights (see Fig. 44 (b)). If the difference between the light detunings vanishes ($d = \delta_{\text{rep}} - \delta_{\text{cool}} = 0$, named “relative detuning”), the system can be written in another basis such that we define a *dark*, $|\psi_D\rangle$, and a *bright* state, $|\psi_B\rangle$, given by:

$$|\psi_D\rangle = \frac{1}{\Omega}(\Omega_2|g_1\rangle - \Omega_1|g_2\rangle) \quad \text{and} \quad |\psi_B\rangle = \frac{1}{\Omega}(\Omega_1|g_1\rangle + \Omega_2|g_2\rangle), \quad (5.1)$$

where Ω_1 and Ω_2 are the Rabi frequencies of the transitions between the ground states, $|g_1\rangle$ and $|g_2\rangle$, to the excited state $|e\rangle$, respectively and $\Omega = \sqrt{\Omega_1^2 + \Omega_2^2}$. It is possible to see that only the *bright* state is affected by the light coupling with the excited state ($\hat{V}|\psi_D\rangle = 0$ while $\langle e|\hat{V}|\psi_B\rangle = \hbar\Omega/2$). Until now, we treated the coupling between the electronic states of the atom. However, these states are not stationary when considering the full Hamiltonian $\hat{H} = \hat{H}_{\text{at}} + \hat{V}$, with \hat{H}_{at} being the Hamiltonian that includes the

kinetic term $\hat{p}^2/2m$ and p being the external momentum of the atom. In this case, since the absorption of one photon also couples different external momentum state, it is possible to obtain the following relation:

$$\langle \psi_{\text{B}}(p) | \frac{\hat{p}^2}{2m} | \psi_{\text{D}}(p) \rangle = -\frac{2\Omega_1\Omega_2}{\Omega^2} \hbar k_{\text{B}} \frac{p}{m}, \quad (5.2)$$

If we define the detuning between the light and the atomic transition to be $D = \omega - \omega_0$, named “absolute detuning”, with ω and ω_0 being the laser and the atomic transition frequencies, the energy shift of the *bright* state will be proportional to the laser intensity such that $E_{\text{B}} = \hbar\Omega^2/D$, while the energy of the *dark* state will remain unchanged. From second order perturbation theory, we can now obtain the probability for one atom in the *dark* state to be transferred to the *bright* state, which is given by:

$$P_{\text{D} \rightarrow \text{B}} = \left| \frac{\langle \psi_{\text{B}}(p) | \frac{\hat{p}^2}{2m} | \psi_{\text{D}}(p) \rangle}{E_{\text{B}} - E_{\text{D}}} \right|^2 = 2 \left(\frac{\Omega_1\Omega_2}{\Omega^3} D k_{\text{B}} \frac{p}{m} \right)^2. \quad (5.3)$$

Thus, the probability of the atoms in the *dark* state to be transferred to the *bright* state increases with the atomic velocity v and with the detuning D , but decreases with the light shift Ω^2/D . (159) The velocity dependence of this probability introduces the velocity selection population trapping and we see that colder atoms tend to accumulate at the *dark* state. On the other hand, its light shift dependence, when considering a stationary wave (as it is illustrated in Fig. 44 (a)), will most probable couple atoms from the *dark* to the *bright* state at the bottom of the *bright* state potential, where $E_{\text{B}} - E_{\text{D}} = E_{\text{B}}$ is minimum and we can recover the initial explanation for the Gray molasses done at the beginning of this section.

5.4.2 Characterizing the Gray molasses for ^{39}K atoms

In our experiment, the light needed to perform the Gray molasses is generated by a Toptica DLX-110 laser tuned at 770nm. The absorption and dispersion signals for the D_1 line of potassium atoms obtained from saturated absorption spectroscopy and used to stabilize the DLX frequency is shown in Fig. 45. Due to the broader energy splitting of the hyperfine states in the excited state of the D_1 line (see Fig. 38), it is possible to resolve

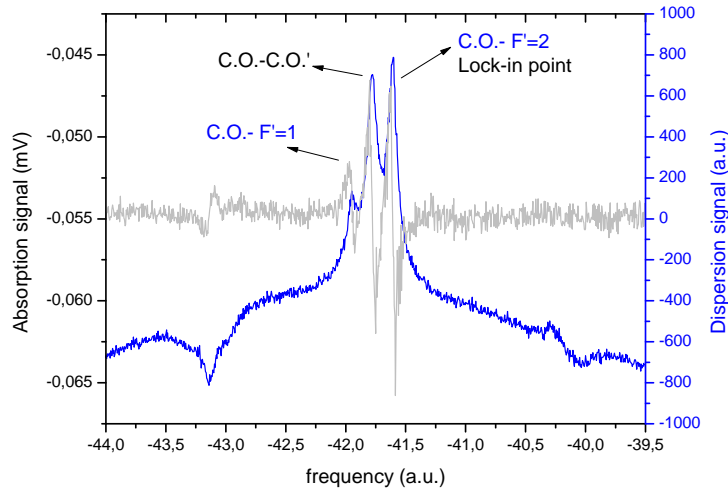


Figure 45 – Absorption (in blue) and dispersion (in gray) signals for the D_1 of potassium atoms obtained through the saturation absorption spectroscopy technique. The transitions related with the crossover of the ground-state as well as the *lock-in* point for stabilizing the DLX-110 laser frequency are indicated.

Source: By the author.

each transition related with the ground-state crossover in the absorption spectrum, as indicated in the figure.

The optical setup for the D_1 line is illustrated in the scheme of Fig. 46. As for the D_2 , we designed a D_1 optical setup that makes it possible to change the studied isotope (from ^{39}K to ^{41}K and vice-versa) with minor changes, which are indicated in the scheme. Since also in the case of the Gray molasses of potassium atoms high power is needed (around 200 mW), the cooling and repumper D_1 lights are combined, coupled into an optical fiber and finally aligned into the 3D-MOPA (see Fig. 80 in Appendix D). In this way we could optimize the D_1 laser power for the Gray molasses to approximately 160 mW for the cooling light and 40 mW for the repumper light ($I_{\text{rep}}/I_{\text{cool}} = 0.25$).

The most critical parameter for the Gray molasses is the relative detuning between the D_1 cooling and repumper lights, $d = \delta_{1R} - \delta_{1C}$ that should be set to zero (“Raman resonance” condition) in order to achieve the best cooling efficiency. (158–161) By considering a positive absolute detuning of $D = \delta_{1C} = 3.9\Gamma_{D1}$, with $\Gamma_{D1} = 5.95$ MHz being the decay rate of the D_1 line transition, we could vary d by changing the detuning of the D_1 repumper light for the optimized laser power. The duration of the Gray molasses was also adjusted in order to provide the most efficient cooling without loss of atoms at the Raman

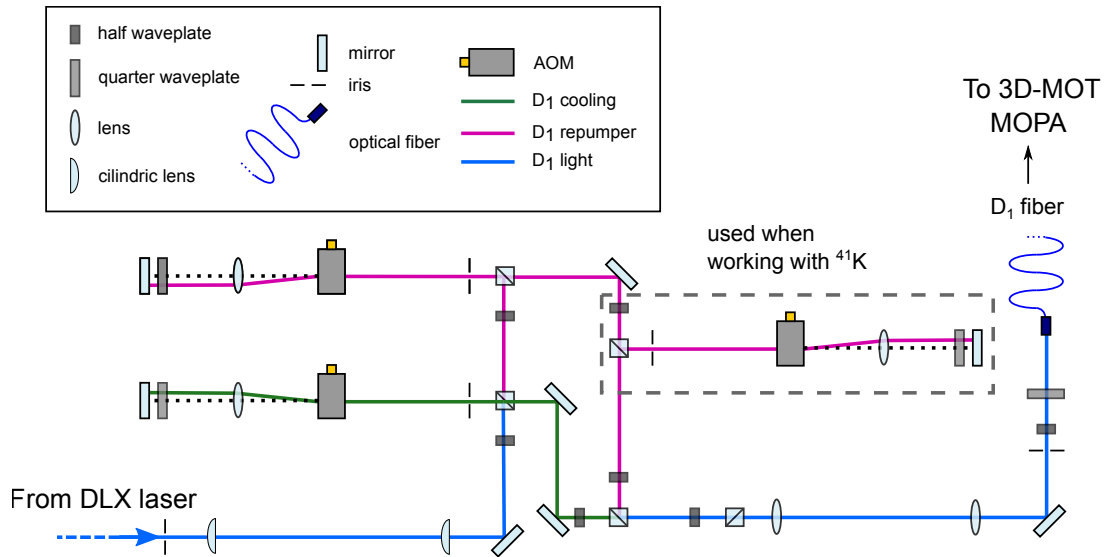


Figure 46 – Optical setup for generating the light resonant with the D_1 transitions of potassium atoms. The possibility of changing the studied bosonic isotope (from ^{39}K to ^{41}K) is done by adding a double-pass AOM to the repumper light, as indicated in the figure. After coupling the light into the D_1 optical fiber, the D_1 light is combined with the 3D-MOT D_2 light and injected into the 3D-MOT MOPA (see Fig. 80 in App. D).

Source: By the author.

resonance. The final characterization of the Gray molasses cooling procedure performed in our experiment to the ^{39}K atomic cloud is presented in Fig. 47, in which it was used $t_{\text{GrayMol}} = 7.5\text{ms}$. It is possible to recognize the typical asymmetric Fano profile for the dependence of the temperature (orange circles) with d , in which the minimum temperature (in our case $T = 57\mu\text{K}$) is achieved around $d = 0$. (80, 162, 165) At this value, the number of atoms (black squares) is maximum, showing the Gray molasses capability in cooling a large atomic cloud to very low temperatures. To the blue of the Raman resonance, we observe a strong heating of the atomic cloud followed by a big atom loss that corresponds to the values of d for which the atoms in the dark state are strongly coupled with the bright states in the top of the hills of the bright potential⁶. Away from the resonance, the temperature achieves a background value around $130\mu\text{K}$ due to the effect of Sisyphus cooling alone. (166)

When comparing our Gray molasses results with previous results (80, 162, 165), we observe a larger width for the Fano profile. This larger width could be due to a poor

⁶ See the discussion presented in the previous section of this chapter.

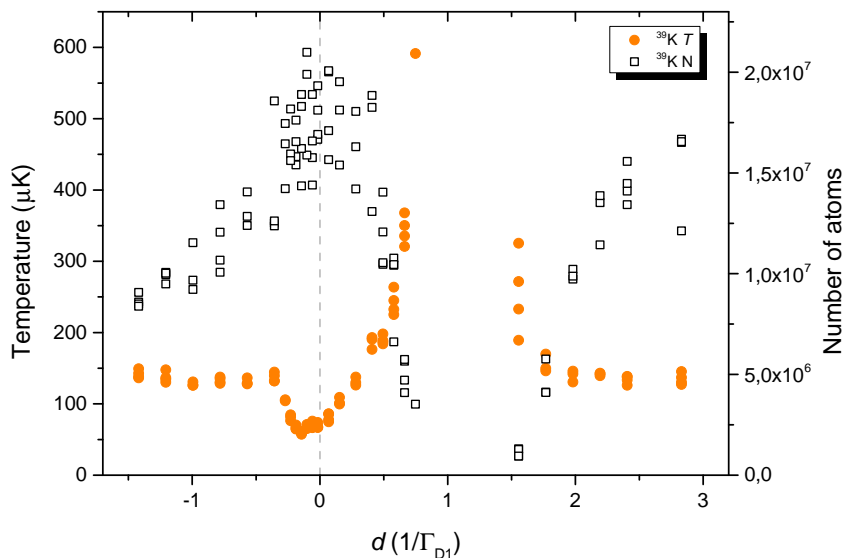


Figure 47 – Temperature and atom number of the ^{39}K atomic cloud as a function of d after 7.5ms of Gray molasses. The absolute detuning was kept constant with $D = \delta_{1C} = 3.9\Gamma_{D1}$ and the total D_1 light power was of 200mW ($P_{1R}/P_{1C} = 0.25$). The number of atoms is maximum at $d = 0$ while the temperature presents the typical Fano profile seen in Gray molasses cooling with a minimum at $T = 57\mu\text{K}$.
Source: By the author.

frequency stabilization of the D_1 DLX laser, which would also explain why we do not reach even lower temperatures (in Ref. (80), they report a minimum temperature of $6\mu\text{K}$). Differently from the absorption spectroscopy setup for stabilizing the laser frequencies generating the D_2 light, in the D_1 setup, the potassium vapor cell used to obtain the absorption spectrum has to be heated since the D_1 transitions have a smaller scattering cross-section. Normally, the cell is heated using a tube that surrounds it, leaving clear the viewports through which the light has to pass. Therefore, the laser frequency stabilization becomes very sensitive to temperature fluctuations and to the loss of signal intensity due to the deposit of atoms on the inner surfaces of the vapor cell. A better scheme can be realized when placing the vapor cell inside a case where the hot air uniformly surrounds it.

Even though we do not achieve the previous reported $6\mu\text{K}$, the Gray molasses procedure in our experiment has shown to produce atomic clouds whose parameters vary very little between each realization. Besides, a temperature of $57\mu\text{K}$ before the transfer to the magnetic trap is smaller than the temperature obtained for sodium atoms at this

stage (of $80\ \mu\text{K}$). Therefore, we could start to work in a scheme for loading both atomic species in the Plug trap. In the last section of this chapter, we briefly present the first two approaches performed in the NaK experiment: the loading of a two-species MOT (in 5.5.1) and the “Two-stage MOT loading” procedure (in 5.5.2).

5.5 Initial work with two-species: ^{23}Na and ^{39}K

Until this point of the thesis, we presented an independent characterization of the experimental sequence for each atomic species (^{23}Na and ^{39}K). In this section, we focus on presenting the results obtained during our initial work with the two-species. Two different approaches were chosen: to perform a simultaneous loading of the two-species MOT and to load each MOT independently, following the “Two-stage MOT loading” procedure described in Ref. (139). In both cases, atomic losses proved to be a limiting factor and a discussion about how we could suppress it is found at the end of the section.

5.5.1 A two-species MOT: ^{23}Na and ^{39}K

The first attempt in working with the two atomic species, ^{23}Na and ^{39}K ⁷, was done with a two-species MOT which used the optimized parameters for the individual sodium and potassium MOTs (except for the magnetic field gradient, which was kept at the ^{39}K MOT value). When loading the sodium MOT, the number of atoms in the potassium MOT abruptly decreased, as it can be seen in the fluorescence signals of each MOT presented in Fig. 48. The inverted situation (loading the sodium and later the potassium MOT) does not affect the number of atoms in the ^{23}Na MOT. Moreover, each individual MOT is not affected if just the light resonant with the other atomic species is on. This type of losses is known as *light-induced losses* and has been widely explored in the first experiments dealing with two-species magneto-optical traps. (167)

However, we could not find any reference in the literature neither treating the case of one of the MOTs operating in the Dark-SPOT configuration nor reporting such a strong loss of one of the atomic species. For this reason, we decided to briefly investigate the

⁷ As previously discussed, we decide to first work with ^{39}K instead of ^{41}K proving the capacity of the experimental system in producing a cold cloud of potassium atoms.

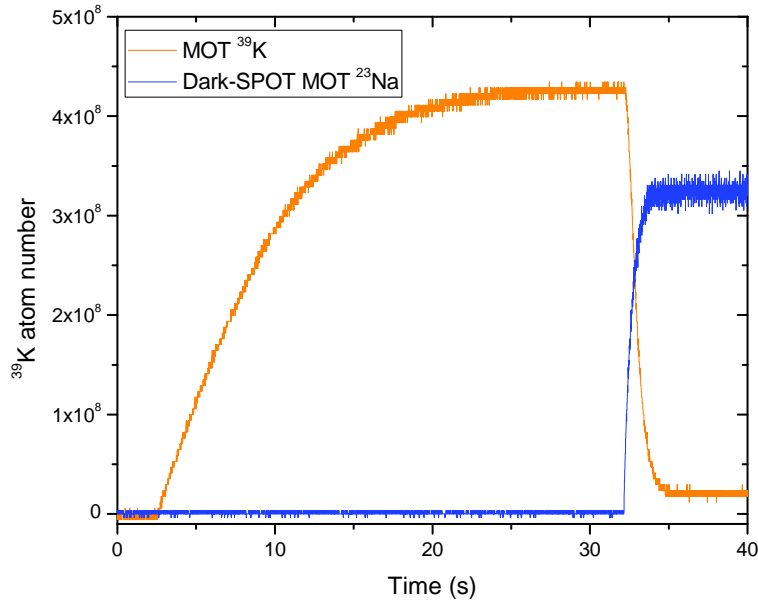


Figure 48 – Fluorescence signal from the sodium (blue curve) and potassium (orange curve) MOTs. When loading the ^{23}Na MOT, the number of atoms in the ^{39}K MOT abruptly decreases.

Source: By the author.

losses mechanism between the ^{39}K *bright*-MOT and the ^{23}Na Dark-SPOT MOT, which are presented in a former master thesis. (79)

5.5.2 Two-stage MOT loading

The light-induced losses that occur in the two-species MOT for ^{23}Na and ^{39}K are a limiting factor in obtaining the two-component BEC. In order to circumvent them one can work with the “Two-stage MOT loading” approach described in reference (139) and applied to a two-component system with ^{23}Na and ^{40}K .

The “Two-stage MOT loading” consists in performing the MOT of each species at different times of the experimental sequence. First, the ^{23}Na MOT is loaded and the experimental sequence for trapping the atoms in the Quadrupole trap is performed. Later, the quadrupole magnetic field is reduced to the ^{39}K MOT value in order to be able to load it. While loading the potassium MOT, the sodium atoms are trapped in a very shallow magnetic trap that still compensates gravity⁸. Now, the experimental sequence

⁸ The choice of which MOT species has to be loaded first is done considering the lightest atom, since it will need a smaller magnetic field gradient to compensate gravity.

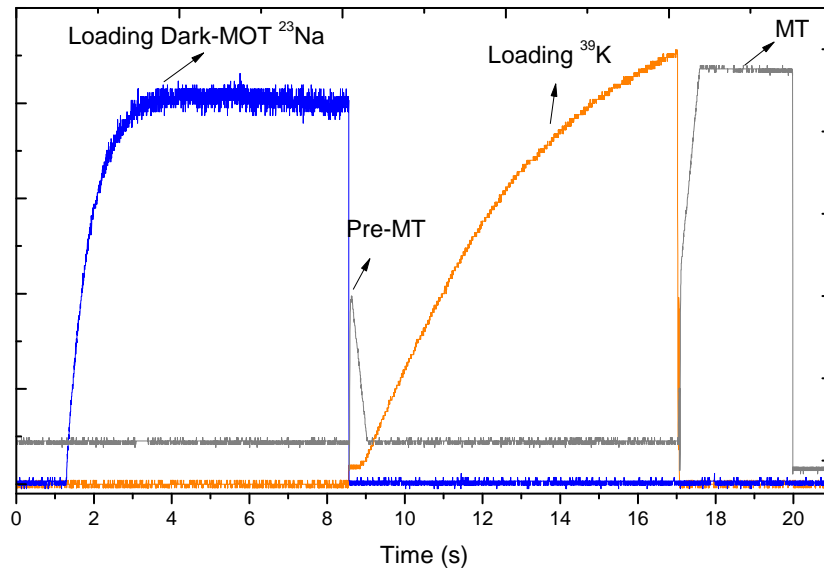


Figure 49 – Simplified experimental sequence for performing the Two-stage MOT loading procedure. The ^{23}Na dark-SPOT MOT is loaded and trapped in a Pre-MT at a magnetic field gradient equal to 90 G/cm. Later, this field is adiabatically reduced to the value optimized for loading the ^{39}K MOT. This MOT is loaded for 8 s and both species are finally trapped in the full magnetic trap. Separated images are done in order to diagnosis each trapped atomic cloud.

Source: By the author.

for trapping the ^{39}K atoms in the Quadrupole trap is performed such that, in the end, both species are trapped in the magnetic trap. The simplified experimental sequence for performing the “Two-stage MOT loading” in the NaK experiment is presented in Fig. 49.

In order to characterize the “Two-stage MOT loading” procedure for each atomic species we start with the complete sequence, but loading one species at each time. We found no difference neither in the number of trapped atoms nor in the temperature of the atomic cloud for the ^{39}K atoms. However, for the case of the ^{23}Na , the number of trapped atoms decreased to half of its optimized atom number while using the experimental sequence described in Chapter 4 ($N_{\text{Na}} \approx 6 - 7 \times 10^8$ atoms) and its temperature increased from 180 μK to almost 340 μK . These results were expected. Indeed, the experimental sequence for potassium atoms remained the same, while for sodium atoms it was radically changed: not only they suffer one extra decompression/compression of the magnetic field, which are never perfectly adiabatic and heat the atomic cloud, but also they remain 8 s in a very shallow trap ($B' \approx 15$ G/cm) while potassium atoms are loaded, causing atomic losses due to its finite lifetime.

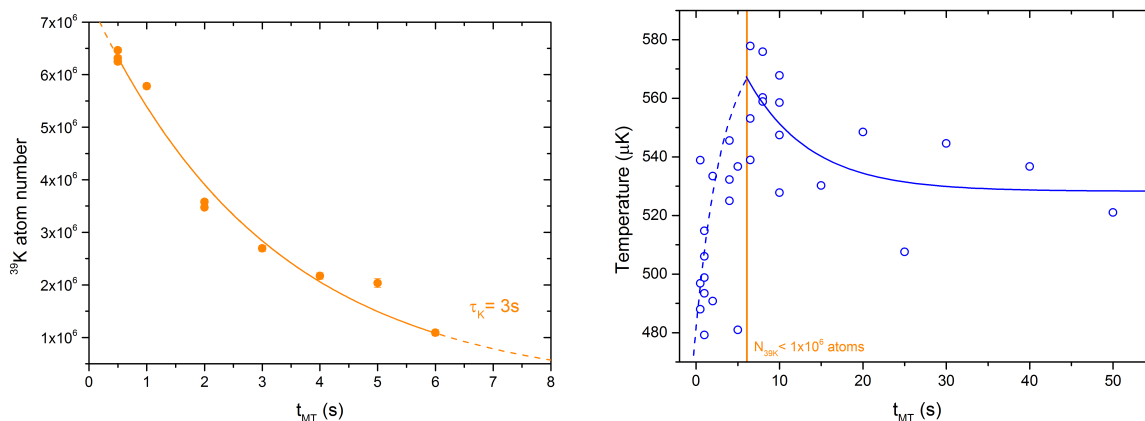


Figure 50 – Number of atoms of ^{39}K (a) and temperature of ^{23}Na (b) as a function of the time in the magnetic trap loaded after the Two-stage MOT loading. The potassium lifetime dramatically decreases in the presence of the sodium with $\tau_{^{39}\text{K}} = 3\text{s}$. During the time the ^{39}K is present in the trap (represented by the solid orange line in (b)), the temperature of the ^{23}Na atoms increase achieving $T_{\text{Na}} \approx 580 \mu\text{K}$. After that, T_{Na} decreases to a static value still much higher than if one do not load the ^{39}K atoms. Source: By the author.

When combining the loading of both species on the full two-stage MOT loading procedure, the number of trapped atoms remained unchanged but the temperature of both species increased, achieving a limit of $T_{\text{Na}} \approx T_{^{39}\text{K}} \approx 580 \mu\text{K}$. The lifetime of trapped potassium atoms dramatically decreased and, by the time the temperature of both species coincided, there were almost no atoms left, as it can be seen in the graph of Fig. 50 (a). The measured ^{39}K lifetime was of only 3 s, which is not long enough to perform the remaining steps to achieve the Bose-Einstein condensate. In addition to that, the increase in the temperature of both species can be explained by the presence of inelastic collisions between sodium and potassium atoms. In fact, we have observed that, when there is no ^{39}K left, the ^{23}Na atomic cloud stops heating, and effectively decreases its temperature due to a natural evaporation of the magnetic trap, as presented in Fig. 50 (b).

In order to avoid the heating and the losses in the potassium atoms, new combinations of $|F, m_F\rangle$ states could be used⁹. The combination that is most probable to work for trapping ^{23}Na and ^{39}K (or ^{41}K) is to have both species in the $|2, 2\rangle$ state (139). For obtaining that, an optical pumping procedure has to be done for both species. For the potassium isotopes, $500 \mu\text{s}$ long optical pumping pulses have proven to be very efficient

⁹ At the results presented on Fig. 50 the sodium atoms were in the $|1, -1\rangle$ state while the potassium were either in the $|2, 1\rangle$ or in the $|2, 2\rangle$ states.

in pumping the atoms to the $|2, 2\rangle$ without relevant additional heating. However, this is not the case for sodium atoms. The usual efficiencies for optically pumping ^{23}Na atoms to the $|2, 2\rangle$ are around 75%. Some of the residual 25% are in the $|2, 1\rangle$ state, which is also magnetically trappable. Their presence in the magnetic trap causes *spin relaxation* (139) and losses in the trapped atoms. In order to minimize these losses, we use a method called *gravity-assisted spin purification*.

5.5.3 Spin Purification for ^{23}Na atoms

The *gravity-assisted spin purification* procedure used to produce an atomic cloud of ^{23}Na atoms all in the $|2, 2\rangle$ state is illustrated in the scheme of Fig. 51, extracted from Ref. (139) The optically pumped ^{23}Na atomic cloud (a) is loaded in a “Low field” Quadrupole trap (b) in which atoms in both $|2, 2\rangle$ and $|2, 1\rangle$ states are trapped (light and dark yellow circles, respectively). After a short time (~ 50 ms), this magnetic field is adiabatically ramped down in 600 ms to a magnetic field gradient that does not compensate gravity for the atoms in $|2, 1\rangle$ (see part (c) in the figure). These atoms fall from the trap under the action of the gravitational force during $t_{\text{SpinPur}} = 400$ ms. After that, the magnetic field is ramped up during another 400 ms to the optimized value for loading the potassium MOT. The potassium MOT is loaded following the previously described “Two-stage MOT loading” procedure and both species are finally trapped in the magnetic trap at the $|2, 2\rangle$ state (part (e) of the figure).

The optimization of the Spin purification parameters is done by looking at the number and the temperature of the sodium atoms trapped in the magnetic trap after $t_{\text{MT}} = 10$ s without loading the potassium MOT¹⁰. In Figure 52 (a), we show the dependence of N_{Na} with the Spin purification magnetic field gradient, B'_{SpinPur} , for $t_{\text{SpinPur}} = 400$ ms, while in (b), we show the dependence on the temperature of the atomic cloud with t_{SpinPur} for $B'_{\text{SpinPur}} = 7.5$ G/cm. The other cloud parameters in each case, temperature for the scan in (a) and number of atoms in (b), remained unchanged during

¹⁰ Here, the potassium MOT is not loaded but the complete sequence is performed such that the spin purified sodium atoms remain 8 s in the very shallow magnetic trap with the magnetic field gradient optimized for the ^{39}K MOT.

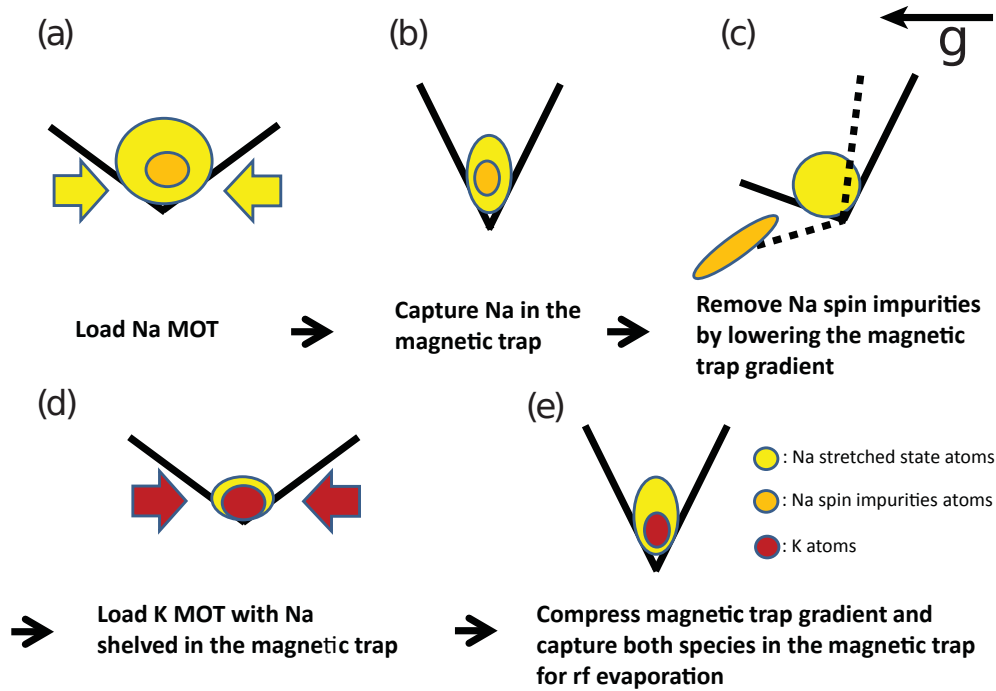


Figure 51 – Gravity assisted spin purification scheme for sodium atoms. The optically pumped atomic cloud (a) is loaded in a “Low field” Quadrupole trap (b) in which atoms in both $|2, 2\rangle$ and $|2, 1\rangle$ states are trapped (light and dark yellow circles, respectively). The magnetic field is reduced until the value it does not compensate gravity for the atoms in $|2, 1\rangle$ (c). Later, in (d), the magnetic field gradient is once again increased to the optimized value for loading the potassium MOT (red circle). In the sequence, the processes to cool and optically pump the potassium atoms are performed. Finally, both species can be trapped in the magnetic trap in the $|2, 2\rangle$ in (e).
 Source: Adapted from Wu. (139)

the total scan. The peak in the trapped atom number for $B'_{\text{SpinPur}} \approx 8 \text{ G/cm}$ represents the exact field gradient that does not compensate gravity for the atoms in the $|2, 1\rangle$ state (see also the characterization done in reference (139), which presents a similar behaviour). Below this value, atoms in the $|2, 2\rangle$ also start to fall under gravity, explaining the fast decrease in the atom number for low magnetic field gradients. At higher magnetic gradients, spin relaxation processes heat the atomic cloud, expelling some atoms until it achieves a stable configuration. In the graph in (b), the fast drop in the temperature while increasing the Spin purification time is due to a complete removal of the atoms in the $|2, 1\rangle$ prior to their transference to the magnetic trap. From 400 ms on, indicated by a blue dashed line in the figure, no significant decrease on the temperature was observed and we kept this value in the last part of this analysis.

Finally, the lifetime of the sodium atoms in the magnetic trap for the $|2, 2\rangle$ state

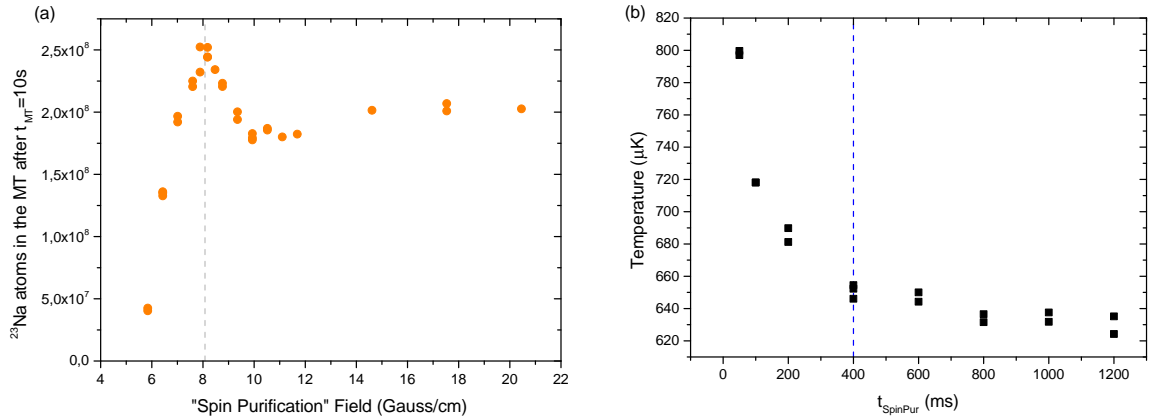


Figure 52 – Characterization of the gravity-assisted spin purification for sodium atoms. In graph (a) (resp. (b)) we present the number (resp. the temperature) of the ^{23}Na atoms trapped in the magnetic trap during $t_{\text{MT}} = 10$ s. In (a), the peak in the atom number while scanning B'_{SpinPur} corresponds to the gradient of magnetic field that exactly compensates gravity for the atoms in the $|2, 1\rangle$ state. The fast temperature decrease while increasing t_{SpinPur} is due to a complete removal of the atoms in the $|2, 1\rangle$ state after 400 ms. The temperature in (a) and number of atoms in (b), remain unchanged while performing the scan and, for simplicity, are not shown in the graphs. Source: By the author.

with and without the spin purification procedure is compared with the lifetime of the atoms in the $|1, -1\rangle$ state presented in Chapter 4. The graphs for the number of trapped atoms and the temperature of the atomic cloud as a function of t_{MT} for the three cases are presented in Fig. 53 (a) and (b), respectively. Even if the spin purified atoms (black squares) present better a lower temperature than the non-purified atoms (oranges circles), both temperatures are higher than the one measured for the atoms in the $|1, -1\rangle$ state (blue triangles). In addition to that, the ^{23}Na in the $F = 2$ states with or without spin purification presented a high atom loss and a decrease in the lifetime of the atoms in the magnetic trap.

The two effects displayed in Fig. 53 (drop in the atom number and increased temperature) deteriorated the initial evaporation of the sodium atoms such that, even without loading the ^{39}K into the magnetic trap, it was not possible to obtain the BEC of ^{23}Na atom in the $|2, 2\rangle$ state. In order to do so we should improve the optical pumping procedure and/or increase the initial atom number in the MOT and/or start with a colder cloud by performing the D_1 Gray molasses also for the sodium atoms. (163) All three solutions are not straightforward. The optimization of the optical pumping for the ^{23}Na is

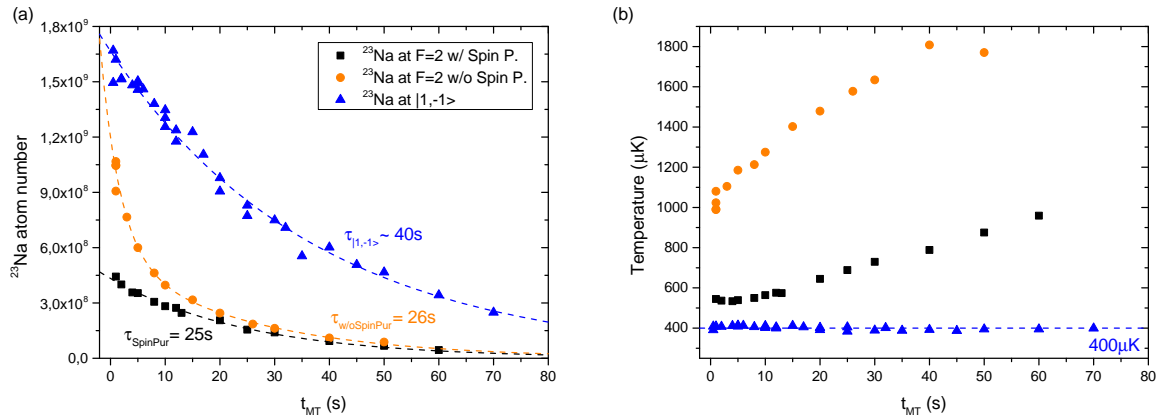


Figure 53 – Comparison between the lifetimes and temperatures of the sodium atoms in the magnetic trap trapped in the $|1, -1\rangle$ (blue triangles) and in the $|2, 2\rangle$ states, with (black squares) and without (orange circles) the spin purification. The number of trapped atoms (in (a)) and the temperature of the atomic cloud (in (b)) as a function of the time in the magnetic trap show that, even by performing the spin purification procedure, the atomic cloud in the $|2, 2\rangle$ state has less atoms, a shorter lifetime and a higher temperature when compared with the optimized atomic cloud in the $|1, -1\rangle$ state.

Source: By the author.

not an easy task and, for this reason, the majority of experiments working with trapped sodium atoms start with the $|1, -1\rangle$ state¹¹. In this sense, there are two more promising strategies that rely on increasing the atomic flux for loading the 3D-MOT¹²: (i) increase the power of the MOT laser beams, specially for the 2D-MOT; (ii) increase the atomic flux that loads the 2D-MOT by refilling the oven. These two strategies, together with the use of the Gray molasses will be implemented in the experiment after re-designing the laser system for sodium atoms.

¹¹ Once the atoms are trapped in the $|1, -1\rangle$ state, microwave radiation can selectively transfer some of the trapped atoms to other hyperfine states. (140)

¹² The short characterization performed with the Dark-SPOT of sodium atoms and presented in Chapter 4 showed that the number of atoms in the MOT would continue to grow linearly with the atomic flux.

6 A ^{23}Na BEC to generate vortex lattices

During the last months of my thesis, we decided to focus on producing a vortex lattice in the ^{23}Na BEC. Some big modifications had to be made to the experimental sequence described in Chapter 4 as, for example, the implementation of a *crossed* optical dipole trap. This trap, besides providing usual longer lifetimes and a more flexible geometry than the Plug traps, is also essential for the future plans of the experiment. These plans strongly rely on the possibility of changing the interspecies interaction with the use of magnetically-induced Feshbach resonances in order to explore different miscibility regimes. As better described in App. A, Feshbach resonances cannot be tuned in magnetic traps, since its technique consists in applying a constant magnetic field, which in most magnetic traps will just change the potential minima position. Moreover, the crossed ODTs are also vastly used in experiments studying vortices and vortex lattices produced by means of a *stirring* beam (28, 33), since the produced BECs present a pancake shape¹.

In the first section of this chapter, we discuss the necessity of adding a new type of trap to the NaK experiment in order to generate vortex lattices and, in the future, tune the interaction between ^{23}Na and ^{41}K atoms. Later, the crossed ODT trapping principles and its configuration for the NaK experiment are presented in section 6.2, followed by the characterization of the new ^{23}Na BEC obtained in the crossed trap, in section 6.3. In section 6.4, we show the optical setup for the vertical imaging system combined with the setup for the *stirring* beam, the laser beam that will be used to rotate the BEC or even “move it” by means of more complicated patterns. And finally, in section 6.5, we present the initial evidences of the nucleation of a vortex lattice in the BEC of sodium.

¹ In describing the case of rotating BECs in Chapter 3, we considered this type of geometry when doing $\omega_z \gg \omega_r$.

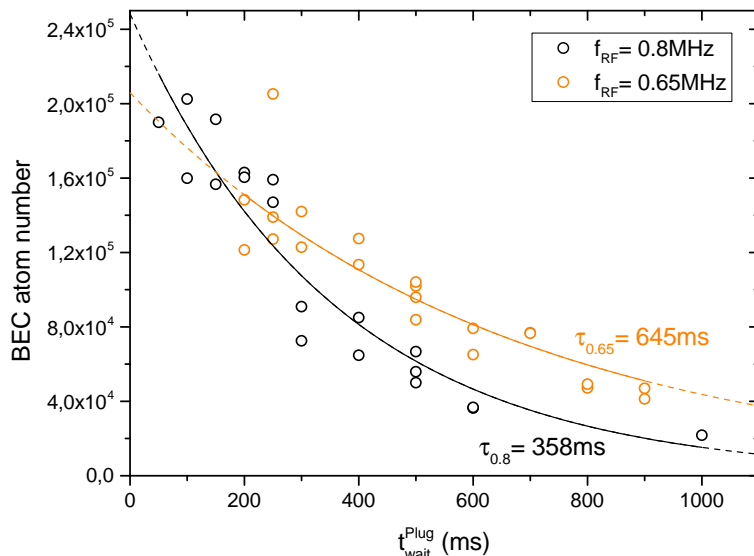


Figure 54 – ^{23}Na BEC atom number as a function of the *wait* time in the Plug trap, $t_{\text{wait}}^{\text{Plug}}$, counted from the end of the evaporation until the trap is turned off. Different final RF frequencies, leading to different BEC fractions, are shown but, in both cases, the BEC lifetime is very short, with $\tau_{\text{BEC}} < 700 \mu\text{s}$. Source: By the author.

6.1 The necessity of a new type of trap

The Plug trap used to produce the BEC of ^{23}Na atoms characterized in the end of Chapter 4 consists in the combination of a quadrupole field with a blue-detuned ODT, resulting in a harmonic potential which strongly depends on the plug beam alignment. If there is any instability (field noise, power drifts or beam position instability), the resulting potential shakes, the atomic cloud gets hotter and the BEC lifetime is compromised. In fact, we observed very short BEC lifetimes with $\tau_{\text{BEC}} < 700\mu\text{s}$, as it is shown in the graph of Figure 54. However, long-lived BECs with a high BEC fraction are desired in order to nucleate vortices and vortex lattices and one can think about using a simpler and more robust trap for confining the atoms during the end of the evaporation.

In our experiment, we decided to implement a crossed ODT since it provides a strong confinement and a good trapping configuration for generating vortices with a stirring beam (28, 33). Moreover, the NaK experiment was designed to make it possible the study of coupled vortices and further Quantum Turbulence in a two-species BEC composed of ^{23}Na and ^{41}K across its different miscibility regimes. These regimes are

only achieved if one can change the interspecies interaction. In the case of ^{23}Na - ^{41}K mixture, magnetically-induced Feshbach resonances are predicted, as discussed in App. A. Therefore, the use of pure optical traps, such as the crossed ODT, is essential in order to tune the Feshbach resonances by applying a constant magnetic field.

6.2 The crossed optical dipole trap

Optical Dipole traps composed of a single focused red-detuned laser beam with a Gaussian intensity profile, as described in section 4.4.2, have a trapping potential given by:

$$U_{\text{ODT}} = U_0 \frac{1}{1 + (x/x_R)^2} \exp\left\{-\frac{2r^2}{w_0^2} \frac{1}{1 + (x/x_R)^2}\right\}, \quad (6.1)$$

where we considered the laser beam propagating along \hat{x} . In the case of small displacements around the trapping minimum, this potential is approximately harmonic and can be written in the following form:

$$U_{\text{ODT}} \approx -U_0 \left[1 - \left(\frac{x}{x_R}\right)^2 - 2 \left(\frac{r}{w_0}\right)^2 \right], \quad (6.2)$$

with frequencies given by:

$$\omega_x = \sqrt{\frac{2U_0}{mx_R^2}}, \quad \omega_{y,z} = \sqrt{\frac{4U_0}{mw_0^2}}. \quad (6.3)$$

Usually, the radial frequencies ($\omega_{y,z}$), related with the waist w_0 of laser beam, are much bigger than the axial one (ω_x), related with the Rayleigh length x_R which is larger than the waist within the Gaussian beam approximation, and quite often the axial frequency is not strong enough to keep the atoms trapped. Even if this is not the case, the condensed atomic cloud always presents a *cigar-shaped* density distribution which is very elongated along the beam propagation direction and it is not a good geometry for studying vortices generated by a stirring beam. (28, 33) With these considerations in mind, it is common to add another ODT crossing the first one at the focus position in a configuration called *crossed* Optical Dipole trap. Supposing two ODT laser beams

travelling along \hat{x}' and \hat{y}' ², the total potential can be written as:

$$U_{\text{cross}} = U_{01} \frac{1}{1 + (x'/x_{R1})^2} \exp^{-\frac{2(y'^2+z^2)}{w_{01}^2} \frac{1}{1+(x'/x_{R1})^2}} + U_{02} \frac{1}{1 + (y'/y_{R2})^2} \exp^{-\frac{2(x'^2+z^2)}{w_{02}^2} \frac{1}{1+(y'/y_{R2})^2}}, \quad (6.4)$$

where the indices 1 and 2 represent the beam propagating along \hat{x}' and \hat{y}' , respectively.

The same harmonic approximation done for the case of a single beam ODT can be done for Eq. 6.4 such that the angular frequencies ω_i of each i -axis is given by $\omega_i = \sqrt{\sum_{j=1,2} \omega_{j,i}^2}$.

In the case of $U_{01} = U_{02} = U_0$, $w_{01} = w_{02} = w_0$ and $x_{R1} = y_{R2} = x_R$, the frequencies can be written as:

$$\omega_{x',y'} = \sqrt{\frac{2U_0}{m} \left[\frac{1}{x_R^2} + \frac{2}{w_0^2} \right]} \approx \sqrt{\frac{4U_0}{mw_0^2}}, \quad \omega_z = \sqrt{\frac{8U_0}{mw_0^2}}, \quad (6.5)$$

which presents a ratio of $\sqrt{2}$ between the frequencies. The crossed ODT depth is two times deeper than the single ODT, $U_0^{\text{cross}} = 2U_0$.

6.2.1 A crossed optical dipole trap for ^{23}Na and ^{41}K

Optical Dipole traps need a red-detuned laser beam in order to create a confining potential and are usually produced with laser beams with $\lambda = 1064$ nm due to the existence of commercial single-mode high power lasers at this wavelength. Differently from the case of the Plug barrier operating at 532 nm, an ODT, operating at 1064 nm, is going to be shallower for sodium than for potassium atoms. This is an important aspect that must be taken into account when designing the crossed ODT.

The laser used to generate the crossed ODT laser beams is a MEPHISTO with a maximum output power of 40 W. As it was discussed in the context of the Plug, in order to efficiently trap atoms at a given temperature, T , the trap depth has to be at least ten times bigger than $k_B T$. Ideally, we would like to transfer the atomic clouds from the Plug trap to the ODT at the highest possible temperature such that the system is not too strongly dependent on the plug beam alignment. However, the cloud has to be cold enough so that its size matches the ODT trapping volume and just a few atoms are lost during the transfer. By setting the ODT beam waists at $80 \mu\text{m}$ (close to the usual values

² The axes \hat{x}' and \hat{y}' are the ones indicated in Fig. 21.

	^{23}Na	^{41}K
$f_{x,y}$	362Hz	446Hz
f_z	514Hz	634Hz
U_0^{cross}	$46\mu\text{K}$	$125\mu\text{K}$

Figure 55 – Calculated values for the frequencies and the depths for sodium and potassium atoms in a crossed ODT with $P_1 = P_2 = 5.5\text{W}$ and $w_{01} = w_{02} = 80\mu\text{m}$.

Source: By the author.

used in ODTs) we could experimentally optimize the Plug-ODT transfer around $7\mu\text{K}$ for sodium atoms starting with 5.5W laser power at each beam. The optical depth and the frequencies calculated for these ODT parameters are presented in the table of Fig. 55.

The optical setup for the Mephisto laser (as for the Verdi laser) is mounted in the *experiment table* and a simple scheme is illustrated in Fig. 56. Right after the Mephisto laser output, an optical isolator is aligned to avoid retro-reflected light from returning to the laser. Later, the beam size is adjusted in order to proper match the optimum size for the AOMs of each ODT beam. The AOMs are used not only to control each beam intensity independently, but also as fast switches. After the AOM, the diffracted beam is coupled into single-mode polarization maintaining high power fibers (NKT fibers LMA-PM-15 with Shaffter & Kirchoff collimators) such that $5.5 - 5.8\text{W}$ laser power exit from the fibers. As it was done for the Plug beam, the output fiber beams are expanded and then focused at the atoms position with $w_0 \sim 80\mu\text{m}$ by a 400mm focal length lens. Mechanical shutters are placed after the fibers output and fast photodiodes are used to monitor the ODT laser powers through the leak of the dichroic mirrors that combine the ODT beams with the 3D-MOT beams around the science chamber (see Fig. 21 in Chapter 4).

6.3 The new ^{23}Na BEC produced in a *crossed* ODT

The experimental sequence for producing the BEC of sodium atoms in the crossed ODT is illustrated in the scheme of Fig. 57. Since the Plug trap has a large capture volume³

³ Due to the large capture volume, there are no big unexpected losses on transferring the atoms from the MOT to the Plug trap

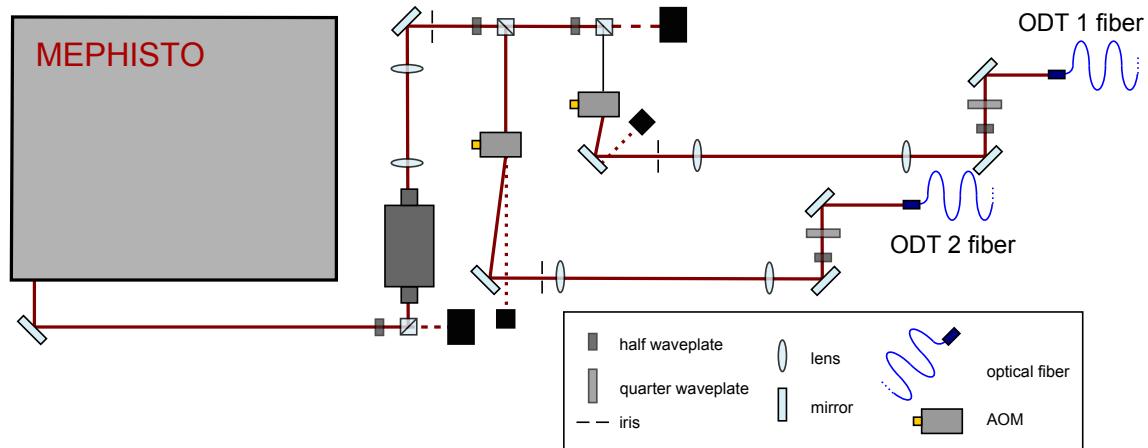


Figure 56 – Optical setup of the laser beams used to produce the crossed optical dipole trap.
Source: By the author.

and an efficient evaporative cooling that does not strongly depend on the plug beam alignment at high temperatures, we choose to keep using this trap as a first trapping stage. The RF-forced evaporation is performed and, as soon as the atoms achieve temperatures around $7 \mu\text{K}$, which corresponds to a RF-frequency of 2.0 MHz, we transfer them to the ODT by adiabatically ramping down the magnetic field during 500 ms, and then, switching off the plug beam.

With the atoms in the crossed ODT, an optical evaporation can continue to cool the atomic sample. Optical dipole traps are not “spin” selective, which means that all m_F states are equally trapped by the optical potential. Therefore, the RF-forced evaporation no longer expels the hottest atoms from the trap. Another evaporative cooling procedure, named *optical evaporation*, can be applied by slowly reducing the ODT depth, U_0^{cross} , with the reduction of the power of the ODT laser beams, as it is illustrated in Fig. 57. While performing such evaporation, one has to realize that also the trapping frequencies change during the process (see Eqs. 6.5) and that, differently from the RF-forced evaporation, the optical evaporation is a one-dimensional process that relies on the gravitational force to remove the atoms from the trap.

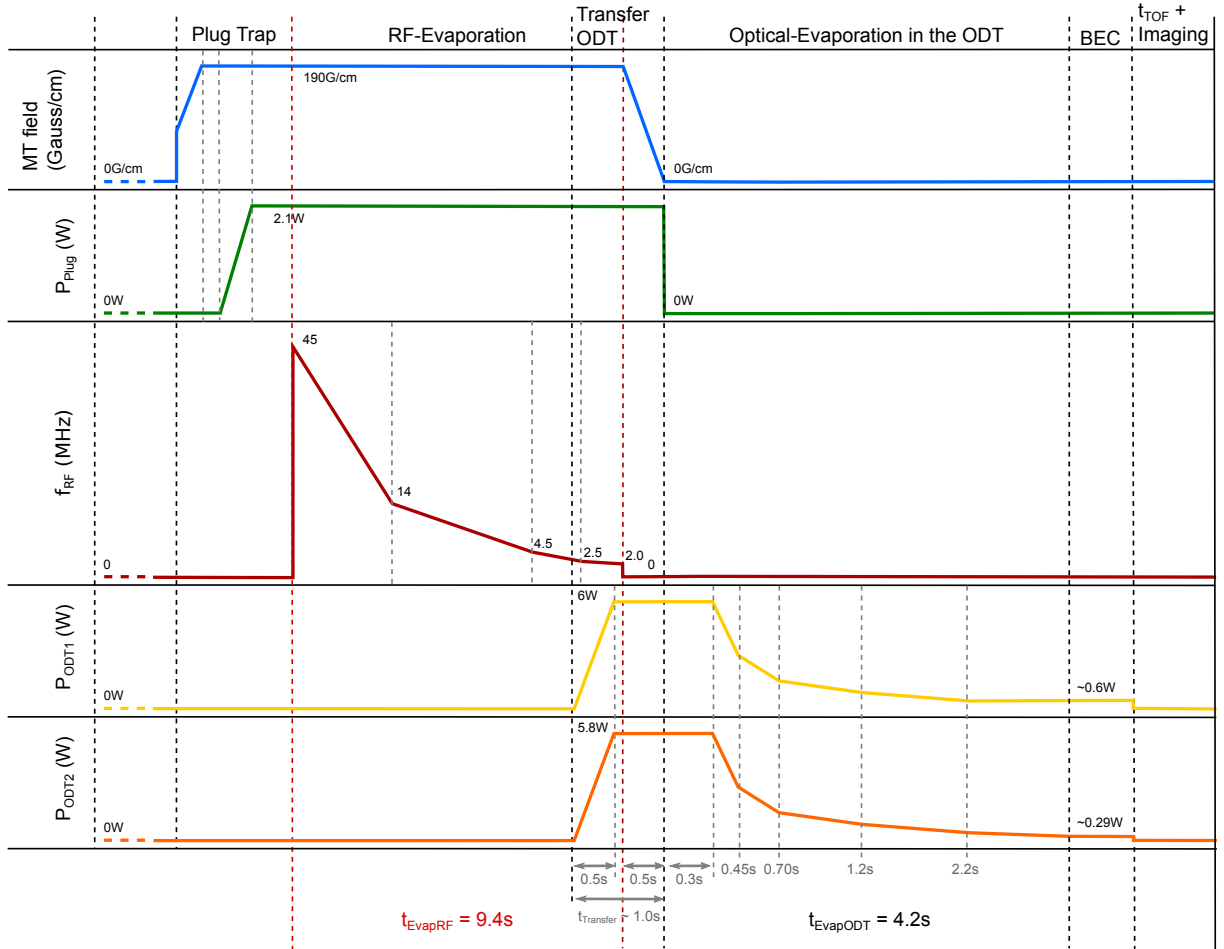


Figure 57 – Scheme of the experimental sequence used to produce the BEC of sodium atoms in the crossed ODT.

Source: By the author.

6.3.1 Characterizing the evaporative cooling in the crossed ODT

In the NaK experiment, the decrease in the ODT laser beams power is done with six linear ramps for each beam resembling an exponential decay (see Fig. 57). The total optical evaporation lasts 3.9 s and the power is finally reduced by a factor of 1/10 for the ODT1 ($P_1^{\text{final}} \approx 610\text{mW}$) and of 1/20 for the ODT2 ($P_2^{\text{final}} \approx 290\text{mW}$) with respect to each initial power. The final ODT depth for ^{23}Na atoms is $U_0^{\text{cross}} \approx 3.54\mu\text{K}$ and the resulting frequencies are $f_x = 80\text{Hz}$, $f_y = 106\text{Hz}$ and $f_z = 126\text{Hz}$ ⁴. In order to evaluate the efficiency of the different evaporative cooling processes during the experimental sequence

⁴ In order to calculate the final ODT parameters we used the beam waists obtained from their direct measurement before aligning the ODT laser beams into the science chamber, with $w_{01} = 84\mu\text{m}$ and $w_{02} = 80\mu\text{m}$.

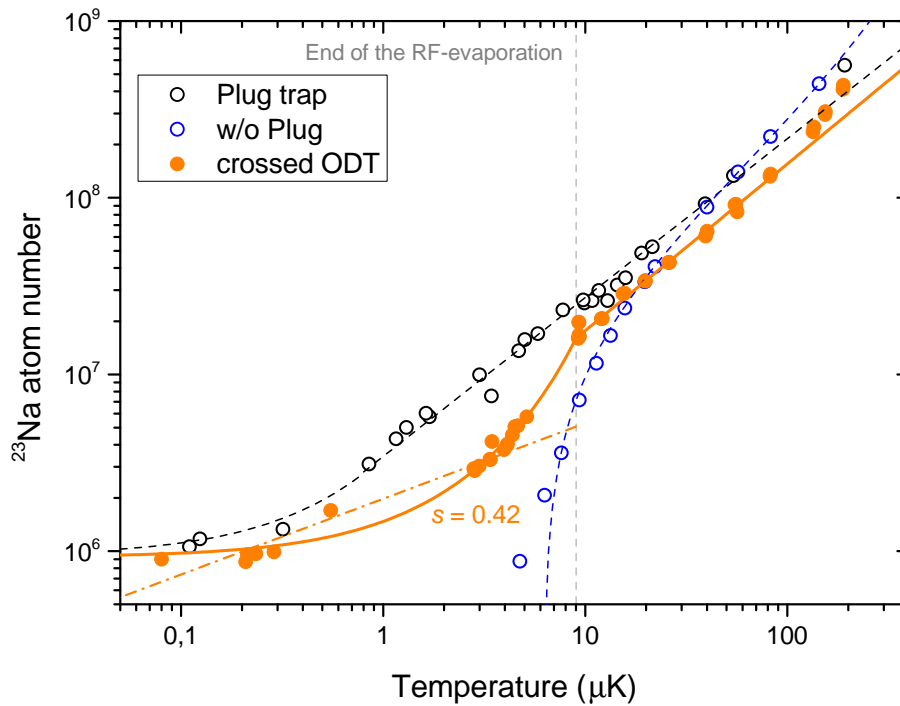


Figure 58 – Log-log graph of N vs. T for the optimized experimental sequence while producing the ^{23}Na BEC in the crossed ODT (orange curves) and in the Plug trap (black and blue curves).

Source: By the author.

we can, as it was done for the case of the Plug trap, look for the behaviour of the total number of trapped atoms as a function of the temperature, and define a dependence of the form $N \propto T^s$, with $s < 1$ for the process to be efficient⁵. In Fig. 58 we present the log-log curves of N vs. T for the sodium BEC produced in the crossed ODT (in orange) in comparison with the already characterized curves for the Plug trap (in black and blue).

The N vs. T curve for the ODT experimental sequence follows the behaviour of the optimized N vs. T curve for the Plug trap (in black) up to the end of the RF-evaporation (indicated by the gray dashed line in the graph) where the atoms are transferred to the crossed ODT. Even after optimizing the transference Plug-ODT, some atoms are lost, as it can be seen in the abrupt decrease on the atom number as soon as we cross the gray line. Another interesting feature is that the log-log curve of N vs. T is no longer linear when we enter in the ODT region. This can be justified by the presence of three-body losses at the beginning of the ODT due to its large atomic densities. These losses quickly

⁵ See the discussion presented in section 4.5.1 of Chapter 4.

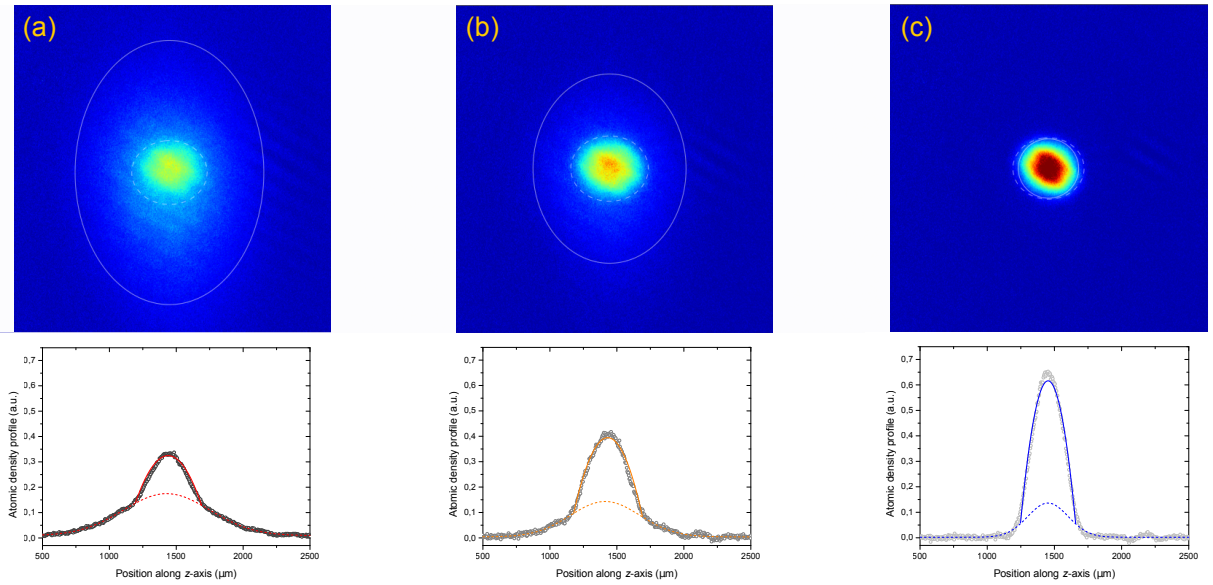


Figure 59 – Bimodal density profile for the atomic cloud in the crossed ODT at different steps of the evaporation. The image in (a), after the first evaporation ramp, the image in (b), after the third ramp, and image in (c) after the full optical evaporation for which we obtain an almost pure BEC with $T < 80$ nK.

Source: By the author.

reduce the number of trapped atoms until a limiting value is reached for which they are suppressed, such that the final part of the optical evaporation presents $s \leq 0.42$, as indicated in Fig. 58.

6.3.2 Characterization of the ^{23}Na BEC produced in the crossed ODT

By the end of the optical evaporation, we obtain an almost pure BEC with $8 - 10 \times 10^5$ atoms at less than 80 nK. As for the BEC in the Plug trap, the appearance of the bimodal density profile presented in Fig. 59, indicates the onset of condensation. The images were taken after $t_{\text{TOF}} = 20$ ms at different steps of the optical evaporation: the image in (a), after the first evaporation ramp, the image in (b), after the third ramp, and image in (c) after the full optical evaporation for which we obtain an almost pure BEC.

When comparing the sizes of the condensed cloud obtained in the Plug trap and in the crossed ODT for a fixed t_{TOF} , it is clear that in the latter the BEC has a smaller size,

which is consistent with the lower frequencies of the ODT⁶. We can measure the trapping frequencies of the crossed ODT by exciting parametric oscillations (as done for the Plug trap) when modulating the power of one of the ODT laser beams. In our case, we choose to modulate the ODT2 such that $P_2(t) = P_2^{\text{final}}[1 + \delta P \sin(2\pi f_{\text{mod}}t)]$. The temperature of the atomic cloud as a function of the modulation frequency is presented in Fig. 60 (a). One can clearly identify five peaks at different frequencies which are related with the ODT frequencies as $f_{x'} \approx 80$ Hz, $f_{y'} \approx 106$ Hz and $f_z \approx 128$ Hz, in a very good agreement with the previously calculated frequencies. In addition to the parametric excitation, we can perform a dipole excitation of the atomic cloud along the \hat{z} -axis by a fast switching OFF-ON of the ODT laser beams. In our case, the trap was kept off for 2 ms, time during which the atoms fall under the action of the gravitational force. When turning the ODT on again, the atomic cloud has acquired a center of mass velocity making the whole cloud to oscillate in phase inside the potential. This oscillation will affect the position of the cloud measured in time-of-flight and displayed in the graph of Fig. 60 (b). The cloud center of mass position along \hat{z} presents a very nice sinusoidal behaviour with frequency $f_z = 128.2$ Hz in a very good agreement with the result obtained from the previous method.

Finally, the lifetime of the BEC can be measured for different condensed fractions. The number of condensed atoms (N_{BEC}) as a function of the wait time in the ODT after the end of the optical evaporation ($t_{\text{wait}}^{\text{ODT}}$) for $N_0/N = 0.64$ and $N_0/N = 0.52$ are shown in Fig. 61. In contrast with the previous lifetimes measured for the BEC obtained in the Plug trap (see Fig. 54), the lifetime for the BEC in the crossed ODT is over ten times longer with $\tau_{\text{ODT}}^{\text{BEC}} = 8.3$ s and does not depend on the condensed fraction. This is already a very good lifetime for performing the stirring technique since, during the typical times for which the BEC is stirred ($t_{\text{stirring}} = 600\text{ms}$), its number of atoms remains practically constant. An additional thermalization time is normally needed and it can vary from 100 ms to 2 s (54) depending on the study one wants to perform. But, even considering a total stirring time of 3 s, less than half of the atoms would be lost and we can start the

⁶ The calculated frequencies for the Plug trap are (213,651,369)Hz (see Chapter 4).

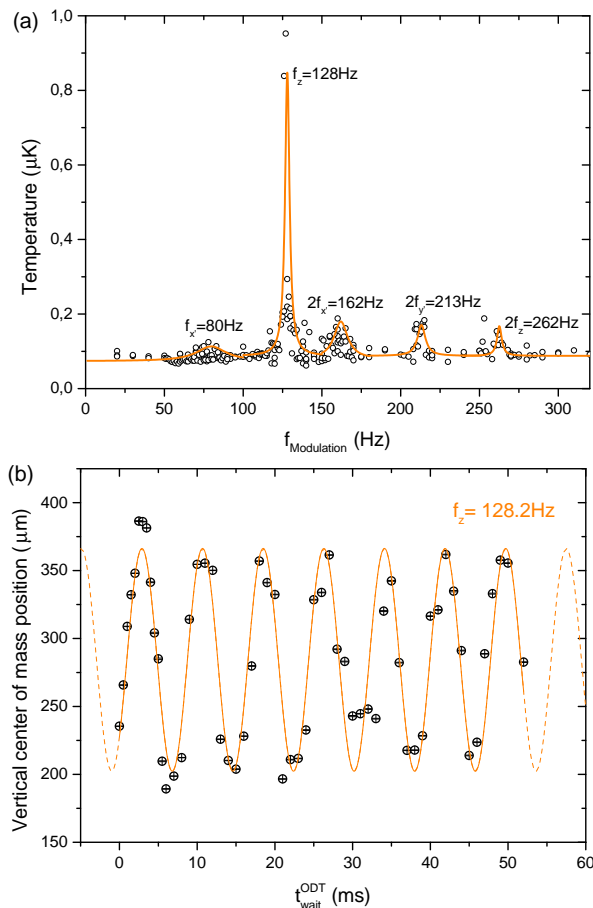


Figure 60 – (a) Temperature of the atomic cloud as a function of the modulation frequency of the ODT2 laser beam when exciting the parametric oscillations. Each peak in the temperature is related with the indicated frequency of the crossed trap. In (b), an additional measurement of the frequency along \hat{z} is presented for which the dipole oscillation along this direction was excited.
Source: By the author.

first attempts in generating the vortex lattice in the BEC of sodium atoms without the need of further improving its lifetime⁷.

6.4 The vertical imaging and the stirring beam systems

The *stirring* beam technique (28,33) that consists in the addition of a blue-detuned laser beam rotating around one axis of the trap that confines the BEC, will produce an effective time-dependent potential that rotates the BEC in strong analogy with the

⁷ A simple way to improve the lifetime of the BEC of ^{23}Na atoms obtained in the crossed ODT is to stabilize the ODT laser beam powers by setting a feedback loop control with a fast logarithmic photodiode and a PID control.

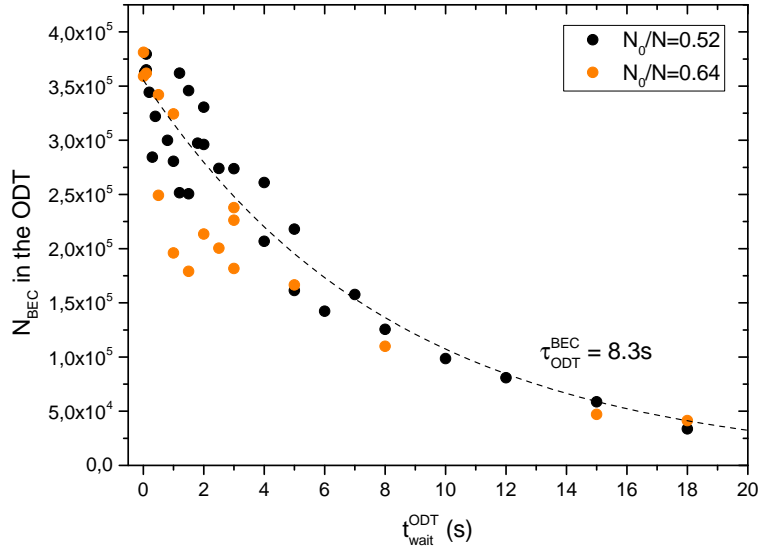


Figure 61 – Lifetime of the condensed cloud in the crossed ODT obtained from the graph of N_{BEC} as a function of the wait time in the ODT, $t_{\text{wait}}^{\text{ODT}}$.

Source: By the author.

rotating bucket experiments performed in liquid ^4He . Therefore, the model derived in Chapter 3 in the context of rotating BECs can be directly applied in this case.

The *stirring* technique is better performed in a “pancake” trap with $\omega_z \gg \omega_{x,y}$ in which the stirring beam is rotated along the strongest confining axis, given by the \hat{z} -axis. In the case of our previous characterized crossed optical dipole trap, $\omega_z = 2\pi \times f_z > \omega_{x,y}$. Even if the BEC cloud does not have a truly pancake-shape⁸, it can still be stirred along \hat{z} in order to nucleate vortices. When rotating the BEC along one direction, the nucleated vortices are all aligned with this direction and, in order to see them, the image of the atomic cloud has to be done along the same direction of the stirring beam. Until this section, all the images taken from the atomic cloud were done along the horizontal direction that coincides with the plug beam direction, as it is illustrated in Fig.21 of Chapter 4. In order to add the stirring, a vertical imaging system that will be used to image the atoms into a CCD and to focus the stirring beam in the atomic cloud had to be designed and implemented. In this section, we first describe the vertical imaging system in 6.4.1, followed by the description of the optical setup used for producing the stirring beam in 6.4.2.

⁸ In our experiment, the ratio between the axial frequency (f_z) with the radial frequencies ($f_{x,y}$) is just equal to $f_z/f_x(f_y) = 1.6(1.2)$ while in other experiments it can be equal to 6 or more. (54)

6.4.1 The vertical imaging system

The optical setup for the vertical imaging system and for producing the stirring beam is illustrated in Figs. 62 and 63. In the first, we show a cross-section view of the vertical MOT beam (represented in light yellow), the imaging beam (in dark yellow) and the stirring beam (in green) around the science chamber. In the second, we present a scheme of the imaging and the stirring laser systems mounted in a new optical table, named *vertical imaging table*, which was added to the *experiment table* above the science chamber.

The vertical imaging system has a magnification of 4, which is obtained by combining an achromatic 75 mm focal length lens (Thorlabs AC508-075-A) with a 300 mm focal length lens (Thorlabs LA1256-A) broad coated such it could be used for light with wavelength of 532 nm (stirring beam), 589 nm (sodium imaging and MOT beams) and 767 nm (potassium MOT beams). A custom designed dichroic mirror combines the vertical imaging beam with the stirring, as illustrated in Fig. 62. The first lens, positioned at 67 mm above the center of the science chamber, focus the vertical beams coming from below (imaging and MOT beams), near a wire-grid polariser that reflects one linear polarization and transmits the other perpendicular polarization. The vertical imaging beam and the MOT beams have opposite circular polarization such that, by adjusting the angle of the indicated quarter-waveplate, the MOT beams are reflected by the wire-grid polariser while the imaging beam is transmitted. Both 3D-MOTs (for sodium and potassium) were almost not affected by the change of their vertical beam optical setup. This whole setup (lens, quarter-waveplate and wire-grid polariser) is mounted in a case made out of Delrin⁹ and placed on a translational stage such that it can be moved in order to adjust the focus of the vertical image.

In Fig. 64, we show two *in situ* images ($t_{\text{TOF}} = 0$) of the crossed ODT before evaporation in order to compare the images obtained with the horizontal imaging system (in (a)) and with the vertical imaging system (in (b)). In both images, we show the

⁹ This is the same material used to build the case of the Quadrupole coils described in Chapter 4

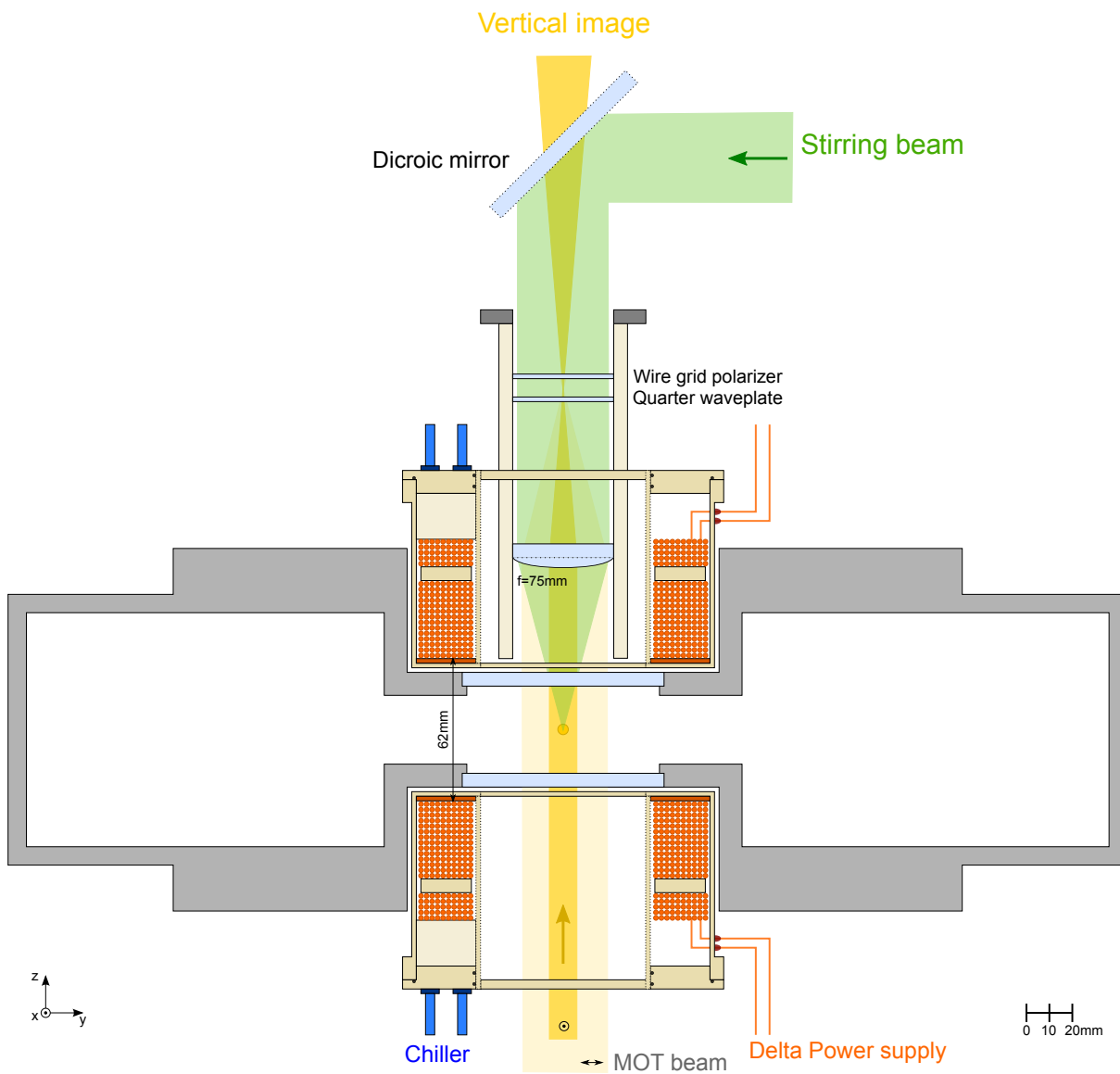


Figure 62 – Cross-section view of the vertical MOT beam (represented in light yellow), the imaging beam (in dark yellow) and the stirring beam (in green) around the science chamber. The atoms position is indicated by a yellow circle in the center of the SC. The upper and lower Quadrupole and Levitation coils, better described in App. C, are also displayed. A 75 mm focal lens is used as the first lens on the vertical imaging system and to focus the stirring beam at the center of the atomic cloud. The polarization of the MOT, imaging and stirring beams are adjusted such that the wire-grid polarizer reflects the MOT beam and transmits the vertical imaging and the stirring beams.

Source: By the author.

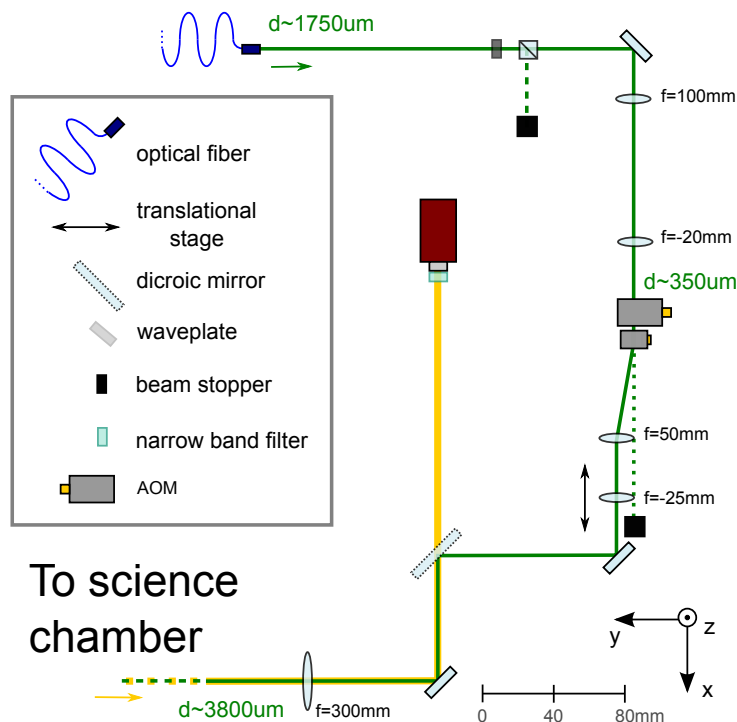


Figure 63 – Scheme for the optical system of the stirring beam. The focal length of the lenses used to adjust the size of the stirring beam, as well as its size at each step of the optical system are indicated.

Source: By the author.

complete image captured for the CCD. It is easy to see that the image taken along the vertical direction (with $M_{\text{vert}} = 4$) is more than two times larger than the one taken along the horizontal (with $M_{\text{NaK}} = 1.6$). Moreover, in Fig. 64 (b) it is possible to see each beam from the crossed ODT and optimize its alignment with the center of the Plug trap right before transferring the atoms.

6.4.2 Characterizing the stirring beam

The stirring beam optical setup illustrated in Fig. 63 was designed in order to produce a stirring beam with $w_0^{\text{stirring}} \approx 7 \mu\text{m}$ aligned at the center of the atomic cloud. The light used to produce the stirring beam is generated by the same Verdi V10 laser used to generate the Plug beam. About 100 mW of the laser power is coupled to a polarization maintaining optical fiber such that around 60 mW arrives at the vertical imaging table. In order to stir the laser beam in the atomic cloud, we align two crossed AOMs, named *vertical* and *horizontal* stirring AOMs, very close to each other as it can

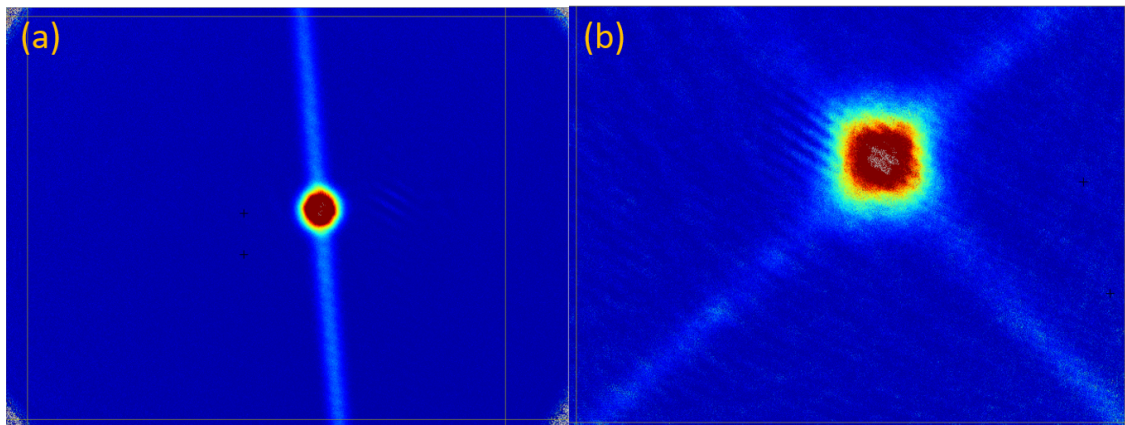


Figure 64 – *In situ* images of the sodium atoms in the crossed ODT taken along the horizontal (a) and vertical (b) directions. Besides the difference in the sizes of the atomic clouds (the vertical imaging system presents a magnification of $M_{\text{vert}} = 4$ while the horizontal imaging system have $M_{\text{NaK}} = 1.6$) it is also possible to see each beam from the crossed ODT, improving its alignment.
Source: By the author.

be seen on the picture presented in Fig. 65 (a) and (b). The diffracted order from the first AOM (*horizontal*) is once again diffracted by the second AOM (*vertical*) such that a two-dimensional diffraction pattern can be produced, as illustrated in (c) of Fig. 65. This two-times diffracted beam (indicated in the figure) is collimated at a bigger size (with $d_{\text{stirring}} \approx 3800 \mu\text{m}$) by a set of three lenses with the last one being the second lens of the vertical imaging system (see scheme in Fig. 63). Finally, the stirring beam is focused at the center of the atomic cloud by the first lens of the vertical imaging system with a predicted waist of $7 \mu\text{m}$.

In working with AOMs, the diffraction angle of the diffracted beam is proportional to the RF-frequency that modulates the crystal inside it, such that the position of the diffracted beam at an specific plane positioned, for example, at the center of the atomic cloud, can be controlled by adjusting this frequency. By continuously changing the frequencies of both AOMs, two-dimensional figures can be drawn by the diffracted beam at its focal plane. If the change on the frequencies oscillates around a central frequency with fixed rate, f_{vert} and f_{horiz} for the vertical and the horizontal AOMs', respectively, Lissajous figures can be drawn by the *stirring* beam on the atomic cloud. In order to characterize the Lissajous figures that could be created with our setup, we mimic the

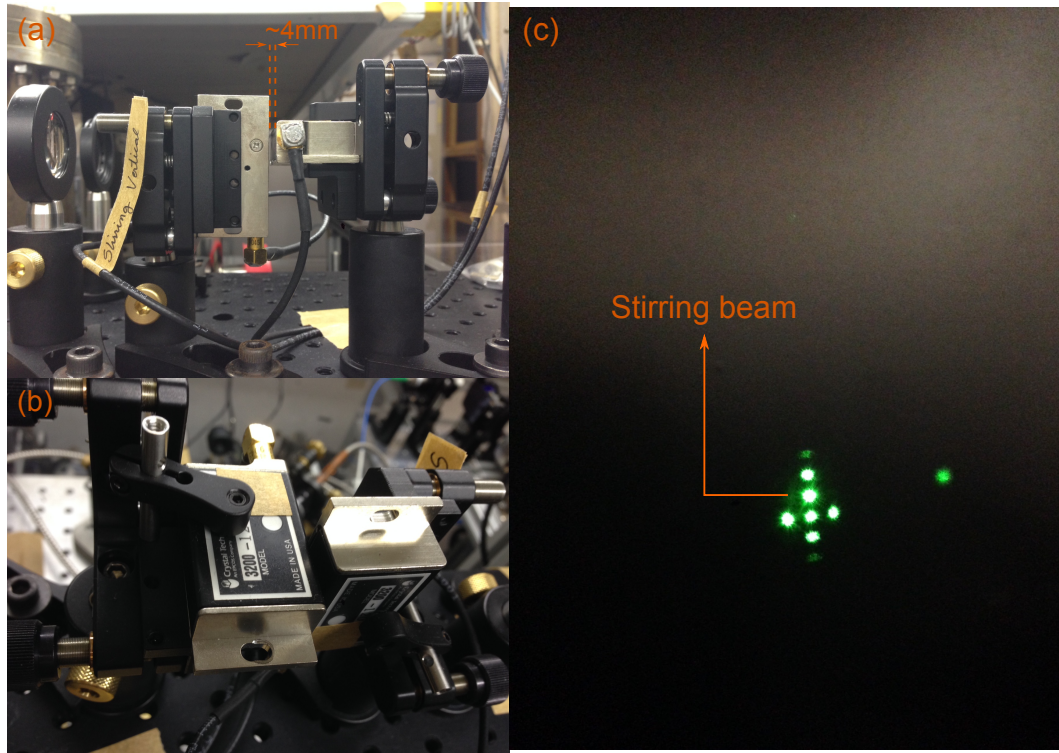


Figure 65 – In (a) and (b) we show pictures of the crossed AOMs used to produce the stirring beam and in (c) a picture of the diffracted pattern after the previous setup. The separation between the AOMs is of around 4 mm in order to avoid misalignments in the second AOM while modulating the first. In (c), the principal diffracted used for the stirring is indicated.

Source: By the author.

beam at the center of the atomic cloud by focusing it outside the science chamber with a 400 mm focal length lens. We imaged the beam and the formed figures while modulating the AOM frequencies at its new focal plane with a beam profile (Thorlabs BC106N-VIS). The exposure time of the beam profile was set to be larger than 500 ms in order to integrate the intensity of the moving beam, such that a steady figure could appear in the resulting image. The modulation amplitude of each AOM frequency was kept the same and in Fig. 66, we present the Lissajous figures produced by setting different modulation frequencies ratios $f_{\text{vert}}/f_{\text{horiz}}$ for four modulation amplitudes: 1.0 V, 2.0 V, 3.0 V and 4.0 V. The expected Lissajous figures are drawn in the right column, which are very similar to the figures produced by the stirring beam. The modulation frequencies were varied between 25 Hz and 75 Hz and the effect of less power in the extremes of the figures can be explained from the decrease in the AOM coupling efficiency as we achieve frequencies far from its nominal operating frequency.

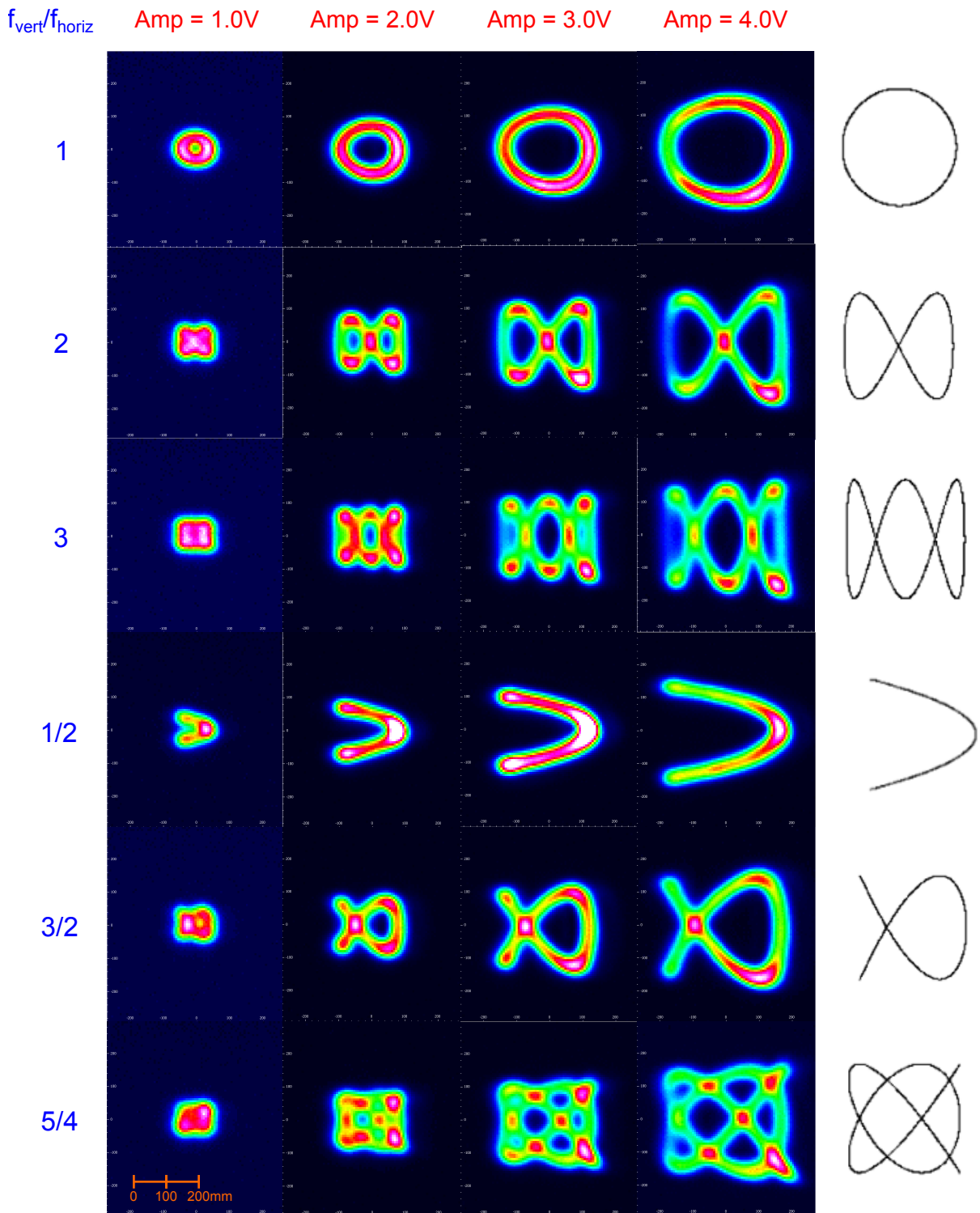


Figure 66 – Lissajous figures produced by the stirring beam and imaged by a beam profile. The ratio between the modulation frequencies of each AOM was varied as well as the modulation amplitudes. In the right column it is drawn the expected Lissajous figures for each frequency ratio. The figures produced by the stirring beam reproduces with a very good quality the predicted Lissajous figures.
Source: By the author.

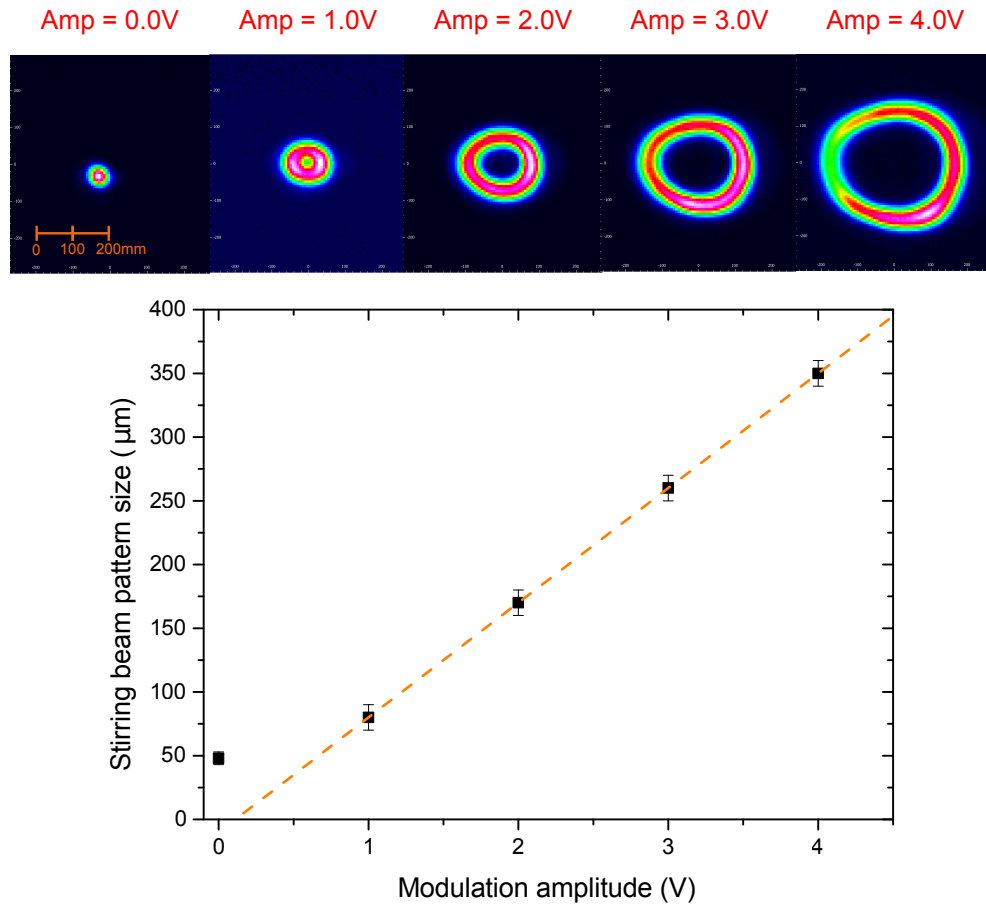


Figure 67 – Size of the Lissajous figures produced for $f_{\text{vert}}/f_{\text{horiz}} = 1$ as a function of the modulation amplitude. As expected, the size of the Lissajous figures increases linearly with the modulation amplitude at a ratio of $90 \mu\text{m}/\text{V}$.

Source: By the author.

In the previous image, a 400 mm focal length lens was used in order to focus the stirring beam into the beam profile. This was done since the expected waist while focusing the stirring beam with the 75 mm focal length lens of the imaging setup would be too small for the beam profile to image. However, an estimation of the size of the figures generated by the real stirring setup can be done by scaling their sizes to the proper focal length. For example, the waist of the beam when focused by the 400 mm focal length lens was of $\approx 48 \mu\text{m}$, which gives $\approx 9 \mu\text{m}$ for the 75 mm lens. The same scaling can be done for the size of the Lissajous figures as a function of the modulation amplitude. In Fig. 67, we plot this relation for the sizes for the Lissajous figures produced for $f_{\text{vert}}/f_{\text{horiz}} = 1$. As expected, the size of the Lissajous figure increases linearly with the modulation amplitude with a ratio of $90 \mu\text{m}/\text{V}$. Re-scaling it for the real stirring setup, one finds $16 \mu\text{m}/\text{V}$.

The alignment of the stirring beam in the atomic cloud is much more difficult than the alignment of the Plug beam described in Chapter 4. Two main reasons contribute to this fact: first, the stirring beam has a waist around four times smaller than the one of the Plug beam and second, the stirring beam travels in the opposite direction than the vertical imaging beam and cannot be imaged into the CCD. All we are able to see from the stirring beam is the hole it produces in the atomic cloud due to its repulsive potential. It is important to point out that in this situation, we can only perform a very indirect measure of the beam waist. Even though, by taking an absorption image of the BEC in the crossed ODT with $t_{\text{TOF}} = 1$ ms and keeping the stirring beam on during the free fall, we were able to obtain $w_0 \approx 8 \mu\text{m}$, in good agreement with our estimations.

In addition to the measurement of the stirring beam waist, it is possible to see its movement along the two plane axis of the atomic cloud, \hat{x} and \hat{y} . The calibration in terms of the analogue control was also in a very good agreement with our previous estimations, obtaining $\sim 13 \mu\text{m}/\text{V}$ in both directions. Finally, in order to produce the vortex lattice in the ^{23}Na BEC, the stirring beam should be rotated around the atomic cloud. We simulate its rotation and mapped its position for different angles of a circle with fixed radius. In Fig. 68, we show a series of images taken while performing a circle with radius of $\sim 40 \mu\text{m}$ at different angles. The dashed circle is a reference for the eye and it is at the same position in all images. Even if the atoms get dislocated from image to image due to the presence of the stirring, the hole done by the stirring beam (which means, the stirring beam position) always fall in the dashed circle. The central image shows the stirring beam positioned at the center of the cloud.

The expected *in situ* radii of the ^{23}Na BEC in the crossed ODT can be obtained from the expression for the Thomas-Fermi radii (Eq. 2.25) presented in Chapter 2. Considering $N = 6 \times 10^5$ atoms (a low BEC atom number for our experiment) and using the measured frequencies presented in section 6.3, we obtain the TF radii $R_x \approx 13 \mu\text{m}$, $R_y \approx 17 \mu\text{m}$ and $R_z \approx 10 \mu\text{m}$. The BEC size in each axis will then be given by twice these radii and the stirring beam pattern has to be drawn inside this region. Therefore, we will be able to use small modulation amplitudes (< 2.0 V), which will cause less fluctuations

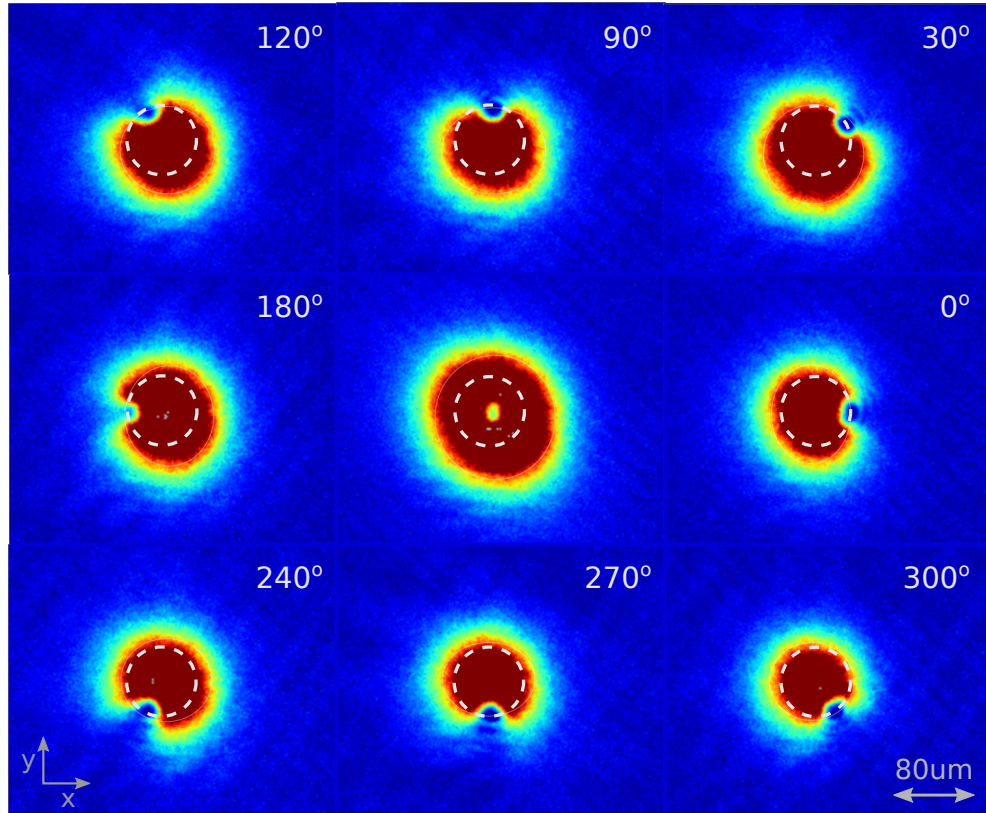


Figure 68 – Mapping of the stirring beam position in the ^{23}Na BEC while simulating a circle with radius of $\sim 40 \mu\text{m}$. The hole in the BEC represents the stirring beam position which fall always in the dashed circle. The central image shows the stirring beam positioned at the center of the atomic cloud.

Source: By the author.

on the laser beam intensity. In fact, in the images shown in Fig. 68, an amplitude of 3.0 V was used and we see that the stirring beam is at the very edge of the BEC.

6.5 Initial evidences of a vortex lattice

The initial attempts towards the nucleation of vortices in the ^{23}Na BEC characterized in this Chapter started to be performed in our laboratory as soon as we finished the characterization of the stirring beam. Some changes were done in the evaporation procedure¹⁰ in order to obtain an almost pure BEC with the same radial frequencies (with $f_x = f_y \approx 107\text{Hz}$) which has a more suitable geometry to be rotated. A first stirring sequence was developed following the parameters from previous works with rotation by a

¹⁰ In order to change the trapping frequencies of the BEC, we changed the final power of the crossed ODT beams and let the atoms thermalize for a longer time, around 1 s, assuring the achievement of an almost pure BEC due to a natural evaporation of the hottest atoms.

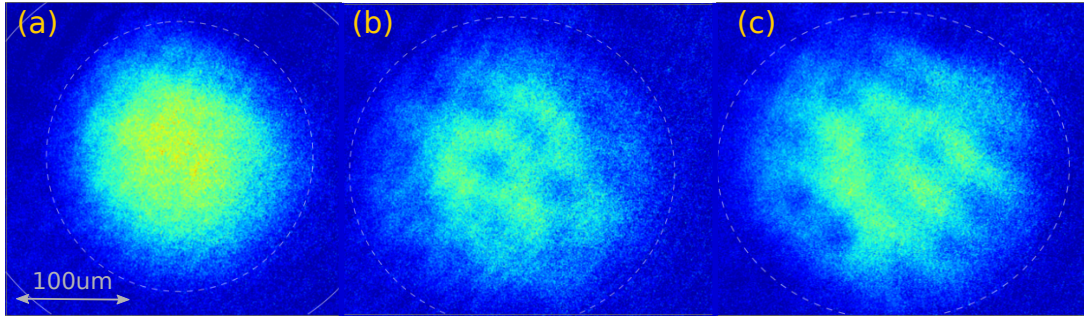


Figure 69 – Recently achieved vortex lattice in the BEC of sodium atoms. All images were taken with the vertical imaging system after $t_{\text{TOF}} = 30$ ms. In (a), we show the static BEC with $N = 6 \times 10^5$ atoms and in (b) and (c), the rotated BEC for $f_{\text{stir}} = 80$ Hz and $t_{\text{hold}} = 100$ ms.
Source: By the author.

stirring beam. After the end of the evaporation, the stirring beam laser power is ramped up during 100 ms up to $75 \mu\text{W}$. During this time, the stirring is already rotating around the BEC. The BEC is rotate for another 1 s at full stirring beam power, before decreasing it during other 50 ms. After the stirring beam is off, the atoms are kept trapped for a variable hold time in order for the vortex lattice to be formed. Then, the atomic cloud is imaged after a time-of-flight of 30 ms, enough to observe the vortices.

In Fig. 69, we show three images taken with the vertical imaging system after $t_{\text{TOF}} = 30$ ms. In (a), we show the static BEC with $N = 6 \times 10^5$ atoms. In (b) and (c), it is illustrated two very poor images recently obtained in our laboratory that indicates the nucleation of vortices and the formation of a vortex lattice. These images were obtained following the procedure described above for $f_{\text{stir}} = 80$ Hz and $t_{\text{hold}} = 100$ ms. The less denser regions forming “holes” in the atomic cloud represent the vortices. Besides these holes, the atomic clouds in (b) and (c) have bigger radius which is also an evidence that the atoms are rotating. As discussed in Chapter 3, while rotating a harmonically trapped Bose-Einstein condensate, the effective radial trapping frequency decreases with the rotation frequency due to the induced centrifugal force.

In order to observe a clear and unambiguous evidence of the formation of a vortex lattice, we should improve the quality of the vertical imaging system, which also essential for the future studies we aim to develop in this new experiment. The efforts to improve the vertical image are now being performed in our laboratory.

7 Conclusions and prospects

In this Chapter, we summarize the main conclusions of the work presented in this thesis and the prospects for the recently built NaK experiment.

7.1 Conclusions

During these last years, our group has been developing a series of works related to the nucleation of quantized vortices in atomic Bose-Einstein condensates composed of ^{87}Rb atoms in which the vortex nucleation procedure (40), the vortex dynamics (35,36,168) and its evolution to a Quantum Turbulent regime (37–39,41) were extensively characterized. These results are summarized in a recent review. (44)

It is in this context that this thesis is inserted. The main motivation for the work developed during the time of this PhD was the possibility to extend such studies, not only to different atomic species, but also to a two-component BEC composed of ^{23}Na and ^{41}K atoms. In such a system, due to the possibility of changing the interspecies interaction, new regimes of coupled vortices and vortex lattices are expected to occur, enriching the previous studies. The main results in this context can be summarized as follows.

1. In Chapter 2, we describe the properties of the ground-state of a two-component BEC with tunable interspecies interactions. The appearance of different miscibility regimes for which the two components overlap (miscible) or remain phase separated (immiscible) changes the ground state of the system (96) and, consequently, its properties. The complete miscible-immiscible phase diagram for trapped cold atomic gases remains not fully characterized.
2. Due to the existence of different miscibility regimes in a two-component BEC, the properties of coupled vortices and vortex lattices (and eventually, Quantum Turbulence) are expected to change, as it was discussed in Chapter 3. The few experimental results dealing with this subject (54,69) cover just a small part of the miscibility

phase-diagram.

In order to verify the theoretical conclusions presented above, a new experimental system had to be designed and built from scratch such that the second part of the main results reported on this thesis is related to the construction of such experiment. These results are listed in the following.

1. Complete development and characterization of the actual status of the experimental system for producing vortices and vortex lattices in the two-component ^{23}Na - ^{41}K BEC with tunable interactions (vacuum system, laser systems, Plug trap and ODT configurations, control program, imaging system, stirring beam setup and Feshbach field system).
2. Efficient production of a cold cloud of ^{39}K atoms by implementing the Gray molasses cooling procedure. As described in Chapter 5, we obtained a final atomic cloud with 2×10^7 atoms at $57 \mu\text{K}$ prior to the magnetic trap.
3. Initial attempts on working with the two atomic species. In the two-species MOT, light-induced losses limited the potassium atom number (see section 5.5.1). Therefore, the two-stage MOT loading procedure was implemented allowing us to trap both species in the magnetic trap. However, losses were once again observed (see section 5.5.2) since the atomic species were at different hyperfine levels. In order to properly cool ^{23}Na and the bosonic isotopes of potassium, we should work with both species at the $|2, 2\rangle$ hyperfine state. When performing the optical pumping procedure for the sodium atoms, we lost a considerable amount of the trapped atoms such that we could not cool it efficiently without increasing its initial atom number (see discussion on section 5.5.3).
4. Production of the Bose-Einstein condensate of ^{23}Na atoms in the Plug-type trap with around $5 - 10 \times 10^5$ condensed atoms at less than 100 nK.
5. Production of a long-lived BEC of ^{23}Na atom in the crossed optical trap. Almost pure BECs with 8×10^5 atoms at less than 80nK were observed. The measured BEC

lifetime was of about 8 s is certainly long enough for performing the first experiments on stirring the BEC.

6. Implementation of the stirring beam into the NaK experiment in order to be able to nucleate vortices and vortex lattices in the single ^{23}Na BEC and further, in the two-component Bose-Einstein condensate.
7. Initial evidences of the nucleation of a vortex lattice in the BEC of sodium atoms produced in the crossed optical dipole trap.

7.2 Prospects

Some of the interesting perspectives for the NaK experimentis experiment, which motivated its construction, were already listed in the main part of this thesis and, in this part, we start by recovering their most interesting aspects. Next, longer term perspectives are presented in which the coupled vortices play a central role in searching for new physical phenomena.

Miscible-immiscible phase diagram for a trapped two-component BEC

In this research line, the main objective is to perform a complete characterization of the miscible-immiscible phase diagram for trapped Bose-Einstein condensates. As previously discussed in Chapter 2, a complete characterization to all the possible miscibility regions is still missing in the context of cold atomic samples. The possibility of changing the interspecies interactions between ^{23}Na and ^{41}K by means of magnetically induced Feshbach resonances, make the NaK experiment a good candidate to perform such characterization. Therefore, the first step in this direction is the production of the two-component BEC of ^{23}Na and ^{41}K , which is likely to be achieved within the next months. Later, the characterization of the corresponding interspecies Feshbach resonances, not yet described in the literature, will give an intermediate result and the tools for scanning the miscibility regions. Finally, by changing the interspecies interaction and the ratio between the number of particles in the two-component BEC ($N_{\text{K}}/N_{\text{Na}}$), we expect to observe the

miscible and phase-separated regimes in the internal and external overlap configurations described in section 2.3.4.

Vortices and vortex lattices in a two-component BEC

In this second research line, the main objective is to study the nucleation of vortices and vortex lattices and its dynamics in a two-component trapped Bose-Einstein condensation in the different miscibility regimes. The expected vortices and vortex lattice configurations considering atomic species with different mass near the Na-K mass ratio ($N_{41\text{K}}/N_{23\text{Na}} = 1.78 \approx 2$) were presented in Chapter 3 for different interspecies scattering lengths, $a_{12} > 0$ (with $\Delta > 0$, for the miscible and $\Delta < 0$, for the immiscible cases) and $a_{12} < 0$ (with $\Delta > 0$).

Besides the possibility of studying the vortex configurations in all the miscibility regimes, the NaK experiment could also provide some new phenomena while studying their dynamical properties. In particular, a great interest is directed to study the decay of coupled vortex lattices in the regime of $a_{12} < 0$ and $\Delta > 0$. At this regime and under some specific parameters (such as the rotation frequency of the BEC in order to produce the vortex lattice), double-charged vortex lattices could be stabilized in one of the two-species (in our case, in the potassium BEC). By following the initial observations of the decay of a vortex lattice in a two-component BEC performed by Schweikhard et al. in (69) and the theoretical proposal of the decay of a multi-charged vortex presented by Cidrim et al. in (169), a Quantum Turbulent regime could be expected for such systems.

New strategies for generating Quantum Turbulence

The study of Quantum Turbulence in trapped atomic clouds was initiated by our group in 2009 in a BEC of ^{87}Rb atoms. Since then, other groups have also investigated the phenomena in slightly different configurations: first, in a two-dimensional system (42) and recently in a homogeneous BEC. (43) However, the mechanisms used in all these experiments are not suitable for the controlled generation of QT in the NaK experiment. The last two mechanisms strongly rely on the symmetry of the trapping potential (2D and

box-like, respectively) and cannot be applied to the crossed dipole trap used for producing our two-component BEC. On the other hand, for the studies performed by our group, the Quantum Turbulent regime was achieved by introducing an oscillatory perturbation to the magnetic field that confined the atoms, which was able to not only displace but also rotate the atomic cloud. Such mechanism did not show to be as reproducible as it should be in order to properly characterize the properties of QT.

The search for a new strategy in generating Quantum Turbulence started in our group with the theoretical study of the decay of a multi-charged vortex. (169) In a two-dimensional system, this decay can give rise to a turbulent regime. However, the nucleation of multi-charged vortices has many experimental difficulties, which could compromise its applicability. In a two-component BEC, a simpler mechanism may be used. The counterflow of two superfluids in the miscible regime, named *countersuperflow*, is expected to nucleate vortices and eventually, a *binary* QT (72), if it exceeds a critical relative velocity between the two components in a strong analogy with previous experiments realized in superfluid helium. Finally, a third and promising option arises for performing different patterns of the stirring beam, such as the 8-shaped pattern. (73) In this context, the vortex nucleation mechanism is quite different from the rotating BEC case discussed in Chapter 3. Here, the possibility of nucleating vortices relies on the fact that moving obstacles in a superfluid create vortices above a certain critical velocity. (170,171) In the numerical simulations presented in (73), the 8-shaped pattern of the stirring beam would create an isotropic array of tangled vortices, one of the characteristics of 3D Quantum Turbulence.

Transference of vorticity between a two-component BEC

In this research line, we aim to study the transference of angular momentum and vorticity between the two-species BEC. In the NaK experiment, this study could be realized by noticing that the potential produced by the stirring beam is much smaller for potassium atoms than it is for sodium (since $U_{\text{Stirr}} \propto P_{\text{Stirr}}/\Delta$, as introduced in the context of the Plug trap in Chapter 4). Therefore, by setting $a_{12} = 0$ and very low stirring

beam laser powers, we could expect to nucleate vortices only in the sodium BEC. Later, the interspecies interaction could be tuned and the transference of vortices between the species at different miscibility regimes, explored.

The transference of vorticity between the species could also be applied in the context of Quantum Turbulence. Consider the case in which the QT regime is generated with the use of a stirring beam with the 8-shaped pattern. Extending the same considerations discussed in the previous paragraph, one species (sodium) could be brought to a turbulent regime while the other species (potassium) remains unchanged if $a_{12} = 0$. Later, the interspecies interaction can be “turned on” such that vorticity may be transferred in a controlled way to the other species. This possibility creates a new way to study the turbulent state of a trapped BEC in which one can accelerate its decay processes, increasing the knowledge of the phenomena.

Massive vortices and quantum phase transitions in a vortex lattice

This last possible research line for the NaK experiment does not count on the coexistence of a two-component BEC, but on the existence of a single-BEC surrounded by a cold cloud of other atomic species. In this context, if one nucleates a vortex lattice in the BEC and tune the interspecies interactions to be strong enough, the uniformly distributed vortices in the BEC will act as a set of potential wells for the cold thermal cloud, resulting in a potential that strongly resembles the potentials produced by two-dimensional optical lattices. In this case, two regimes are expected as a function of the interspecies interaction strength: one, for low interspecies interaction, in which the cold thermal cloud is free to occupy all the trapping volume; and another one, for high interspecies interaction, in which the atoms of the thermal cloud localize themselves in the vortex cores of the vortex lattice in the BEC. This last regime would be the analogous of the Mott-insulator regime observed in optical lattices produced by a vortex lattice. This effect was theoretically studied in a previous master thesis by our group found in. (172)

Another related study could be performed by noticing that in the strongly interacting regime described before the vortices in the BEC are filled with atoms from the

other species, such that we could call them as “massive” vortices. A single massive vortex have been already studied in the context of two-component BECs composed of different hyperfine states of the same atomic species. (173) Depending on the number of atoms of the species filling the vortex, its core size increased by a factor of 13 from the expected *healing length*, resulting in a increased superfluid rotation rate by a factor of 150. For more than one vortex, the dynamics of vortices in trapped BECs strongly relies on vortex reconnections. (174) In considering “massive” vortices, one would expect that this dynamics would be strongly modified. This is a very new subject for which neither experimental nor theoretical investigation have been done so far, such that the NaK experiment could give some pioneer insight on the physics of such “massive” vortices.

References

- 1 KAPTIZA, P. Viscosity of liquid helium the λ point. *Nature*, v. 141, n. 3558, p. 74, 1938.
- 2 ALLEN, J.; MISENER, A. Flow of liquid helium II. *Nature*, v. 141, n. 3558, p. 75, 1938.
- 3 ONSAGER, L. Nuovo cimento, 6. *Suppl*, v. 2, p. 249, 1949.
- 4 FEYNMAN, R. P. Chapter II application of quantum mechanics to liquid helium. *Progress in Low Temperature Physics*, v. 1, p. 17–53, 1955.
- 5 VINEN, W. F. The detection of single quanta of circulation in liquid helium II. v. 260, n. 1301, p. 218–236, 1961.
- 6 HALL, H. E.; VINEN, W. F. The rotation of liquid helium II. i. experiments on the propagation of second sound in uniformly rotating helium II. *Proceedings of the Royal Society of London A: Mathematical, Physical and Engineering Sciences*, v. 238, n. 1213, p. 204–214, 1956. ISSN 0080-4630.
- 7 HALL, H. E. An experimental and theoretical study of torsional oscillations in uniformly rotating liquid helium II. *Proceedings of the Royal Society of London A: Mathematical, Physical and Engineering Sciences*, v. 245, n. 1243, p. 546–561, 1958. ISSN 0080-4630.
- 8 YARMCHUK, E. J.; GORDON, M. J. V.; PACKARD, R. E. Observation of stationary vortex arrays in rotating superfluid helium. *Physical Review Letters*, v. 43, n. 3, p. 214–217, 1979.
- 9 VINEN, W. Mutual friction in a heat current in liquid helium II. i. experiments on steady heat currents. *Proceedings of the Royal Society of London Series A: mathematical and physical sciences*, v. 240, n. 1220, p. 114–127, 1957.
- 10 VINEN, W. Mutual friction in a heat current in liquid helium II. iv. critical heat currents in wide channels. *Proceedings of the Royal Society of London Series A: mathematical and physical sciences*, v. 243, n. 1234, p. 400–413, 1958.
- 11 VINEN, W. Mutual friction in a heat current in liquid helium II. iii. theory of the mutual friction. *Proceedings of the Royal Society of London Series A: mathematical and*

- physical sciences*, v. 242, n. 1231, p. 493–515, 1957.
- 12 VINEN, W. Mutual friction in a heat current in liquid helium II. iv. critical heat currents in wide channels. *Proceedings of the Royal Society of London Series A: mathematical and physical sciences*, v. 243, n. 1234, p. 400–413, 1958.
- 13 STALP, S. R.; SKRBEBEK, L.; DONNELLY, R. J. Decay of grid turbulence in a finite channel. *Physical Review Letters*, v. 82, n. 24, p. 4831–4834, 1999.
- 14 MAURER, J.; TABELING, P. Local investigation of superfluid turbulence. *EPL (Europhysics Letters)*, v. 43, n. 1, p. 29, 1998.
- 15 ANDERSON, M. H. et al. Observation of Bose-Einstein condensation in a dilute atomic vapor. *Science*, v. 269, n. 5221, p. 198–201, 1995.
- 16 DAVIS, K. B. et al. Bose-Einstein condensation in a gas of sodium atoms. *Physical Review Letters*, v. 75, p. 3969–3973, 1995. doi:10.1103/PhysRevLett.75.3969.
- 17 BRADLEY, C. C. et al. Evidence of Bose-Einstein condensation in an atomic gas with attractive interactions. *Physical Review Letters*, v. 75, p. 1687–1690, 1995. doi:10.1103/PhysRevLett.75.1687.
- 18 BOSE, S. N. Plancks gesetz und lichtquantenhypothese. *Zeitschrift fur Physik*, v. 26, n. 3, p. 178, 1924.
- 19 EINSTEIN, A. Quantentheorie de einatomigen idealen gases-zweite. *Sitzungsberichte der Preussischen Akademie der Wissenschaften*, v. 1, p. 3–14, 1925.
- 20 LONDON, F. The λ -phenomenon of liquid helium and the Bose-Einstein degeneracy. *Nature*, v. 141, p. 643–644, 1938.
- 21 LEGGETT, A. J. *Quantum liquids: Bose condensation and Cooper pairing in condensed-matter systems*. [S.l.]: Oxford: Oxford University Press, 2006.
- 22 PITAEVSKII, L. P.; STRINGARI, S. *Bose-Einstein condensation*. [S.l.]: Oxford: Oxford University Press, 2003.
- 23 ANDREWS, M. et al. Observation of interference between two Bose condensates. *Science*, v. 275, n. 5300, p. 637–641, 1997.

-
- 24 KETTERLE, W.; DURFEE, D. S.; STAMPER-KURN, D. M. Making, probing and understanding Bose-Einstein condensates. *Amsterdam: IOS Press*, 1999.
- 25 JIN, D. S. et al. Collective excitations of a Bose-Einstein condensate in a dilute gas. *Physical Review Letters*, v. 77, n. 3, p. 420–423, 1996.
- 26 CORNELL, E. A.; ENSHER, J. R.; WIEMAN, C. E. Experiments in dilute atomic Bose-Einstein condensation. *Amsterdam: IOS Press*, p. 15–66, 1999.
- 27 MATTHEWS, M. R. et al. Vortices in a Bose-Einstein condensate. *Physical Review Letters*, v. 83, p. 2498–2501, 1999. doi:10.1103/PhysRevLett.83.2498.
- 28 MADISON, K. W. et al. Vortex formation in a stirred Bose-Einstein condensate. *Physical Review Letters*, v. 84, n. 5, p. 806–809, 2000.
- 29 RAMAN, C. et al. Vortex nucleation in a stirred Bose-Einstein condensate. *Physical Review Letters*, v. 87, n. 21, p. 210402, 2001.
- 30 HODBY, E. et al. Vortex nucleation in Bose-Einstein condensates in an oblate, purely magnetic potential. *Physical Review Letters*, v. 88, n. 1, p. 010405, 2001.
- 31 BUTTS, D.; ROKHSAR, D. Predicted signatures of rotating Bose-Einstein condensates. *Nature*, v. 397, n. 6717, p. 327–329, 1999.
- 32 FEDER, D. L.; CLARK, C. W. Superfluid-to-solid crossover in a rotating Bose-Einstein condensate. *Physical Review Letters*, v. 87, n. 19, p. 190401, 2001.
- 33 ABO-SHAEER, J. et al. Observation of vortex lattices in Bose-Einstein condensates. *Science*, v. 292, n. 5516, p. 476–479, 2001.
- 34 CODDINGTON, I. et al. Experimental studies of equilibrium vortex properties in a Bose-condensed gas. *Physical Review A*, v. 70, n. 6, p. 063607, 2004.
- 35 HENN, E. A. L. et al. Observation of vortex formation in an oscillating trapped Bose-Einstein condensate. *Physical Review A*, v. 79, n. 4, p. 043618, 2009.
- 36 SEMAN, J. A. et al. Three-vortex configuration in trapped Bose-Einstein condensates. *Physical Review A: Atomic, Molecular, and Optical Physics*, v. 82, n. 3, p. 033616, 2010.

- 37 HENN, E. A. L. et al. Emergence of turbulence in an oscillating Bose-Einstein condensate. *Physical Review Letters*, v. 103, n. 4, p. 045301, 2009.
- 38 SEMAN, J. A. et al. Route to turbulence in a trapped Bose-Einstein condensate. *Laser Physics*, v. 8, n. 9, p. 691, 2011.
- 39 SEMAN, J. A. et al. Turbulence in a trapped Bose-Einstein condensate. *Journal of Physics: Conference Series*, v. 264, n. 1, p. 012004, 2011.
- 40 TAVARES, P. E. S. et al. Out-of-phase oscillation between superfluid and thermal components for a trapped Bose-Einstein condensate under oscillatory excitation. *Laser Physics Letters*, v. 10, n. 4, p. 045501, 2013.
- 41 THOMPSON, K. et al. Evidence of power law behavior in the momentum distribution of a turbulent trapped Bose-Einstein condensate. *Laser Physics Letters*, v. 11, n. 1, p. 015501, 2014.
- 42 NEELY, T. W. et al. Characteristics of two-dimensional quantum turbulence in a compressible superfluid. *Physical Review Letters*, v. 111, n. 23, p. 235301, 2013.
- 43 NAVON, N. et al. Emergence of a turbulent cascade in a quantum gas. *Nature*, v. 539, n. 7627, p. 72–75, 2016.
- 44 TSATSOS, M. C. et al. Quantum turbulence in trapped atomic Bose-Einstein condensates. *Physics Reports*, v. 622, p. 1–52, 2016. doi: 10.1016/j.physrep.2016.02.003.
- 45 BILLY, J. et al. Direct observation of Anderson localization of matter waves in a controlled disorder. *Nature*, v. 453, n. 7197, p. 891–894, 2008.
- 46 ROATI, G. et al. Anderson localization of a non-interacting Bose-Einstein condensate. *Nature*, v. 453, n. 7197, p. 895–898, 2008.
- 47 GREINER, M. et al. Quantum phase transition from a superfluid to a Mott insulator in a gas of ultracold atoms. *Nature*, v. 415, n. 6867, p. 39–44, 2002.
- 48 MYATT, C. J. et al. Production of two overlapping Bose-Einstein condensates by sympathetic cooling. *Physical Review Letters*, v. 78, n. 4, p. 586–589, 1997. doi:10.1103/PhysRevLett.78.586.

- 49 PARK, J. W.; WILL, S. A.; ZWIERLEIN, M. W. Ultracold dipolar gas of fermionic $^{23}\text{Na}^{40}\text{K}$ molecules in their absolute ground state. *Physical Review Letters*, v. 114, n. 20, p. 205302, 2015.
- 50 MODUGNO, G. et al. Collapse of a degenerate Fermi gas. *Science*, v. 297, n. 5590, p. 2240–2243, 2002. ISSN 0036-8075. Disponível em: <<http://science.sciencemag.org/content/297/5590/2240>>.
- 51 OSPELKAUS, C. et al. Interaction-driven dynamics of ^{40}K – ^{87}Rb fermion-boson gas mixtures in the large-particle-number limit. *Physical Review Letters*, v. 96, n. 2, p. 020401, 2006.
- 52 VIVERIT, L.; PETHICK, C. J.; SMITH, H. Zero-temperature phase diagram of binary boson-fermion mixtures. *Phys. Rev. A*, v. 61, n. 5, p. 053605, 2000.
- 53 FERRIER-BARBUT, I. et al. A mixture of Bose and Fermi superfluids. *Science*, v. 345, n. 6200, p. 1035–1038, 2014.
- 54 YAO, X.-C. et al. Observation of coupled vortex lattices in a mass-imbalance Bose and Fermi superfluid mixture. *Physical Review Letters*, v. 117, n. 14, p. 145301, 2016.
- 55 MADDALONI, P. et al. Collective oscillations of two colliding Bose-Einstein condensates. *Physical Review Letters*, v. 85, n. 12, p. 2413–2417, 2000. doi:10.1103/PhysRevLett.85.2413.
- 56 PAPP, S. B.; PINO, J. M.; WIEMAN, C. E. Tunable miscibility in a dual-species Bose-Einstein condensate. *Physical Review Letters*, v. 101, n. 4, p. 040402, 2008.
- 57 SUGAWA, S. et al. Bose-Einstein condensate in gases of rare atomic species. *Physical Review A*, v. 84, n. 1, p. 011610, 2011.
- 58 MODUGNO, G. et al. Bose-Einstein condensation of potassium atoms by sympathetic cooling. *Science*, v. 294, n. 5545, p. 1320–1322, 2001.
- 59 MODUGNO, G. et al. Two atomic species superfluid. *Physical Review Letters*, v. 89, n. 19, p. 190404, 2002.
- 60 THALHAMMER, G. et al. Double species Bose-Einstein condensate with tunable interspecies interactions. *Physical Review Letters*, v. 100, n. 21, p. 210402, 2008.

- 61 MCCARRON, D. J. et al. Dual-species Bose-Einstein condensate of ^{87}Rb and ^{133}Cs . *Physical Review A*, v. 84, n. 1, p. 011603, 2011.
- 62 PASQUIOU, B. et al. Quantum degenerate mixtures of strontium and rubidium atoms. *Physical Review A*, v. 88, n. 2, p. 023601, 2013.
- 63 WACKER, L. et al. Tunable dual-species Bose-Einstein condensates of ^{39}K and ^{87}Rb . *Physical Review A*, v. 92, n. 5, p. 053602, 2015.
- 64 WANG, F. et al. A double species ^{23}Na and ^{87}Rb Bose-Einstein condensate with tunable miscibility via an interspecies feshbach resonance. *Journal of Physics B*, v. 49, n. 1, p. 015302, 2016.
- 65 KASAMATSU, K.; TSUBOTA, M.; UEDA, M. Vortex phase diagram in rotating two-component Bose-Einstein condensates. *Physical Review Letters*, v. 91, n. 15, p. 150406, 2003.
- 66 KASAMATSU, K.; TSUBOTA, M.; UEDA, M. Vortices in multicomponent Bose-Einstein condensates. *International Journal of Modern Physics B*, v. 19, n. 11, p. 1835–1904, 2005.
- 67 MASON, P.; AFTALION, A. Classification of the ground states and topological defects in a rotating two-component Bose-Einstein condensate. *Physical Review A*, v. 84, n. 3, p. 033611, 2011.
- 68 KUOPANPORTTI, P.; HUHTAMÄKI, J. A. M.; MÖTTÖNEN, M. Exotic vortex lattices in two-species Bose-Einstein condensates. *Physical Review A*, v. 85, n. 4, p. 043613, 2012.
- 69 SCHWEIKHARD, V. et al. Vortex-lattice dynamics in rotating spinor Bose-Einstein condensates. *Physical Review Letters*, v. 93, n. 21, p. 210403, 2004.
- 70 CHIN, C. et al. Feshbach resonances in ultracold gases. *Reviews of Modern Physics*, v. 82, p. 1225, 2010. doi:10.1103/RevModPhys.82.1225.
- 71 VIEL, A.; SIMONI, A. Feshbach resonances and weakly bound molecular states of boson-boson and boson-fermion pairs. *Physical Review A*, v. 93, p. 042701, 2016.
- 72 TAKEUCHI, H.; ISHINO, S.; TSUBOTA, M. Binary quantum turbulence arising from counter-superflow instability in two-component Bose-Einstein condensates. *Physical Review Letters*, v. 105, n. 20, p. 205301, 2010.

- 73 ALLEN, A. J. et al. Isotropic vortex tangles in trapped atomic Bose-Einstein condensates via laser stirring. *Physical Review A*, v. 89, n. 2, p. 025602, 2014.
- 74 LANDINI, M. *A tunable Bose-Einstein condensate for quantum interferometry*. 2012. 146 p. Ph. D. Thesis (Physics) – Università degli Studi di Trento, Trento, 2012. Available at: <http://quantumgases.lens.unifi.it/theses/thesislandiniphd.pdf>. Accessible at: 23 jan. 2017.
- 75 SEMEGHINI, G. et al. Measurement of the mobility edge for 3d anderson localization. *Nature Physics*, v. 11, n. 7, p. 554–559, 2015.
- 76 TRENKWALDER, A. et al. Quantum phase transitions with parity-symmetry breaking and hysteresis. *Nature Physics*, 2016.
- 77 PEÑAFIEL, E. E. P. *Production of a Bose-Einstein condensate of sodium atoms and investigation considering non-linear atom-photon interactions*. 2016. 175 p. Tese (Doutorado em Ciências) – Instituto de Física de São Carlos, Universidade de São Paulo, São Carlos, 2016.
- 78 PEDROZO-PENAFIEL, E. et al. Two-photon cooperative absorption in colliding cold na atoms. *Physical Review Letters*, v. 108, p. 253004, 2012. Disponível em: <<http://journals.aps.org/prl/abstract/10.1103/PhysRevLett.108.253004>>.
- 79 ULBRICH, K. de F. *Estudo das taxas de perdas em uma armadilha magneto-óptica: casos homonuclear e heteronuclear*. Tese (Doutorado) — Universidade do Estado de Santa Catarina.
- 80 SALOMON, G. et al. Gray-molasses cooling of 39 k to a high phase-space density. *EPL (Europhysics Letters)*, v. 104, n. 6, p. 63002, 2013. Disponível em: <<http://stacks.iop.org/0295-5075/104/i=6/a=63002>>.
- 81 DALFOVO, F.; STRINGARI, S. Bosons in anisotropic traps: Ground state and vortices. *Phys. Rev. A*, v. 53, p. 2477–2485, 1996.
- 82 PETHICK, C. J.; SMITH, H. *Bose-Einstein condensation in dilute gases*. [S.l.]: Cambridge: Cambridge University Press, 2008.
- 83 HUANG, K. *Introduction to statistical physics*. [S.l.]: London: Taylor & Francis, 2002.
- 84 GAUNT, A. L. et al. Bose-Einstein condensation of atoms in a uniform potential. *Physical Review Letters*, v. 110, n. 20, p. 200406, 2013.

- 85 D'ERRICO, C. et al. Feshbach resonances in ultracold ^{39}K . *New Journal of Physics*, v. 9, n. 7, p. 223, 2007.
- 86 EAGLES, D. M. Possible pairing without superconductivity at low carrier concentrations in bulk and thin-film superconducting semiconductors. *Physical Review*, v. 186, n. 2, p. 456–463, 1969.
- 87 CHEN, Q. et al. Bcs–bec crossover: From high temperature superconductors to ultracold superfluids. *Physics Reports*, v. 412, n. 1, p. 1–88, 2005.
- 88 BAGNATO, V.; PRITCHARD, D. E.; KLEPPNER, D. Bose-Einstein condensation in an external potential. *Physical Review A*, v. 35, n. 10, p. 4354–4358, 1987.
- 89 ROGEL-SALAZAR, J. The Gross-Pitaevskii equation and Bose-Einstein condensates. *European Journal of Physics*, v. 34, n. 2, p. 247, 2013.
- 90 DALFOVO, F. et al. Theory of Bose-Einstein condensation in trapped gases. *Review of Modern Physics*, v. 71, n. 3, p. 463–512, 1999.
- 91 RUPRECHT, P. A. et al. Time-dependent solution of the nonlinear Schrödinger equation for Bose-condensed trapped neutral atoms. *Physical Review A*, v. 51, n. 6, p. 4704–4711, 1995.
- 92 SACKETT, C. A.; STOOFF, H. T. C.; HULET, R. G. Growth and collapse of a Bose-Einstein condensate with attractive interactions. *Physical Review Letters*, v. 80, n. 10, p. 2031–2034, 1998.
- 93 ROATI, G. et al. ^{39}K Bose-Einstein condensate with tunable interactions. *Physical Review Letters*, v. 99, n. 1, p. 010403, 2007.
- 94 ROBERTS, J. L. et al. Controlled collapse of a Bose-Einstein condensate. *Physical Review Letters*, v. 86, n. 19, p. 4211–4214, 2001.
- 95 LEE, K. L. et al. Phase separation and dynamics of two-component Bose-Einstein condensates. *Physical Review A*, v. 94, n. 1, p. 013602, 2016.
- 96 RIBOLI, F.; MODUGNO, M. Topology of the ground state of two interacting Bose-Einstein condensates. *Physical Review A*, v. 65, n. 6, p. 063614, 2002.

- 97 CATANI, J. *A New Apparatus for ultracold K-Rb Bose-Bose atomic mixtures*. 168 p. Tese (Doutorado) — Ph. D. Thesis (Physics), Facolta di Scienze Matematiche, Fisiche e Naturali, Universita Degli Studi di Firenze, Firenze, 2006.
- 98 LAW, C. K. et al. “Stability signature” in two-species dilute Bose-Einstein condensates. *Physical Review Letters*, v. 79, n. 17, p. 3105–3108, 1997.
- 99 ESRY, B. D. et al. Hartree-fock theory for double condensates. *Physical Review Letters*, v. 78, n. 19, p. 3594–3597, 1997.
- 100 TIMMERMANS, E. Phase separation of Bose-Einstein condensates. *Physical Review Letters*, v. 81, n. 26, p. 5718–5721, 1998.
- 101 AO, P.; CHUI, S. T. Binary Bose-Einstein condensate mixtures in weakly and strongly segregated phases. *Physical Review A*, v. 58, n. 6, p. 4836–4840, 1998.
- 102 TRIPPENBACH, M. et al. Structure of binary Bose-Einstein condensates. *Journal of Physics B*, v. 33, n. 19, p. 4017, 2000.
- 103 KISHIMOTO, T. et al. Direct evaporative cooling of ^{41}K into a Bose-Einstein condensate. *Physical Review A*, v. 79, n. 3, p. 031602, 2009.
- 104 INOUE, S. et al. Observation of feshbach resonances in a Bose-Einstein condensate. *Nature*, v. 392, n. 6672, p. 151–154, 1998.
- 105 FEYNMAN, R. P. Chapter II application of quantum mechanics to liquid helium. *Progress in Low Temperature Physics*, v. 1, p. 17–53, 1955. doi:10.1016/S0079-6417(08)60077-3.
- 106 LANDAU, L.; LIFSHITZ, E. *Fluid Mechanics 2nd ed.* [S.l.]: England: Pergamon Press, 1987.
- 107 DONNELLY, R. J. *Quantized vortices in helium II*. [S.l.]: Cambridge: Cambridge University Press, 1991. v. 2.
- 108 Castin, Y.; Dum, R. Bose-Einstein condensates with vortices in rotating traps. *European Physics Journal D*, v. 7, n. 3, p. 399–412, 1999.
- 109 HO, T.-L. Bose-Einstein condensates with large number of vortices. *Physical Review Letters*, v. 87, n. 6, p. 060403, 2001.

- 110 COOPER, N. R.; WILKIN, N. K.; GUNN, J. M. F. Quantum phases of vortices in rotating Bose-Einstein condensates. *Physical Review Letters*, v. 87, n. 12, p. 120405, 2001.
- 111 HO, T.-L. Bose-Einstein condensates with large number of vortices. *Physical Review Letters*, v. 87, n. 6, p. 060403, 2001.
- 112 REGNAULT, N.; JOLICOEUR, T. Quantum hall fractions in rotating Bose-Einstein condensates. *Physical Review Letters*, v. 91, n. 3, p. 030402, 2003.
- 113 STRINGARI, S. Phase diagram of quantized vortices in a trapped Bose-Einstein condensed gas. *Physical Review Letters*, v. 82, n. 22, p. 4371–4375, 1999.
- 114 HALJAN, P. C. *Vortices in a Bose-Einstein Condensate*. Tese (Theses) — University of Alberta, 2003.
- 115 HALJAN, P. C. et al. Driving Bose-Einstein condensate vorticity with a rotating normal cloud. *Physical Review Letters*, v. 87, n. 21, p. 210403, 2001.
- 116 RAMAN, C. et al. Vortex nucleation in a stirred Bose-Einstein condensate. *Physical Review Letters*, v. 87, n. 21, p. 210402, 2001.
- 117 SCHWEIKHARD, V. et al. Rapidly rotating Bose-Einstein condensates in and near the lowest Landau level. *Physical Review Letters*, v. 92, n. 4, p. 040404, 2004.
- 118 TKACHENKO, V. On vortex lattices. *Soviet Physics JETP*, v. 22, n. 6, p. 1282–1286, 1966.
- 119 TKACHENKO, V. Stability of vortex lattices. *Soviet Physics JETP*, v. 23, n. 6, p. 1049–1056, 1966.
- 120 BRETIN, V. et al. Fast rotation of a Bose-Einstein condensate. *Physical Review Letters*, v. 92, n. 5, p. 050403, 2004.
- 121 FETTER, A. L. Rotating trapped Bose-Einstein condensates. *Review of Modern Physics*, v. 81, n. 2, p. 647–691, 2009.
- 122 HALL, D. S. et al. Dynamics of component separation in a binary mixture of Bose-Einstein condensates. *Physical Review Letters*, v. 81, n. 8, p. 1539–1542, 1998.

-
- 123 KHAWAJA, U. A.; STOOF, H. Skyrmions in a ferromagnetic Bose–Einstein condensate. *Nature*, v. 411, n. 6840, p. 918–920, 2001.
- 124 MUELLER, E. J. Spin textures in slowly rotating Bose-Einstein condensates. *Physical Review A*, v. 69, n. 3, p. 033606, 2004.
- 125 PHILLIPS, W. D.; METCALF, H. Laser deceleration of an atomic beam. *Physical Review Letters*, v. 48, n. 9, p. 596–599, 1982.
- 126 MYATT, C. et al. Multiply loaded magneto-optical trap. *Optics letters*, v. 21, n. 4, p. 290–292, 1996.
- 127 DIECKMANN, K. et al. Two-dimensional magneto-optical trap as a source of slow atoms. *Physical Review A*, v. 58, n. 5, p. 3891–3895, 1998.
- 128 CATANI, J. et al. Intense slow beams of bosonic potassium isotopes. *Physical Review A*, v. 73, n. 3, p. 033415, 2006.
- 129 TIECKE, T. G. et al. High-flux two-dimensional magneto-optical-trap source for cold lithium atoms. *Physical Review A*, v. 80, n. 1, p. 013409, 2009.
- 130 LAMPORESI, G. et al. Compact high-flux source of cold sodium atoms. *Review of Scientific Instruments*, v. 84, n. 6, p. 063102, 2013.
- 131 STAM, K. V. D. et al. Large atom number Bose-Einstein condensate of sodium. *Review of Scientific Instruments*, v. 78, n. 1, p. 013102, 2007.
- 132 FENG, Z. et al. High-performance sodium Bose-Einstein condensate apparatus with a hybrid trap and long-distance magnetic transfer. *Chinese Physics Letters*, v. 32, n. 12, p. 123701, 2015.
- 133 PEDROZO-PENAFIEL, E. et al. Direct comparison between a two-dimensional magneto-optical trap and a zeeman slower as sources of cold sodium atoms. *Laser Physics Letters*, v. 13, n. 6, p. 065501, 2016.
- 134 PHILLIPS, W. D. Nobel lecture: Laser cooling and trapping of neutral atoms. *Review of Modern Physics*, v. 70, n. 3, p. 721–741, 1998.
- 135 KETTERLE, W. et al. High densities of cold atoms in a dark spontaneous-force optical trap. *Physical Review Letters*, v. 70, n. 15, p. 2253–2256, 1993.

- 136 STELLMER, S. et al. Laser cooling to quantum degeneracy. *Physical Review Letters*, v. 110, n. 26, p. 263003, 2013.
- 137 KETTERLE, W.; DRUTEN, N. V. Evaporative cooling of trapped atoms. *Advances in atomic, molecular, and optical physics*, v. 37, p. 181–236, 1996. doi: 10.1016/S1049–250X(08)60101–9.
- 138 DAVIS, K. B. et al. Evaporative cooling of sodium atoms. *Physical Review Letters*, v. 74, n. 26, p. 5202–5205, 1995.
- 139 WU, C.-H. *Strongly interacting quantum mixtures of ultracold atoms*. 2013. 212 p. Ph. D. Thesis (Physics) – Department of Physics, Massachusetts Institute of Technology, Massachusetts, 2013. Available at: <http://www.rle.mit.edu/uqg/documents/CHWThesisFinal.pdf>. Accessible at: 15 jan. 2017.
- 140 GÖRLITZ, A. et al. Sodium Bose-Einstein condensates in the $f = 2$ state in a large-volume optical trap. *Physical Review Letters*, v. 90, n. 9, p. 090401, 2003.
- 141 PETRICH, W. et al. Stable, tightly confining magnetic trap for evaporative cooling of neutral atoms. *Physical Review Letters*, v. 74, n. 17, p. 3352–3355, 1995.
- 142 ESSLINGER, T.; BLOCH, I.; HÄNSCH, T. W. Bose-Einstein condensation in a quadrupole-ioffe-configuration trap. *Physical Review A*, v. 58, n. 4, p. R2664–R2667, 1998.
- 143 STECK, D. A. Sodium d line data. *Report, Los Alamos National Laboratory, Los Alamos*, v. 124, 2000.
- 144 MAJORANA, E. Atomi orientati in campo magnetico variabile. *Il Nuovo Cimento (1924-1942)*, v. 9, n. 2, p. 43–50, 1932.
- 145 LIN, Y.-J. et al. Rapid production of ^{87}Rb Bose-Einstein condensates in a combined magnetic and optical potential. *Physical Review A*, v. 79, n. 6, p. 063631, 2009.
- 146 WU, C.-H. et al. Strongly interacting isotopic Bose-Fermi mixture immersed in a Fermi sea. *Physical Review A*, v. 84, n. 1, p. 011601, 2011.
- 147 HEO, M.-S.; CHOI, J.-y.; SHIN, Y.-i. Fast production of large ^{23}Na Bose-Einstein condensates in an optically plugged magnetic quadrupole trap. *Physical Review A*, v. 83, n. 1, p. 013622, 2011.

- 148 GRIMM, R.; WEIDEMÜLLER, M.; OVCHINNIKOV, Y. B. Optical dipole traps for neutral atoms. *Advances in atomic, molecular, and optical physics*, v. 42, p. 95–170, 2000. doi: 10.1016/S1049–250X(08)60186–X.
- 149 DUBESSY, R. et al. Rubidium-87 Bose-Einstein condensate in an optically plugged quadrupole trap. *Physical Review A*, v. 85, n. 1, p. 013643, 2012.
- 150 MASUHARA, N. et al. Evaporative cooling of spin-polarized atomic hydrogen. *Physical Review Letters*, v. 61, n. 8, p. 935–938, 1988.
- 151 FERNANDES, D. R. Trapping and cooling of fermionic alkali atoms to quantum degeneracy. Sub-Doppler cooling of Potassium-40 and Lithium-6 in gray molasses. 2014. 260 p. Ph. D. Thesis (Physics) – Université Pierre et Marie Curie, Paris, 2014. Available at: <https://tel.archives-ouvertes.fr/tel-01082122>.
- 152 CHEN, H.-Z. et al. Production of large ^{41}K Bose-Einstein condensates using D_1 gray molasses. *Physical Review A*, v. 94, n. 3, p. 033408, 2016.
- 153 INOUE, S. et al. Observation of heteronuclear feshbach resonances in a mixture of bosons and fermions. *Physical Review Letters*, v. 93, n. 18, p. 183201, 2004.
- 154 CHU, S. et al. Three-dimensional viscous confinement and cooling of atoms by resonance radiation pressure. *Physical Review Letters*, v. 55, n. 1, p. 48–51, 1985.
- 155 LANDINI, M. et al. Sub-doppler laser cooling of potassium atoms. *Physical Review A*, v. 84, n. 4, p. 043432, 2011.
- 156 BOIRON, D. et al. Laser cooling of cesium atoms in gray optical molasses down to 1.1 μK . *Physical Review A*, v. 53, n. 6, p. R3734–R3737, 1996.
- 157 PRESTON, D. W.; WIEMAN, C. E.; SIEGBAHN, K. M. Doppler free-saturated absorption spectroscopy: Laser spectroscopy. *American Journal of Physics*, v. 64, n. 11, p. 1432–1436, 1996.
- 158 GRYNBERG, G.; COURTOIS, J.-Y. Proposal for a magneto-optical lattice for trapping atoms in nearly-dark states. *EPL (Europhysics Letters)*, v. 27, n. 1, p. 41, 1994.
- 159 WEIDEMÜLLER, M. et al. A novel scheme for efficient cooling below the photon recoil limit. *EPL (Europhysics Letters)*, v. 27, n. 2, p. 109, 1994.

- 160 BOIRON, D. et al. Three-dimensional cooling of cesium atoms in four-beam gray optical molasses. *Physical Review A*, v. 52, n. 5, p. R3425–R3428, 1995.
- 161 BOIRON, D. et al. Cold and dense cesium clouds in far-detuned dipole traps. *Physical Review A*, v. 57, n. 6, p. R4106–R4109, 1998.
- 162 BURCHIANTI, A. et al. Efficient all-optical production of large ^6Li quantum gases using D_1 gray-molasses cooling. *Physical Review A*, v. 90, n. 4, p. 043408, 2014.
- 163 COLZI, G. et al. Sub-doppler cooling of sodium atoms in gray molasses. *Physical Review A*, v. 93, n. 2, p. 023421, 2016.
- 164 PAPOFF, F.; MAURI, F.; ARIMONDO, E. Transient velocity-selective coherent population trapping in one dimension. *Journal of the Optical Society of America B*, v. 9, n. 3, p. 321–331, 1992.
- 165 FERNANDES, D. R. et al. Sub-doppler laser cooling of fermionic 40 k atoms in three-dimensional gray optical molasses. *EPL (Europhysics Letters)*, v. 100, n. 6, p. 63001, 2012.
- 166 GRIER, A. T. et al. λ -enhanced sub-doppler cooling of lithium atoms in d_1 gray molasses. *Physical Review A*, v. 87, n. 6, p. 063411, 2013.
- 167 WEINER, J. et al. Experiments and theory in cold and ultracold collisions. *Review of Modern Physics*, v. 71, n. 1, p. 1–85, 1999.
- 168 SHIOZAKI, R. F. et al. Transition to quantum turbulence in finite-size superfluids. *Laser Physics Letters*, v. 8, n. 5, p. 393–397, 2011.
- 169 CIDRIM, A. et al. Controlled polarization of two-dimensional quantum turbulence in atomic Bose-Einstein condensates. *Physical Review A*, v. 93, n. 3, p. 033651, 2016.
- 170 FRISCH, T.; POMEAU, Y.; RICA, S. Transition to dissipation in a model of superflow. *Physical Review Letters*, v. 69, n. 11, p. 1644–1647, 1992.
- 171 NEELY, T. W. et al. Observation of vortex dipoles in an oblate Bose-Einstein condensate. *Physical Review Letters*, v. 104, n. 16, p. 160401, 2010.
- 172 CHAVIGURI, J. R. H. *Transição de fase quântica de sistema 2D em rede de vortices*. Tese (Doutorado) — Universidade de São Paulo.

- 173 ANDERSON, B. P. et al. Vortex precession in Bose-Einstein condensates: Observations with filled and empty cores. *Physical Review Letters*, v. 85, n. 14, p. 2857–2860, 2000.
- 174 ALLEN, A. J. et al. Vortex reconnections in atomic condensates at finite temperature. *Physical Review A*, v. 90, n. 1, p. 013601, 2014.
- 175 FESHBACH, H. A unified theory of nuclear reactions. *Annals of Physics*, v. 5, p. 357–390, 1958.
- 176 FESHBACH, H. A unified theory of nuclear reactions II. *Annals of Physics*, v. 19, p. 287–313, 1962.
- 177 FANO, U. Effects of configuration interaction on intensities and phase shifts. *Physical Review*, v. 124, p. 1866, 1961.
- 178 STWALLEY, W. C. Stability of spin-aligned hydrogen at low temperatures and high magnetic fields: New field-dependent scattering resonances and predissociations. *Physical Review Letters*, v. 37, p. 1628, 1976.
- 179 TIESINGA, E.; VERHAAR, B. J.; STOOF, H. T. C. Threshold and resonance phenomena in ultracold ground-state collisions. *Physical Review A*, v. 47, p. 4114, 1993.
- 180 COURTEILLE, P. et al. Observation of a feshbach resonance in cold atom scattering. *Physical Review Letters*, 1998.
- 181 D'ERRICO, C. et al. Feshbach resonances in ultracold ^{39}K . *New Journal of Physics*, v. 9, p. 223, 2007.

APPENDIX

APPENDIX A – The magnetically induced Feshbach resonances

In this Appendix, we first present a brief theoretical description of the mechanism of the magnetically induced Feshbach resonances in the context of cold atoms experiments, in section A.1. Later, we discuss the specific case for the interspecies Feshbach resonances between ^{23}Na and ^{41}K atoms, in section A.2. And finally, the experimental setup developed in the laboratory for generating the needed magnetic field, is described in sections A.2.1.

A.1 Feshbach resonances in cold atomic systems

In cold atomic systems, the interaction between particles can be changed by means of the magnetically induced Feshbach resonances (70). At the end of 1950, Feshbach, in the field of nuclear physics, and Fano, in atomic physics, treated the problem of the coupling between discrete states with a continuum (175–177), but it was Stwalley, in 1976, that first suggest the existence of magnetically induced “Feshbach resonances” in the context of quantum gases as a way to explain the scattering processes between hydrogen and spin-polarized deuterium atoms (178). In this section, we want to give a simple introduction on the mechanism of Feshbach resonances and how they are sintonized and observed in the laboratory. A more precise description can be found in reference (70).

Let us consider two atoms with molecular potentials, $V_{bg}(R)$ and $V_c(R)$, as illustrated in Fig. 70. When considering the energy of the system to be given by E (represented in blue), $V_{bg}(R)$ represents an open channel while $V_c(R)$, a closed channel. The Feshbach resonance occurs when the molecular state of $V_c(R)$, with energy E_c , approaches the energy of the free particles E . The energy difference $E - E_c$ can be controlled by applying an external magnetic field. A simple equation can be used to characterize the behaviour of the scattering length, $a_s(B)$, near a Feshbach resonance:

$$a_s(B) = a_{bg} \left(1 - \frac{\Delta}{B - B_0} \right) \quad (\text{A.1})$$

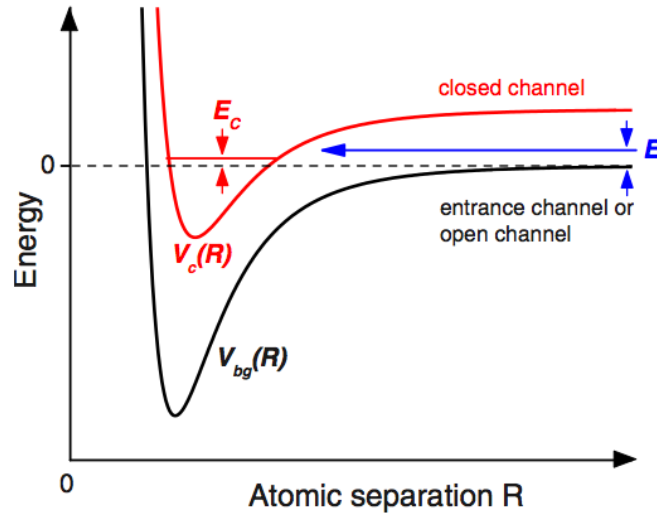


Figure 70 – Molecular potentials between two atoms. $V_{bg}(R)$ represents an open channel while $V_c(R)$ a closed channel with a molecular state with energy E_c . The difference between the energies $E - E_c$ can be tuned by applying an external magnetic field. Source: Adapted from Chin et al. in. (70)

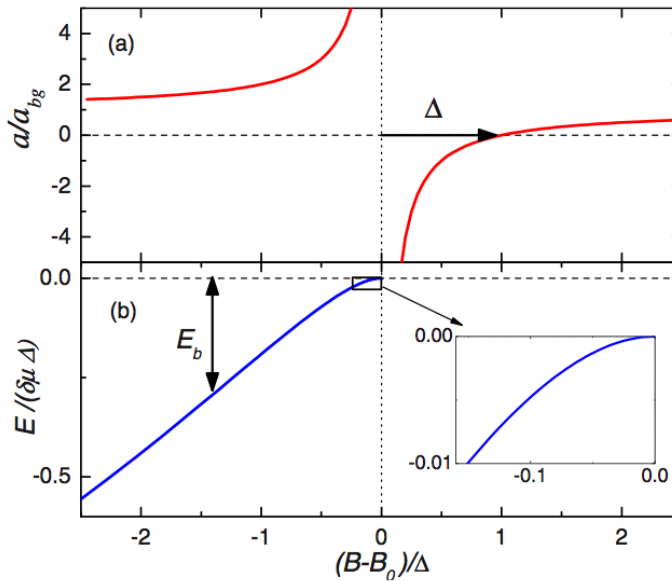


Figure 71 – (a) Scattering length a/a_{bg} as a function of the external magnetic field as given by Eq. A.1. (b) Molecular energy E_b as a function of the external magnetic field. Close to the resonance it assumes a quadratic behaviour. Source: Adapted from Chin et al. in. (70)

where a_{bg} is the background scattering length, related with the energy of the last bound-state of $V_{bg}(R)$, B_0 is the field at which the resonance occurs ($a_s \rightarrow \pm\infty$) and Δ is the width of the resonance. The *zero-crossing point* happens at $B_0 + \Delta$ and it represents the situation free of interactions. The curve of equation A.1 is depicted in Figure 71.

Tiesinga, in 1993 was the first one to point out the positive aspects of the Feshbach resonances, showing that it could be used to change the sign and the magnitude of the interactions in cold atomic systems (179). The first experimental observations in such systems happened five years later performed by Inouye *et al.* in a BEC of ^{23}Na atoms (104), and by Courteille *et al.*, in cold sample of ^{85}Rb (180). From this first observations to now, many more Feshbach resonances were characterized and it is important to point out the large Feshbach resonances presented for example, in ^{39}K (85) which provides the realization of non-interacting systems (75) with very high accuracy. But, there are still resonances predicted to occur that need to be identified, as it is the case of the mixture ^{23}Na - ^{41}K we aim to produce in our laboratory.

Once it is known the expected resonance positions from previous numerical simulations, identify and characterize such resonances can be done by looking at the atom number as a function of the applied magnetic field. At $B = B_0$ a great loss in the atom number is expected due to three-body collisions and the formation of molecules. A typical experimental calibration curve for a Feshbach resonance is shown in Fig. 72, taken from reference (104). The atom number vanishes as one approaches the resonance and the scattering length can be inferred by the atomic losses rates.

A.2 The Feshbach resonances between ^{23}Na and ^{41}K

The possibility of change the interspecies interactions between ^{23}Na and ^{41}K is necessary to perform a complete study on the vortex generation and transference mechanisms in the two-component BEC. However, the characterization of such resonances is still missing in the literature. In collaboration with Andrea Simoni (181), we obtained the expected values (B_0 and Δ) of the Feshbach resonances for ^{41}K - ^{41}K and ^{23}Na - ^{41}K at different configurations of the hyperfine states. The behaviour of scattering lengths $a_{41\text{K}}$ and $a_{\text{Na-K}}$ considering both species in the $|F = 1, m_F = 1\rangle$ state as a function of the magnetic field is shown in Fig. 73. The choice of both species in the $|F = 1, m_F = 1\rangle$ was done since this combination presented the broader resonances for the two-component. The resonances for the ^{41}K are really narrow ($\Delta < 0.5$ G) and are just illustrated in the

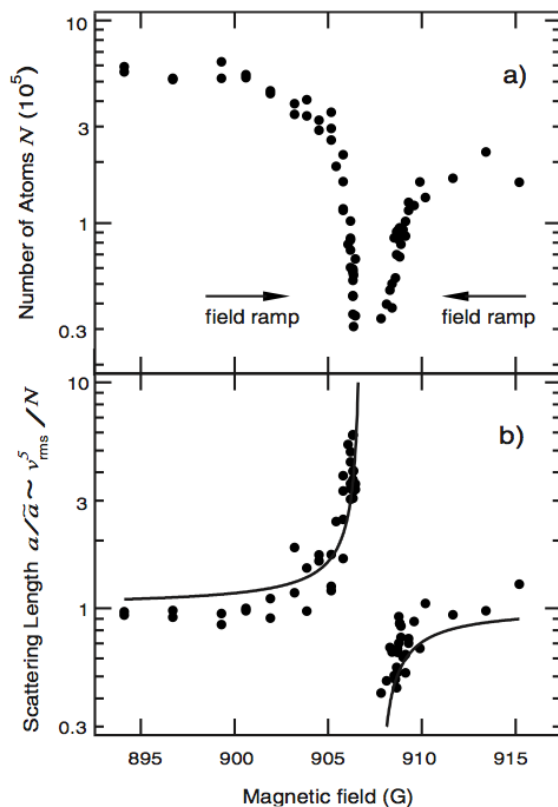


Figure 72 – Measurement of the Feshbach resonances by means of atom loss. In (a), the number of trapped atoms dramatically decreases close to the magnetic field for which occur the Feshbach resonance. The behaviour of the scattering length as given by Eq. A.1 is illustrated in (b).

Source: Adapted from Inouye et al. in. (104)

figure to show that they are not going to influenced the system near the two-component resonances. It is the same for the resonances for ^{23}Na that happens at much higher field ($B_0 \geq 900$) (104) than the ^{23}Na - ^{41}K resonances expected to occur for $B_0 < 600$ G. Two of the expected resonances are reasonably large (with $\Delta \approx 5 - 10$ G) and happen at $B_0^1 = 73.35$ G and $B_0^2 = 470$ G. These are the resonances we want to characterize in the NaK experiment and the magnetic field has to be designed in order to easily achieve B_0^1 and B_0^2 .

A.2.1 Designing the Feshbach coils

The Feshbach resonances are tuned by applying an uniform magnetic field to the atomic cloud. Ideally, this magnetic field should be the same for the whole cloud such that the interaction stretch is kept constant. In order to obtain such a field it is common

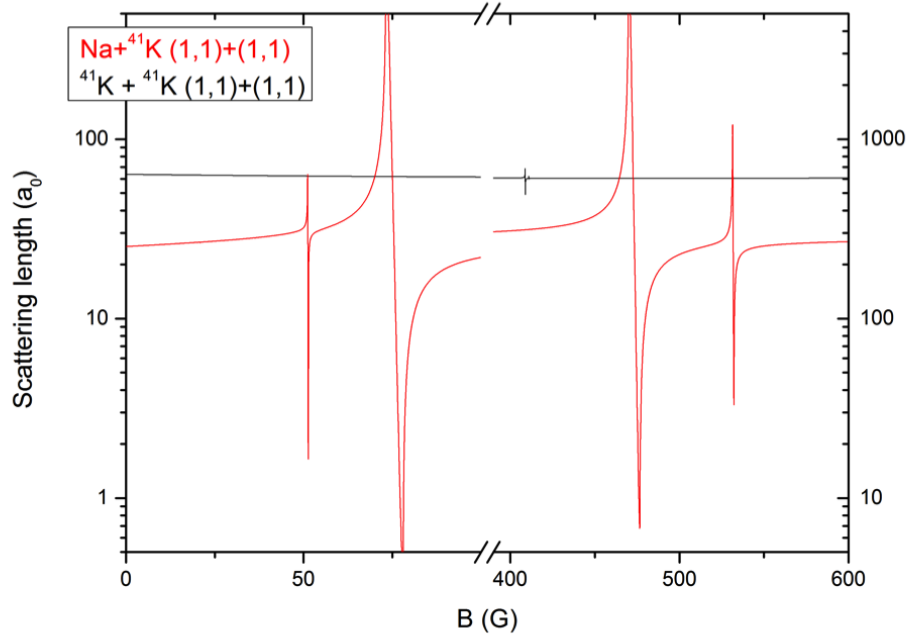


Figure 73 – Simulated Feshbach resonances between ^{23}Na and ^{41}K atoms at the $|1, 1\rangle$ hyperfine state, given by the red curve. The black curve represents the simulated values of the Feshbach resonances of the potassium atoms.
Source: By the author.

the use of a pair of coils assembled in a Helmholtz configuration in which the distance between the coils is equal to its radius.

While designing the Feshbach coils one should try to minimize the current needed to achieve fields close to B_0 since at lower currents the thermal effects are less important and it become easier to stabilize the generated field. In the case of the NaK experiment, the Feshbach coils are mounted around the quadrupole coils and above the re-entrating viewports limiting the internal radius of the coils to be larger than 102 mm. A scheme of the Feshbach coils mounted around the science chamber is illustrated in Fig. 74. The limitation on the internal radius also sets the separation between the coils and currents higher than 40 A are needed to achieve magnetic fields around B_0^2 . Due to the use of high currents, a case similar to the one described for the quadrupole coils (see section 4.4.3 of this chapter) is also necessary in order to proper cool the Feshbach coils.

The final configuration of the Feshbach coils is composed of a pair of circular coils

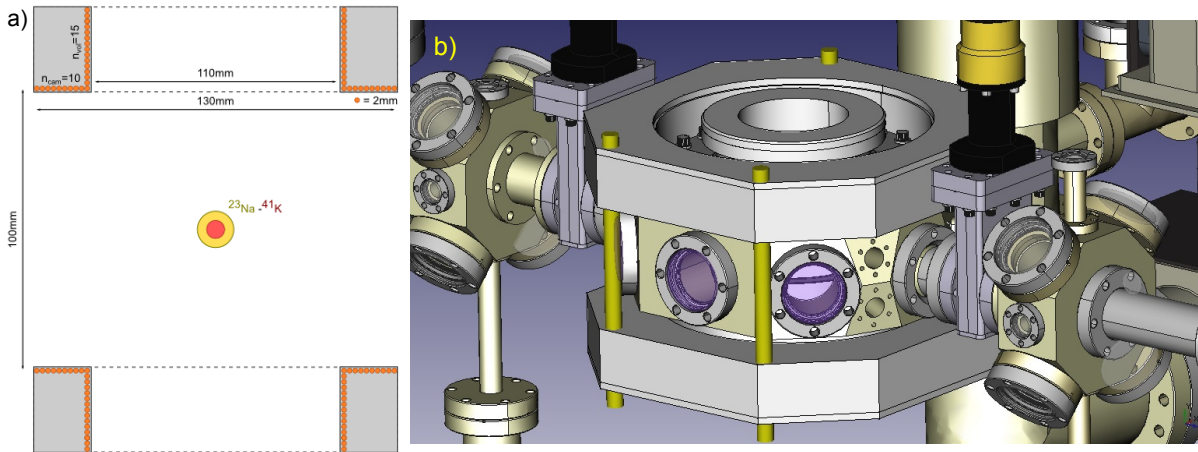


Figure 74 – Scheme (a) and illustration (b) of the Feshbach coils around the science chamber of the NaK experiment.

Source: By the author.

with internal radius equal to 110 mm and composed of 10 layers with 15 turns each of a 2 mm cooper wire. The separation between the coils is approximately of 100 mm, keeping them close to a Helmholtz configuration when considering the central position of the coils and its average radius. Similar to the quadrupole coils, the Feshbach coils were done in our laboratory in an aluminium removable reel and glued with the Duralco 132 epoxy. When mounted the coils inside the case, there are 2 mm of free space around them in order to circulate water at 14°C coming from the same chiller used for the Quadrupole. The upper and lower cases are fixed in each other so that the magnetic field generated by the coils could be measured as it will really be at the experiment. In Fig. 75 the steps in producing the Feshbach coils (a), setting them into the case (b) and mounting up the setup as it is going to be on the experiment (c) are displayed.

The Feshbach field for $I = 1$ A along the main axis of the coils (\hat{z}) measured by a hall probe (CSA-1V) is shown in Fig. 76. The measured field (black dots) is compared with the simulated field (blue curve), showing very small discrepancies. The vertical orange dashed lines represents the center position of each coil. Cold atomic trapped clouds have sizes of a few millimeters and, at these conditions, the measured field is almost constant in its central region. In addition to the field profile measurement, the central value for the magnetic field along \hat{z} , B_0^z , was measured for different currents and we obtained

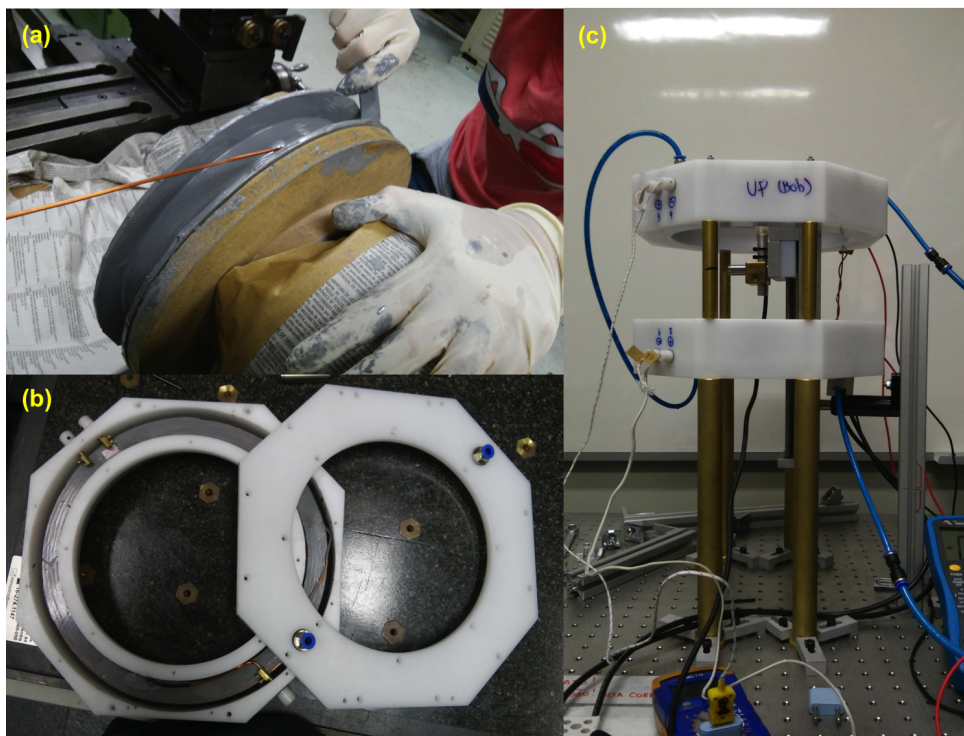


Figure 75 – Stages on building up the Feshbach coils setup. In (a), we show a picture of the Feshbach coils being done in our laboratory. In (b), we show the coil mounted in the case made of Delrin. And in (c) we show the complete Feshbach coil setup as it will be installed around the science chamber of the NaK experiment.
Source: By the author.

$\delta B_0^z / \delta I = 11.2 \text{ G/A}$ while the expected from the simulations was of 10.7 G/A . The fields B_0^1 and B_0^2 are obtained for currents $I_0^1 \sim 6.5 \text{ A}$ and $I_0^2 \sim 42 \text{ A}$.

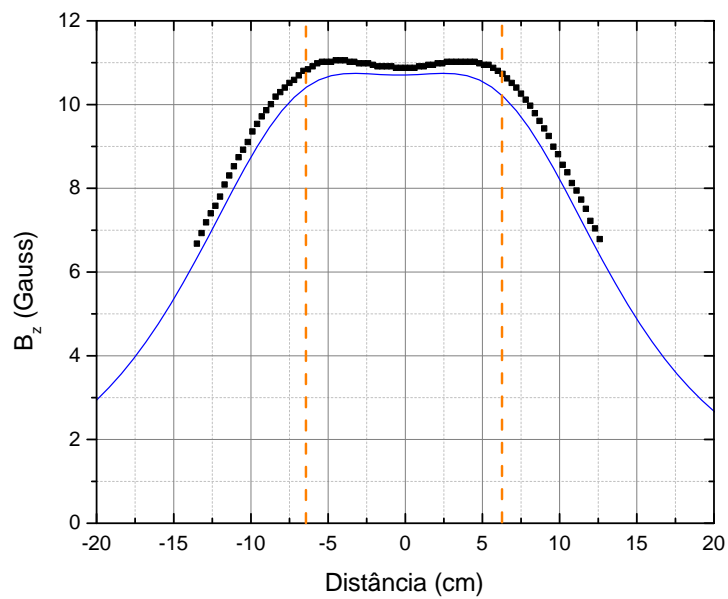


Figure 76 – Characterization of the magnetic field produced by the Feshbach coils for $I = 1$ A. The measure magnetic field is represented by the black squares. The blue curve represents the field obtained through the simulation and the vertical dashed orange lines represents the coils positions.

Source: By the author.

APPENDIX B – Numerical simulation: dimensionless coupled Gross-Pitaevskii equations

Numerical simulations are better performed when working with dimensionless equations in order to keep the results close to unity. A detailed normalization of the Gross-Pitaevskii equation for a single component BEC is presented in Ref. (81) however, for the case of a two-component BEC, we had to derive the dimensionless coupled GPEs adding the gravity contribution, crucial for obtaining the proper ground-state of the system, by ourselves before starting with the simulations. In this Appendix, we present the derivation of the dimensionless coupled GPEs used to perform the numerical simulations with imaginary time evolution in order to obtain the ground-state of the two-component BEC composed of ^{23}Na and ^{41}K discussed in the end of Chapter 2.

The time evolution of an arbitrary trial wavefunction is given in terms of the Hamiltonian that describes the system. In the case of a two-component Bose-Einstein condensate, the statical properties of the system are described in terms of the time-independent coupled Gross-Pitaevskii equations written as:

$$\left[-\frac{\hbar^2}{2m_1} \nabla^2 + \vartheta_1(\mathbf{r}) + u_{11}|\psi_1|^2 + u_{12}|\psi_2|^2 \right] \psi_1 = \mu_1 \psi_1 \quad (\text{B.1})$$

$$\left[-\frac{\hbar^2}{2m_2} \nabla^2 + \vartheta_2(\mathbf{r}) + u_{22}|\psi_2|^2 + u_{12}|\psi_1|^2 \right] \psi_2 = \mu_2 \psi_2, \quad (\text{B.2})$$

where $\vartheta_i(\mathbf{r})$ represents the external potential, $u_{11} = 4\pi\hbar^2 a_{11}/m_1$ and $u_{22} = 4\pi\hbar^2 a_{22}/m_2$ are the strength of the intraspecies interaction, with a_{11} (a_{22}) and m_1 (m_2) being the s -wave scattering length and the mass of species 1 (2). The term $u_{12} = 2\pi\hbar^2 a_{12}/m_{12} = u_{21}$ that couples the two equations represents the interspecies interaction, with a_{12} being the interspecies s -wave scattering length and $m_{12} = m_1 m_2 / (m_1 + m_2)$, the reduced mass of

the system.

In dealing with atomic species of different masses, the external potential should also account for the gravity contribution and we can consider:

$$\vartheta_i(\mathbf{r}) = \frac{1}{2}m_i \sum_{j=x,y,z} \omega_j^i x_j^2 + m_i g z, \quad i = 1, 2, \quad (\text{B.3})$$

where ω_j^i is the angular trapping frequency for species i and axis j and g is the gravitational acceleration constant.

The dimensionless GPEs are obtained by rescaling energies and lengths by a common parameter for both species. For simplicity, it is possible to choose the parameters related with species 1 such that all energies are rescaled by $\hbar\bar{\omega}_1$ and the dimensionless lengths (x_1, y_1, z_1) are related to the usual lengths (x, y, z) as:

$$x = a_x^1 x_1, \quad y = a_y^1 y_1 \quad \text{and} \quad z = a_z^1 z_1, \quad (\text{B.4})$$

with $a_i^1 = (\hbar/m_1\omega_i^1)^{1/2}$. Following this choice of parameters, the dimensionless wavefunctions for each species ψ_i^1 are given by:

$$\psi_1(\mathbf{r}) = \sqrt{\frac{N_1}{a_{\text{ho}1}^3}} \psi_1^1(\mathbf{r}_1), \quad (\text{B.5})$$

$$\psi_2(\mathbf{r}) = \sqrt{\frac{N_2}{a_{\text{ho}1}^3}} \psi_2^1(\mathbf{r}_1), \quad (\text{B.6})$$

and the dimensionless chemical potential are written as $\mu_{1(2)} = \hbar\bar{\omega}_1\mu_{1(2)}^1$.

In order to calculate the dimensionless coupled GPEs, it is possible to treat each term of Eqs. B.1 and B.2 independently. By starting with the equation for species 1, each of its five terms are written with the new parameters $x_1, y_1, z_1, \psi_1^1(\mathbf{r}_1)$ and $\psi_2^1(\mathbf{r}_1)$ as:

$$-\frac{\hbar^2}{2m_1} \nabla^2 \psi_1(\mathbf{r}) = -\frac{\hbar^2}{2m_1} \left[\frac{1}{(a_x^1)^2} \frac{\partial^2}{\partial x_1^2} + \frac{1}{(a_y^1)^2} \frac{\partial^2}{\partial y_1^2} + \frac{1}{(a_z^1)^2} \frac{\partial^2}{\partial z_1^2} \right] \sqrt{\frac{N_1}{a_{\text{ho}1}^3}} \psi_1^1(\mathbf{r}_1), \quad (\text{B.7})$$

$$\vartheta_1(\mathbf{r})\psi_1(\mathbf{r}) = \left[\frac{\hbar^2}{2m_1} \left(\frac{x_1^2}{(a_x^1)^2} + \frac{y_1^2}{(a_y^1)^2} + \frac{z_1^2}{(a_z^1)^2} \right) + m_1 g a_z^1 z_1 \right] \sqrt{\frac{N_1}{a_{\text{ho}1}^3}} \psi_1^1(\mathbf{r}_1), \quad (\text{B.8})$$

$$\frac{4\pi\hbar^2 a_{11}}{m_1} |\psi_1(\mathbf{r})|^2 \psi_1(\mathbf{r}) = \frac{4\pi\hbar^2 a_{11}}{m_1} \left(\frac{N_1}{a_{\text{ho}1}^3} \right)^{3/2} |\psi_1^1(\mathbf{r}_1)|^2 \psi_1^1(\mathbf{r}_1), \quad (\text{B.9})$$

$$\frac{2\pi\hbar^2 a_{12}}{m_{12}} |\psi_2(\mathbf{r})|^2 \psi_1(\mathbf{r}) = \frac{2\pi\hbar^2 a_{12}}{m_{12}} \frac{(N_2^2 N_1)^{1/2}}{(a_{\text{ho}1}^3)^{3/2}} |\psi_2^1(\mathbf{r}_1)|^2 \psi_1^1(\mathbf{r}_1) \quad \text{and} \quad (\text{B.10})$$

$$\mu_1 \psi_1(\mathbf{r}) = \mu_1 \sqrt{\frac{N_1}{a_{\text{ho}1}^3}} \psi_1^1(\mathbf{r}_1). \quad (\text{B.11})$$

Multiplying these new terms by $\frac{2m_1}{\hbar^2} a_{\text{ho}1}^2 \sqrt{\frac{a_{\text{ho}1}^3}{N_1}}$, one can finally obtain the dimensionless Gross-Pitaevskii equation for species 1 as:

$$\left[- \left(\frac{1}{\lambda_x^2} \frac{\partial^2}{\partial x_1^2} + \frac{1}{\lambda_y^2} \frac{\partial^2}{\partial y_1^2} + \frac{1}{\lambda_z^2} \frac{\partial^2}{\partial z_1^2} \right) + \left(\frac{x_1^2}{\lambda_x^2} + \frac{y_1^2}{\lambda_y^2} + \frac{z_1^2}{\lambda_z^2} \right) + G_1 z_1 \right. \\ \left. + u_{\text{GP}1} |\psi_1^1(\mathbf{r}_1)|^2 + u_{\text{GP}12} |\psi_2^1(\mathbf{r}_1)|^2 \right] \psi_1^1(\mathbf{r}_1) = 2\mu_1^1 \psi_1^1(\mathbf{r}_1), \quad (\text{B.12})$$

with $G_1 = 2m_1^2 a_z^1 a_{\text{ho}1}^2 g / \hbar^2$, $u_{\text{GP}1} = 8\pi a_{11} N_1 / a_{\text{ho}1}$ and $u_{\text{GP}12} = 4\pi a_{12} N_2 m_1 / a_{\text{ho}1} m_{12}$.

The same can be done for the equation of species 2, such that each term is written in term of the new parameters as:

$$-\frac{\hbar^2}{2m_2} \nabla^2 \psi_2(\mathbf{r}) = -\frac{\hbar^2}{2m_2} \left[\frac{1}{(a_x^1)^2} \frac{\partial^2}{\partial x_1^2} + \frac{1}{(a_y^1)^2} \frac{\partial^2}{\partial y_1^2} + \frac{1}{(a_z^1)^2} \frac{\partial^2}{\partial z_1^2} \right] \sqrt{\frac{N_2}{a_{\text{ho}1}^3}} \psi_2^1(\mathbf{r}_1), \quad (\text{B.13})$$

$$\vartheta_2(\mathbf{r}) \psi_2(\mathbf{r}) = \left[\frac{\hbar^2}{2m_2} \left(\frac{(a_x^1)^2}{(a_x^2)^4} x_1^2 + \frac{(a_y^1)^2}{(a_y^2)^4} y_1^2 + \frac{(a_z^1)^2}{(a_z^2)^4} z_1^2 \right) + m_2 g a_z^1 z_1 \right] \sqrt{\frac{N_2}{a_{\text{ho}1}^3}} \psi_2^1(\mathbf{r}_1), \quad (\text{B.14})$$

$$\frac{4\pi\hbar^2 a_{22}}{m_2} |\psi_2(\mathbf{r})|^2 \psi_2(\mathbf{r}) = \frac{4\pi\hbar^2 a_{22}}{m_2} \left(\frac{N_2}{a_{\text{ho}1}^3} \right)^{3/2} |\psi_2^1(\mathbf{r}_1)|^2 \psi_2^1(\mathbf{r}_1), \quad (\text{B.15})$$

$$\frac{2\pi\hbar^2 a_{12}}{m_{12}} |\psi_1(\mathbf{r})|^2 \psi_2(\mathbf{r}) = \frac{2\pi\hbar^2 a_{12}}{m_{12}} \frac{(N_1^2 N_2)^{1/2}}{(a_{\text{ho}1}^3)^{3/2}} |\psi_1^1(\mathbf{r}_1)|^2 \psi_2^1(\mathbf{r}_1) \quad \text{and} \quad (\text{B.16})$$

$$\mu_2 \psi_2(\mathbf{r}) = \mu_2 \sqrt{\frac{N_2}{a_{\text{ho}1}^3}} \psi_2^1(\mathbf{r}_1). \quad (\text{B.17})$$

Multiplying these new terms by $\frac{2m_2}{\hbar^2} a_{\text{ho}1}^2 \sqrt{\frac{a_{\text{ho}1}^3}{N_2}}$ and defining $\beta_i = a_{\text{ho}1}^2 \frac{(a_i^1)^2}{(a_i^2)^4}$, the dimensionless Gross-Pitaevskii equation for species 2 becomes:

$$\left[- \left(\frac{1}{\lambda_x^2} \frac{\partial^2}{\partial x_1^2} + \frac{1}{\lambda_y^2} \frac{\partial^2}{\partial y_1^2} + \frac{1}{\lambda_z^2} \frac{\partial^2}{\partial z_1^2} \right) + \left(\beta_x^2 x_1^2 + \beta_y^2 y_1^2 + \beta_z^2 z_1^2 \right) + G_2 z_1 \right. \\ \left. + u_{\text{GP}2} |\psi_2^1(\mathbf{r}_1)|^2 + u_{\text{GP}21} |\psi_1^1(\mathbf{r}_1)|^2 \right] \psi_2^1(\mathbf{r}_1) = 2 \frac{m_2}{m_1} \mu_2^1 \psi_2^1(\mathbf{r}_1), \quad (\text{B.18})$$

with $G_2 = 2m_2^2 a_z^1 a_{\text{ho}1}^2 g / \hbar^2$, $u_{\text{GP}2} = 8\pi a_{22} N_2 / a_{\text{ho}1}$ and $u_{\text{GP}21} = 4\pi a_{12} N_1 m_2 / a_{\text{ho}1} m_{12}$.

The numerical simulation with imaginary time evolution is performed making it evolve two initial Gaussian trial functions (one for each species), centred with the center of the trapping potential, subjected to the dimensionless coupled GPEs derived above. In order to keep the same time interval for each species at each step in our simulation, the mass ratio term m_2/m_1 in the right side of the GPE for species 2 need to be taken into account, passing to the left side of the equation.

APPENDIX C – The Plug trap setup and configuration

In this Appendix we present the experimental details of the Plug trap. We start by presenting the characterization of the Quadrupole field produced by a pair of coils produced in our laboratory. Latter, we describe the optical setup and the characterization of the plug beam.

C.1 The Quadrupole field configuration

The coils used to produce the quadrupole field necessary for the Quadrupole trap were made in the laboratory and consist of circular coils with internal radius of 40.4 mm. They are composed by 10 layers with 16 turns each of an isolated cooper wire with a diameter of 2.18 mm. The coils were winded up around a removable aluminium reel with an epoxy (Duralco 132) that has a high thermal conductivity ensuring a good dissipation of the dissipated power while operating the trap. However, this dissipation is not enough and a more sophisticated cooling system is needed. For this purpose, after the epoxy is dried, the coils were mounted inside a case with channels through which water at 14°C coming from a chiller could circulate. One of the coils mounted in the case is illustrated on Fig. 77 (a). The cases are made of Delrin, a resistant non-magnetic material to avoid induced currents and they are placed inside the re-entrating viewports along the \hat{z} axis of the science chamber (see Fig. 15 in the main part of this theses). A simple scheme of the quadrupole coils setup around the vacuum system is illustrated on Fig. 77 (b). Even inside the re-entrating viewports, the coils are separated by 62 mm and 45 A are necessary to generate a magnetic field gradient of 200 G/cm. Besides the quadrupole coils, there is an extra pair of coils mounted in the case which can also be seen in the scheme. These coils are used to generate a compensation field that improves the transfer of the atoms from the MOT to the Quadrupole trap.

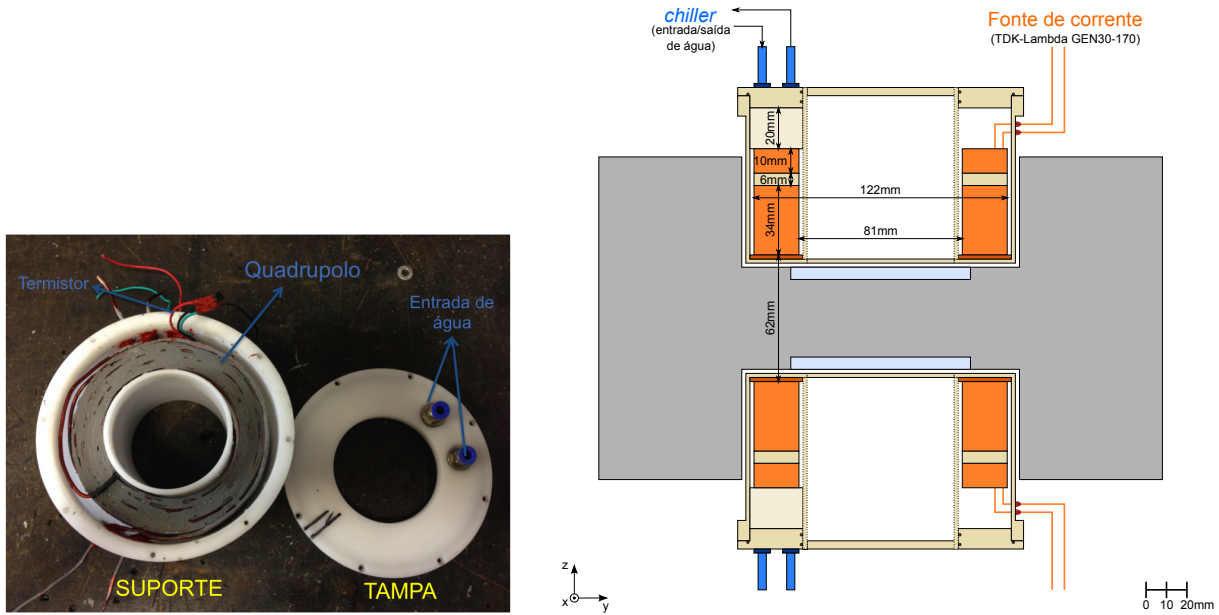


Figure 77 – (a) Picture of the one Quadrupole coil mounted inside the housing. (b) Scheme of the quadrupole coils setup around the science chamber of the NaK vacuum system, represented in gray.

Source: By the author.

The power supply used to generate the current needed for the Quadrupole trap is a Delta Power Supply 3300 series operating as a voltage power supply. This power supply has been widely used in cold atom experiments due to its low signal to noise ratio and to the possibility of easy remote control by means of an analogue channel. A transducer (LEM LT 25-NP) monitors the Quadrupole current and, in the future, it could be used to stabilize it together with a PID controller. Finally, a ultra-fast IGB (SKM150GAR12T4) is connected in series with the coils in order to enable a fast turn on/off switch of the magnetic field (with $t_{1/e} \sim 500\mu s$). The magnetic field profile along the axis of the trap was measured with a hall probe (CSA-1V) just before installing the coils into the experiment and it differs less than 5% of one should expect from the simulations performed with the Radia package for Mathematica.

C.2 The Plug optical setup

The blue-detuned light used to produce the plug beam is generated by a Coherent Verdi V10 laser with $\lambda = 532\text{nm}$ and maximum output power of 10W. The optical setup was done in order to provide a good Gaussian beam shape and beam position stability

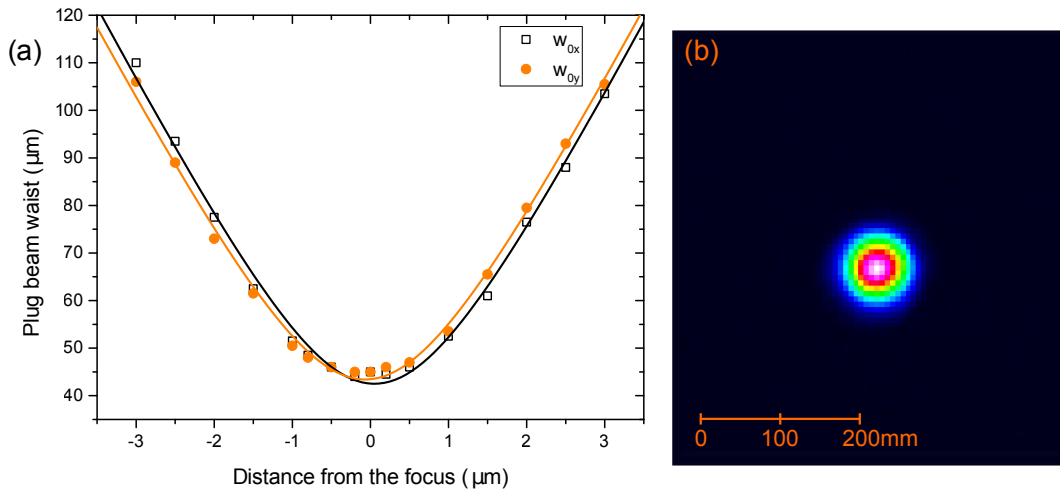


Figure 78 – (a) Measurement of the Plug beam waist around the focus. The behaviour of w_{0x} and w_{0y} follow the expected behaviour for a Gaussian beam. In (b), it is shown a picture of the Plug beam at the focus.

Source: By the author.

such that a high power polarization maintaining optical fiber (NKT fiber with Shafter & Kirchoff input/output collimators) was used.

The light coming out from the Verdi V10 is separated in order to generate the Plug beam and the *stirring* beam that will be used to generate vortices in the ^{23}Na BEC as it was described in Chapter 6. The Plug beam passes through an AOM that controls the beam intensity and also works as a fast switch. Later, the light is coupled into the optical fiber. Since we are dealing with a high power laser, a lot of care has to be put in coupling it to the fiber and, even so, the efficiencies obtained are still low (around 60%). After the fiber, the beam has a very good Gaussian profile and it is expanded such that it can be focused at the atoms position by a 600 mm focal length lens with $w_0 = 43 \mu\text{m}$. This last part of the Plug beam optical setup is illustrated in Fig. 21 of Chapter 4.

The Plug beam profile around its focus region was measured outside the experiment and its waist propagation matches the expected behaviour for a Gaussian beam. The graph in Fig. 78 (a) shows the measured w_{0x} and w_{0y} as a function of position and in (b) we show a picture of the beam at the focus.

A mechanical shutter is added right before the Plug beam enters into the science chamber in such a way that the Plug beam could be on during the whole experimental

sequence ensuring a better thermal stability. Finally, the plug power is monitored by a fast photodiode through the leak of the dichroic mirror used to combine the plug beam with the horizontal imaging beam, as depicted in Fig. 21.

APPENDIX D – The laser system for Potassium atoms

In order to generate all the light necessary to trap, cool and manipulate the internal states of Potassium atoms during the experimental sequence, we use two Toptica lasers TA-Pro with $\lambda = 767\text{nm}$. The first one, generating the light with frequency close to the cooling transition ($|F = 2\rangle \rightarrow |F' = 3\rangle$), is called *Cooling Laser* and the second one, generating light with frequency close to the repumper transition ($|F = 1\rangle \rightarrow |F' = 2\rangle$), is called *Repumper Laser*. The emission frequencies of the lasers are kept fixed by frequency locking it with respect to the dispersion signal generated from the absorption signal obtained through the use of the saturated absorption spectroscopy technique. (157) For this purpose, we use the Toptica digital lock-in software and a typical absorption (in red) and dispersion (in gray) signals are shown in Figure 79. The transitions from each ground state to the D_2 excited states are indicated as well as the ground state crossover (C.O.)¹ which is used for locking the laser. Since the ^{39}K is the most abundant isotope, its transitions are more evident in the absorption profile but it is also possible to observe the ^{41}K $F = 2$ and C.O. transitions.

By taking the ^{39}K crossover transition as reference, the cooling and repumper transitions for the ^{39}K (^{41}K) are dislocated of ± 230 MHz ($\pm 230 + 236$ MHz) and the laser system was designed in order to be able to change the isotope by just changing the AOM in the saturated absorption spectroscopy scheme. For the ^{39}K atoms, a double-pass AOM at 200MHz is used for the *Cooling Laser* and a single-pass AOM at 200 MHz for the *Repumper Laser*. In changing for the ^{41}K a double-pass AOM at 80 MHz is used

¹ The crossover transition of the ground state happens at the middle frequency between the energies of $F = 1$ and $F = 2$ states. Different from the crossover transitions that occur between the excited states, in the ground state we observe an inverted peak with respect to the real transitions, which means, we observe an abrupt increase in the absorption of light. This can be explained by noticing that, at such frequency, the same atoms with an specific velocity can absorb photons from any of the two beams used in the saturated absorption spectroscopy technique in such a way that both ground states transitions could be done, increasing the light absorption. (157)

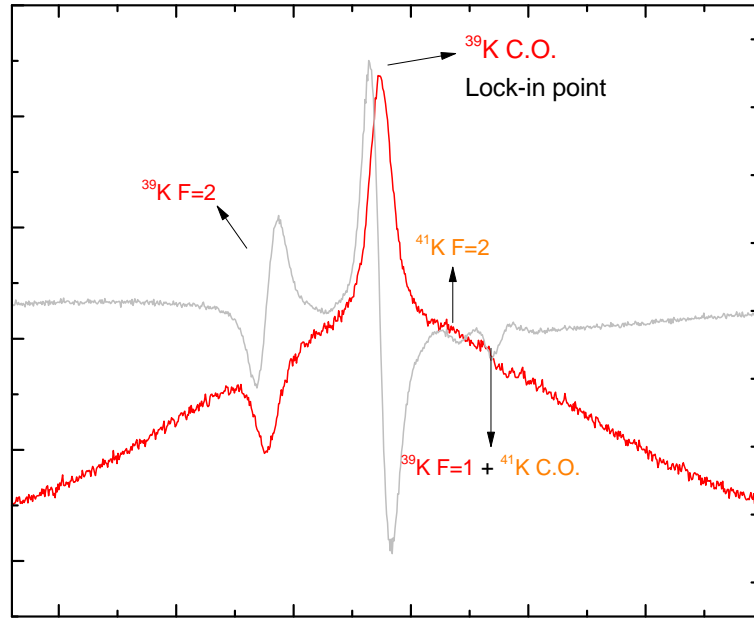


Figure 79 – Typical absorption (in red) and dispersion (in gray) signals obtained from the saturated absorption spectroscopy and used to frequency lock the Potassium lasers. The transitions from each ground state to the D_2 line excited states are indicated as well as the ground state crossover (C.O.), which is the locking point.
Source: By the author.

only for the pump beam of the saturated absorption spectroscopy scheme for both lasers. The optical setup scheme for the saturated absorption together with the whole D_2 line optical system for Potassium atoms is illustrated in Figure 80. The double-pass AOMs are used to fine tune the frequencies during the different stages of the experimental sequence described in Chapter 5.

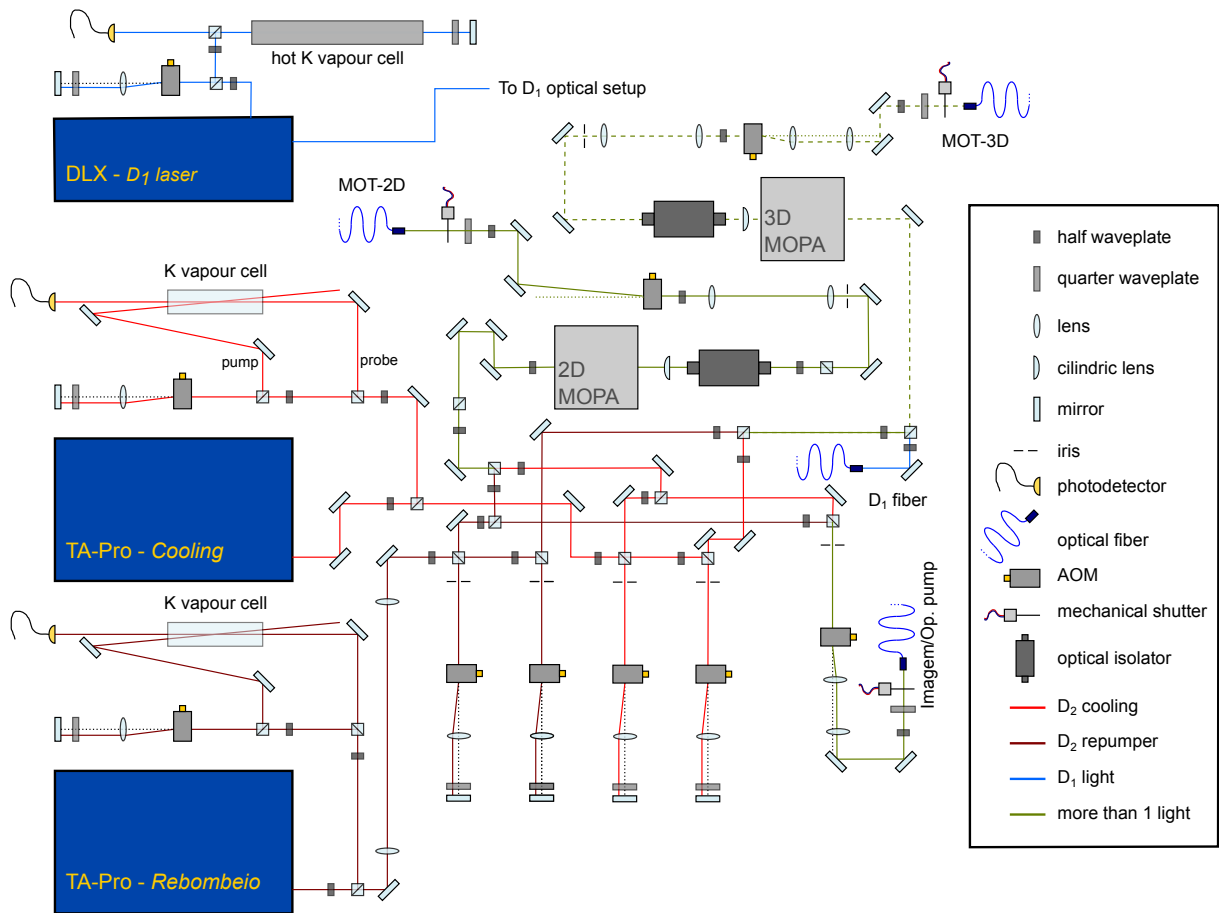


Figure 80 – Scheme of the laser setup for potassium atoms. The saturated absorption spectroscopy scheme is placed above the lasers and the pump and probe beams are indicated. The homemade MOPAs are also indicated in the figure. The D₂ light is represented with light red lines (for lights with frequencies close to the cooling transition) and with dark red lines (for lights with frequencies close to the repumper transition). The D₁ light is represented with blue lines. The green lines represent lights with more than one frequency: solid black line (D₂ lights) and dashed black line (D₂ + D₁ lights)

Source: By the author.

